# Confirmation of exoplanet candidates in the Wide-Angle Search for Planets survey via Doppler tomography

**Lorna Yvonne Temple**

Doctor of Philosophy

Department of Physics, Keele University

June 2020

# Abstract

This work reports the discovery of four new exoplanets, with host stars in the relatively sparse spectral type range mid-F–A. The planets were discovered using the transit method and confirmed via Doppler tomography. The first is WASP-167b/KELT-13b, a hot Jupiter with a radius of $1.5\,\mathrm{R_{Jup}}$ and a mass $<8\,\mathrm{M_{Jup}}$, on a retrograde, 2.02-d orbit around a $V=10.5$, F1V star with $[\mathrm{Fe/H}]=0.1\pm0.1$. The measured sky-projected spin–orbit angle is $\lambda = -165^\circ \pm 5^\circ$. Evidence of non-radial stellar pulsations were detected in the tomographic data, making the host star a $\delta$-Scuti or $\gamma$-Dor variable. The second planet is WASP-174b, a $<1.3\,\mathrm{M_{Jup}}$ planet with a near-grazing transit on a 4.23-d orbit around a $V=11.9$, F6V star with $[\mathrm{Fe/H}]=0.09\pm0.09$. The measured obliquity is $\lambda=31^\circ\pm1^\circ$. Owing to the grazing transit the planet's radius is uncertain, with a possible range of 0.8–$1.8\,\mathrm{R_{Jup}}$. The third planet, WASP-190b, is a hot Jupiter on a 5.37-day orbit around a mildly-evolved F6 IV-V star with $V=11.7$, $T_{\rm eff}=6400\pm100\,\mathrm{K}$, $M_*=1.35\pm0.05\,M_\odot$ and $R_*=1.6\pm0.1\,R_\odot$. The planet has a radius of $R_{\rm P}=1.15\pm0.09\,R_{\rm Jup}$ and a mass of $M_{\rm P}=1.0\pm0.1\,M_{\rm Jup}$. WASP-190b was the first hot Jupiter confirmed via Doppler tomography with an orbital period $>5$ days. The orbit is also marginally misaligned with respect to the stellar rotation, with $\lambda=21\pm6^\circ$ measured using Doppler tomography. And fourth, WASP-180Ab is a hot Jupiter with $M_{\rm P}=0.9\pm0.1\,M_{\rm Jup}$ and $R_{\rm P}=1.24\pm0.04\,R_{\rm Jup}$. The orbit is misaligned and retrograde, with $\lambda=-157\pm2^\circ$. The host star has $T_{\rm eff}=6500\,\mathrm{K}$ and a moderate rotation speed of $v\sin i_\star=19.9\,\mathrm{km\,s^{-1}}$, and is the primary of a $V=10.7$ binary, where a secondary separated by $\sim5''$ ($\sim$1200 AU) contributes $\sim30\%$ of the light. These discoveries are in line with the known tendency for orbits around hotter stars to be more likely to be misaligned. Of the pre-vetted candidate planetary systems selected for tomographic analysis, 3 in 5 were found to be genuine planet detections.

# Acknowledgements

Firstly, I would like to thank my Supervisor, Prof. Coel Hellier, for his guidance and invaluable knowledge. I would also like to thank the WASP team for their support, and for developing the instruments, tools and codes used in this work. Specifically, A. Collier Cameron, D.J.A. Brown and D.R. Anderson made extensive contributions to the development of the WASP data reduction pipeline and MCMC analysis code used for WASP candidate planets. D.R. Anderson was also largely responsible for the reduction of the WASP data for the planets presented in this work. A significant number of the WASP team members are also members of the TRAPPIST and/or SPECULOOS teams, and were involved in the development and commissioning of those telescopes as well as in the taking and reduction of the photometric follow up data used in this work: Y. Almleaky, F. Bouchy, A. Burdanov, L. Delrez, E. Ducrot, M. Gillon, R. Hall, E. Jehin, J. McCormac, C. Murray, F. Pepe, D. Queloz, D. Ségransan, S. Sohy, S. Thompson and S. Udry. A.H.M.J. Triaud, L. D. Nielsen and O.D. Turner were involved with taking follow-up spectra with the Euler/CORALIE spectrograph, and with reducing CORALIE and HARPS data, producing cross-correlation functions and measuring radial velocities of WASP candidates. B. Smalley, with his expertise in stellar spectroscopy, carried out the spectral analyses for the candidate host stars, and in some cases also performed an IRFM analysis. P.F.L Maxted was responsible for the development of the open source software BAGEMASS that is used as standard to determine the ages of WASP systems, and also for searching for periodicities of stellar origin in WASP data.

WASP-South was hosted by the South African Astronomical Observatory. Funding for WASP came from consortium universities and from the UK's Science and Technology Facilities Council. The Euler Swiss telescope is supported by the Swiss National Science Foundation. TRAPPIST-South is funded by the Belgian Fund for Scientific Research (Fond National de la Recherche Scientifique, FNRS) under the grant FRFC 2.5.594.09.F, with the participation of the Swiss National Science Foundation (SNF).

M. Gillon is a FNRS Research Associate and E. Jehin is a FNRS Senior Research Associate. This research received funding from the European Research Council under the FP/2007-2013 ERC Grant Agreement n 336480, and from the ARC grant for Concerted Research Actions, financed by the Wallonia-Brussels Federation, and partially from a grant from the Simons Foundation (ID 327127 to Didier Queloz). L. Delrez acknowledges support from the Gruber Foundation Fellowship. We acknowledge use of the ESO 3.6-m/HARPS under programs 096.C-0762 (PI C. Hellier), 0100.C-0847(A) (PI C. Hellier), and 0102.C-0414 (PI L. Nielsen).

Now, turning to a specific work, Temple et al. (2017) was written in collaboration with the Kilodegree Extremely Little Telescope (KELT) team, so I would also like to extend my thanks to them for the excellent work done in obtaining and reducing follow up data for WASP-167b/KELT-13b, and for their detailed SED analysis. Work performed by P.A. Cargile was supported by NASA grant NNX13AI46G. D.J. Stevens and B.S. Gaudi were partially supported by NSF CAREER Grant AST-1056524. S. Villanueva Jr. is supported by the National Science Foundation Graduate Research Fellowship under Grant No. DGE-1343012. Work performed by J.E. Rodriguez was supported by the Harvard Future Faculty Leaders Postdoctoral fellowship.

Lorna Temple
MSci (Hons.) Astrophysics UCL
August 2019

# Contents

**Abstract** . . . . . **i**
**Acknowledgements** . . . . . **ii**
**1 Introduction** . . . . . **1**
1.1 The search for exoplanets . . . . . 1
1.2 Defining an 'exoplanet' . . . . . 8
1.2.1 The working definition of an exoplanet . . . . . 8
1.2.2 The formation of planets and brown dwarfs . . . . . 10
1.2.3 What might a formation-based definition look like? . . . . . 12
1.3 Exoplanet discovery via the transit method . . . . . 14
1.3.1 What is the transit method? . . . . . 14
1.3.2 The probability of transits . . . . . 20
1.3.3 How to find transiting planets . . . . . 21
1.3.4 Transit false positives . . . . . 22
1.4 Confirmation of transiting planet candidates . . . . . 23
1.4.1 Measuring the radial velocity orbit . . . . . 24
1.4.2 The Rossiter-McLaughlin effect . . . . . 24
1.4.3 The Kraft Break and the hot stars problem . . . . . 26
1.4.4 Candidate confirmation for hot stars: Doppler tomography . . . 27
1.5 Aims and objectives . . . . . 30
1.6 The hottest of hot Jupiters: Further characterisation . . . . . 30
1.6.1 Atmospheric Characterisation of transiting hot Jupiters . . . . . 32
1.6.2 Mass loss from hot Jupiter atmospheres . . . . . 35
1.6.3 Formation and evolution of hot Jupiter systems . . . . . 37
**2 Instrumentation and Methods** . . . . . **39**
2.1 Initial detection and Candidate Vetting . . . . . 39
2.1.1 The WASP-South survey . . . . . 39
2.1.2 WASP data reduction . . . . . 40
2.1.3 Transit search and candidate selection . . . . . 41
2.2 Candidate WASP targets for tomographic confirmation . . . . . 43
2.3 Follow-up Observations . . . . . 44
2.3.1 Photometry: the TRAPPIST and SPECULOOS telescopes . . . 44
2.3.2 Radial velocities: Euler/CORALIE . . . . . 45
2.3.3 Tomographic data: ESO3.6m/HARPS . . . . . 46
2.3.4 Inspection of tomographic data . . . . . 47
2.4 Combined MCMC analysis Characterisation of transiting exoplanets . 49
2.4.1 Step 1: Spectral analysis . . . . . 49
2.4.2 Step 2: Photometric, RV and tomographic analysis . . . . . 50

**3 WASP-167b/KELT-13b . . . 53**
3.1 Abstract . . . 53
3.2 Data and observations . . . 53
3.3 Spectral analysis . . . 56
3.4 Photometric and radial velocity analysis . . . 57
3.5 Doppler tomography . . . 61
3.6 Evolutionary status . . . 66
3.7 Discussion and conclusions . . . 67
3.7.1 Stellar rotation rate and tidal interaction . . . 67
3.7.2 The retrograde orbit . . . 69
3.7.3 Stellar pulsations . . . 70
**4 WASP-174b . . . 72**
4.1 Abstract . . . 72
4.2 Data and observations . . . 72
4.3 Spectral analysis . . . 73
4.4 Combined analyses . . . 75
4.4.1 A grazing transit . . . 76
4.4.2 The planet's mass . . . 79
4.4.3 The Doppler track . . . 80
4.5 Stellar age determination . . . 81
4.6 Discussion and conclusions . . . 82
**5 WASP-190b . . . 86**
5.1 Abstract . . . 86
5.2 Data and observations . . . 86
5.3 Stellar parameters from spectral analysis . . . 87
5.4 Combined MCMC analysis . . . 89
5.5 Results for the star . . . 91
5.6 Results for the planet . . . 94
5.7 Discussion and Conclusions . . . 96
**6 WASP-180Ab . . . 99**
6.1 Abstract . . . 99
6.2 Data and Observations . . . 99
6.3 Spectral analysis . . . 101
6.4 The distant co-moving companion . . . 103
6.4.1 Correcting for dilution . . . 103
6.4.2 IRFM analysis . . . 104
6.4.3 Rotational modulation search . . . 105
6.5 Combined MCMC analysis . . . 107
6.6 System age determination . . . 111
6.7 Conclusions and discussion . . . 113

**7 Tomographic non-detections of exoplanet candidates . . . . . 116**
7.0.1 Candidate SW0551 . . . . . 116
7.0.2 Candidate SW0647 . . . . . 117
7.0.3 Candidate SW0623 . . . . . 117
7.0.4 Candidate SW0025 . . . . . 119
**8 Discussion . . . . . 120**
8.1 The known exoplanet population . . . . . 120
8.2 Mass-radius diagram . . . . . 123
8.3 The distribution of obliquities . . . . . 125
8.4 Prospects for further characterisation . . . . . 129
8.5 The future of exoplanet search . . . . . 130
**Publications . . . . . 133**
**Bibliography . . . . . 135**

# List of Figures

1.1 Chart showing the number of exoplanet discoveries per year since the first in 1989, as of 2019/08/27. The discoveries are grouped by detection method. Data were taken from the NASA Exoplanet Archive[1]. . . . . 7

1.2 Schematic diagram showing a planetary transit taken from Fig. 2 of Winn et al. (2010) and adapted to match the notation used in this work. At time $t_1$, the transit begins and the flux received from the star starts to decrease. At $t_2$, the planet is fully in front of the stellar disc and thus the flux from the star has reached its minimum level, at which it will remain until the planet begins to exit the stellar disc at time $t_3$: the total change in flux is labelled as $\Delta F$. The flux level then rises again, reaching its original level at time $t_4$ when the planet has completely left the stellar disc. The time taken for the planet to go from $t_1$ to $t_2$ is known as the transit ingress, while the time taken from $t_3$ to $t_4$ is the transit egress. $t_1$, $t_2$, $t_3$ and $t_4$ are referred to as the four transit contact points. Also labelled are the transit duration $T_{14}$, the ingress duration $T_{12}$, and the impact parameter $b$. . . . . 15

1.3 The face-on geometry of an inclined transiting system, defining the quantity $l$ which is half of the transit chord. Adapted from Fig. 3.3 in Haswell 2010b. . . . . 17

1.4 The side-on geometry of a transiting system. During transit, the planet passes from point A to point B, subtending an angle $\alpha$ at the centre of the star. Also shown are the inclination $i$, the transit chord $2l$, and the orbital separation $a$. Adapted from Fig. 3.4 in Haswell 2010b. . . . . 18

1.5 Transit lightcurves for different passbands, generated using the BATMAN software of Kreidberg (2015), which demonstrate the effects of limb darkening in different wavelengths. In constructing this plot, four-parameter non-linear limb darkening coefficients were extracted from the tables of Claret (2000);Claret (2004) for a star of $T_{\rm eff}$ =5500 K and $logg_\star = 4.4$ dex, for passbands UJ (violet), BJ (blue), VJ (green), RC (yellow), IC (orange), JJ (red), HJ (dark red). System parameters were set to $P = 2$ days, $R_{\rm p} = 0.1\,R_\odot$, $a = 15\,R_\odot$ and $i = 87°$. . . . . 20

1.6 The three main types of false positives detected by exoplanet transit searches. 1. An EB with a low-mass secondary. 2. A grazing EB. 3. BEBs: an EB diluted in the light of a nearby bright star (left) or an EB with a low-mass secondary diluted in the light of a nearby bright star (right). Adapted from Fig. 1 Santerne et al. (2013). . . . . 22

1.7 Taken from Figure 2 in Collier Cameron et al. 2010a, which shows a time-series Doppler map of planet residuals obtained for HD 189733b. In constructing this plot a model stellar line profile was subtracted from each CCF, leaving behind a clear Doppler transit signal superimposed on a residual spectrum. The four transit contact points are marked with crosses and $T_C$ is marked with a horizontal dotted line. The vertical dotted line shows the position of the $\gamma$ velocity of the system and is bounded by two dashed lines at $\pm\, v \sin i_\star$. The planet trace is inclined bottom left to top right, indicating a prograde orbit (i.e. the planet moves from the blue-shifted side of the tomogram to the red-shifted side). 28

3.1 The WASP (top) and KELT (bottom) discovery lightcurves for WASP 167b/KELT-13b, folded on the orbital period. The blue lines show the final model obtained in the MCMC fitting (see Section 3.4). . . . . 57

3.2 The 18 follow-up transit lightcurves. The blue lines show the final model obtained in the MCMC fitting (see Section 3.4). The label to the left of each dataset corresponds to an entry in the final column of Table 3.1. . 58

3.3 The 21 CORALIE RVs (green) and 20 TRES RVs (red) obtained for WASP-167/KELT-13. The blue line shows the best fitting semi-amplitude, which we do not regard as reliable. The magenta line shows the RV amplitude for a planet mass of $8\, M_{\rm Jup}$, which we regard as a conservative upper limit. . . . . 60

3.4 The line profiles through transit. We interpret this as showing prograde-moving stellar pulsations and a retrograde-moving planet trace. The white dashed vertical lines mark the positions of the $\gamma$ velocity of the system and the positions of $\gamma \pm v \sin i_\star$ (i.e. the centre and edges of the stellar line profile). The phase of mid-transit is marked by the white horizontal dashed line. The white + symbols indicate the four transit contact points, calculated using the ephemeris obtained in the analysis in Section 3.4. . . . . 62

3.5 The Fourier transform of the line profiles. The stellar pulsations are seen as the diagonal feature from bottom-left to top-right. The weaker diagonal feature running bottom-right to top-left is produced by the planet. . . . . 63

3.6 Centre: the spectral profiles through transit after removing the stellar pulsations via Fourier filtering. The planet trace is then readily seen moving in a retrograde direction. Left: the simultaneous TRAPPIST photometry of the transit. Right: the spectral profiles through transit after removing the planet shadow via Fourier filtering. The stellar pulsations are seen moving in a prograde direction. . . . . 64

3.7 The best fitting evolutionary tracks and isochrones of WASP-167/KELT-13 obtained using BAGEMASS. Dotted blue line: ZAMS at best-fit [Fe/H]. Green dashed lines: evolutionary track for the best-fit [Fe/H] and mass, plus $1\sigma$ bounds. Red lines: isochrone for the best-fit [Fe/H] and age, plus $1\sigma$ bounds. . . . . 68

4.1 The WASP discovery photometry (top) and follow-up transit lightcurves (middle). The blue lines show the final model obtained in the MCMC fitting (see Section 4.4). The bottom panel then shows the residuals of the fit. . . . . 77

4.2 Probability distributions for the parameters $R_{\rm p}$, $R_*$ and $b$, created from the results of the second-mode MCMC run. . . . . 78

4.3 Top: The 16 CORALIE RVs (red points) obtained for WASP-174b . The magenta line shows the expected RV amplitude for a planet of $1.3\,{\rm M_{Jup}}$, our derived upper limit (95 % confidence). The blue line shows the best-fit model including the RM fit. Bottom: the 23 through-transit HARPS RVs (green points). The blue line shows the best-fit model with the Keplerian RV curve subtracted, leaving only the fit to the RM effect. . 79

4.4 Middle: The line profiles through transit, with the mean of the out-of-transit CCFs subtracted. This shows a prograde-moving planet signal in the red-shifted section of the tomogram. Right: the line profile residuals after subtracting the planet model. In each, the white dotted vertical lines mark the positions of $\gamma$ and $\gamma \pm v \sin i_\star$. The phase of mid-transit is marked by the white horizontal dotted line. The white + symbols indicate $T_1$ and $T_4$, calculated using the adopted ephemeris. Left: The TRAPPIST-South lightcurve taken simultaneously with the tomographic observation. . . . . 80

4.5 The transit chord calculated from the fitted values of $R_{\rm p}$, $R_*$, $b$ and $\lambda$ (see Table 4.3.) The dashed circles show the positions of the planet at $1^{\rm st}$ and $4^{\rm th}$ contacts. . . . . 81

4.6 The best fitting evolutionary tracks and isochrones of WASP-174 obtained using BAGEMASS. Black points: individual steps in the MCMC. Dotted blue line: Zero-Age Main Sequence (ZAMS) at best-fit [Fe/H]. Green dashed lines: evolutionary track for the best-fit [Fe/H] and mass, plus $1\sigma$ bounds. Red lines: isochrone for the best-fit [Fe/H] and age, plus $1\sigma$ bounds. Orange star: measured values of $T_{\rm eff}$ and $\rho_*$ for WASP-174 obtained in the spectral and photometric analyses respectively. . . . . 82

5.1 Top: the discovery lightcurve for WASP-190b (WASP-South). Middle: the two follow-up lightcurves with the best-fitting model shown in blue. Bottom: the residuals of the fits to the follow-up lightcurves. . . . . 90

5.2 The best fitting evolutionary tracks and isochrones of WASP-190 obtained using BAGEMASS. Black points: individual realisations of the MCMC. Dotted blue line: Zero-Age Main Sequence (ZAMS) at best-fit [Fe/H]. Green dashed lines: evolutionary track for the best-fit [Fe/H] and mass, plus $1\sigma$ bounds. Red lines: isochrone for the best-fit [Fe/H] and age, plus $1\sigma$ bounds. Orange star: measured values of $T_{\rm eff}$ and $\rho_*$ for WASP-190 obtained in the spectral and photometric analyses respectively. 94
5.3 Top: The HARPS RV measurements used in the analysis of WASP-190b. The blue line shows the best-fit Keplerian RV curve and the fit to the RM effect. Centre: the bisectors for the out-of-transit RVs plotted against phase, which show no correlation with the RV measurements. Bottom: The region around transit on a larger scale. . . . . 95
5.4 Centre-left: The Doppler tomogram comprised of the time series of residual HARPS CCFs calculated by subtracting the average of the out-of-transit CCFs from all CCFs. Left: the SPECULOOS-Europa lightcurve taken simultaneously with the HARPS observation. Centre-right: The best-fit planet model. Right: the residuals remaining after subtracting the best-fit planet model from the centre-left tomogram. In the three tomographic panels, the start and end times of the transit are marked with horizontal white dashes, while the vertical dashes mark respectively the positions of $\gamma$-$v \sin i_\star$ , $\gamma$ and $\gamma$+$v \sin i_\star$ . We interpret the tomogram as showing a very faint, prograde planet signal which in places is completely masked by background noise. . . . . 96
5.5 $R_{\rm p}$ vs. $T_{\rm eql}$, colour coded by mass, of all known planets with $0.6\,M_{\rm Jup} < M_{\rm p} < 4.0\,M_{\rm Jup}$. WASP-190b is displayed including the error bars on the measured radius and temperature. . . . . 98
6.1 Results of the rotational modulation search of the WASP photometry of WASP-180. The three rows show the periodogram (left) and phase-folded light curve (right) for each chunk of data, displayed in the same order as they are listed in Table 6.4. The horizontal dashed line in each of the periodograms corresponds to a confidence level of 99%. . . . . 106
6.2 The WASP discovery photometry (top) and follow-up transit lightcurves (bottom) with the best-fitting model shown in blue. (see Section 6.5). The data for the three follow-up lightcurves, prior to the dilution correction, are available online as supporting material. . . . . 108
6.3 Top: All RV measurements of WASP-180A used in this work together with the best-fit model shown in green. The red points are CORALIE measurements and the blue points are HARPS measurements. Middle: the bisector (BS) measurements corresponding to the RVs in the top panel. Bottom: The RV measurements taken during transit and best-fit RM model. . . . . 109

6.4 The Doppler tomogram for WASP-180Ab, showing the strong retrograde planet trace (middle) and simultaneous photometric observation alongside (left). The right-hand panel shows the residuals remaining after subtracting the fit to the perturbation due to the planet (see Section 6.5). The white vertical dashes in the centre and right-hand panels mark the positions of $\gamma$ and $\gamma \pm v \sin i_\star$ while the white horizontal dashes indicate the times of 1$^{\text{st}}$ and 4th contacts of the planet. . . . . 111

6.5 The best fitting evolutionary tracks and isochrones of WASP-180A obtained using BAGEMASS. Black points: individual steps in the MCMC. Green dashed lines: evolutionary track for the best-fit [Fe/H] and mass, plus $1\sigma$ bounds. The Red lines: isochrone for the best-fit [Fe/H] and age, plus $1\sigma$ bounds. The lower bound isochrone is also the Zero-Age Main Sequence (ZAMS) at best-fit [Fe/H]. Orange star: measured values of $T_{\text{eff}}$ and $\rho_*$ for WASP-180A obtained in the spectral and photometric analyses respectively. . . . . 112

6.6 A colour-magnitude diagram showing the positions of WASP-180A and its comoving companion star with respect to isochrones from Marigo et al. (2017) for the ages 0.1, 1, 2, 3 and 5 Gyr ($Z = 0.024 \sim [Fe/H] = 0.09$, Y=0.27). . . . . 113

7.1 The tomogram taken on the night of 2016-01-02 of SW0551. The expected transit start and end phases are marked with white crosses. The white vertical dotted lines show the positions of the $\gamma$-velocity of the system and $\gamma \pm v_\star \sin i$. . . . . 117

7.2 The tomogram taken on the night of 2016-01-15 of SW0647. The expected transit start and end phases are marked with white crosses. The white vertical dotted lines show the positions of the $\gamma$-velocity of the system and $\gamma \pm v_\star \sin i$. . . . . 118

7.3 The tomogram taken on the night of 2017-10-30 of SW0623. The expected transit start and end phases are marked with white crosses. The white vertical dotted lines show the positions of the $\gamma$-velocity of the system and $\gamma \pm v_\star \sin i$. . . . . 118

7.4 The tomogram taken on the night of 2017-10-28 data of SW0025. The expected transit start and end phases are marked with white crosses. The white vertical dotted lines show the positions of the $\gamma$-velocity of the system and $\gamma \pm v_\star \sin i$. . . . . 119

8.1 A mass-period diagram showing the known exoplanet population with masses below the deuterium-burning limit ($13\,M_{Jup}$), as listed in the NASA exoplanet archive[1]. The colour of the points indicates the discovery method, with black marking those discovered via the transit method and confirmed using Doppler tomography. The positions of WASP-167b/KELT-13b, WASP-174b, WASP-190b and WASP-180b are indicated. With the exception of WASP-167b/KELT-13b and WASP-174b, which have only an upper limit for the mass and are thus displayed with an outline, only planets whose masses have been measured are included. 122

8.2 (a) A mass-radius diagram showing the known exoplanet population with masses below the deuterium-burning limit ($13\,M_{Jup}$), as listed in the NASA exoplanet archive[1]. (b) As for (a), but only showing masses up to $4\,M_{Jup}$. The colour of the points indicates the planetary equilibrium temperature. The positions of WASP-167b/KELT-13b, WASP-174b, WASP-190b and WASP-180b are indicated. With the exception of WASP-167b/KELT-13b and WASP-174b, which have only an upper limit for the mass and are thus displayed with an outline, only planets whose masses have been measured are included. . . . . 124

8.3 $\lambda$ vs. $T_{\rm eff}$ for all known planets with obliquity measurements listed in the TEPCat database. The positions of WASP-167b/KELT-13b, WASP-174b, WASP-190b and WASP-180Ab are marked. Red points indicate other systems which were confirmed via Doppler tomography. The vertical dashed line at $T_{\rm eff} = 6250\,K$ marks the position of the Kraft break. The horizontal dashed lines mark $\lambda$ values of 90° and 270°, between which an orbit is considered to be retrograde. . . . . 126

8.4 $\lambda$ vs. $a$ for all known planets with obliquity measurements listed in the TEPCat database. The positions of WASP-167b/KELT-13b, WASP-174b, WASP-190b and WASP-180Ab are marked. Red points indicate other systems which were confirmed via Doppler tomography. The horizontal dashed lines mark $\lambda$ values of 90° and 270°, between which and orbit is considered to be retrograde. . . . . 127

8.5 $\lambda$ vs. $M_{\rm p}$ for all known planets with obliquity and mass measurements listed in the TEPCat database. The positions of WASP-167b/KELT-13b, WASP-174b, WASP-190b and WASP-180Ab are marked. Red points indicate other systems which were confirmed via Doppler tomography. The tomography planets with only upper limits measured for the mass are shown as an outline. The horizontal dashed lines mark $\lambda$ values of 90° and 270°, between which and orbit is considered to be retrograde. 128

# List of Tables


1.1 The total number of exoplanet discoveries per detection method. Data retrieved from the NASA Exoplanet Archive[1], accessed on 2019/08/27. 7
1.2 List of all known transiting planets confirmed by the Doppler tomography technique to date, in order of discovery. . . . . 31
3.1 Details of all observations of WASP-167b/KELT-13b used in this work, including the discovery photometry, the follow-up photometry and the spectroscopic observations. The label in the final column corresponds to a lightcurve in Fig. 3.2. . . . . 55
3.2 Radial velocities and bisector spans for WASP-167b/KELT-13b . . . . . 56
3.3 System parameters obtained for WASP-167b/KELT-13b in this work. . 65
3.4 Stellar parameters obtained for WASP-167/KELT-13 in the SED analysis (see Section 3.6). . . . . 67
4.1 Details of all observations of WASP-174b used in this work, including the discovery photometry, the follow-up photometry and the spectroscopic observations. . . . . 74
4.2 Radial velocities and bisector spans for WASP-174b. . . . . 74
4.3 All system parameters obtained for WASP-174b in this work. . . . . 83
5.1 Observations of WASP-190b. . . . . 88
5.2 RV measurements of WASP-190, taken using the CORALIE and HARPS spectrographs for this work. . . . . 88
5.3 All system parameters obtained in the combined analyses for WASP-190b. 92
5.4 Parameters for WASP-190 from BAGEMASS: . . . . . 94
6.1 Details of the photometric and spectroscopic observations of WASP-180Ab carried out for this work. . . . . 101
6.2 RV measurements for WASP-180A taken using the CORALIE and HARPS spectrographs for this work. The values in italics are of low signal-to-noise due to an auto-guiding issue during observation. . . . . 102
6.3 Third light dilution factors and stellar flux ratios obtained for WASP-180. 104
6.4 The results of the rotational modulation search of the WASP photometry of WASP-180. The strongest peak in the periodogram for the first set of data lies at $P_{\rm mod}/2$ (see Fig. 6.1). The additional peaks around 1–2 days are ascribed to a combination of harmonics of the rotation period and 1-day aliases. . . . . 106
6.5 All system parameters obtained for WASP-180 in this work. The quantities marked with * were used as priors in the combined MCMC analysis described in Section 6.5. . . . . 110
6.6 Results for the masses of WASP-180A and WASP-180B, and the age of the system. . . . . 113

# 1 Introduction

## 1.1 The search for exoplanets

Exoplanet science is a relatively young, but rapidly growing area of astrophysics. The motivation for finding new planets outside the solar system stems from an innate desire to explore and understand the universe. The study of the physical, chemical and geometrical properties of planetary systems informs models of their formation and evolution, giving a wider context in which to place the solar system in terms of the properties of its planets. This may one day give answers to some of the biggest questions in science, such as whether or not the Earth and the life that developed upon it are unique. The discoveries already made have called into question the basis upon which planet formation and evolution models previously stood. For instance, the prevalence of gas giant bodies in very short orbits (called hot Jupiters) is in direct contradiction to the theory that gas giants must form at greater distances from the star, giving rise to the development of theories describing the migration of such bodies to smaller orbits (e.g., Lin, Bodenheimer & Richardson 1996; Nagasawa, Ida & Bessho 2008). Another example is the discovery of planets in eccentric orbits, whereas previously planets were believed to only have circular orbits (e.g., Black 1997). As such, the models of planet formation and evolution are being constantly developed and improved in an attempt to better match the observed population of exoplanets.

Prior to the first exoplanet detections, there was a lot of interest in studying stellar binary systems (comprising of two gravitationally bound stars). Close binary systems which undergo eclipses, whereby one or both of the stars pass in front of each other along the line-of-sight over the course of an orbit, were particularly sought after. In combining photometric observations of the eclipses with measurements of the line-of-sight (or radial) velocities of the stars over an orbit, one could accurately determine the stellar masses and radii. Combining this information with spectroscopically measured stellar surface temperatures and metallicities could then provide the basis for testing

models of stellar structure and evolution, thus allowing the determination of the masses of single stars based on their spectral type.

The first measurement of a stellar binary eclipse was of the famously bright Algol (or $\beta$ Persei) by Goodricke (1783), who believed the periodic dip in the measured brightness of the star could have been due to eclipse by a fainter companion star, or due to starspots rotating in and out of view. Algol was later confirmed to be an eclipsing binary through the work of Vogel (1890), who detected a periodic variation in the measured Doppler shift of the star indicative of a stellar companion. This latter method became known as the radial velocity (RV) method. Over the 20th century, the methodology for analysing stellar eclipse lightcurves was developed (Russell 1912a; Russell 1912b; Russell & Shapley 1912; Russell & Shapley 1912) and optimised (e.g., Kopal 1950b; Kopal 1950a; Russell & Merrill 1952; Ruciński 1973; Wood 1973; Kopal 1979). Meanwhile, a number of groups were searching for binary systems, as well as conducting wider variable-star searches, discovering a great number of binary systems which have become targets for such analyses (e.g., Argelander 1844; Prager 1931; Samus' et al. 2017). Hilditch (2001) provides a more detailed summary of the major developments in the study of binary systems.

Struve (1952) proposed that the aforementioned RV method could also be applied to the detection of exoplanets, in particular to search for theoretical Jupiter-mass objects on short-period orbits, and also proposed that such planets could produce photometrically detectable eclipses. Despite this, early exoplanet detections involving RV measurements were met with some scepticism, as this method was still being developed for that purpose and there was the precedent of early exoplanet claims using other methods which turned out to be false. One of the earliest claims was of a planet in the 70 Ophiuchi binary system, which was an explanation given for an inability to compute an orbit that was consistent with the measured change in separation and position angles of the stars over time (Jacob 1855; See 1895). It was later proved that such a planet would not be stable in its orbit and so could not exist (Moulton 1899). Another well-known example is the claimed detection of two planets of $0.5\,\mathrm{M_{Jup}}$ and $0.7\,\mathrm{M_{Jup}}$ orbiting Barnard's star following 44 years of astrometric observations (van de

Kamp 1982). The star was shown to move in a way that suggested the existence of one or more unseen companions. However, a series of later studies have found no evidence of such companions (e.g. Benedict et al. 1999; Choi et al. 2013; Bonfils et al. 2013), although a recent study has instead found evidence of a $3.2\,M_{\rm Earth}$ planet in the system, via a long-term, intensive, high-resolution RV campaign (Ribas et al. 2018).

The first detection of a genuine exoplanet was of $\gamma$ Cephei Ab (Campbell, Walker & Yang 1988), using the RV method. Being cautious about announcing the discovery of an exoplanet, the authors claimed that the signal could also be attributed to stellar activity and released a further paper in 1992, showing that the period of the RV variations was the same as the period of a weak variation in the Ca II 8662Å emission line index, indicating a likely stellar origin for the signal (Walker et al. 1992). The authors did not completely rule out the planetary interpretation of the RV data, however, and the exoplanet was later confirmed to exist in 2002, using all existing RV measurements taken over the course of 20 years (Cochran et al. 2002).

The first exoplanets to be confirmed were planets of a similar mass to Earth, but were found orbiting the 6.2ms pulsar PSR B1257+12. Variations in pulse timing were first detected in 1992, and in 1994 were confirmed to be caused by the presence of two Earth-mass planets (Malhotra et al. 1992; Wolszczan 1994). The idea of planets existing in such a radiation-intense environment intrigued astronomers, raising questions about the climates experienced thereof. The first planet found with a main-sequence solar-type host star was the hot Jupiter 51 Pegasi b, discovered in 1995 with the RV method (Mayor & Queloz 1995). The existence of the gas giant was challenged: the Doppler RV signal was attributed to a planet with a very short orbit of $\sim$4.2 days, which was hitherto unheard of, and in contradiction to theories of planet formation which showed that gas giants could only form at larger distances from their stars. In an attempt to refute the discovery, a number of papers followed which claimed that the periodicity could also be explained by stellar oscillations or non-radial pulsations (e.g., Hatzes, Cochran & Johns-Krull 1997; Gray 1997; Gray & Hatzes 1997), despite the earlier assertions of Struve (1952) that there was no reason to rule out the possibility of a Jupiter-mass object in such a short orbit.

The discovery of the first multi-planet system orbiting a main sequence star, containing three planets, soon followed in 1999, again using the RV method (Butler et al. 1999). In the same year, RV observations led to the detection of the hot Jupiter HD 209458b, which was followed up with successful attempts to photometrically observe the occultation of a portion of the stellar disc by the planet, making it the first detection of the transit of an exoplanet (Henry et al. 2000; Charbonneau et al. 2000). These discoveries paved the way for more intensive exoplanet searches, bolstering support for the planetary interpretation of RV signals, while later the existence of 51 Pegasi b was reaffirmed by Naef et al. (2004) using the ELODIE spectrograph (Baranne et al. 1996).

The overall contribution of RV discoveries to the population of known exoplanets has been fairly steady since the earliest detections. The transit method was at first slow to produce planets, but grew more rapidly with the introduction of dedicated ground-based projects such as TrES (Alonso et al. 2007), HATnet (Hartman et al. 2004), XO (McCullough et al. 2005), SuperWASP (Pollacco et al. 2006; Hellier et al. 2011) and KELT (Pepper et al. 2007). Ground-based transit searches have proved to be comparatively cheap, having low running costs and requiring only small telescopes which can survey a large area of the sky at once. The first space-based exoplanet research mission was CoRoT, which launched in 2006 and was also used for the study of asteroseismology (Baglin et al. 2006). CoRoT paved the way for space-based transit searches, and 2009 saw the launch of the Kepler space telescope, marking the beginning of a wave of transit discoveries: in 2014 an unprecedented 715 planetary candidates were discovered by Kepler alone, followed by 1284 new candidates in 2016 (Akeson et al. 2013; Akeson et al. 2017). Thus the transit method became by far the most successful method for finding new worlds. Although Kepler has found so many new planets, however, the majority of these are in systems which are much fainter than those discovered from the ground, which can be followed up with RV measurements to constrain more of the system parameters. Thus there have also been several additional, successful ground-based projects initiated over the years, like KELT-South (Pepper et al. 2012), HATSouth (Bakos et al. 2013), MASCARA (Talens et al. 2017c) and NGTS (Wheatley et al. 2018).

The RV method is limited by the precision required to detect the small changes in stellar spectral line positions caused by the planet. Larger, close-in planets will be more easily detected than smaller ones since they will have a greater gravitational effect on the parent star (Haswell 2010). The transit method is similarly biased towards larger planets on short orbits, as these will produce deeper transits whilst also being more likely to transit in the first place (more on this in Section 1.3). The most recent addition to the series of transit search projects is the launch of TESS, an all-sky mission optimised for a similar magnitude range to the ground-based telescopes. The goal of TESS is to find planets around the brightest and nearest stars, to enable extensive photometric and spectroscopic follow-up (Ricker et al. 2015). It is expected to produce a large number of Earth-mass planets and so will in part counter the bias towards larger planets that is inherent in the transit method. Some interesting detections have already been made, such as a super-Earth orbiting the very bright star $\pi$ Mensae (Gandolfi et al. 2018; Huang et al. 2018) and the 'hot Earth' orbiting the M dwarf LHS 3844 (Vanderspek et al. 2019).

Other exoplanet detection methods have made smaller contributions to the pool of known planets. One example is the gravitational microlensing technique. Light travelling from distant stars can be bent and distorted by the gravitational field of foreground stars, much like when light passes through a lens. If the foreground star also has a planet, then the gravitational field of that planet contributes to this lensing effect, leading to the use of gravitational microlensing for the detection of planets. In order for gravitational lensing to occur, the foreground and background stars must be aligned along the line of sight. Since the Earth and the stars are constantly moving, lensing events occur often but are short-lived, sometimes as short as a few hours. In order to increase the probability of detecting a planet through this method, continuous monitoring of foreground stars with a dense population of background stars, e.g., towards the galactic centre, is necessary. Gravitational microlensing is most effective in the semi-major axis range 0.7–10 AU, but can also detect planets on wide orbits or free-floating planet-mass objects. This makes the microlensing technique complimentary to the transit method, which finds planets on shorter orbits. The lower limit on

the detectable planet mass depends on the angular size of the background star. The larger the background star, the higher the lower limit on the detectable mass, because a low-mass planet will only deflect a fraction of the light from a giant star towards the observer, producing a broader lightcurve (Bennett & Rhie 2002). The first planet discovered in this way was OGLE-2003-BLG-235L b (Bond et al. 2004).

It is also possible to directly image a planet. The direct imaging method is suitable for detecting and observing planets at larger separations, and can also be used to confirm the existence of microlensing planets, such as in the case of OGLE-2003-BLG-235L b (Bennett et al. 2006). This method involves the use of a coronagraph to block out the majority of the stellar light, allowing the light from planets in wider orbits to be detected directly. High resolution imaging is best suited to this technique, requiring space-based instruments or adaptive optics systems. By combining direct photometric and spectroscopic observations of an exoplanet, one can characterise their physical properties and the structure of their atmospheres and construct a very detailed depiction of the planetary system (Marois et al. 2008). However, this method cannot be used for close-in planets, which comprise the bulk of planet detections to date. The first directly imaged planet was 2M1207 b, which orbits a brown dwarf (Chauvin et al. 2004; Chauvin et al. 2005).

Variations in the timing of periodic stellar phenomena can indicate the presence of unseen, perturbing planetary bodies. Examples include pulsar timing variations, as in the case of PSR B1257+12, eclipse timing variations in binary systems and pulsation timing variations. Additional planets in systems with known transiting bodies can also cause transit timing variations and transit duration variations. Detecting and disentangling these signals is challenging, however, since they can be easily masked by noise or the periodic effects themselves (Wright & Gaudi 2013).

Finally, astrometry can also be used to detect planets. By looking at the measured proper motions of stars, one can infer the presence of unseen planetary bodies (Sahlmann et al. 2013). This method therefore requires long and continuous observations of the same stars in order to track their motions on the sky. The orbital brightness modulation method looks at changes in stellar brightness that result from

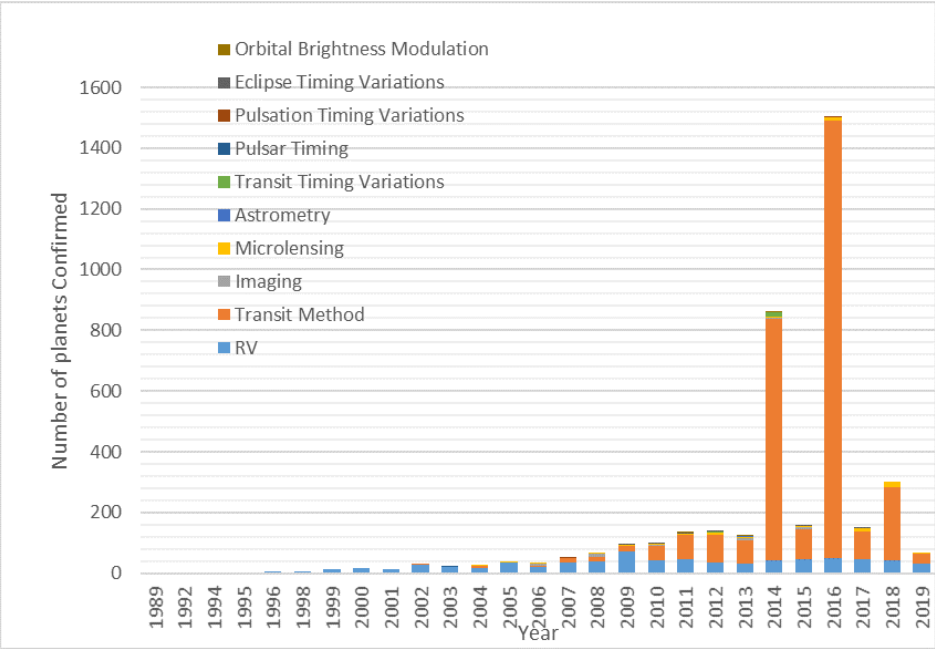


Figure 1.1: Chart showing the number of exoplanet discoveries per year since the first in 1989, as of 2019/08/27. The discoveries are grouped by detection method. Data were taken from the NASA Exoplanet Archive[1].

Table 1.1: The total number of exoplanet discoveries per detection method. Data retrieved from the NASA Exoplanet Archive[1], accessed on 2019/08/27.

| Detection Method | Number of Discoveries |
|---|---|
| RV | 764 |
| Transit Method | 3107 |
| Imaging | 47 |
| Microlensing | 77 |
| Astrometry | 1 |
| Transit Timing Variations | 17 |
| Pulsar Timing | 6 |
| Pulsation Timing Variations | 2 |
| Eclipse Timing Variations | 10 |
| Orbital Brightness Modulation | 6 |
| Total Number of Discoveries | 4037 |

the orbital motion of the star and planet, such as ellipsoidal modulation, reflection of stellar light from the planet, or Doppler beaming (Rybicki & Lightman 1979; Pfahl, Arras & Paxton 2008).

According to the NASA Exoplanet Archive[1] (Akeson et al. 2013), more than 4000 exoplanets have been confirmed or validated to date. The current number of detections per year, grouped by detection method, are listed in Table 1.1 and also displayed in Fig. 1.1.

## 1.2 Defining an 'exoplanet'

### 1.2.1 The working definition of an exoplanet

The International Astronomical Union (IAU) put forward a formal definition of a planet in the 26th General Assembly Meeting in 2006[2]. This definition states that:

> "A planet is a celestial body that (a) is in orbit around the Sun, (b) has sufficient mass for its self-gravity to overcome rigid body forces so that it assumes a hydrostatic equilibrium (nearly round) shape, and (c) has cleared the neighbourhood around its orbit."

When considering planets outside the solar system, a different definition is required. These 'exoplanets' are currently classified by a working definition that was first put forward in 2001 and was last updated in 2003 (Boss et al. 2007). By the current definition, an exoplanet is an object which:

- is in orbit around a star or stellar remnant;
- has a true mass above the lower limit set by conditions b) and c) in the definition of a planet;
- has a true mass below that which is the limit for thermonuclear fusion of deuterium to occur ($\approx 13\,\mathrm{M}_{Jup}$)

[1] Available at: https://exoplanetarchive.ipac.caltech.edu/

[2] Available at: http://www.iau.org/news/pressreleases/detail/iau0603/ Accessed 01/05/2018

This working definition of a planet has sparked much debate among astronomers over its suitability and applicability to the population of exoplanets as a whole. For instance, the first condition excludes free-floating objects which meet the mass requirements to satisfy the other conditions. Such objects have been detected in active star forming regions when they are still young and thus hot enough to emit a detectable infrared signature (e.g., Lucas & Roche 2000), are frequently discovered in microlensing surveys (e.g., Sumi et al. 2011; Udalski, Szymański & Szymański 2015; Mróz et al. 2017), and are instead referred to in the literature as 'sub-brown dwarfs' or 'free-floating planet mass objects'. They are thought to have either formed through gravitational collapse of low-mass pre-stellar cores or globulettes (Haworth, Facchini & Clarke 2015; Caballero 2018) or to have been ejected from protoplanetary discs via planet–planet dynamical interactions (Rasio & Ford 1996). Meanwhile, it is difficult to prove that the second condition is satisfied, since there is no certain way to show that an exoplanet has cleared its orbit of debris. Thus this definition does not truly address the need for a precise lower limit on the mass of an exoplanet.

The final condition is then intended to set an upper limit on the mass of a planet in order to separate them from higher-mass companions undergoing deuterium fusion in their cores, called brown dwarfs. This condition creates the most contention amongst astronomers. Firstly, it is inherent with ambiguity, since the minimum mass required for the fusion of deuterium to occur in the core is dependent on the composition of the planet in question. The mass limit of $13\,M_{Jup}$ is a reasonable approximation for a planet of solar metallicity, but does not apply to metal-rich or metal-poor planets. Thus this definition results in a moving boundary between high-mass hot Jupiters and low-mass brown dwarfs, which can range from $11\,M_{Jup}$ to $\sim 17\,M_{Jup}$ depending on the initial conditions considered (e.g., Spiegel, Burrows & Milsom 2011; Bodenheimer et al. 2013). Secondly, it has been shown that deuterium burning has little to no effect on the formation or evolution of stars and brown dwarfs (Chabrier et al. 2000; Chabrier 2003), and so it has been claimed that this definition carries no physical justification (e.g., Chabrier et al. 2014). Thirdly, the discovery of systems that contain a brown dwarf and a planet-mass object, such as 2M1207 b (Chauvin et al. 2005), 2M J044144

(Todorov, Luhman & McLeod 2010) and KMT-2016-BLG-1820 (Jung et al. 2018), has created further contention over this definition, since with the planet-mass object being a significant fraction of the total mass of the system it appears more akin to a scaled-down version of a typical stellar binary than a planetary system.

There is much support for an alternative definition that separates exoplanets from brown dwarfs purely by their formation mechanism. Advocates of such a definition argue that this kind of boundary would be more clear-cut and more universally applicable. This has sparked a breadth of research into refining models of planet and star formation processes, and into consolidating those theories with the observed population, necessitating frequent and detailed reviews (some examples include Chabrier et al. 2014; Baruteau et al. 2016; Dawson & Johnson 2018; Schneider 2018; Kley 2019; Adibekyan 2019).

### 1.2.2 The formation of planets and brown dwarfs

There are three main formation mechanisms thought to produce planets, planet-mass objects and brown dwarfs: a slow process of coagulation of dust into grains, pebbles and eventually planetessimals, called core accretion; disc instability leading to the fragmentation of a protoplanetary disc into dense clumps and subsequent gravitational collapse; gravitational collapse of a cloud comprising mostly of hydrogen and helium.

Gravitational collapse is the widely-accepted mechanism by which stars form. A cloud comprised mostly of hydrogen and helium may begin to collapse under its own gravity, perhaps triggered by some perturbing event, thus forming a dense pre-stellar embryo at its centre. The material in the cloud begins to rotate and flattens out as it moves inwards, conserving angular momentum, while the embryo continues to accrete mass, eventually forming a protostar. The protostar becomes a star when it is massive enough and hot enough to ignite hydrogen fusion in the core. Sometimes, more than one embryo is created, and a multiple-star system is produced. The minimum mass required for a cloud to collapse under its own gravity is quite low, however, at $\sim 3\,\mathrm{M_{Jup}}$(Whitworth 2018). Thus gravitational collapse can also, in principle, produce

free-floating brown dwarfs and planetary mass objects, as well as bound planets.

Objects can also form within the disc that surrounds a protostar via core accretion or disc instability. The core accretion model is able to explain the existence of many types of planets, including rocky planets, gas giants and ice giants. It is consistent with the observed heavy-element enhancement of the gas and ice giants in our own solar system, as well as with the observed trend between the occurrence rate of giant planets and the metallicity of the planet host. It is also consistent with the correlation between the surface metallicity of a giant planet and that of its host star, and the lower occurrence rate of giant planets orbiting low-mass stars (Helled et al. 2014). It cannot explain, however, the formation of high-mass objects ($>10\,M_{Jup}$) at large separations, such as in the case of the HR 8799 system (Marois et al. 2008), nor can it explain the formation of giant planets in low-metallicity environments. There is also an issue in consolidating the theory with Type I migration theory, as it is unclear whether or not core accretion can produce a core massive enough to then undergo runaway gas accretion before the onset of migration, or indeed before the protostar becomes a star and photoevaporates the remaining gas and dust in the disc. In addition, there are significant gaps in our understanding of grain and planetessimal formation and evolution, which makes estimates of the timescale of formation difficult. Nevertheless, core accretion is widely thought to be the formation mechanism behind the majority of planets (Chabrier et al. 2014), and is also capable of producing bodies beyond the deuterium burning limit, up to $\sim 40\,M_{Jup}$ (Mordasini et al. 2012).

Finally, gravitational instabilities within a protoplanetary disc can lead to fragmentation of the disc into dense clumps of matter, which subsequently collapse to form gas giants or brown dwarfs. This is not a metallicity-dependent process and so does not naturally explain the correlation between gas giant occurrence rate and stellar metallicity, but can explain the formation of high-mass gas giants and brown dwarfs on wide orbits or in low-metallicity environments (Helled et al. 2014). It occurs when the destabilizing force of a protoplanetary disc's self gravity is sufficient to overcome both internal pressure and the Coriolis force that arises due to the spinning of the disc (Safronov 1960; Goldreich & Lynden-Bell 1965). The disc must be of sufficient mass

for this to occur, and also be able to cool efficiently during contraction so that the internal (thermal) pressure does not increase enough to re-stabilize the disc. In the inner parts of the disc, fragmentation is very unlikely because the cooling timescale is too long compared to the local dynamical timescale (Chabrier et al. 2014). Objects formed from the subsequent gravitational collapse could: become planets or brown dwarfs; be tidally disrupted or migrate into the star while still in the disc (e.g., Machida, Inutsuka & Matsumoto 2011; Baruteau, Meru & Paardekooper 2011; Vorobyov 2013), or; continue to accrete mass from the disc and become a star (Whitworth 2018). They may also be ejected from the system due to tidal interactions with other objects of similar masses that have also formed within the disc. As such, it is thought that disc instability can only explain $< 30\%$ of planets and brown dwarf companions to BA-type stars and $< 10\%$ of those with FGKM stars (Janson et al. 2011; Janson et al. 2012). It may, however, explain the existence of all or most single brown dwarfs (Whitworth 2018).

### 1.2.3 What might a formation-based definition look like?

A proposed formation-based definition could place all objects formed from a protoplanetary disc via either core accretion or disc instability in the 'planet' category. Meanwhile, all objects formed via gravitational collapse of a cloud would be either a brown dwarf or a star depending on whether or not hydrogen fusion is occurring in the core. This removes the mass boundary set by the deuterium-burning limit, and thus free-floating objects which are not massive enough to fuse deuterium would also be considered brown dwarfs under this framework, unless it can be proven that they originally formed within a disc. In the case of systems containing what would currently be considered a brown dwarf with a planet (where the mass of the secondary body is a significant fraction of the mass of the primary), such a system could be reclassified as a brown dwarf binary if the secondary can be proven to have formed via gravitational collapse. One could use the surface metallicity of the body as an indicator of the way in which it formed, since bodies formed within a protoplanetary disc tend

to have enhanced surface metallicities compared to their stars due to collisions with planetessimals (e.g., Marley et al. 2007; Fortney et al. 2008b; Miller & Fortney 2011).

This definition is not simple to put into practice, as it is not always possible to determine the metallicity of a planet. It is also controversial, as it could result in systems containing a star and a $3\,M_{Jup}$ body being reclassified as a binary system rather than a planetary system, should the $3\,M_{Jup}$ body be revealed to not have enhanced metallicity, indicating that it would have formed through gravitational collapse. This configuration is likely to be considered equally as unusual as the 'brown dwarf with a gas giant' configuration considered earlier. Thus the overlap in the mass ranges of bodies produced by the different mechanisms is an issue.

One could also argue that objects formed via disc instability should not be considered planets, given that this process is essentially another form of gravitational collapse, and as stated earlier it has been shown that this process is comparatively inefficient at producing planet and brown dwarf companions to stars. Schlaufman (2018) attempts to find a mass-limit boundary that separates objects formed by core accretion from those formed via disc instability, by looking at a large population of solar-type host stars. They search for a dependence of the occurrence rate of hot Jupiter and brown dwarf companions on the metallicity of their host stars (since core accretion is more effective at producing gas giants in higher metallicity discs). They find that objects with masses below $4\,M_{Jup}$ favour stars of higher metallicity and conclude that they must have formed via core accretion, while those with masses $> 10\,M_{Jup}$ do not favour high-metallicity stars and thus form through gravitational instability, concluding that they should not be considered planets. Objects in the mid-mass range may have formed through either mechanism, making it difficult to classify them. Other works have also found results in agreement with a mass boundary at $4\,M_{Jup}$ between different formation mechanisms (e.g., Santos et al. 2017; Narang et al. 2018). Adibekyan (2019), on the other hand, revisits the conclusions of previous works and does not find evidence of the boundary at $4\,M_{Jup}$. A further study by Goda & Matsuo (2019) extends the sample of planet hosts to include earlier spectral types. They argue that the boundary at $4\,M_{Jup}$ applies to solar-type planet hosts, but for earlier spectral types the upper limit on the

mass of a core-accreted planet becomes $25\,M_{Jup}$.

Thus, a formation based definition of an exoplanet would not be as clear-cut as one may suppose. The significant overlap in the masses of gaseous objects formed via the different mechanisms is an issue that so far has not been overcome. In further support of the current definition, it has been shown that there is a natural boundary between Jupiters and brown dwarfs (e.g., Sahlmann et al. 2011): the so-called 'brown dwarf desert' covering the mass range 10–100 $M_{Jup}$, where there are an order-of-magnitude fewer companion objects compared to those with masses $<10\,M_{Jup}$.

## 1.3 Exoplanet discovery via the transit method

### 1.3.1 What is the transit method?

Some planetary systems are aligned along the line of sight such that the planet will periodically pass between the Earth and its parent star during its orbit. This event is known as a 'transit', and can be observed by detecting the subsequent drop in the amount of light received from the star that occurs as a result of the planet occulting a portion of its surface. An exoplanet transiting its parent star provides a great opportunity to characterise the system. A summary of the key equations that can be used to derive system parameters from observable quantities will now be provided, for more information see Chapter 3 of Haswell (2010).

Fig. 1.2 shows a schematic diagram of a transit taken from Fig. 2 of Winn (2010) and adapted to match the notation used in this work. The figure defines the key observable transit parameters which can be used to derive some physical system parameters. In this summary, it assumed that the star being occulted is a uniformly illuminated disc, and the transiting planet in question lies on a circular orbit.

Using the four transit contact points shown in Fig. 1.2, the transit and ingress(egress) durations are defined respectively as:

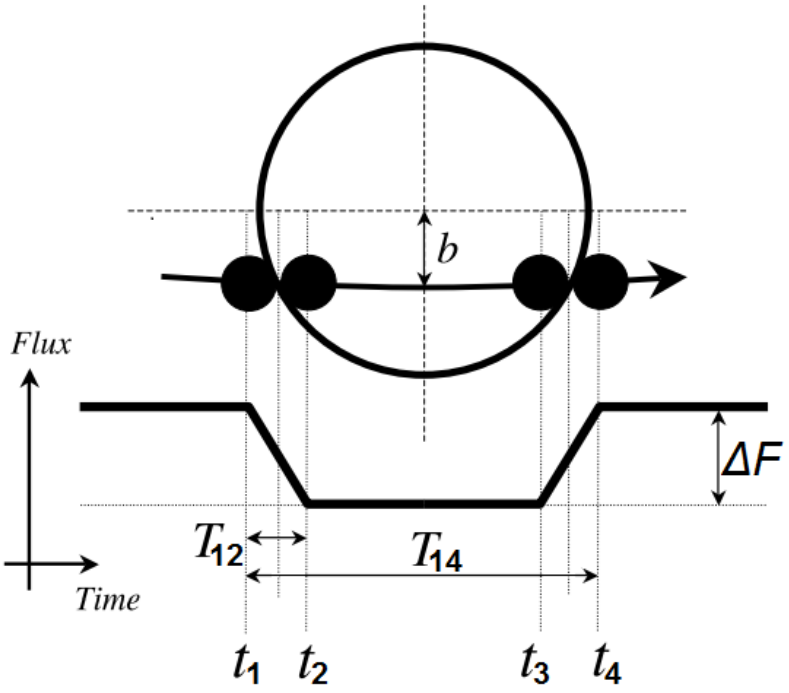


Figure 1.2: Schematic diagram showing a planetary transit taken from Fig. 2 of Winn et al. (2010) and adapted to match the notation used in this work. At time $t_1$, the transit begins and the flux received from the star starts to decrease. At $t_2$, the planet is fully in front of the stellar disc and thus the flux from the star has reached its minimum level, at which it will remain until the planet begins to exit the stellar disc at time $t_3$: the total change in flux is labelled as $\Delta F$. The flux level then rises again, reaching its original level at time $t_4$ when the planet has completely left the stellar disc. The time taken for the planet to go from $t_1$ to $t_2$ is known as the transit ingress, while the time taken from $t_3$ to $t_4$ is the transit egress. $t_1$, $t_2$, $t_3$ and $t_4$ are referred to as the four transit contact points. Also labelled are the transit duration $T_{14}$, the ingress duration $T_{12}$, and the impact parameter $b$.

$$T_{14} = t_4 - t_1 \tag{1.1}$$

$$T_{12} = t_2 - t_1 (= T_{34} = t_4 - t_3) \tag{1.2}$$

The shape of a transit lightcurve depends on the geometry of the system in

question. The depth of the transit is proportional to the fractional area of the stellar disc that is occulted by the planet, equivalent to the ratio of the planet-to-stellar radii squared:

$$\frac{\Delta F}{F} = \left(\frac{R_{\rm p}}{R_\star}\right)^2 \tag{1.3}$$

where $F$ is the total flux received from the star out-of-transit and $\Delta F$ is the amount of flux which is blocked by the transiting planet. A planet of Jupiter radius transiting a star of solar radius will produce a transit with a depth of $\sim 1\,\%$ of the total flux.

The duration of the transit, or transit width, is then related to the period of the orbit, the size of the orbit, and the inclination of the orbit with respect to the stellar rotation axis. Consider initially a system with a transiting planet on a circular orbit which is inclined at $i = 90^\circ$ from the stellar rotation axis, such that it crosses the widest part of the stellar disc. During the transit event the planet subtends an angle at the centre of the star as it moves through a small arc in its orbit. The chord joining the positions of the planet at $T_1$ and $T_4$ has a length of $2R_\star$. The duration of the event, $T_{14}$, is then simply given by the division of the length of the arc (orbital radius$\times$angle subtended in radians) by the speed of the planet (orbital period/circumference):

$$T_{14}\,(i = 90^\circ) = \frac{P}{2\pi a}.2a\sin^{-1}\left(\frac{R_\star}{a}\right) = \frac{P}{\pi}\sin^{-1}\left(\frac{R_\star}{a}\right) \tag{1.4}$$

where $P$ is the period of the orbit, $a$ is the radius of the orbit and $R_\star$ is the stellar radius.

Now consider an orbit which is still circular, but is inclined at an angle $i < 90^\circ$ with respect to the stellar rotation axis. In order to incorporate the inclination of the orbit into eq. 1.4, it is necessary to define another quantity called the impact parameter ($b$): the vertical distance between the centre of the stellar disc and the position of the planet at the time of mid-transit as shown in Fig. 1.2, which is often quoted as a fraction of the stellar radius. The impact parameter then relates to the inclination of the orbit as follows:

$$b = a\,cos\,(i)\ \left(\text{or}\, b = \frac{a}{R_\star} cos\,(i)\right) \tag{1.5}$$

Fig. 1.3 shows the face-on geometry of the system as would be seen by the observer, and defines a quantity $l$, which is half of the length of the chord joining the positions of the planet at $T_1$ and $T_4$.

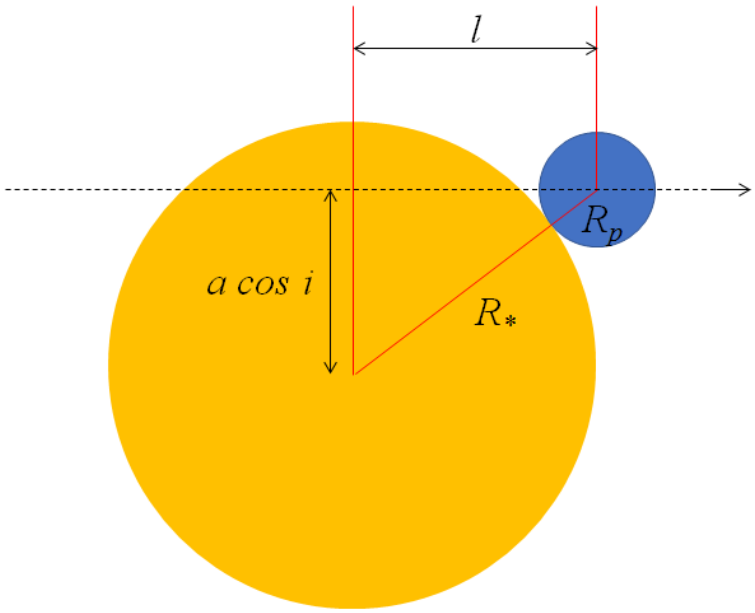


Figure 1.3: The face-on geometry of an inclined transiting system, defining the quantity $l$ which is half of the transit chord. Adapted from Fig. 3.3 in Haswell 2010b.

$l$ is thus given by:

$$l = \sqrt{\left(R_\star + R_\mathrm{p}\right)^2 - b^2} = \sqrt{\left(R_\star + R_\mathrm{p}\right)^2 - a^2 cos^2\,(i)} \tag{1.6}$$

Fig. 1.4 now shows the geometry of the system from a side-on perspective, and shows how the planet subtends an angle $\alpha$ at the centre of the star as it moves from position 'A' at $T_1$ to position 'B' at $T_4$.

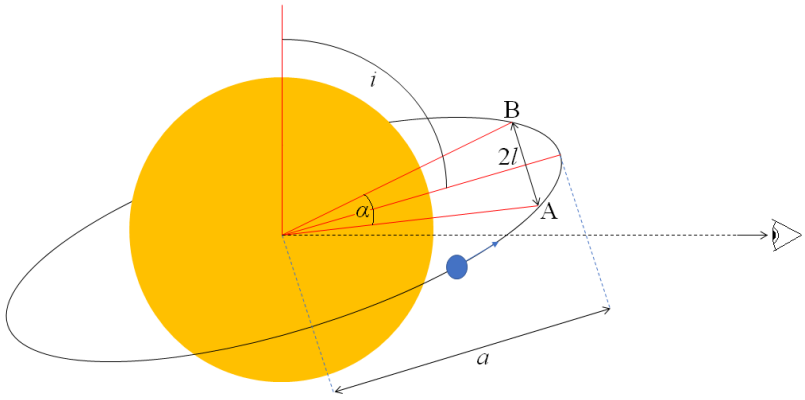


Figure 1.4: The side-on geometry of a transiting system. During transit, the planet passes from point A to point B, subtending an angle $\alpha$ at the centre of the star. Also shown are the inclination $i$, the transit chord $2l$, and the orbital separation $a$. Adapted from Fig. 3.4 in Haswell 2010b.

Referring to the geometry of the orbit displayed in Fig. 1.4, the planet travels a distance $a\alpha$ during transit at speed of $2\pi a/P$. The angle $\alpha$ can be derived from the triangle formed by the star's centre and points A and B, leading to the following equation for the transit duration when $i < 90°$:

$$T_{14}\left(i < 90°\right) = \frac{a\alpha}{2\pi a/P} = \frac{P}{2\pi a}.2a\sin^{-1}\left(\frac{l}{a}\right)$$
$$= \frac{P}{\pi}\sin^{-1}\left(\frac{\sqrt{\left(R_\star + R_\mathrm{p}\right)^2 - a^2 cos^2\left(i\right)}}{a}\right) \tag{1.7}$$

A transit lightcurve thus enables a direct measurement of the ratio of the orbital radius to stellar radius $(a/R_\star)$, the square of the ratio of planetary and stellar radii $((R_p/R_\star)^2)$ and the impact parameter $b$ and thus orbital inclination $i$. The planetary radius $R_p$ can then be estimated by assuming a stellar radius using knowledge of the spectral type (temperature) of the star (and stellar models). Interestingly, it is also possible to determine the planet's surface gravity independently of stellar properties,

and to determine the stellar mean density without any prior knowledge of other stellar parameters (see Winn 2010).

Throughout this summary, the planet hosting star has been assumed to be a uniformly illuminated disc. In reality, this is not the case: a star appears darker and redder at the limbs than at the centre. This is due to differences in temperature and optical depth in different parts of the stellar atmosphere. Light from the limbs is more likely to scatter in a direction which leads away from the observer due to the longer path lengths it must travel to escape the stellar atmosphere towards the observer from any given depth, whereas light from the centre is almost all emitted towards the observer, thus making the star appear brighter in the centre. The result of this is that a transit lightcurve does not appear perfectly flat-bottomed, but is instead more curved, with the transitions going out of ingress and into egress being less sharply defined than is shown in Fig. 1.2. Most of the light coming from the centre of the stellar disc also comes from deeper within the atmosphere, where temperatures are hotter, and thus appears bluer than at the limb. The amount of curvature in the transit lightcurve is thus wavelength dependent, and is greater for bluer wavelengths since there is a greater difference in brightness between the centre and the limb at those wavelengths. Thus a transit lightcurve will be shaped differently if observed using different passbands. Fig. 1.5 shows lightcurves generated for different passbands using the open source software BATMAN (Kreidberg 2015), demonstrating the wavelength dependence of the effects of limb darkening on a transit lightcurve.

Planets can have eccentric orbits, but the equations given in this Section apply to circular orbits. Introducing eccentricity into a planetary orbit increases the complexity of these equations, since the orbital separation becomes time-varying and this must be taken into account. However, as will be discussed in Sec. 1.3.2, the planets most likely to transit and thus be detected via the transit method are gas giant planets on very short orbits called hot Jupiters. Most hot Jupiters are considered to have circular orbits because they are expected to circularize on timescales shorter than their ages (Pont et al. 2011), and so the eccentric orbit case will not be considered here. Winn (2010) provides a summary of the key equations describing eccentric orbits, while Murray &

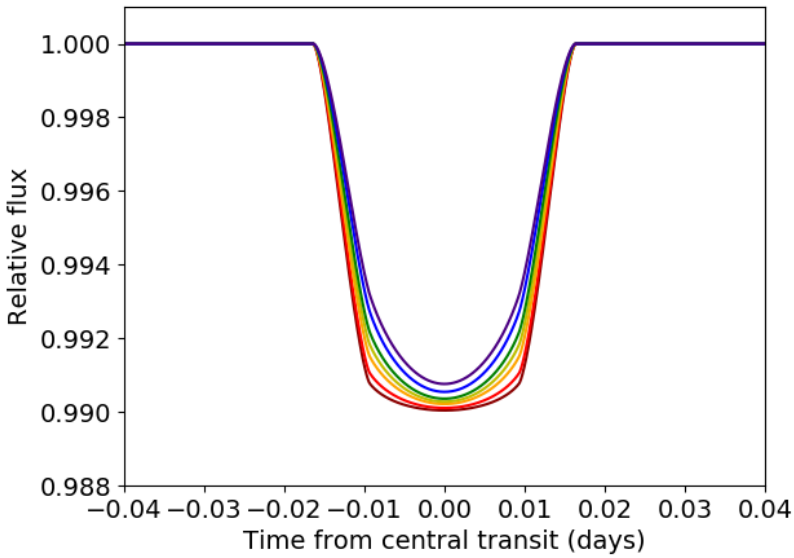


Figure 1.5: Transit lightcurves for different passbands, generated using the BATMAN software of Kreidberg (2015), which demonstrate the effects of limb darkening in different wavelengths. In constructing this plot, four-parameter non-linear limb darkening coefficients were extracted from the tables of Claret (2000);Claret (2004) for a star of $T_{\rm eff}$ =5500 K and $logg_\star = 4.4$ dex, for passbands UJ (violet), BJ (blue), VJ (green), RC (yellow), IC (orange), JJ (red), HJ (dark red). System parameters were set to $P = 2$ days, $R_{\rm p} = 0.1\,R_\odot$, $a = 15\,R_\odot$ and $i = 87°$.

Correia (2010) gives a more detailed derivation.

### 1.3.2 The probability of transits

In order for a planet to transit, the orbit must be inclined such that the impact parameter of the orbit (the distance from the centre of the star to the centre of the planet at inferior conjunction) must be smaller than the sum of the stellar and planetary radii, so that at least part of the disc of the planet will overlap with the stellar disc along the line of sight. For a circular orbit (see Chapter 3 of Haswell 2010):

$$b\,(= a cos\,(i)) < R_\star + R_{\rm p} \tag{1.8}$$

Thus an inclination close to 90° is required for transits to occur. The probability of a particular planet undergoing transits can be calculated by evaluating the ratio of the number of orbits which satisfy this condition to the total number of possible orbits:

$$P_{\text{transit}} = \frac{\int_0^{(R_\star + R_\text{p})/a} dx}{\int_0^1 dx} = \frac{R_\star + R_\text{p}}{a} \approx \frac{R_\star}{a} \tag{1.9}$$

The transit method is therefore biased towards selecting large planets on short-period orbits. For many rocky planets and gas giants on wider orbits, it is unlikely that transits will be seen. The majority of transiting planets discovered so far are hot Jupiters.

### 1.3.3 How to find transiting planets

When searching for transiting planets, there is no way to know from the outset which stars host planets, or which of those planets will transit. In order to increase the likelihood of finding a transiting planet, transit search projects use telescopes with wide fields of view, since the expected number of transits observed in a given time period is proportional to the solid angle size of the field (see Chapter 2 of Haswell 2010). A given field may include millions of stars, thousands of which can be measured reliably. Each field will be observed for several weeks to several months in one go. Several fields are observed per night and each one is often revisited multiple times over several years. The instruments used generally have a very short cadence, leading to the collection of thousands of photometric science frames for each field over the course of an observing period. In this way, transit search teams are able to maximise the number of potential candidate planets while building up a sufficiently long baseline of observations to make confident transit detections. Details of the instrumentation used by the WASP group, and the transit search methodology followed, will be provided in Chapter 2.

### 1.3.4 Transit false positives

There are a number of configurations of eclipsing binary (EB) systems which produce photometric effects that are very similar in appearance to an exoplanet transit. Such objects may be picked up in transiting exoplanet surveys, and as such can become "false positive" detections of planets. The types of EB system that can mimic transits are listed below and shown in Fig. 1.6, which is adapted from Fig. 1 in Santerne et al. (2013).

1. An EB with a low-mass secondary (e.g. brown dwarf), whose radius is similar to that of a hot Jupiter.

2. A grazing EB, where the secondary star occults only a small portion of the primary's surface.

3. Blended Eclipsing Binaries (BEBs), where an EB is diluted in the light of a nearby bright star, thus producing eclipses which appear shallower and more planet-like. This can happen either because the EB resides in a higher order multiple-star system (e.g., a hierarchical triple system), or because there is a coincidental line-of-sight alignment between the star being observed and an EB in the background.

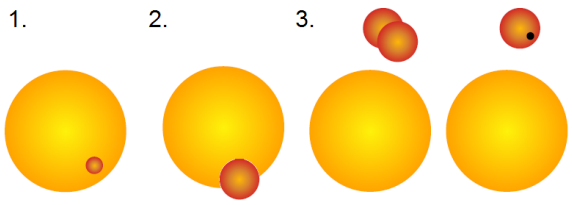


Figure 1.6: The three main types of false positives detected by exoplanet transit searches. 1. An EB with a low-mass secondary. 2. A grazing EB. 3. BEBs: an EB diluted in the light of a nearby bright star (left) or an EB with a low-mass secondary diluted in the light of a nearby bright star (right). Adapted from Fig. 1 Santerne et al. (2013).

## 1.4 Confirmation of transiting planet candidates

In order to confirm a transit detection as the detection of a planet, one must discount the false positive scenarios outlined in Section 1.3.4. To discount the BEB scenario, for instance, one could observe the transit in different passbands to prove the achromaticity of the transit depth: unless the BEB in question is comprised of two near-identical stars one would expect the depth of the transit to change across different passbands, unlike the transit of a planet. In the case of a grazing EB, it is possible to identify such a lightcurve by eye, as the transit will be V-shaped as opposed to the flat-bottomed shape common amongst planet transits. However, it is also possible for a planet to undergo grazing transits, producing a V-shaped lightcurve, and so this is not always a sufficient reason to discount such candidates from the offset. Meanwhile, a transit signature produced by brown dwarf is indistinguishable from that produced by a hot Jupiter, owing to the lack of self luminance in the occulting body combined with these objects having similar radii. Therefore, in order to discern the genuine detections of transiting exoplanets from mimics, one must detect the planet again using other, independent methods, capable of discounting all false positive scenarios.

Observing a transiting system by another means not only enables confirmation of a candidate transiting planet, but also allows a more detailed analysis of the system properties. The most commonly used confirmation method is the radial velocity (RV) method, which involves the detection of the dynamical effect of the orbiting planet on its host star via the measurement of Doppler shifts. This method can become difficult to use, however, when the candidate host star has $T_{\rm eff} > 6250\,{\rm K}$, as the weaker and broader spectral features typical of such stars make it difficult to obtain accurate and precise radial velocity measurements (RVs). In such cases a different method is employed, called Doppler tomography. This Section summarises the two methods, and gives a more detailed explanation of the problem encountered when dealing with hotter planet hosts.

### 1.4.1 Measuring the radial velocity orbit

The bodies in a planetary system orbit a common centre of mass located close to, but not at, the host star's centre. As a result, a star which hosts a planet will "wobble" about this position, a motion which can be measured as Doppler shifts in the stellar spectrum. In this way it is possible to detect and measure the RV orbit of a planet-hosting star, thus confirming that the object producing the transit effect is indeed orbiting the star being observed. This discounts the blend scenario.

The motion of the star is described by Kepler's third law as follows:

$$a^3 = \frac{G\,M\star}{4\pi^2.P^2} \tag{1.10}$$

while the RV semi-amplitude $K$ is given by Haswell (2010):

$$K = \frac{2\pi\,a\,M_p\,\sin i}{M_\star P} \tag{1.11}$$

Thus if one estimates the mass of the star using stellar models (and knowledge of the spectral type/temperature) it is also possible to determine the mass of the occulting body $M_p$, confirming that it lies in the planetary domain and thus discounting both the grazing EB scenario and the low-mass eclipsing secondary scenario. There is also the great advantage of being able to determine absolute system properties, rather than relative quantities, by combining transit and RV observations of the same system.

### 1.4.2 The Rossiter-McLaughlin effect

While passing in front of its star, a transiting exoplanet occults a portion of the stellar light. The occulted light is Doppler shifted by some amount due to the stellar rotation. The magnitude and direction of the shift depends on the stellar rotation rate and the part of the stellar surface being occulted, and so will change over the course of the transit. This leads to the Rossiter–McLaughlin (RM) effect, whereby the star appears overall more red-shifted or blue-shifted than it should at any given time during transit (Rossiter 1924; McLaughlin 1924). The RM effect causes a perturbation to stellar line

profiles, which thus appear asymmetrical, and this translates into an apparent reflex velocity shift in the RV curve of the star. The amplitude and shape of the apparent shift to RV depends on: the amount of light being occulted (the size of the planet compared to the star, $R_{\rm p}/R_\star$); the path taken by the planet across the stellar disc (the projected spin-orbit misalignment angle $\lambda$ and the impact parameter $b$); and the projected stellar rotational velocity ($v \sin i_\star$).

$\lambda$ is defined as the angle between the stellar rotation axis and the normal to the orbital plane of the planet, which depending on the adopted convention can either take values in the range $-180^\circ < \lambda \leq 180^\circ$ or the range $0^\circ \leq \lambda < 360^\circ$ (both are seen in the literature). Thus a value of $|\lambda| = 0^\circ$ indicates an aligned orbit, $|\lambda| = 90^\circ$ indicates a polar orbit and values in the range $90^\circ < |\lambda| < 270^\circ$ indicate a retrograde orbit.

Like the RV method and transit method, the RM effect was used in the study of binary systems before it was applied to planets. It was first noticed by Schlesinger (1910) in observations of $\delta$ Librae, and later established through the works of Rossiter (1924) and McLaughlin (1924). It has been used in the study of the rotation of close binary stars, confirming that the stars' rotation axes are nearly perpendicular to the orbtial plane, and that the direction of stellar spin is, as expected, the same as the direction of orbital motion (Giménez 2006).

The first detection of such an effect in an exoplanetary system was of HD 209458, by Queloz et al. (2000). It has since been used for many systems in order to measure $\lambda$ (e.g., Triaud 2017). The current alignment or misalignment of a planet's orbit with its host's spin axis is an indicator of the planet's dynamical history: a strong misalignment or retrograde orbit is indicative of a violent past. Trends in the overall distribution of alignment angles with respect to other system parameters may lend insight to theories of planetary system formation and evolution.

The observation of the RM effect in radial velocities also provides additional confirmation of the transiting exoplanet. It proves that the occulting body which causes the transit is indeed passing in front of the star we are observing, and not a blended star. Without a constraint on the object's mass placing it within planetary range, however, it is again not possible to rule out low-mass stellar companions from

the transit observation alone.

### 1.4.3 The Kraft Break and the hot stars problem

Stars hotter than $T_{\rm eff} = 6250\,{\rm K}$ differ greatly from those which are cooler in terms of their internal structure and overall properties. Cool stars have efficient magnetic dynamos coupled with subsurface convection layers, leading to strong magnetic activity and stellar winds which carry angular momentum away from the star. This process of 'magnetic braking' results in a rapid and drastic slowing down of the stellar rotation after formation. Conversely, hotter stars are mostly radiative, having small or non-existent convection layers. Thus, they do not undergo magnetic braking and so remain rotating at a much faster rate than their cooler counterparts. The divide between these two classes of stars is known as the 'Kraft break' (Kraft 1967).

This difference in rotation rate has a significant effect on spectroscopic observations. Spectral lines become very broad for stars that rotate rapidly. In addition, due to high surface temperatures most of the material in the stellar photosphere exists in an ionised state, limiting the number and strength of the spectral lines. As a consequence, it is difficult to measure precise and accurate RVs for stars hotter than $6250\,{\rm K}$, meaning that it is not always possible to use this method to confirm the existence of transiting planet candidates orbiting hot, fast-rotating stars. This has lead to transiting planet candidates found with host stars in the A–mid-F spectral-type range being largely ignored by both transit and RV surveys, until recently.

In reality, the divide between the so-called 'hot' and 'cool' stars is not so sharply defined as implied by the Kraft break. The Kraft boundary of $T_{\rm eff} = 6250\,{\rm K}$ marks the point at which the subsurface convection layer shrinks to the point that its effect on the stellar rotation rate is noticeably lessened. It is still possible, however, to confirm transiting planet candidates using RVs for some stars beyond this boundary, as the decrease in the strength and number of spectral lines is fairly gradual, as is the increase in rotation rate. The number of RV-confirmed transiting planets falls off quickly for $T_{\rm eff} > 6500\,{\rm K}$, but the hottest of these systems include HAT-P-49b with $T_{\rm eff} = 6820\,{\rm K}$

(Bieryla et al. 2014) and WASP-100b and WASP-172b with $T_{\rm eff} = 6900\,{\rm K}$ (Hellier et al. 2014; Hellier et al. 2019b). A recent exception to this trend is the discovery of WASP-178b (Hellier et al. 2019a), which despite the high host-star temperature of $T_{\rm eff} = 9350\,{\rm K}$ has a relatively low rotation speed of $v \sin i_\star = 8.2\,{\rm km\,s^{-1}}$ and a slightly enhanced metal content, leading to a precise RV curve.

For hotter candidates, astronomers are now using a method called Doppler tomography for transiting planet confirmation, a method which until recently had only been used in a few cases for planet confirmation (the first being WASP-33b (Collier Cameron et al. 2010b), the second being Kepler-448b (Bourrier et al. 2015a)) or characterisation (HD189733b (Collier Cameron et al. 2010a)). The next subsection will describe this technique.

### 1.4.4 Candidate confirmation for hot stars: Doppler tomography

Due to the difficulty in obtaining accurate RV measurements for stars of A-mid-F spectral types, such targets were previously paid less attention by transit and RV surveys alike, their efforts being focussed on the more easily confirmed candidates. As such, there are far fewer hot-Jupiter exoplanets known to transit hot stars with $T_{\rm eff} > 6700\,{\rm K}$ than those transiting later-type stars. In recent years, astronomers have begun using a method called Doppler tomography, sometimes called 'Doppler imaging', to confirm planet candidates which transit host stars in this spectral range. This method involves taking a time-series of high-resolution spectra over a transit event, cross-correlating them with respect to a model spectrum to produce velocity-space cross-correlation functions (CCFs), in order to directly detect the RM effect in the stellar line profiles. The higher rotation rate produces a broader stellar line profile and a broader perturbation, so the perturbation to the CCF becomes resolvable. This technique requires a higher signal-to-noise ratio than RV measurements, and thus a bigger telescope for a given host-star magnitude. A high spectral resolution is also preferred, to better resolve the perturbation, or 'planet bump'.

In tracking the motion of the planet bump across the profile during transit, one can again derive the misalignment angle $\lambda$, since the path of the bump maps to the apparent path of the planet across the stellar disc. For this purpose, a 'tomogram' is produced, which is a time-series of CCFs taken including a transit event. A stellar model is fitted to and subtracted from the CCFs, leaving behind a 'Doppler shadow', which is the residual perturbation to the line profiles caused by the transit. Figure 1.7 is taken from the work of Collier Cameron et al. (2010a), which details the tomographic analysis of the known planet HD 189733b. It shows an example of a clear Doppler shadow of an exoplanet, which is in an aligned, prograde orbit with an obliquity angle of $\lambda \sim -0.4°$. As well as $\lambda$, fitted values for $v \sin i_\star$ and $\gamma$ are obtained when modelling the stellar line profile.

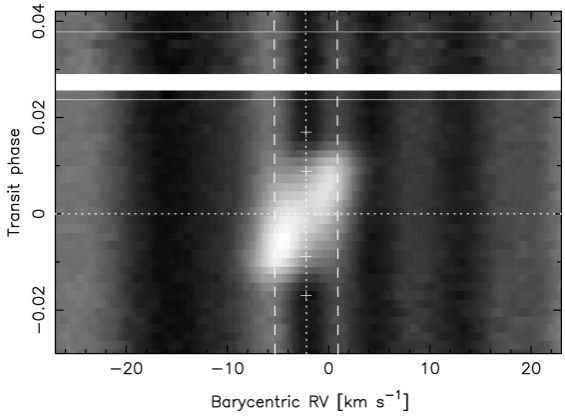


Figure 1.7: Taken from Figure 2 in Collier Cameron et al. 2010a, which shows a time-series Doppler map of planet residuals obtained for HD 189733b. In constructing this plot a model stellar line profile was subtracted from each CCF, leaving behind a clear Doppler transit signal superimposed on a residual spectrum. The four transit contact points are marked with crosses and $T_C$ is marked with a horizontal dotted line. The vertical dotted line shows the position of the $\gamma$ velocity of the system and is bounded by two dashed lines at $\pm\, v \sin i_\star$. The planet trace is inclined bottom left to top right, indicating a prograde orbit (i.e. the planet moves from the blue-shifted side of the tomogram to the red-shifted side).

As with the detection of the RM effect in RV measurements, the detection of the Doppler shadow of a planet confirms that the object producing the transit signal

is passing in front of the star being observed, but does not rule out low-mass non-planetary companions. However, although it is more difficult to obtain accurate orbital RV measurements for hotter targets, it is usually possible to at least obtain an upper limit on the amplitude of the RV curve and thus prove that the mass of the transiting object is within the planetary domain. It is necessary to both measure an upper limit on the mass of the transiting object and the Doppler shadow in order to confirm that there is indeed a planet orbiting the star being observed.

As with other techniques already discussed, Doppler tomography has been used for studying binary systems. Horne (1985, Marsh & Horne (1988, Rutten & Dhillon (1994) worked towards developing the technique as a means of producing maps of accretion discs surrounding cataclysmic variables. Bagnuolo & Gies (1991) showed that it could be used to separate the combined spectral lines of components of multiple-star systems. It has also been used to produce temperature maps of single stars (Vogt & Penrod 1983) and stars in binaries, for the study of magnetic activity and the motion and evolution of starspots (Vincent, Piskunov & Tuominen 1993). When using Doppler tomography to detect planets, the technique has been seen to reveal internal stellar motions, such as differential rotation and convection (Cegla et al. 2016b), as well as stellar pulsations (e.g., Temple et al. 2017).

Brown et al. (2017) perform tomographic and RM analyses of the same data for six WASP systems, which are close to the Kraft break in temperature, and compare the results. The tomographic method is found to consistently give better constraints on $v \sin i_\star$ and $\lambda$. It is worth noting, however, that the tomographic method is more direct and uses more of the line profile information, whereas for the RM method the change in the shape of the line profiles is translated into a perturbation to the measured RV (e.g., Hirano et al. 2011; Boué et al. 2013).

## 1.5 Aims and objectives

With the number of known exoplanets being greater than 4000, there is a need to push new planet discoveries into regimes where few known planets reside. Very little is known about planets with hot host stars and about their formation and evolution, due to the difficulty in obtaining accurate RV measurements for confirmation of their existence (Rowe et al. 2015). It has been seen, however, through an RV survey looking at A-type stars, that there is a dearth of hot Jupiters around stars with masses $> 1.5 M_{\odot}$(Borgniet et al. 2017). Thus planets of Jupiter mass with hot and fast-rotating host stars might be both much harder to find, and much rarer. To date, a total of 21 exoplanets have been confirmed via tomographic means, which are listed in Table 1.5 for reference with some key details of the systems.

The aim of this work is to confirm the existence of transiting planet candidates in the WASP survey with stars in the A–mid-F spectral type range via Doppler tomography. Specific details of the methods used in this work to analyse the combined photometric, velocity and tomographic datasets of transiting candidates will be given in Chapter 2. Of the systems listed in Table 1.5, WASP-167b/KELT-13b, WASP-174b, WASP-190b and WASP-180Ab were confirmed in this work and will be discussed in much detail in subsequent chapters.

## 1.6 The hottest of hot Jupiters: Further characterisation

In this work, the discovery of four new transiting hot Jupiters with host stars of A–mid-F spectral types is discussed. Such planets are likely to have different properties from those orbiting cooler stars. First, planets with hot stars will be more highly irradiated, producing hotter and sometimes "ultra-hot" Jupiters (with $T_{eq} \geq 2200\,K$). The high irradiation is thought to be related to the inflated radii seen in many hot Jupiters (e.g., Hartman et al. 2016), and might also result in these planets having magnetic fields

Table 1.2: List of all known transiting planets confirmed by the Doppler tomography technique to date, in order of discovery.

| Planet name | Period /days | $T_{\rm eff}$ /K | $\lambda$ /° | $v \sin i_\star$ /km s$^{-1}$ | Discovery paper |
|---|---|---|---|---|---|
| WASP-33b | 1.22 | 7308 | –108.8 | 90 | Collier Cameron et al. (2010b) |
| Kepler-448b | 17.86 | 6820 | 12.5 | 60.00 | Bourrier et al. (2015b) |
| HAT-P-57b | 2.47 | 7500 | $6 < \lambda < 57$ | 102.1 | Hartman et al. (2015) |
| KELT-17b | 3.08 | 7454 | –115.9 | 44.2 | Zhou et al. (2016b) |
| XO-6b | 3.77 | 6720 | –20.7 | 48 | Crouzet et al. (2017) |
| HAT-P-67b | 4.81 | 6406 | $< 12$ | 35.8 | Zhou et al. (2017) |
| MASCARA-1b | 2.15 | 7550 | 69.5 | 109.0 | Talens et al. (2017a) |
| WASP-167b/ KELT-13b | 2.02 | 7043 | –165.0 | 49.94 | Temple et al. (2017) |
| KELT-9b | 1.48 | 10170 | –84.8 | 111.4 | Gaudi et al. (2017) |
| KELT-20b (MASCARA-2b) | 3.47 | 8720 | 3.1 | 117.4 | Lund et al. (2017), Talens et al. (2018) |
| WASP-189b | 2.72 | 8000 | 89.3 | 97.1 | Anderson et al. (2018) |
| KELT-19Ab | 4.61 | 7500 | –179.7 | 84.8 | Siverd et al. (2018) |
| KELT-21b | 3.61 | 7598 | –5.6 | 146.03 | Johnson et al. (2018) |
| WASP-174b | 4.23 | 6400 | 31 | 16.5 | Temple et al. (2018) |
| WASP-190b | 5.37 | 6400 | 21 | 13.3 | Temple et al. (2019a) |
| MASACARA-4b | 2.82 | 7800 | 247.5 | 46.5 | Dorval et al. (2019) |
| HATS-70b | 1.89 | 7930 | 8.9 | 40.61 | Zhou et al. (2019a) |
| HAT-P-69b | 4.79 | 7650 | 21.2 | 77.40 | Zhou et al. (2019b) |
| HAT-P-70b | 2.74 | 8400 | 113.1 | 99.87 | Zhou et al. (2019b) |
| KELT-24b (MASCARA-3b) | 5.55 | 6508 | 2.6 | 19.46 | Rodriguez et al. (2019), Hjorth et al. (2019) |
| WASP-180Ab | 3.41 | 6500 | –162 | 19.6 | Temple et al. (2019b) |

which are stronger than in cooler ones: the continuous injection of thermal energy into a gas giant's interior might create a more efficient planetary dynamo (Yadav & Thorngren 2017). Second, a topic of avid discussion in recent literature is the tendency first noted by Winn et al. (2010) for hot Jupiters transiting hotter stars to be more likely to have misaligned orbits (e.g., Valsecchi & Rasio 2014; Mazeh et al. 2015; Dai & Winn 2017, for a review, see Triaud 2017). Third, in systems where the host star is a fast rotator, the rotation period can be shorter than the planet's orbital period, leading to a systematically different tidal interaction than is expected for most hot-Jupiter systems (see, e.g., Crouzet et al. 2017). As such, these systems are of great interest for further study, with a view to understanding their properties and histories, and ultimately completing the picture of planet formation and evolution. This Section describes some of the larger areas of further exoplanet research currently being carried out, and for which the planets presented in this work may become targets.

### 1.6.1 Atmospheric Characterisation of transiting hot Jupiters

Transiting hot Jupiters often make ideal candidates for studies of exoplanet atmospheres, which is one of the most active areas of exoplanet research today. The high levels of stellar irradiation causes the atmospheres of hot Jupiters to be inflated, producing a large scale height ($\mathrm{H} = \mathrm{k}\,\mathrm{T_p}/\mu\,\mathrm{g_p}$) and making them amenable targets of transmission spectroscopy during transit (e.g., Kreidberg et al. 2015; Wyttenbach et al. 2015; Gibson et al. 2017; Yan & Henning 2018). As well as this, the increased irradiation causes high temperatures on the tidally-locked day-side of the planet, which results in the constituent molecules existing in states above the ground level. These molecules may spontaneously decay through the emission of a photon of infrared wavelength. The result is continuum emission which is isotropic and equivalent to a blackbody ($\mathrm{B}_\lambda(\mathrm{T})$), which can be seen just before secondary eclipse when the planet passes behind the star and its day-side emission becomes visible (e.g., Gillon et al. 2010; Stevenson et al. 2014). Ultra-hot Jupiters are very close to blackbody emitters on the dayside because more highly-irradiated planets are less efficient at recirculating the injected heat within the

atmosphere (Heng & Showman 2015). Hot Jupiters with stars in the A–mid-F spectral type range can be particularly useful targets of atmospheric characterisation, since for a given orbital separation they will receive more insolation and thus be hotter than a counterpart hot Jupiter with a cooler host star.

Transmission spectroscopy involves observing the stellar light that transmits through the planet's atmosphere during transit. There are two methods employed: low resolution slit spectroscopy and high resolution echelle spectroscopy. Low resolution spectroscopy entails observing a transit event spectroscopically with both the target star and a comparison star within a long slit. This produces a spectrum which is dispersed by the slit and which contains two peaks, one for each star. The spectroscopic flux of the target star relative to the comparison star is then measured in different wavelength bins, in order to produce spectrophotometric transit lightcurves for each waveband. Changes in the depth of this lightcurve as a function of wavelength is an indicator of changes in the level of absorption due to the atmosphere of the planet. Increased absorption is a consequence of increased opacity in the atmosphere at that wavelength, so the disc of the planet appears larger and thus the depth of the transit becomes deeper. The wavelength slices are chosen such that they encompass areas of the spectrum which are strongly affected by particular molecules, so that one can infer the presence of particular absorbers in the planet's atmosphere (see, e.g., Kempton et al. 2017). Alternatively, echelle spectrographs are used to take high resolution spectra outside and during a transit event in order to look for enhancement of individual stellar absorption features by the planet's atmosphere (after telluric line correction). The relative strength of the planet:star absorption features is an indicator of the abundance of particular molecules. The former method is not well suited to systems with A–mid-F type host stars due to the lack of suitable companion stars in close proximity to the target, since there are few early-type stars in the local neighbourhood compared to later-type stars. On the other hand, they are well suited to the latter method since the stars themselves have very few weak spectral lines, making the absorption contribution of the planet's atmosphere easier to detect. Both forms of transmission spectroscopy enable the determination of the chemical composition of a

hot Jupiter atmosphere while also tracing the altitude and extent of clouds and hazes.

Emission spectroscopy is suitable for the study of ultra-hot Jupiters with $T_{\rm eff} \geq 2200\,{\rm K}$ . It involves taking an infrared spectrum of a planetary system just before, during and if possible after a secondary eclipse. In doing so one can compare the in-eclipse and out-of-eclipse spectra to determine the contribution of the planet's day-side relative to the stellar contribution. This is done in several infrared wavebands, and so it is possible to compare the measured eclipse depths with model atmospheres calculated for different chemical compositions and infer the presence of particular emitters. The depth of the secondary eclipse also provides information about the presence of clouds or hazes or thermal inversions in the atmosphere.

An example of an ultra-hot Jupiter which has been the subject of much atmospheric study is KELT-9b. With an extreme temperature of $T_{\rm eql} \sim 4000\,{\rm K}$ (Gaudi et al. 2017), the planet's atmosphere is expected to contain only atomic species and thus be free from complex chemical processes, making it an ideal target for determining the chemical composition of a planet's atmosphere. Several recent works have found evidence of a variety of species in KELT-9b's atmosphere using transmission spectroscopy, including Na I, Cr II, Mg I, Fe I, Fe II, and Ti II (Hoeijmakers et al. 2018; Cauley et al. 2019; Hoeijmakers et al. 2019). Another area of interest is the study of thermal inversions in the atmospheres of ultra-hot Jupiters. These are expected to be produced via the combination of high irradiation and absorption in the upper atmosphere by molecules like TiO and VO (Fortney et al. 2008a). This effect has been seen in some ultra-hot Jupiters, such as WASP-121b (Evans et al. 2017), while others show no evidence of an inversion, such as Kepler-13Ab (Beatty et al. 2017). In some cases, there is evidence of a thermal inversion on the day-side of the planet but not on the much cooler night-side (e.g., WASP-103b Kreidberg et al. 2018a). The suggestion is that cold-trap processes (e.g., Spiegel, Silverio & Burrows 2009; Parmentier, Showman & Lian 2013 may lead to the depletion of gas-phase TiO and VO from a hot Jupiter's upper atmosphere. Water has been seen to produce prominent spectral features in observations of cooler hot Jupiters, such as WASP-107b (Kreidberg et al. 2018b), while the more blackbody-like spectra of hotter Jupiters show almost no evidence of water,

a trait that has been attributed to a combination of increased opacity in ultra-hot Jupiters due to the presence of $H^-$ ions and the disassociation of water molecules on the day-side (Kreidberg et al. 2018a; Arcangeli et al. 2018; Parmentier et al. 2018).

### 1.6.2 Mass loss from hot Jupiter atmospheres

It is expected that hot Jupiters will undergo some degree of mass loss over their lifetimes due to the high level of irradiation experienced. The amount of mass loss depends on the amount of high-energy electromagnetic radiation incident on the planet and thus depends on the spectral type of the host star. More extreme mass loss is expected for planets with hotter host stars, which peak more towards the UV part of the spectrum. Other factors which can affect mass-loss rates include the composition and density of the exoplanet atmosphere being considered and the star-planet separation.

Locci, Cecchi-Pestellini & Micela (2019) study the photoevaporation of hot Jupiters with dM and dG host stars. For such stars, the majority of mass loss is expected to occur at early times, when the level of XUV irradiation is still high, and therefore this is thought to be one of the mechanisms by which the size distribution of such planets is determined. Locci, Cecchi-Pestellini & Micela (2019) find that 2% of hot Jupiters ($P < 6\,d$) with dM-type hosts and 4% with dG-type hosts are vaporized within 1 Gyr, while a significant level of evaporation is seen in 2% of planets with dM stars and 1% of those with dG stars.

Hot Jupiters with magnetically active M- and K-type host stars can experience mass loss during their lifetime due to enhanced emission in XUV wavelengths. Chadney et al. (2015) show that such planets are more likely to experience mass loss at larger orbital separations when compared to planets orbiting stars with low magnetic activity.

The planets which are more likely to experience mass loss for most of their lifetimes are close-in, high-mass, low-density planets around stars of earlier spectral types. The hotter the planet, the more material exists in a dissociated volatile state, making it easier for particles to gain the required escape velocity.

In the case of hot Jupiters with Sun-like stars, mass loss can occur over long

timescales, but at fairly low rates. HD 209458b is a $1.27\,R_{Jup}$ planet in a 3.52-d orbit around an F8 star (Cody & Sasselov 2002). In comparing moderate-resolution, high signal-to-noise UV spectra taken at quadrature, during transit and during secondary eclipse, Linsky et al. (2010) were able to detect signatures of the expanding planetary atmosphere, measuring a mass-loss rate of $(8–40) \times 10^{10}\,g\,s^{-1}$. This mass-loss rate is consistent with outflows containing volatile metals.

For comparison, the hottest planet currently known is KELT-9b, with an inflated radius of $1.9\,R_{Jup}$, a period of 1.48 d and an A0 host star that puts the planet's day-side temperature at 4600 K (Gaudi et al. 2017). This makes the planet as hot as a K4-type star and so it is likely that the day-side atmosphere is composed almost entirely of atomic metals. The planet is also being subjected to a much larger amount of XUV radiation than cooler counterparts, implying much greater mass loss rates. It is expected that the planet's gaseous envelope will be mostly ablated over the star's main sequence lifetime. WASP-178b ($T_{eql} = 2470\,K$, $R_p = 1.8\,R_{Jup}$) has the second hottest host star of all transiting planets with $T_{eff} = 9350\,K$ and is also considered to have the potential for photo-evaporation (Hellier et al. 2019a). Hellier et al. (2019a) also find that there is a tendency for the hottest of hot Jupiters to have higher masses on average than cooler Jupiters, perhaps reflective of lower-mass ultra-hot Jupiters having short photo-evaporation timescales (Owen & Lai 2018).

Another possibility is for a hot Jupiter on a close-in orbit to exceed its Roche lobe and lose material which would then be accreted onto the host star. WASP-12b is an ultra-hot Jupiter with a radius of $1.79\,R_{Jup}$, a mass of $1.41 M_{Jup}$, a period of 1.09 d and a host star of G0 spectral type (Hebb et al. 2009). Transit observations in the NUV (Fossati et al. 2010; Haswell et al. 2012; Nichols et al. 2015) and the study of Spitzer phase curves (Bell et al. 2019) have shown evidence of mass loss in the upper atmosphere of the planet which is consistent with a flow of hot, dense gas towards/away from the star.

### 1.6.3 Formation and evolution of hot Jupiter systems

Often, the orbits of hot Jupiters are not aligned with the rotation axis of their stars. The two main mechanisms thought to produce misaligned orbits are: high-eccentricity migration due to perturbation by additional bodies, leading to a range of measured obliquities (e.g., Dong, Katz & Socrates 2014; Anderson, Storch & Lai 2016); and migration of the planet within a protoplanetary disc that is itself tilted with respect to the rotation axis of the star, possibly also due to the presence of additional bodies (Crida & Batygin 2014; Fielding et al. 2015). There has been much work towards understanding the migration of hot Jupiters leading to aligned or misaligned orbits, but the picture is as yet incomplete (e.g., Matsumura, Peale & Rasio 2010; Madhusudhan, Amin & Kennedy 2014; Storch, Lai & Anderson 2017; Bitsch et al. 2019). The possibility of in-situ formation has also been considered, for example by Bodenheimer, Hubickyj & Lissauer (2000, Batygin, Bodenheimer & Laughlin (2016, Boley, Granados Contreras & Gladman (2016, Hasegawa, Yu & Hansen (2019). Such studies have shown that in-situ formation can only occur if certain conditions are met and that a hot Jupiter that formed in-situ would likely be accompanied by low-mass planets on short period orbits. Dawson & Johnson (2018) provides a good review of the different paths to the observed range of hot-Jupiter orbits.

Observations of hot Jupiters with early-type stars have shown that they are more likely to have misaligned orbits than their cooler counterparts (Winn et al. 2010; Albrecht et al. 2012). This implies that they must have undergone a different dynamical evolution. The leading theory is that, after the misalignment of a hot-Jupiter orbit with a host star below the Kraft break (discussed in Section 1.4.3), the stellar rotation axis would be realigned with the normal to the orbital plane via tidal dissipation. For planet hosts beyond the Kraft break, which have negligible convection zones, realignment may not be possible within the planet's lifetime. Hot Jupiters that are not misaligned with respect to the stellar rotation, but have early-type hosts, may simply have migrated in a less violent manner within an aligned protoplanetary disc, or formed in-situ. Thus far, however, tidal dissipation studies have been unable to satisfactorially reproduce

the observed distribution of planetary obliquities.

One of the difficulties had in forming migration theories is in determining how the migration of a hot Jupiter is halted before the planet is engulfed by the star, particularly in the case of disc migration. A very recent study by Heller (2019) promotes disc migration combined with evolving stellar tides as a suitable mechanism. They are able to reproduce the observed range of semi-major axes of hot jupiters, and find that the survival rate of migrating hot Jupiters is greater for high viscocity discs, leading to an increased number of hot Jupiters orbiting metal rich stars (consistent with observations). A key part of their theory is a 'tidal migration barrier', which is a region of zero total torque (where stellar tides counteract planet-disc interactions) from which migrating hot Jupiters are rebound. However, the barrier only occurs for planets which are migrating in an aligned plane.

Another key point of interest is the fact that hot Jupiters which orbit their stars more quickly than the stellar rotation rate are being discovered (e.g., Wu & Murray 2003; Fabrycky & Tremaine 2007; McQuillan, Mazeh & Aigrain 2013). One may then expect that the usual tidal interaction that drains angular momentum from a planet's orbit would be reversed in such cases, provided the planet is in a prograde orbit. This may also have consequences for theories of orbital evolution.

# 2 Instrumentation and Methods

This Chapter will provide an overview of the methods by which the WASP team select, follow-up and analyse candidate planetary systems. This information is provided to supplement that given in subsequent Chapters, which will detail the analyses of specific targets.

## 2.1 Initial detection and Candidate Vetting

### 2.1.1 The WASP-South survey

The Wide-Angle Search for Planets (WASP) is a transiting planet survey consisting of two sites: WASP-North at the Roque de los Muchachos Observatory in La Palma, and WASP-South at the South African Astronomical Observatory (SAAO) in South Africa (Pollacco et al. 2006; Hellier et al. 2011). WASP is the leading ground-based planet search project: in surveying both hemispheres for more than a decade it is responsible for the discovery of more than 150 new planets. WASP-North preceded WASP-South, operating for 8 months in 2004 with five cameras. In 2005 the site was upgraded and then joined by WASP-South in 2006, each site operating with a fully robotic, remotely operated 8-camera array. WASP-South then surveyed the skies almost continuously from 2006 to 2017, excepting instances when the site was closed for upgrading or repair. This has lead to the collection of tens of thousands of magnitude measurements for tens of thousands of stars. The results presented in this work are based on data taken from both sites, though primarily data from WASP-South is used.

The WASP camera arrays were mounted on a robotic equatorial fork mount, with a tracking accuracy better than $0''.01$ s$^{-1}$. The majority of the data used in this work was taken using 200-mm f/1.8 lenses, covering a $7.8^\circ \times 7.8^\circ$ field of view, which were installed for most of the project. In 2014, 85-mm lenses were installed at the WASP-South site with the intention of searching for planets around the brightest of stars,

and some of the data used in this work was taken post-upgrade. Up to eight fields were observed simultaneously, each one for several months at a time, and there was significant overlap in the observed fields year-to-year. This enabled the collection of data over a sufficiently long baseline for confident detections of transits. A broad-band filter was used (400–700nm) with typically 30-s exposures and a short cadence of $\sim$10 minutes, yielding a signal-to-noise of $\sim$100 at $V \sim 12.5$.

### 2.1.2 WASP data reduction

A pipeline was developed for reducing and analysing WASP data in order to quickly select strong candidate transiting planet systems from the many stars observed. The reduction procedures are described in detail by Collier Cameron et al. (2006) and a short summary will now be provided.

The SuperWASP pipeline first classifies the frames taken as bias, flat field, dark, or object frames, and then performs standard data reduction processes to correct the object frames for systematic effects and artefacts. Master bias, flat-field and dark frames are created by calculating a weighted average of all frames of each type, excluding outliers. The bias and dark master frames are then subtracted from the object frames, followed by dividing the object frames by the flat field master frame. This respectively accounts for the CCD bias, dark current (hot pixels) and optical vignetting.

Aperture photometry is carried out on the corrected object frames to extract magnitude measurements for all stars in the frame. The Extractor software (Bertin & Arnouts 1996) is used to create a catalogue of the stars in each frame, which are then paired with TYCHO-2 objects (Høg et al. 2000). All objects with red magnitudes brighter than $\sim$15.0 at second epoch are measured using apertures of 2.5, 3.5 and 4.5 pixels. The ratio of an object's flux level between apertures is used to identify extended objects such as galaxies and to determine the likelihood of stellar blends. The measured fluxes are corrected for first and second order extinction, and each object is assigned an identifier of the form '1SWASP Jhhmmss.ss+ddmmss.s' containing the object's coordinates at J2000. Finally, the measured fluxes are converted to so-called 'WASP V

magnitudes' using a relation between instrumental magnitudes and TYCHO-2 V-band magnitudes, and the zero-point of each frame is determined using a network of local secondary standards. These WASP magnitudes are stored in the SuperWASP data archive located at the University of Leicester.

Before the WASP magnitude measurements can be searched for transit signals, the data must be decorrelated to remove residual systematic signals that remain after the standard data reduction procedure. An initial course decorrelation compares each stellar magnitude to the average for that star, removing small deviations from the star's zero-point that occur from night-to-night and frame-to-frame, while measuring variations caused by stellar variability or clouding. This is followed by the application of the SysRem algorithm (Tamuz, Mazeh & Zucker 2005), which removes the effects of correlated errors such as those arising from: errors in TYCHO-2 magnitudes; a lack of magnitudes for fainter stars; Sahara dust events; optical vignetting; changes in temperature during observations, etc. The Tamuz, Mazeh & Zucker (2005) algorithm is robust and effective at removing correlated errors, and thus no further decorrelation is required after its application.

### 2.1.3 Transit search and candidate selection

The WASP data is searched for transit signals using a Box Least Squares (BLS) algorithm adapted from the work of Kovács, Zucker & Mazeh (2002), which is described in full by Collier Cameron et al. (2006). This method uses a search grid composed of frequencies and epochs to look for signals resembling a periodic box function, whereby the subset of in-transit points is set by the transit period, duration and phase. The step between frequencies is set so that the total accumulated phase difference between frequencies over the full dataset is equal to the expected transit duration at the longest search period. The step in phase between proposed transit epochs is then set to the expected transit duration at each frequency. The duration for each frequency is calculated with Kepler's third law for a planet mass of $0.9\,\mathrm{M_{Jup}}$. For each model in the search grid, the transit depth and a goodness-of-fit $\chi^2$ statistic are calculated.

After application of the BLS algorithm, the candidate systems must pass a series of plausibility tests before they are selected for further analysis. This is a multiple-stage filtering procedure that aims to select the targets most likely to be genuine planet detections. In the first stage, stars with a post-fit $\chi^2 > 3.5N$, where $N$ is the number of data points, are rejected as variable stars. Candidates with a phase-folded lightcurve containing gaps wider than 2.5 times the transit width, or with fewer than 2 transits in the best-fit model, are also rejected. The remaining candidates must then meet two statistical conditions which ensure that the signal being fitted is a significant periodic dimming rather than a periodic brightening, consistent with a planetary transit. This stage eliminates $\sim 96.5\,\%$ of potential targets from consideration, which are either intrinsically variable stars or stars affected by systematics that could not be corrected by the application of the SysRem algorithm.

In the second stage, the remaining candidates are entered into a further BLS search using a finer search grid, after which the transit parameters of the most promising candidate systems are refined. A softened box-like function is adopted, whose shape depends on the transit epoch, duration, period and depth, enabling refinement following a Newton-Raphson approach. The third stage is a by-eye inspection of the transit lightcurves, and those containing clear secondary eclipses and/or out-of-transit variability are rejected. A series of further tests are then carried out as described in Section 6 of Collier Cameron et al. (2006), which eliminates targets that: have lightcurves containing ellipsoidal modulations (indicative of an eclipsing binary); have transit durations more or less than 1.5 times the predicted value; have a transit depth consistent with an occulting object with a radius above $1.6\,\mathrm{R_{Jup}}$; are blended with stars less than three magnitudes fainter than the target and have proper motions and $V - K$ colours (from various catalogues) that are not consistent with main-sequence stars. What remains after this rigorous process is a shortlist of high-priority candidate exoplanet systems.

The final stage in the selection of WASP candidates for photometric and spectroscopic follow-up with higher resolution telescopes is a preliminary Bayesian analysis of the reduced WASP data, described in full by Collier Cameron et al. (2007). A

Markov-Chain Monte Carlo (MCMC) algorithm is used to derive posterior probability distributions for transit parameters, adopting a Bayesian prior on the stellar mass and radius that ensures they are consistent with a main-sequence star. This eliminates $\sim$67% of spectroscopic binaries in the shortlist, including most grazing binaries. The process selects roughly 1 in 5 targets from the high-priority shortlist as candidates for extensive follow-up.

## 2.2 Candidate WASP targets for tomographic confirmation

A total of 15 WASP-South candidate systems were selected for tomographic follow-up, with the intention of confirming or refuting the planet hypothesis. Of these, tomographic data were obtained for 10 candidates over two observing cycles with the ESO 3.6-m/HARPS spectrograph. The first group of targets were observed under program 096.C-0762: these were 1SWASP J130410.53-353258.2 (SW1304), 1SWASP J130310.57-412305.3 (SW1303), 1SWASP J055111.44-491521.7 (SW0551) and 1SWASP J064757.25-443142.7 (SW0647). Candidates SW1304 and SW1303 were indeed proved to be genuine planet detections and were renamed WASP-167b/KELT-13b and WASP-174b, respectively (see Chapters 3, 4).

Following the success of the first round of candidates, a second round of observations were attempted under program 0100.C-0847(A), leading to the collection of tomographic data for candidates 1SWASP J002535.01-184856.8 (SW0025), 1SWASP J003050.23-403424.3 (SW0030), 1SWASP J062317.58-330615.9 (SW0623), 1SWASP J081334.15-015857.9 (SW0813), 1SWASP J083747.01-193804.8 (SW0837), 1SWASP J142029.49-311207.4 (SW1420) and 1SWASP J150244.86-030152.9 (SW1502). Of these, SW0030, SW0813, SW0837 and SW1502 were shown to be planets. SW0030 and SW0813 were renamed WASP-190b and WASP-180b and are described in detail in Chapters 5, 6. SW1502 was pursued by another member of the WASP team and dubbed WASP-189b (Anderson et al. 2018). SW0837 will also be followed up by an-

other member of the WASP team, in future work. SW1420 was published by another survey team with the name NGTS-2b (Raynard et al. 2018). The remaining candidates, SW0025, SW0551, SW0623 and SW0647, were found to be false positive transit detections and will be discussed in Chapter 7.

## 2.3 Follow-up Observations

### 2.3.1 Photometry: the TRAPPIST and SPECULOOS telescopes

Once the reduction and vetting procedures described in Section 2.1 are complete, follow-up photometric observations of the most promising candidates are taken using larger, higher resolution telescopes. These serve to confirm the shape and timing of the transit, since the low signal-to-noise of the discovery data can mean that the system parameters obtained from fitting that data alone may be inaccurate or imprecise. Confirmation of the timing of the transit is especially important for planning the spectroscopic measurements required to confirm the planetary nature of the transiting object, via radial velocities and, if appropriate, Doppler tomography.

Most of the follow-up photometry of WASP-South candidate planets is carried out using the TRAPPIST-South telescope, which has operated since 2010 and is located at the European Southern Observatory (ESO) in La Silla, Chile (Gillon et al. 2011; Jehin et al. 2011). TRAPPIST-South was known simply as TRAPPIST until the installation of the TRAPPIST-North facility in 2016, which is based at the Oukaïmden Observatory in Morocco (Barkaoui et al. 2017; Barkaoui et al. 2019). TRAPPIST-South is a 0.6-m telescope with a $22' \times 22'$ field of view, equipped with a CCD camera that yields an angular resolution of $0''.65$ per pixel over a $2048 \times 2048$ chip. It has been used extensively in WASP discovery papers for the characterisation of exoplanet systems (e.g., Gillon et al. 2012). TRAPPIST-North is also a 0.6-m telescope with a $2048 \times 2048$ CCD, but yields a $19'.8 \times 19'.8$ field of view and a $0''.60$ per pixel resolution.

More recently, a project called the Search for habitable Planets EClipsing ULtra-

cOOl Stars (SPECULOOS) based at ESO Paranal observatory began the commissioning of four new identical telescopes called SPECULOOS-Europa, -Ganymede, -Io and -Callisto. SPECULOOS is a ground-based transit survey targeting the nearest ultracool dwarf stars in the search for planets of Earth-like masses (Burdanov et al. 2018; Delrez et al. 2018). The commissioning phase has included some follow-up of WASP candidates. The SPECULOOS telescopes are all robotic Ritchey-Chretien (F/8) telescopes with 1-m apertures and 2K $\times$ 2K CCD cameras, yielding a $12' \times 12'$ field of view and a resolution of $0.35''$ per pixel. Data from a SPECULOOS telescope was first featured in a WASP paper in the work on WASP-174b (see Chapter 4 and Temple et al. (2018)).

The reduction of TRAPPIST data is described by Gillon et al. (2013). The reduction pipeline for SPECULOOS is still being developed (Murray et al. in prep), but the data used in this work was reduced following a very similar procedure to the TRAPPIST data. This consists of a standard correction for bias, dark and flat-field variations, followed by aperture photometry using IRAF/DAOPHOT (Stetson 1987). Comparison stars and aperture sizes for the photometry are selected manually, producing the best possible photometric quality in terms of the out-of-transit flux standard deviation. Quantities which may introduce correlated error into the data, such as airmass, are calculated for each observation so that detrending can be performed if necessary.

### 2.3.2 Radial velocities: Euler/CORALIE

For the majority of WASP planets, the spectra used for radial velocity measurements (RVs) of candidate exoplanets are taken using the CORALIE spectrograph attached to the Euler/1.2-m telescope at ESO in Chile (Queloz et al. 2001b). The CORALIE spectrograph is a fibre-fed echelle spectrograph with a spectral resolution of 50,000. For hotter candidates a higher spectral resolution is sometimes needed in order to confidently measure the RV semi-amplitude (or an upper limit on that quantity). This is done with the ESO 3.6m/HARPS spectrograph, which is described in the next

Section.

Only a few orbital RV measurements are required to rule out stellar-mass transiting objects: the amplitude of the RV curve for such an object will be orders of magnitude greater than for a planet, so a couple of good quality measurements around quadrature points will be a good indication of the nature of the object producing the transit signal. For precise modelling, however, the curve will need to be well sampled, and so measurements will be made over the full range of orbital phase, as well as multiple points around quadrature if possible. These measurements may be taken close together, or spaced out over an observing season in order to have optimal observing conditions for each of them.

Observed CORALIE spectra are reduced using the standard CORALIE Data Reduction Software described by Baranne et al. (1996) and Queloz et al. (2001b). Cross-Correlation Functions (CCFs) are produced by correlating the spectra over a window several times the expected width of the stellar line profile, using a binary mask (containing zeroes at the position of absorption lines and ones in the continuum) that is appropriate to the spectral type of the star being observed. During this process, the velocity information associated with the CCF is saved in the .fits headers in the form of a start value and step size and an initial estimate for the system velocity $\gamma$ is measured assuming a Gaussian shape for the stellar line profile, which is also entered into the header. RVs are measured as the position of the centre of the stellar line profile by fitting it with a rotationally-broadened Gaussian. Velocity bisector spans are also measured between $\sim$20% and $\sim$80% of the line depth to look for correlation with the measured RVs, which would indicate that the transit signal is likely the product of stellar activity rather than a planet (Queloz et al. 2001a).

### 2.3.3 Tomographic data: ESO3.6m/HARPS

HARPS is a spectrograph which was based on CORALIE, but which has a much higher spectral resolution of 120,000 combined with the higher light-collecting power of ESO's 3.6-m telescope at ESO Observatory, La Silla, Chile. HARPS is fully enclosed in a

vacuum tank, whereas CORALIE is not. This makes it ideal for tomographic analysis, which requires higher resolution in order to bring out very small perturbations to the stellar line profile. In cases where it is difficult to discern the shape of the RV curve due to increased scatter or low signal-to-noise (e.g., when looking at a hot or faint target), HARPS is sometimes also used to take RVs for WASP-South systems.

For tomography of an exoplanet, a series of HARPS spectra are taken including a transit event. The spectra are converted to CCFs following the same methodology as for CORALIE spectra: the data are reduced using the standard HARPS Data Reduction Software as described by Baranne et al. (1996) and Pepe et al. (2002). RVs are measured in the same way as CORALIE RVs. RV measurements taken including a transit can be used in RM analysis (see Section 1.4.2), or the CCFs can be fitted directly in tomographic analysis (see Section 1.4.4).

### 2.3.4 Inspection of tomographic data

Once a set of CCFs covering a transit event have been obtained, the data must be inspected for evidence of a planet and then converted into the form required for analysis. For this purpose, I developed some software in Python. The software searches for CCFs taken within a specified range of Barycentric Julian Dates (BJDs) to select observations taken on the same night. It then reads the contrast values from each .fits file and uses the information provided in the header (see Section 2.3.2) to calculate the Barycentric Radial Velocity (BRV) value to be assigned to each pixel. The user must provide initial estimates of the transit epoch in BJD, the orbital period and the transit duration, all of which can be obtained via a preliminary analysis of the WASP lightcurve. This information is used to calculate the orbital phase of each observation and the expected transit duration in phase. The user can also input one of the options 'mean' or 'minimum', which will determine how the stellar line profile is removed from the CCFs, in order to search for the signature of a planet.

Each CCF is normalised with respect to the median of the first 100 values in the CCF. The normalised CCFs are then displayed in a plot of contrast vs. BRV, which

allows the user to identify poor quality data (which may have been affected by cloud or autofocus drift, for example) and to estimate $v \sin i_\star$, which they are then asked to provide.

An estimate for the stellar line profile is then computed. If the 'mean' option was inputted, then an average of the out-of-transit CCFs is computed by taking the mean value in each pixel from the range of phases outside the expected transit duration. The mean CCF is then subtracted from all CCFs. If 'minimum' was chosen, then the minimum value in each pixel from the range of phases is taken to construct a 'minimum CCF', which is then subtracted from all CCFs. Both of these options serve to remove the stellar line profile from the CCFs. Taking the mean of the out-of-transit CCFs generally produces a better representation of the stellar line profile. However, in cases where there is evidence of stellar pulsations in the host star, a minimum subtraction is more appropriate, lest the pulsation signal be averaged out. Using minimum subtraction is not advisable when there is no evidence of stellar modulations, as this often introduces artefact signals when an anomalously low value is subtracted from all CCFs.

The mean-subtracted (or minimum-subtracted) CCFs are then plotted in phase as a colour map (this is the 'tomogram'). The positions of the estimated start and end phases of the transit are marked on the figure, as are the positions of the system velocity $\gamma$ (from the header) and the positions of $\gamma \pm v \sin i_\star$. This clearly marks the area of the tomogram in which the planet shadow is expected to appear, allowing efficient inspection of the data. If some of the CCFs are identified as having low signal-to-noise, they can be removed at this stage and the process repeated to create a cleaner tomogram. Finally, a file containing the BJD timestamps for each observation is created, as is another file containing all of the normalised CCFs in the format "[BRV] [contrast] [CCF ID]". The files are used by the MCMC fitting code described in the next Section.

A second piece of software was developed to produce publication-ready figures from the results of an MCMC. It takes the outputted planet model, the original data files and the best-fit system parameters to produce the final tomogram along with the

residuals from subtracting the planet model.

## 2.4 Combined MCMC analysis Characterisation of transiting exoplanets

There are a number of different approaches to finding the best possible solution to the sets of equations that define the morphology of transit lightcurves, RV curves and the Doppler shadow of a planet. A common and well-established method is to use a Markov-Chain Monte Carlo (MCMC) fitting approach. MCMC is a robust $\chi^2$ minimisation algorithm which trials a series of parameter sets until the set which best fits all available data is found. The WASP team has developed an MCMC pipeline which is described in detail by Collier Cameron et al. (2007), Pollacco et al. (2008) and Collier Cameron et al. (2010a). This Chapter will describe the general procedure carried out for the analysis of the planets presented in this work. More specific details of the analyses of the targets confirmed by this work are presented in subsequent Chapters.

### 2.4.1 Step 1: Spectral analysis

The first step in analysing the combined photometric, velocity and tomographic data is to determine some stellar properties to be used as priors. Each of the targets studied in this work has a time series of high resolution spectra taken using the HARPS spectrograph over the course of a transit. A spectral analysis is performed on a median-stacked HARPS spectrum, created from the time series of spectra, following the methods of Doyle et al. (2013). This provides measurements of the stellar effective temperature $T_{\rm eff}$, stellar surface gravity $\log g_\star$ , the stellar metallicity [Fe/H] and the projected stellar rotational velocity $v \sin i_\star$. An initial estimate of $\log g_\star$ is calculated for a zero-age main-sequence star (ZAMS) of the same spectral type as the target (Gray 1992). To measure $v \sin i_\star$, some constraints on the macro- and micro-turbulent velocities are needed. For stars in the applicable temperature ranges, these would be estimated

using the calibrations of Bruntt et al. (2010) (5000–6500 K) and Doyle et al. (2014) (5200–6400 K). If the stellar temperature lies outside these ranges, one could extrapolate these calibrations to estimate the macro- and micro-turbulence, adopt an upper limit on these quantities, or set them to $0\,\mathrm{km\,s^{-1}}$ and take the fitted $v \sin i_\star$ as an upper limit on $v \sin i_\star$. The values of $T_{\rm eff}$ and $v \sin i_\star$ obtained in this analysis can then be used as Gaussian priors to constrain parameters in the MCMC.

### 2.4.2 Step 2: Photometric, RV and tomographic analysis

The MCMC code is able to fit the photometric, RV and tomographic data simultaneously. Trial solutions are accepted only if the $\chi^2$ value for each solution is within a certain range. We set the required number of accepted jump steps between parameter sets, which ultimately determines how many trial solutions will be tested. A number of the parameters can be constrained using solutions obtained in other parts of the analysis. The early MCMC fit of the WASP lightcurve provides initial estimates of the transit epoch, period, duration, depth and the orbital impact parameter, with jump sizes set to $1\sigma$. As mentioned in the previous Section, the spectral $v \sin i_\star$ and $T_{\rm eff}$ are used as priors on those quantities. For the tomography, a preliminary Gaussian fit to the CCF profiles gives a start value for $\gamma$. Initial runs are then carried out using small numbers of accepted jumps to estimate the parameters for which there is no prior measurement ($\lambda$ and $K$). A 'correlation length' is calculated for each parameter at the end of a run, which is the average number of accepted steps between independent solutions. Outputs from the preliminary runs are then used as inputs in the final production runs, whose lengths will be set such that the total number of accepted steps is much greater than the measured correlation lengths, to ensure an unbiased fit.

The code includes provisions for dealing with photometric and RV datasets taken with different instruments, since the data will be subject to different systematics. The error bars in the lightcurves are re-scaled to give $\chi^2_\nu = 1$. This down-weights poor quality datasets so that the fit is then dominated by the better datasets. We also allow for a possible offset between radial velocity datasets from different instruments.

We do not fit limb darkening coefficients as jump parameters, since the data is not of sufficient quality to do so. Instead, we use four-parameter non-linear coefficients interpolated from the tables of Claret (2000);Claret (2004). We use the tables appropriate for the passband used for each observation. Coefficients are interpolated at each step in the MCMC using the new values of $T_{\rm eff}$, [Fe/H] and $\log g_\star$. We use the Enoch-Torres relation (Enoch et al. 2010);Torres, Andersen & Giménez (2010) to calculate the stellar mass at each step, which is suitable for stars with $T_{\rm eff} > 5500\,{\rm K}$. We are thus able to also calculate parameters for the planet: $R_p$, $\rho_p$, $M_p$ and $\log g_p$.

The tomographic part of the code deconstructs the CCFs into their constituent parts and fits them separately, then combines the best-fit solutions into a composite model. The components of the CCF are the stellar line profile, the (moving) planet bump and the background residual spectrum that remains after subtraction of the other two components. The tomographic analysis gives values for $\lambda$, $v \sin i_\star$ and $\gamma$. It is also necessary to fit the local line width $v_{\rm FWHM}$, resulting from stellar turbulence and instrumental broadening, which influences the width of the planetary perturbation of the line profiles, and whose shape is assumed to be Gaussian. When it is possible to perform the more traditional RM analysis in terms of RV measurements, this is done using the semi-analytic method of Hirano et al. (2011).

Once the production runs are complete, the code outputs the posterior probability distributions for each parameter, along with a results file containing the median value from the range of solutions for each parameter. These median values are adopted as the solution for the system, with uncertainties equal to $1\sigma$. In this way, the final quoted parameters are a better representation of the accepted solutions as a whole. Generally, the actual best-fit value is not very discrepant from the median of the distribution.

Several production runs may be carried out with differing sets of constraints in order to test the extent to which the results may be biased by the various priors. Priors are used because the parameter space is large, and it is easy for the MCMC to fall into a local minimum rather than find the actual solution if it is looking in the wrong place. It is also sometimes the case that a dataset is not of sufficient quality to constrain all parameters independent of priors. A solution is only adopted, however, if it is shown to

be reproducible with different combinations of priors. In this way we are able to guide the fit in the right direction, without overly constraining any individual quantities.

# 3 WASP-167b/KELT-13b

**The material in this Chapter was published, largely in its current form, as part of Temple et al. (2017). Acknowledgements are given where significant contributions were made by the co-authors thereof.**

## 3.1 Abstract

We report the joint WASP/KELT discovery of WASP-167b/KELT-13b, a transiting hot Jupiter with a 2.02-d orbit around a $V = 10.5$, F1V star with $[\mathrm{Fe/H}] = 0.1 \pm 0.1$, $T_{\mathrm{eff}} = 7000\,\mathrm{K}$ and $v \sin i_\star \approx 50\,\mathrm{km\,s^{-1}}$. This discovery was made in collaboration with the Kilodegree Extremely Little Telescope (KELT) Group. The $1.5\,\mathrm{R_{Jup}}$ planet was confirmed by Doppler tomography of the stellar line profiles during transit. We place a limit of $< 8\,\mathrm{M_{Jup}}$ on its mass. The planet is in a retrograde orbit with a sky-projected spin–orbit angle of $\lambda = -165^\circ \pm 5^\circ$. This is in agreement with the known tendency for orbits around hotter stars to be more likely to be misaligned. WASP-167/KELT-13 is one of the few systems where the stellar rotation period is less than the planetary orbital period. We find evidence of non-radial stellar pulsations in the host star, making it a $\delta$-Scuti or $\gamma$-Dor variable. The similarity to WASP-33, a previously known hot-Jupiter host with pulsations, adds to the suggestion that close-in planets might be able to excite stellar pulsations.

## 3.2 Data and observations

*With thanks to the WASP and KELT teams for the acquisition and reduction of photometric and spectroscopic data.*

WASP-167b/KELT-13b was observed with WASP-South from 2006 May–2012

June and with KELT-South from 2010 March–2013 August. WASP-South is an eight-camera array using 200-mm f/1.8 lenses, covering a $7.8^\circ \times 7.8^\circ$ field of view. Further details of WASP-South are given in Section 2.1.1. Details of the data reduction and candidate selection processes are given in Sections 2.1.2 and 2.1.3.

The KELT-South site consists of a single 80-mm f/1.9 camera with a $26^\circ \times 26^\circ$ field of view and a pixel scale of 23". Survey observations use 150-s exposures and a cadence of 10–20 minutes per field. Further details of KELT-South are given in Pepper et al. (2007);Pepper et al. (2012). Details of data reduction, processing and candidate selection procedures are given by Siverd et al. (2012) and Kuhn et al. (2016).

The WASP and KELT teams independently found a planet-like transit signal with a $\sim$2-day period (see Fig. 3.1) and set about obtaining a total of 18 follow-up lightcurves of the transit. The observations are listed in Table 3.1 while the lightcurves are shown in Fig. 3.2. The techniques for obtaining relative photometry have been reported in previous WASP and KELT discovery papers, and since we have 18 transit curves from disparate facilities we refer the reader to such papers for full details of the instrumentation and analysis (e.g., Hellier et al. 2014; Maxted et al. 2016; Kuhn et al. 2016; Pepper et al. 2017; Rodriguez et al. 2016). We give key details of the instrumentation used in Table 3.1.

In an attempt to refute the planetary hypothesis we, on three occasions, attempted to detect an eclipse (of the occulting body by the star) using TRAPPIST with a $z'$ filter (see Table 3.1 for details). This is discussed in Sec. 3.4.

The two teams also began monitoring the radial velocity of the star using the Euler/CORALIE and TRES spectrographs (Queloz et al. 2001b; Fűresz 2008). The measured values are listed in Table 3.2. The crucial tomographic data, revealing the planet shadow, then came from an observation over a transit on the night of March 1$^{\rm st}$ 2016 using the ESO 3.6-m/HARPS spectrograph (Pepe et al. 2002).

We have searched the combined WASP and KELT photometry of WASP-167/KELT-13 for modulations indicating the rotational period of the star, as described by Maxted et al. (2011), but did not find any modulations above $\sim$0.7 mmag at periods longer than 1 day.

Table 3.1: Details of all observations of WASP-167b/KELT-13b used in this work, including the discovery photometry, the follow-up photometry and the spectroscopic observations. The label in the final column corresponds to a lightcurve in Fig. 3.2.

| Facility | Location | Aperture | FOV ($'\times'$) | Pixel Scale ($''$pixel$^{-1}$) | Date | Notes | Label |
|---|---|---|---|---|---|---|---|
| *Discovery Photometry* | | | | | | | |
| WASP-South | SAAO[1], South Africa | 111 mm | $7.8 \times 7.8$ | 14 | 2006 May–2012 Jun | 26114 points | - |
| KELT-South | SAAO, South Africa | 42 mm | $26 \times 26$ | 23 | 2010 Mar–2013 Aug | 4563 points | - |
| *Transit observations* | | | | | | | |
| TRAPPIST | ESO[2], La Silla, Chile | 0.6 m | $22 \times 22$ | 0.65 | 2012 Feb 22 | I+z' | a |
| TRAPPIST | ESO, La Silla, Chile | 0.6 m | $22 \times 22$ | 0.65 | 2012 Apr 30 | I+z' | b |
| LCOGT-LSC | CTIO[3], Chile | 1 m | $26.5 \times 26.5$ | 0.4 | 2014 May 17 | i' | c |
| PEST | Perth, Australia | 0.3 m | $31 \times 21$ | 1.2 | 2014 Jun 22 | Rc | d |
| PEST | Perth, Australia | 0.3 m | $31 \times 21$ | 1.2 | 2015 Jan 14 | V | e |
| Skynet/Prompt4 | CTIO, Chile | 0.4 m | $10 \times 10$ | 0.59 | 2015 Feb 22 | z' | f |
| T50 Telescope | SSO[4], Australia | 0.43 m | $16.2 \times 15.7$ | 0.92 | 2015 Mar 24 | B | g |
| T50 Telescope | SSO, Australia | 0.43 m | $16.2 \times 15.7$ | 0.92 | 2015 Mar 26 | B | h |
| Mt. John | UC[5], New Zealand | 0.6 m | $14 \times 14$ | 0.549 | 2015 Mar 26 | V | i |
| LCOGT-COJ | SSO, Australia | 1 m | $15.8 \times 15.8$ | 0.24 | 2015 Mar 28 | r' | j |
| PEST | Perth, Australia | 0.3 m | $31 \times 21$ | 1.2 | 2015 Mar 28 | Ic | k |
| LCOGT-COJ | SSO, Australia | 1 m | $15.8 \times 15.8$ | 0.24 | 2015 Mar 28 | i' | l |
| Hazelwood | Victoria, Australia | 0.32 m | $18 \times 12$ | 0.73 | 2015 Mar 30 | B | m |
| Ivan Curtis | Adelaide, Australia | 0.235 m | $16.6 \times 12.3$ | 0.62 | 2015 Mar 30 | V | n |
| Ellinbank | Victoria, Australia | 0.32 m | $30.4 \times 14.1$ | 1.12 | 2015 Apr 03 | B | o |
| PEST | Perth, Australia | 0.3 m | $31 \times 21$ | 1.2 | 2015 Apr 03 | B | p |
| LCOGT-CPT | SAAO, South Africa | 1 m | $15.8 \times 15.8$ | 0.24 | 2015 Apr 17 | Z | q |
| TRAPPIST | ESO, La Silla, Chile | 0.6 m | $22 \times 22$ | 0.65 | 2016 Mar 01 | z' | r |
| *Occultation window observations* | | | | | | | |
| TRAPPIST | ESO, La Silla, Chile | 0.6 m | $22 \times 22$ | 0.65 | 2011 Feb 13 | z' | - |
| TRAPPIST | ESO, La Silla, Chile | 0.6 m | $22 \times 22$ | 0.65 | 2011 Apr 25 | z' | - |
| TRAPPIST | ESO, La Silla, Chile | 0.6 m | $22 \times 22$ | 0.65 | 2011 May 09 | z' | - |
| *Spectroscopic Observations* | | | | | | | |
| CORALIE | ESO, La Silla, Chile | 1.2 m | - | - | 2010 Apr–2017 Mar | 21 RVs | - |
| TRES | FLWO[6], Arizona | 1.5 m | - | - | 2015 Feb–2016 Apr | 20 RVs | - |
| HARPS | ESO, La Silla, Chile | 3.6 m | - | - | 2016 Mar 01 | 17 CCFs | - |

[1]South African Astronomical Observatory, [2]European Southern Observatory, [3]Cerro Tololo Inter-American Observatory, [4]Siding Spring Observatory, [5]University of Canturbury, [6]Fred Lawrence Whipple Observatory

Table 3.2: Radial velocities and bisector spans for WASP-167b/KELT-13b .

| BJD (TDB) | RV ($\mathrm{km\,s^{-1}}$) | $\sigma_{\mathrm{RV}}$ ($\mathrm{km\,s^{-1}}$) | BS ($\mathrm{km\,s^{-1}}$) | $\sigma_{\mathrm{BS}}$ ($\mathrm{km\,s^{-1}}$) | BJD (TDB) | RV ($\mathrm{km\,s^{-1}}$) | $\sigma_{\mathrm{RV}}$ ($\mathrm{km\,s^{-1}}$) | BS ($\mathrm{km\,s^{-1}}$) | $\sigma_{\mathrm{BS}}$ ($\mathrm{km\,s^{-1}}$) |
|---|---|---|---|---|---|---|---|---|---|
| TRES RVs: | | | | | CORALIE RVs: | | | | |
| 2457055.9950 | –1.01 | 0.41 | –0.12 | 0.33 | 2455310.5205 | –3.82 | 0.059 | –2.38 | 0.12 |
| 2457057.0280 | 0.00* | 0.23 | 0.03 | 0.21 | 2455310.8005 | –3.74 | 0.061 | –0.42 | 0.12 |
| 2457058.0115 | –0.57 | 0.28 | 0.53 | 0.37 | 2455311.8282 | –2.83 | 0.059 | –1.30 | 0.12 |
| 2457060.9845 | –0.39 | 0.31 | 0.33 | 0.21 | 2455320.5338 | –3.50 | 0.063 | 1.80 | 0.13 |
| 2457086.9123 | –0.63 | 0.29 | 0.04 | 0.24 | 2455320.7628 | –2.23 | 0.066 | –2.30 | 0.13 |
| 2457122.8138 | –1.85 | 0.42 | –0.05 | 0.17 | 2455568.8079 | –2.72 | 0.060 | –2.70 | 0.12 |
| 2457123.8544 | –1.15 | 0.39 | –0.23 | 0.28 | 2455572.8753 | –3.09 | 0.066 | – | – |
| 2457137.7848 | –2.39 | 0.24 | –0.29 | 0.14 | 2455574.8568 | –3.57 | 0.061 | –4.96 | 0.12 |
| 2457139.7803 | –2.00 | 0.39 | 0.15 | 0.24 | 2455646.7729 | –2.51 | 0.070 | –2.96 | 0.14 |
| 2457141.7805 | –1.27 | 0.45 | 0.17 | 0.11 | 2455712.5532 | –3.36 | 0.059 | 0.26 | 0.12 |
| 2457143.7671 | –2.19 | 0.23 | 0.17 | 0.14 | 2455722.5360 | –2.27 | 0.058 | –4.94 | 0.12 |
| 2457144.7561 | –1.81 | 0.35 | –0.05 | 0.18 | 2455979.6816 | –3.76 | 0.062 | –3.44 | 0.12 |
| 2457145.7548 | –1.39 | 0.32 | –0.02 | 0.16 | 2455979.8955 | –3.74 | 0.059 | –7.50 | 0.12 |
| 2457149.7475 | –1.16 | 0.42 | 0.12 | 0.25 | 2455981.7270 | –4.62 | 0.065 | –1.09 | 0.13 |
| 2457150.7423 | –2.33 | 0.44 | 0.05 | 0.20 | 2457600.5011 | –4.28 | 0.071 | – | – |
| 2457151.7486 | –1.19 | 0.44 | –0.20 | 0.23 | 2457616.4971 | –4.70 | 0.066 | 0.048 | 0.13 |
| 2457152.7481 | –2.52 | 0.36 | –0.29 | 0.18 | 2457759.8370 | –4.71 | 0.065 | –1.86 | 0.13 |
| 2457406.0418 | –1.03 | 0.34 | – | – | 2457760.8366 | –3.77 | 0.066 | –3.70 | 0.13 |
| 2457491.8087 | –0.84 | 0.34 | – | – | 2457804.7057 | –4.08 | 0.065 | – | – |
| 2457504.7985 | –1.62 | 0.28 | – | – | 2457809.7750 | –5.18 | 0.064 | –2.88 | 0.13 |
| | | | | | 2457818.6607 | –4.73 | 0.067 | –0.25 | 0.13 |

* This observation was used as the template for the extraction of the TRES radial velocities.

## 3.3 Spectral analysis

*With thanks to B. Smalley (Keele Astrophysics Group) for carrying out the spectral analysis.*

To determine the spectral parameters of the host star we produced a median-stacked spectrum from the 17 HARPS spectra and used it to find the stellar effective temperature $T_{\mathrm{eff}}$, the stellar metallicity [Fe/H], and the projected stellar rotational velocity $v \sin i_{\star}$. The spectra were line-poor and broad-lined, owing to the host star's spectral type, which meant that a determination of the stellar surface gravity $\log g_{\star}$ was not possible. We therefore assume here a value of $\log g_{\star} = 4.3$, the expected value for a similar star at zero age (Gray 1992). The $T_{\mathrm{eff}}$ was measured using the H$\alpha$ line, which was strong and unblended. The values obtained for each of these parameters

are given in Table 3.3. Fuller details of our spectral analysis procedure can be found in Doyle et al. (2013). We also used the MKCLASS program (Gray & Corbally 2014) to obtain a spectral type of F1V.

## 3.4 Photometric and radial velocity analysis

We carried out a Markov Chain Monte Carlo (MCMC) fitting procedure, simultaneously modelling the WASP and KELT lightcurves, the 18 follow-up lightcurves, and the out-of-transit RVs. We use the latest version of the code described by Collier Cameron et al. (2007) and Pollacco et al. (2008).

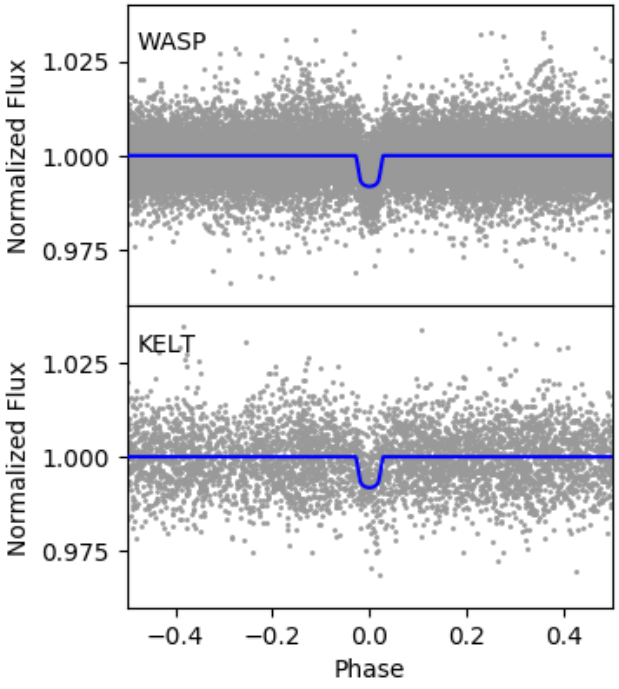


Figure 3.1: The WASP (top) and KELT (bottom) discovery lightcurves for WASP 167b/KELT-13b, folded on the orbital period. The blue lines show the final model obtained in the MCMC fitting (see Section 3.4).

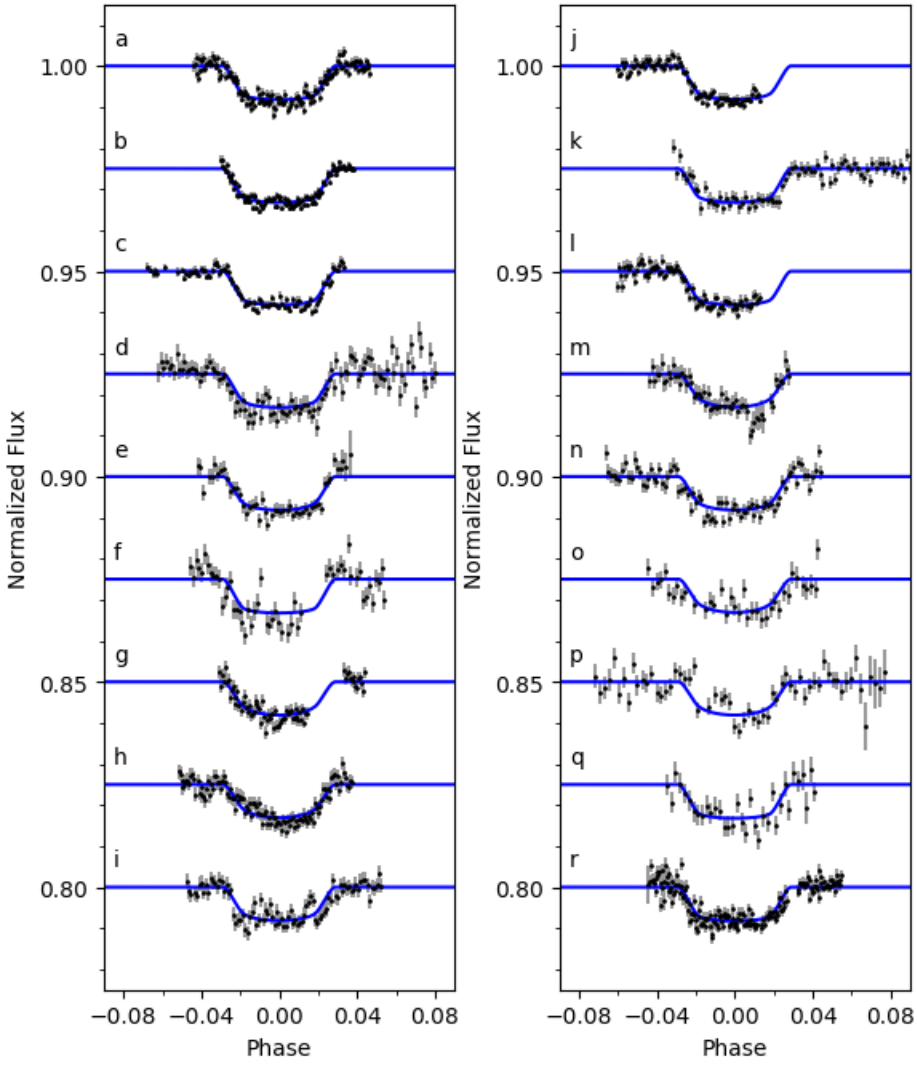


Figure 3.2: The 18 follow-up transit lightcurves. The blue lines show the final model obtained in the MCMC fitting (see Section 3.4). The label to the left of each dataset corresponds to an entry in the final column of Table 3.1.

Prior to the fit, the KELT team's follow-up lightcurves were detrended by first fitting them using the online EXOFAST applet (Eastman, Gaudi & Agol 2013), removing the effects of airmass and some systematics (this was not needed for TRAPPIST lightcurves). For consistency, we also converted all datasets to the $\mathrm{BJD_{TDB}}$ time stan-

dard using the Eastman, Siverd & Gaudi (2010) BJD conversion code.

Following the procedure described in Section 2.4, limb darkening was accounted for using the Claret (2000, Claret (2004) four-parameter non-linear law, with coefficients being interpolated from the Claret tables at each step of the MCMC that were appropriate to the passband used and the new values of $T_{\rm eff}$, [Fe/H] and $\log g_\star$. Hot Jupiters settle into a circular orbit on time-scales that are often shorter than their host stars' lifetimes through tidal circularization (Pont et al. 2011). We therefore assume a circular orbit, since this will give the most likely parameters (Anderson et al. 2012).

The system parameters which determine the shape of the transit lightcurve are: the epoch of mid-transit $T_{\rm c}$, the orbital period $P$, the planet-to-star area ratio $(R_{\rm p}/R_\star)^2$ or transit depth $\delta$, the transit duration $T_{14}$, and the impact parameter $b$ (recall eq. 1.1–1.3.1 in Section 1.3.1). In the RV modelling, we fit the value of the stellar reflex velocity semi-amplitude $K_1$ and the barycentric system velocity $\gamma$. The proposed values of stellar and planetary masses and radii are constrained by the Enoch–Torres relation (Enoch et al. 2010; Torres, Andersen & Giménez 2010). We allow for a possible offset in RVs between the CORALIE and TRES datasets.

Since we collect data from many sources with differing data qualities, our code includes a provision for re-scaling the error bars of each dataset to give $\chi^2_\nu = 1$. This means that datasets that don't fit as well are down-weighted, such that the final result is dominated by the better datasets. With 18 transit lightcurves, this means that the final parameters are relatively insensitive to red noise in particular lightcurves.

The radial velocities and the best-fitting model are shown in Figure 3.3. There is a clear scatter in the RVs about the model, beyond that attributable to the error bars. This could, for example, be caused by the pulsations in the host star distorting the stellar line profiles (see Sections 3.5 and 3.7.3), or by a third body in the system.

Attempting to fit for a second planet does not properly explain the scatter, but does significantly change the semi-amplitude fitted to the first planet. For this reason we do not regard the fitted semi-amplitude as a reliable measure of the planet's mass, but instead report an upper limit of $8\,{\rm M_{Jup}}$, which we regard as conservative but sufficient to demonstrate that the transiting body has a planetary mass. We are continuing

to monitor the system in order to discover the cause of the scatter. The parameters obtained in this analysis are given in Table 3.3.

The TRAPPIST observations of the eclipse (of the planet by the star) produced no detection, with an upper limit of 1100 ppm. Given the stellar and planetary radii (Table 3.3) this implies that the heated face of the planet must be cooler than 3750 K. The fitted system parameters imply a planet temperature of $T_{eql} = 2330 \pm 65$ K, and thus the non-detection of the eclipse is consistent with the planetary hypothesis.

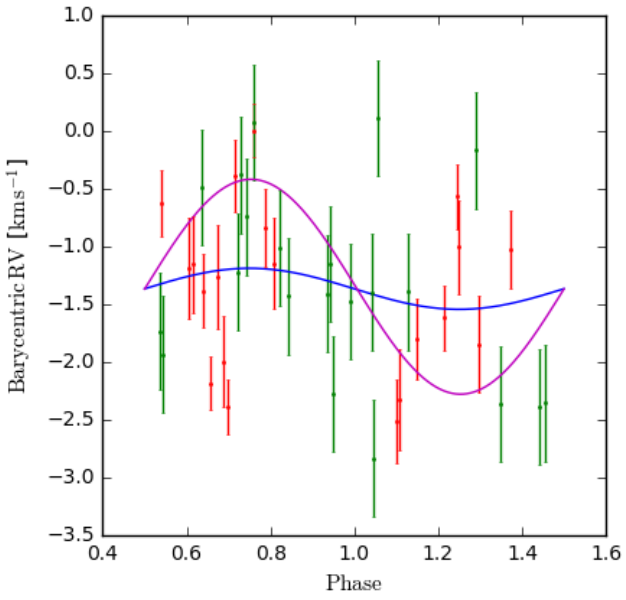


Figure 3.3: The 21 CORALIE RVs (green) and 20 TRES RVs (red) obtained for WASP-167/KELT-13. The blue line shows the best fitting semi-amplitude, which we do not regard as reliable. The magenta line shows the RV amplitude for a planet mass of $8\,M_{\rm Jup}$, which we regard as a conservative upper limit.

## 3.5 Doppler tomography

We obtained 17 spectra with the ESO 3.6-m/HARPS spectrograph through a transit on the night of March 1st 2016. We also observed the same transit photometrically using TRAPPIST (see lightcurve r in Fig. 3.2, Table 3.1). The standard HARPS Data Reduction Software was used to produce a cross correlation function (CCF) correlated over a window of $\pm 300\,\mathrm{km\,s^{-1}}$ (as described in Sections 2.3.2, 2.3.3). The CCFs were created using a mask matching a G2 spectral type, containing zeroes at the positions of absorption lines and ones in the continuum.

We display the resulting CCFs as a function of the planet's orbital phase in Fig. 3.4, where phase 0 is mid-transit. In producing this plot we have first subtracted the invariant part of the CCF profile. We do this by constructing a 'minimum CCF', which at each wavelength has the lowest value from the range of phases.

We interpret the CCFs as showing stellar pulsations moving in a prograde direction (moving redward over time). Similar pulsations are seen in the tomograms of WASP-33 (Collier Cameron et al. 2010b; Johnson et al. 2015), which is regarded as a $\delta$-Scuti pulsator (Herrero et al. 2011).

To try to remove the pulsations by separating the features into prograde-moving and retrograde components we followed the method of Johnson et al. (2015), adopted for WASP-33, by Fourier transforming the CCFs, such that the prograde and retrograde components appear in different quadrants in velocity space.

This separation technique will not be perfect, and we expect some residual contamination from the pulsations. We thus experimented with which data to include. We found that we get the best separation of the components and thus the clearest planetary signal if we do not include in the Fourier transform the last two spectra. These were in any case obtained outside the transit and so cannot contain information about a planet. It is thus valid to try Fourier transforms both with and without these two, in order to see which better separates the pulsations and leaves the clearest planet trace.

Fig. 3.5 shows the Fourier-transformed data, where the feature running from

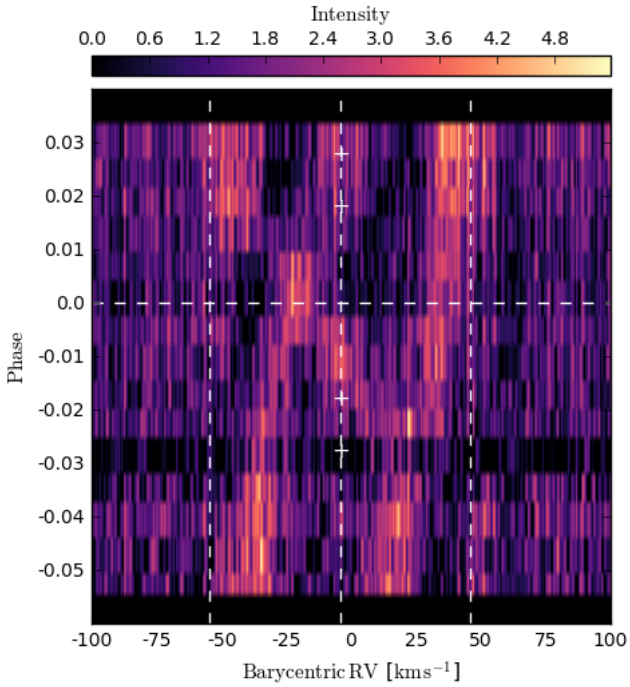


Figure 3.4: The line profiles through transit. We interpret this as showing prograde-moving stellar pulsations and a retrograde-moving planet trace. The white dashed vertical lines mark the positions of the $\gamma$ velocity of the system and the positions of $\gamma \pm v \sin i_\star$ (i.e. the centre and edges of the stellar line profile). The phase of mid-transit is marked by the white horizontal dashed line. The white + symbols indicate the four transit contact points, calculated using the ephemeris obtained in the analysis in Section 3.4.

bottom-left to top-right can be attributed to the pulsations. We thus applied the filter used by Johnson et al. (2015), which contained zeroes in the quadrants containing the prograde pulsation signal and unity in the quadrants containing the retrograde signal, with a Hann function bridging the discontinuity.

We then Fourier transform the masked data back into phase versus velocity and display that in Fig. 3.6. This shows an apparent retrograde trace, which we attribute to the shadow of a planet. This is again similar to what is seen in WASP-33 (Johnson et al. 2015). In Fig. 3.6 we also show the pulsations without the planet trace, obtained by filtering to leave only the prograde quadrants, and then transforming back into

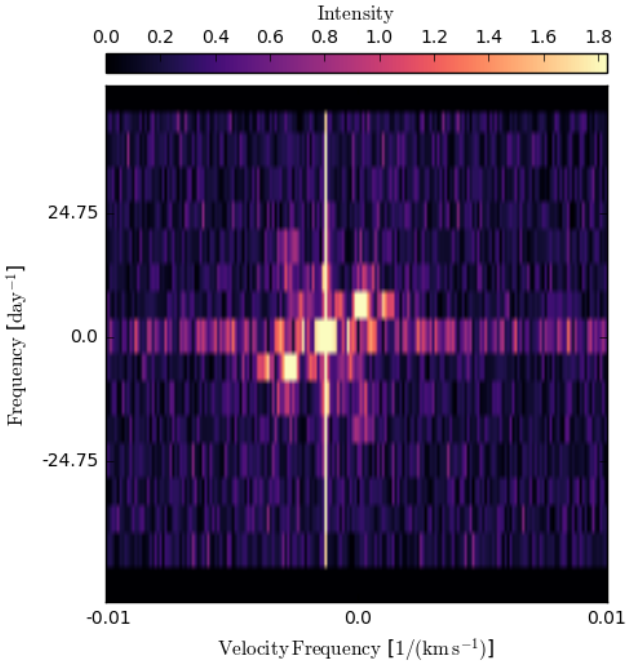


Figure 3.5: The Fourier transform of the line profiles. The stellar pulsations are seen as the diagonal feature from bottom-left to top-right. The weaker diagonal feature running bottom-right to top-left is produced by the planet.

velocity space.

The planet's Doppler shadow seems to disappear towards the end of the transit (see Fig. 3.6). It is likely that it has been reduced during the filtering process, as a result of imperfect separation of the planetary and stellar-pulsation signals. This might have some effect on fitting the alignment angle $\lambda$, which depends on the slope of the Doppler shadow, but should have less effect on the other fitted quantities.

In order to parametrise the planet's orbit we then fitted the CCFs through transit, in a manner similar to the methods in Brown et al. (2017). Since we had subtracted the 'minimum CCF' above, we first add that back in to the filtered CCFs in order to reintroduce the stellar line profile, which is a key feature for constraining the value of $v \sin i_\star$.

The parameters which define the shape of the CCF line profile are: the projected

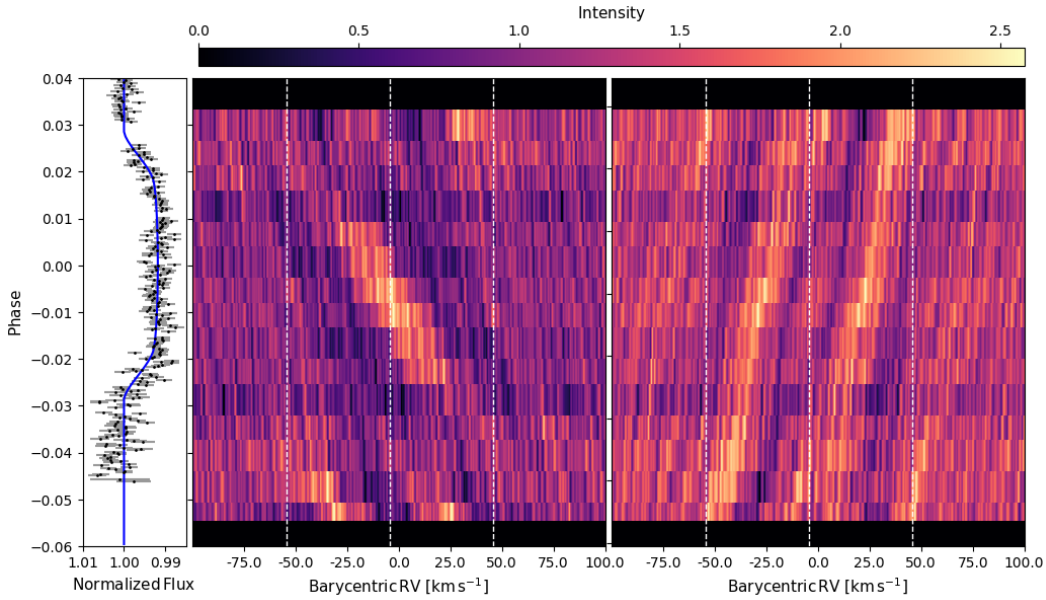


Figure 3.6: Centre: the spectral profiles through transit after removing the stellar pulsations via Fourier filtering. The planet trace is then readily seen moving in a retrograde direction. Left: the simultaneous TRAPPIST photometry of the transit. Right: the spectral profiles through transit after removing the planet shadow via Fourier filtering. The stellar pulsations are seen moving in a prograde direction.

spin-orbit misalignment angle $\lambda$; the stellar line-profile Full-Width at Half-Maximum (FWHM); the FWHM of the line perturbation due to the planet $v_{\rm FWHM}$; the stellar $\gamma$-velocity, and $v \sin i_\star$. These parameters were fitted using a MCMC fitting algorithm which assumes a Gaussian shape for the line perturbation caused by the planet. Both $v \sin i_\star$ and $v_{\rm FWHM}$ have two data constraints, one from the shape of the line-broadening profile, and one from the slope of the trajectory of the bump across the line profile (given knowledge of $\lambda$). The value of $v \sin i_\star$ obtained in the spectral analysis was used as a prior in the fit. Initial values for the stellar line FWHM and the $\gamma$-velocity were obtained by fitting a Gaussian profile to the CCFs. The $\lambda$ angle and $v_{\rm FWHM}$ were given no prior. Details of the fitting algorithm are given in Collier Cameron et al. (2010a), and the resulting system parameters are listed in Table 3.3.

Table 3.3: System parameters obtained for WASP-167b/KELT-13b in this work.

| | |
|---|---|
| 1SWASP J130410.53–353258.2 | |
| 2MASS J13041053–3532582 | |
| RA = $13^{h}04^{m}10.53^{s}$, Dec = $-35°32'58.28''$ (J2000) | |
| $V = 10.5$ | |
| IRFM $T_{\rm eff} = 6998 \pm 151$ K | |
| *Gaia* Proper Motions: (RA) $-19.0 \pm 1.4$ mas | |
| Dec) $0.66 \pm 1.24$ mas/yr | |
| Parallax: $2.28 \pm 0.62$ mas | |
| Rotational Modulations: $< 0.7$ mmag (95%) | |
| Parameter (Unit) | Value |
| Stellar parameters from spectral analysis: | |
| $T_{\rm eff}$ (K) | $6900 \pm 150$ |
| $\log A$(Fe) | $7.46 \pm 0.18$ |
| [Fe/H] | $-0.04 \pm 0.18$ |
| $v \sin i_*$ (km s$^{-1}$) | $52 \pm 8$ |
| Parameters from photometry and RV analysis: | |
| $P$ (d) | $2.0219596 \pm 0.0000006$ |
| $T_{\rm c}$ (BJD) | $2456592.4643 \pm 0.0002$ |
| $T_{14}$ (d) | $0.1135 \pm 0.0008$ |
| $T_{12} = T_{34}$ (d) | $0.0212 \pm 0.0010$ |
| $\Delta F = R_{\rm P}^2/R_*^2$ | $0.0082 \pm 0.0001$ |
| $b$ | $0.77 \pm 0.01$ |
| $a$ (AU) | $0.0365 \pm 0.0006$ |
| $i$ (°) | $79.9 \pm 0.3$ |
| $T_{\rm eff}$ (K) | $7000 \pm 250$ |
| $\log g_*$ (cgs) | $4.13 \pm 0.02$ |
| $\rho_*$ ($\rho_\odot$) | $0.28 \pm 0.02$ |
| [Fe/H] | $0.1 \pm 0.1$ |
| $M_*$ ($M_\odot$) | $1.59 \pm 0.08$ |
| $R_*$ ($R_\odot$) | $1.79 \pm 0.05$ |
| $T_{\rm eql}$ (K) | $2329 \pm 64$ |
| $M_{\rm P}$ ($M_{\rm Jup}$) | $<8$ |
| $R_{\rm P}$ ($R_{\rm Jup}$) | $1.58 \pm 0.05$ |
| Parameters from tomography: | |
| $\gamma$ (km s$^{-1}$) | $-3.409 \pm 0.007$ |
| $v \sin i_*$ (km s$^{-1}$) | $49.94 \pm 0.04$ |
| $\lambda$ (°) | $-165 \pm 5$ |
| $v_{\rm FWHM}$ (km s$^{-1}$) | $20.9 \pm 0.9$ |

## 3.6 Evolutionary status

*With thanks to P. Maxted and P. Cargile for their assistance in determining the age of WASP-167/KELT-13.*

We then used MINES*weeper*, a newly developed Bayesian approach to determining stellar parameters using the MIST stellar evolution models (Choi et al. 2016). Examples of the use of MINES*weeper* in determining stellar parameters are shown in Rodriguez et al. (2017b), Rodriguez et al. (2017a). We model the available $B_T$, $V_T$ photometry from Tycho-2, J, H, $K_s$ from 2MASS, and WISE W1-3 photometry. We also include in the likelihood calculation the measured parameters from the spectroscopic analysis ($T_{\rm eff} = 6900 \pm 150$ K and [Fe/H] = -0.04$\pm$ 0.18), as well as the *Gaia* DR1 parallax ($\pi = 2.28 \pm 0.62$ mas; Gaia Collaboration et al. (2016a); Gaia Collaboration et al. (2016b)) and the fitted transit stellar density ($0.28 \pm 0.02\,\rho_\odot$). We applied non-informative priors on all parameters within the MIST grid of stellar evolution models, and a non-informative prior on extinction ($A_V$) between 0–2.0 mags. Our final parameters are determined from the value at the highest posterior probability for each parameter, and the errors are based on the marginalized inner-68th percentile range. These are given in Table 3.4.

For comparison, we also use the open source software BAGEMASS[1], which uses the Bayesian method described by Maxted, Serenelli & Southworth (2015), to estimate the stellar age and mass. The models used in BAGEMASS were calculated using the GARSTEC stellar evolution code (Weiss & Schlattl 2008). We use the grid of stellar models in BAGEMASS and the same temperature, metallicity and density constraints as for the MINESweeper calculation. We also apply a luminosity constraint of $\log L_{\rm T} = 1.00^{+0.28}_{-0.22}$, which was derived using the *Gaia* parallax and the total line-of-sight reddening as determined by Schlafly & Finkbeiner (2011); Maxted et al. (2014) (E(B–V) = $0.051 \pm 0.034$). The resulting age and mass values are in Table 3.4. Both

[1]Available at: http://sourceforge.net/projects/bagemass

values are compatible with those from MINESweeper. The best-fit stellar evolution tracks and isochrones are shown in Fig. 3.7.

Table 3.4: Stellar parameters obtained for WASP-167/KELT-13 in the SED analysis (see Section 3.6).

| Parameter (Unit) | Value |
|---|---|
| MINES*weeper*: | |
| Age (Gyr) | $1.29^{+0.36}_{-0.27}$ |
| $M_*$ ($M_\odot$) | $1.518^{+0.069}_{-0.087}$ |
| $R_*$ ($R_\odot$) | $1.756^{+0.067}_{0.057}$ |
| $\log L_*$ ($L_\odot$) | $0.835^{+0.040}_{-0.034}$ |
| $T_{\rm eff}$(K) | $7043^{+89}_{-68}$ |
| $\log g_*$ | $4.131^{+0.018}_{-0.028}$ |
| $[{\rm Fe/H}]_{\rm surface}$ | $-0.01^{+0.17}_{-0.10}$ |
| $[{\rm Fe/H}]_{\rm init}$ | $-0.04^{+0.16}_{-0.09}$ |
| Distance (pc) | $381^{+15}_{-13}$ |
| $A_V$ (mag) | $0.044^{+0.057}_{-0.025}$ |
| BAGEMASS: | |
| Age (Gyr) | $1.56 \pm 0.40$ |
| $M_*$ ($M_\odot$) | $1.49 \pm 0.09$ |

## 3.7 Discussion and conclusions

### 3.7.1 Stellar rotation rate and tidal interaction

As an F1V star with $T_{\rm eff} = 6900 \pm 150$ K, WASP-167/KELT-13 is among the hottest stars known to host a transiting hot Jupiter. At the time of discovery, others included WASP-33 (Collier Cameron et al. 2010b), Kepler-13 (Shporer et al. 2011; Shporer et al. 2014), KELT-17 (Zhou et al. 2016b) and HAT-P-57 (Hartman et al. 2015). These systems have since been superseded by hotter examples like KELT-9 ($T_{\rm eff} = 10170$ K,

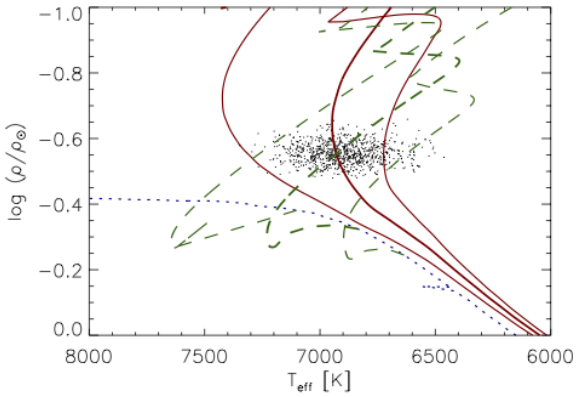


Figure 3.7: The best fitting evolutionary tracks and isochrones of WASP-167/KELT-13 obtained using BAGEMASS. Dotted blue line: ZAMS at best-fit [Fe/H]. Green dashed lines: evolutionary track for the best-fit [Fe/H] and mass, plus $1\sigma$ bounds. Red lines: isochrone for the best-fit [Fe/H] and age, plus $1\sigma$ bounds.

Gaudi et al. 2017), WASP-178b ($T_{\rm eff} = 9350\,{\rm K}$, Hellier et al. 2019a) and KELT-20b ($T_{\rm eff} = 8720\,{\rm K}$, (Lund et al. 2017)).

In addition, WASP-167/KELT-13 appears to be one of the most rapidly rotating stars known to host a hot Jupiter, and one of the few with a stellar rotation period shorter than the planet's orbit. The measured $v \sin i_\star$ of $49.94 \pm 0.04\,{\rm km\,s^{-1}}$ and the fitted radius of $1.79 \pm 0.05\,{\rm R_\odot}$ imply a rotation period of $P_{\rm rot} < 1.81$-d, which compares with the planet's orbital period of 2.02-d.

Thus WASP-167/KELT-13 joins examples such as WASP-33 ($P_{\rm orb} = 1.22$-d; $P_{\rm rot} < 0.79$-d, Collier Cameron et al. 2010b), KELT-7 ($P_{\rm orb} = 2.7$-d, $P_{\rm rot} < 1.32$-d, Bieryla et al. 2015) and CoRoT-11b ($P_{\rm orb} = 3.0$-d; $P_{\rm rot} < 1.73$-d, Gandolfi et al. 2010) in having a hot Jupiter in a $< 3$-d orbit and an even shorter rotation rate. Some more recent examples include HAT-P-70b ($P_{\rm rot} < 0.94\,{\rm days}$, $P_{\rm orb} = 2.74\,{\rm days}$, Zhou et al. 2019b) and MASCARA-1b ($P_{\rm rot} < 0.97\,{\rm days}$, $P_{\rm orb} = 2.15\,{\rm days}$, Talens et al. 2017b). See, also, Crouzet et al. (2017) for a discussion of other systems with $P_{\rm rot} < P_{\rm orb}$ but with longer period orbits.

The tidal interaction will be different in such systems compared to the more-usual

$P_{\rm rot} > P_{\rm orb}$. In most hot Jupiters, the tidal interaction is expected to drain angular momentum from the orbit, leading to tidal decay of the orbital period (e.g., Levrard, Winisdoerffer & Chabrier 2009). This would be reversed, however, for systems with $P_{\rm rot} < P_{\rm orb}$, and with the planet in a prograde orbit (such as KELT-7b and CoRoT-11b), thus leading to a different dynamical history.

If, though, $P_{\rm rot} < P_{\rm orb}$ and with the planet in a retrograde orbit, such as WASP-167b/KELT-13b or WASP-33b, tidal infall would again be expected. McQuillan, Mazeh & Aigrain (2013) analysed *Kepler* detections and found a dearth of close-in planets around fast rotators, saying that only stars with rotation periods longer than 5–10 days have planets with periods shorter than 3 days. Teitler & Königl (2014) then attributed this to the destruction of close-in planets, with the result of spinning up the star. While WASP-167/KELT-13 and the others just named are examples of systems with $P_{\rm rot} < P_{\rm orb}$ they are undoubtedly rare and their dynamics deserves further investigation.

### 3.7.2 The retrograde orbit

The planet WASP-167b/KELT-13b has a radius of $1.6\,{\rm R_{Jup}}$ and is thus inflated, though not exceptionally so. This is in line with WASP-33b, which has a $1.5\,{\rm R_{Jup}}$ radius, and is expected for a hot Jupiter orbiting a hot star, given that a relation between inflated radii and stellar irradiation is now well established (e.g., Demory & Seager 2011; Enoch, Collier Cameron & Horne 2012; Hartman et al. 2016). We should, though, warn of a selection effect against observing non-inflated planets around relatively large A/F stars, in that the transits would be shallower and may escape detection in WASP-like surveys.

Crouzet et al. (2017) list 6 planets with measured sky-projected obliquity angles ($\lambda$) that transit host stars hotter than 6700 K (these are XO-6b, CoRoT-3b, KELT-7b, KOI-12b, WASP-33b & Kepler-13Ab). Of these, five seem to be misaligned but only moderately so, having non-zero $\lambda$ values with $|\lambda|$ typically 10–40°. HAT-P-57b (Hartman et al. 2015) is also likely to be moderately misaligned with $27^\circ < \lambda < 58^\circ$.

The KELT-9b system (Gaudi et al. 2017) is another example, with the hottest star known to host a transiting planet ($\sim$10,000 K) and the planet itself on a near-polar orbit ($\lambda \sim -85°$). WASP-33b is the exception in the list of Crouzet et al. (2017), being highly retrograde with $\lambda = -109° \pm 1°$ (Collier Cameron et al. 2010b), and the same is now seen in WASP-167b/KELT-13b with $\lambda = -165° \pm 5°$.

As has been widely discussed (e.g., Albrecht et al. 2012; Crida & Batygin 2014; Fielding et al. 2015; Li & Winn 2016), stars hotter than 6250 K host hot Jupiters with a large range of obliquities, whereas cooler stars tend to have planets in aligned orbits (see, e.g., Fig. 8 of Crouzet et al. (2017)). The suggestion is that hotter stars are less effective at tidally damping a planet's obliquity, perhaps owing to their relatively small convective envelopes (e.g., Winn et al. 2010). The discovery of WASP-167b/KELT-13b now reinforces this trend.

### 3.7.3 Stellar pulsations

WASP-167/KELT-13 is one of a growing number of hot-Jupiter hosts that have shown non-radial pulsations. The first was WASP-33b (Collier Cameron et al. 2010b), which shows $\delta$-Scuti pulsations with a dominant period near 21 cycles/day (86 mins) and an amplitude of several mmag (Kovács et al. 2013; von Essen et al. 2014). Further, Herrero et al. (2011) noted that one of the pulsation frequencies was very near 26 times the orbital frequency of the planet, which suggests that the planet might be exciting the pulsations.

HAT-P-2b is an eccentric massive planet ($8\,M_{Jup}$, $e \sim 0.5$) in a 5-d orbit. de Wit et al. (2017) detect pulsations in *Spitzer* lightcurves of HAT-P-2b, at a level of 40 ppm, much lower than in WASP-33b, but at a similar timescale of $\sim$87 mins. Owing to the commensurability between the pulsation and orbital frequencies, de Wit et al. (2017) again suggest that the planet is exciting the pulsations.

A third example is WASP-118, which shows pulsations at a timescale of $\sim$1.9-d and an amplitude of $\sim$200 ppm in *K2* observations (Močnik et al. 2017). Another is HAT-P-56, a $\gamma$-Dor pulsator with a primary pulsation period of $1.644 \pm 0.03$-d, which

were also seen in *K2* observations (Huang et al. 2015).

It is worth noting that both planets WASP-33b and WASP-167b/KELT-13b have retrograde orbits, whereas that of HAT-P-2b is highly eccentric, which may be relevant to the excitation of the pulsations.

In WASP-167/KELT-13, judging from Fig. 3.4, the pulsations appear to have a timescale of $\sim$4-hours, though with limited data we cannot be more precise. The pulsations in WASP-167/KELT-13 have a longer timescale than in WASP-33 and HAT-P-2 and are near the borderline between $\delta$-Scuti and $\gamma$-Dor behaviour, and so we are unsure which class to assign the star to.

It may be that the pulsations are contributing to the scatter in the RV measurements seen in Fig. 3.3. Indeed, de Wit et al. (2017) attribute radial-velocity scatter in HAT-P-2 to the pulsations. Hay et al. (2016) also report excess RV scatter in WASP-118.

We have looked for the pulsations in the WASP and KELT photometry, but do not detect any signal, with an upper limit of 0.5 mmags. However, we caution that the WASP data are not particularly suitable for searching for periodicities of 4 to 8 hours. This is comparable to the length of observation on each night, and is thus the timescale of greatest red noise in WASP data. For this reason WASP data are processed to reduce sinusoidal-like variations on such timescales (Collier Cameron et al. 2006). Similar considerations apply to the KELT data, which in any case have lower photometric precision. The higher-quality follow-up photometry was aimed at observing the transits, before we were aware of the presence of pulsations, and none of the observations are long enough to search for the pulsations.

It is also possible that the particular mode of pulsations can lead to scatter in the RV measurements but smaller photometric variations owing to geometric cancellation. Axisymmetric non-radial pulsations of order l$\geq$3 are subject to partial geometric cancellation: the greater the value of l, the larger the cancellation effect, and odd-numbered modes are near invisible in intensity measurements (Aerts, Christensen-Dalsgaard & Kurtz 2010).

# 4 WASP-174b

**The material in this Chapter was published, largely in its current form, as part of Temple et al. (2018). Acknowledgements are given where significant contributions were made by the co-authors thereof.**

## 4.1 Abstract

We report the discovery and tomographic detection of WASP-174b, a planet with a near-grazing transit on a 4.23-d orbit around a $V = 11.9$, F6V star with $[\mathrm{Fe/H}] = 0.09 \pm 0.09$. The planet is in a moderately misaligned orbit with a sky-projected spin–orbit angle of $\lambda = 31^\circ \pm 1^\circ$. This is in agreement with the known tendency for orbits around hotter stars to be misaligned. Owing to the grazing transit the planet's radius is uncertain, with a possible range of 0.8–1.8 $\mathrm{R_{Jup}}$. The planet's mass has an upper limit of 1.3 $\mathrm{M_{Jup}}$. WASP-174 is the faintest hot-Jupiter system so far confirmed by tomographic means.

## 4.2 Data and observations

*With thanks to the WASP team for the acquisition and reduction of photometric and spectroscopic data.*

The discovery photometry for WASP-174b was obtained using WASP-South, an array of eight cameras based at the South African Astronomical Observatory (SAAO), from 2006 May–2012 June. We used 30-s exposures and typically 10-minute cadence with a 400–700 nm broad-band filter. Details of the data reduction and candidate selection processes for WASP-South data are given in Sections 2.1.2 and 2.1.3.

Following the detection of a planet-like transit signal with a $\sim$4-day period we

selected the object for our follow-up programme. While the dip is V-shaped, more typical of an eclipsing binary than a planet transit, such dips are also produced by planet transits with a high impact factor. Rejecting eclipsing-binary mimics usually takes only one or two spectra and so we don't reject V-shaped candidates from WASP follow-up.

We thus obtained 16 RV measurements using the Euler/CORALIE spectrograph (see Section 2.3.2). These were compatible with the transiting object being a planet, however, the broad spectral features meant that the error bars are large and thus could not produce a secure orbital variation and hence a mass. To confirm the planet we therefore decided to also use Doppler tomography, and observed a series of 23 spectra with the HARPS spectrograph (see Section 2.3.3) covering a transit on the night of Mar 13th 2016. Simultaneously with this we observed the transit photometrically with TRAPPIST-South. Details of the observations are given in Table 4.1 while the measured radial velocities are given in Table 4.2.

We have also obtained photometry of three other transits with TRAPPIST-South and SPECULOOS (see Table 4.1). While TRAPPIST-South has been used extensively for the discovery and parametrisation of WASP planets (Gillon et al. 2012), this work is the first for a WASP planet to feature data from the newer SPECULOOS. Details of these instruments are given in Section 2.3.1.

Lastly, we report that we searched the WASP photometry looking for stellar rotational modulations in the range 0–1.5 cycles day$^{-1}$, using the methods of Maxted et al. (2011). We did not detect any modulations, or evidence of pulsations, with an upper limit of 0.8 mmag.

## 4.3 Spectral analysis

*With thanks to B. Smalley (Keele Astrophysics Group) for carrying out the spectral analysis.*

Table 4.1: Details of all observations of WASP-174b used in this work, including the discovery photometry, the follow-up photometry and the spectroscopic observations.

| Facility | Date | Notes |
|---|---|---|
| WASP-South | 2006-05–2012-06 | 35883 points |
| TRAPPIST-South | 2014-03-20 | I+z'. 14s exp. |
| TRAPPIST-South | 2016-03-13 | I+z'. 8s exp. |
| TRAPPIST-South | 2017-03-08 | V. 15s exp. |
| SPECULOOS-Europa | 2017-07-13 | I+z'. 10s exp. |
| CORALIE | 2014-03–2017-08 | 16 out-of-transit spectra |
| HARPS | 2016-03-13 | 23 spectra taken including a transit |

Table 4.2: Radial velocities and bisector spans for WASP-174b.

| BJD (TDB –2,450,000) | RV (km $s^{-1}$) | $\sigma_{RV}$ (km $s^{-1}$) | BS (km $s^{-1}$) | $\sigma_{BS}$ (km $s^{-1}$) | BJD (TDB –2,450,000) | RV (km $s^{-1}$) | $\sigma_{RV}$ (km $s^{-1}$) | BS (km $s^{-1}$) | $\sigma_{BS}$ (km $s^{-1}$) |
|---|---|---|---|---|---|---|---|---|---|
| CORALIE RVs: | | | | | 7461.604248 | 4.85 | 0.02 | –0.16 | 0.04 |
| 6719.750940 | 4.87 | 0.05 | –0.28 | 0.10 | 7461.615140 | 4.89 | 0.02 | –0.15 | 0.04 |
| 6770.634386 | 4.91 | 0.05 | –0.15 | 0.10 | 7461.625708 | 4.86 | 0.02 | –0.10 | 0.04 |
| 6836.575290 | 4.84 | 0.09 | 0.11 | 0.18 | 7461.636692 | 4.85 | 0.02 | –0.12 | 0.04 |
| 7072.738390 | 4.71 | 0.06 | 0.17 | 0.12 | 7461.647260 | 4.89 | 0.02 | –0.10 | 0.04 |
| 7888.597863 | 4.79 | 0.09 | –0.21 | 0.18 | 7461.657920 | 4.86 | 0.02 | –0.03 | 0.04 |
| 7890.515926 | 4.73 | 0.14 | 0.24 | 0.28 | 7461.668696 | 4.88 | 0.02 | –0.14 | 0.04 |
| 7894.502532 | 4.79 | 0.08 | –0.10 | 0.16 | 7461.679576 | 4.83 | 0.02 | –0.09 | 0.04 |
| 7903.605663 | 4.66 | 0.13 | –0.42 | 0.26 | 7461.690352 | 4.78 | 0.02 | 0.12 | 0.04 |
| 7905.689111 | 4.85 | 0.07 | –0.30 | 0.14 | 7461.701024 | 4.77 | 0.01 | 0.07 | 0.02 |
| 7917.567974 | 4.85 | 0.07 | –0.06 | 0.14 | 7461.711800 | 4.79 | 0.01 | –0.03 | 0.02 |
| 7924.505661 | 4.82 | 0.06 | –0.35 | 0.12 | 7461.722576 | 4.78 | 0.02 | –0.13 | 0.04 |
| 7951.506527 | 4.73 | 0.17 | –0.41 | 0.34 | 7461.733457 | 4.81 | 0.01 | –0.15 | 0.02 |
| 7954.495100 | 4.83 | 0.07 | 0.01 | 0.14 | 7461.743804 | 4.83 | 0.02 | –0.10 | 0.04 |
| 7959.517031 | 4.70 | 0.09 | –0.03 | 0.18 | 7461.754893 | 4.84 | 0.02 | –0.00 | 0.04 |
| 7973.492569 | 4.82 | 0.12 | 0.17 | 0.24 | 7461.765565 | 4.88 | 0.02 | –0.10 | 0.04 |
| 7974.518841 | 4.65 | 0.09 | –0.16 | 0.18 | 7461.776549 | 4.85 | 0.02 | –0.19 | 0.04 |
| HARPS RVs: | | | | | 7461.787013 | 4.87 | 0.02 | –0.15 | 0.04 |
| 7461.571827 | 4.87 | 0.02 | –0.09 | 0.04 | 7461.797985 | 4.87 | 0.02 | –0.02 | 0.04 |
| 7461.582499 | 4.89 | 0.02 | –0.16 | 0.04 | 7461.808866 | 4.84 | 0.02 | –0.19 | 0.04 |
| 7461.593380 | 4.88 | 0.02 | –0.09 | 0.04 | | | | | |

We first performed a spectral analysis on a median-stacked HARPS spectrum created from the 23 we obtained, in order to determine some stellar properties. We

follow the method described by Doyle et al. (2013) to determine values for the stellar effective temperature $T_{\rm eff}$, stellar surface gravity $\log g_*$, the stellar metallicity [Fe/H], the stellar lithium abundance $\log {\rm A(Li)}$ and the projected stellar rotational velocity $v \sin i_\star$. To constrain the latter we obtain a macroturbulence value of $v_{\rm mac} = 6.3$ km s$^{-1}$ using the Doyle et al. (2014) calibration. $T_{\rm eff}$ was measured using the H$\alpha$ line while $\log g_*$ was measured from the Na D lines. We also determine the spectral type of the star to be F6V, by using the MKCLASS program (Gray & Corbally 2014). The values obtained for each of the fitted parameters are given in Table 4.3.

## 4.4 Combined analyses

We performed an MCMC fitting procedure which uses the stellar parameters obtained in the spectral analysis (Section 4.3) to constrain the fit, as described in Section 2.4. We used the latest version of the MCMC code described by Collier Cameron et al. (2007) and Pollacco et al. (2008), which is capable of fitting photometric, RV and tomographic data simultaneously (Collier Cameron et al. 2010a).

The system parameters which are determined from the photometric data are $T_{\rm c}$, $P$, $(R_{\rm p}/R_\star)^2$, $T_{14}$ and $b$. Limb darkening was accounted for using the Claret (2000); Claret (2004) four-parameter non-linear law: for each new value of $T_{\rm eff}$ a set of parameters is interpolated from the Claret tables. The proposed values of the stellar mass are calculated using the Enoch–Torres relation (Enoch et al. 2010; Torres, Andersen & Giménez 2010).

The RV fitting then provides values for the stellar reflex velocity semi-amplitude $K_1$ and the barycentric system velocity $\gamma$. We assume a circular orbit, since we do not have sufficient quality in the out-of-transit RVs to constrain the eccentricity. In any case, hot Jupiters often settle into circular orbits on time-scales that are shorter than their lifetimes through tidal circularization (Pont et al. 2011), so usually their orbits are circular. If there are accurate RVs taken through transit, it is also possible to measure the projected spin-orbit misalignment angle $\lambda$ by fitting the RM effect.

The 23 HARPS spectra were cross-correlated using the standard HARPS Data Reduction Software over a window of $\pm$ 350 km s$^{-1}$ (as described in Sections 2.3.2, 2.3.3). The cross-correlation functions (CCFs) were created using a mask matching a G2 spectral type, containing zeroes at the positions of absorption lines and ones in the continuum. The tomographic data are then comprised of the time series of CCFs taken through transit. The CORALIE spectra were also correlated using the same methodology.

We used the MCMC code in two modes. The first mode fits the CCFs to obtain RV values, and then uses the calibrations of Hirano et al. (2011) to model the RM effect and thus measure $\lambda$. The second mode fits the in-transit CCFs directly, modelling the perturbations of the CCFs due to the path of the planet across the stellar disc (e.g., Brown et al. 2017; Temple et al. 2017). The parameters determined in this part of the analysis are $v \sin i_\star$, $\lambda$, the stellar line-profile Full-Width at Half-Maximum (FWHM), the local FWHM of the line perturbation due to the planet $v_{\rm FWHM}$ and the system $\gamma$-velocity. The MCMC code assumes a Gaussian shape for the line perturbation caused by the planet. We obtain initial values for the stellar line FWHM and the $\gamma$-velocity by fitting a Gaussian profile to the CCFs and apply the spectral $v \sin i_\star$ and $T_{\rm eff}$ as priors. Neither $\lambda$ nor $v_{\rm FWHM}$ had a prior applied.

We give the solutions obtained using the two modes in Table 4.3. Both fits gave strongly consistent results. We adopt the solution of the fit including tomography, since it is a more direct method that uses more of the line-profile information.

### 4.4.1 A grazing transit

*With thanks to B. Smalley (Keele Astrophysics Group) for carrying out the IRFM analysis.*

The photometry and the best-fitting model are shown in Fig. 4.1. We found that constraining the photometric fit was difficult since the transit is either grazing or near-grazing and does not show clear 2$^{\rm nd}$ and 3$^{\rm rd}$ contacts. This means that $R_{\rm p}/R_*$ and the

impact parameter $b$ are poorly constrained. We show the probability distributions of $R_{\rm p}$,$R_*$ and $b$ in Fig. 4.2.

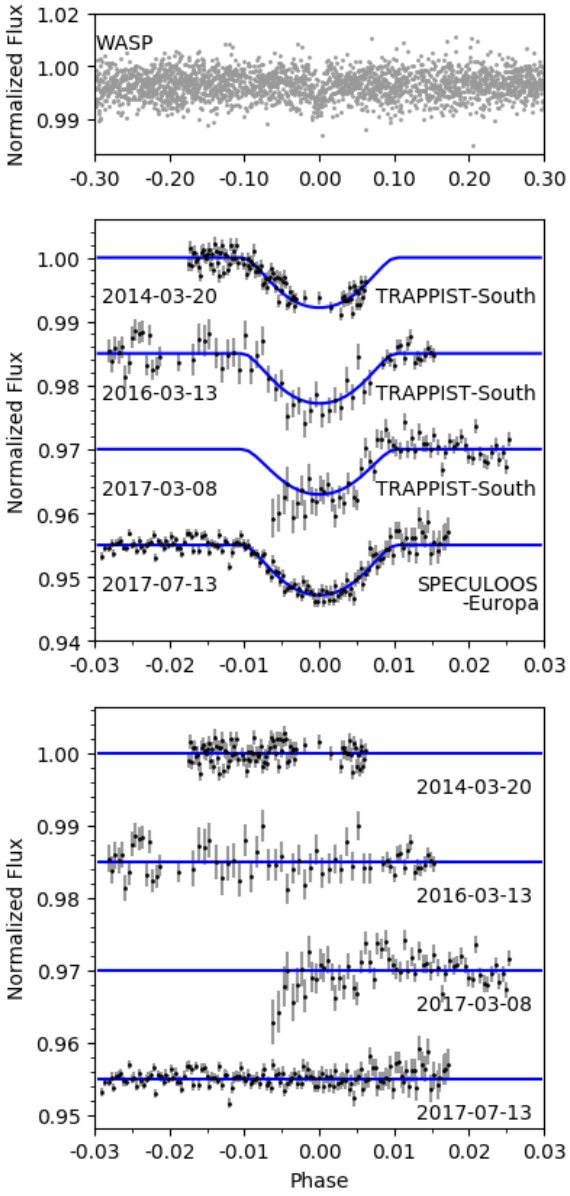


Figure 4.1: The WASP discovery photometry (top) and follow-up transit lightcurves (middle). The blue lines show the final model obtained in the MCMC fitting (see Section 4.4). The bottom panel then shows the residuals of the fit.

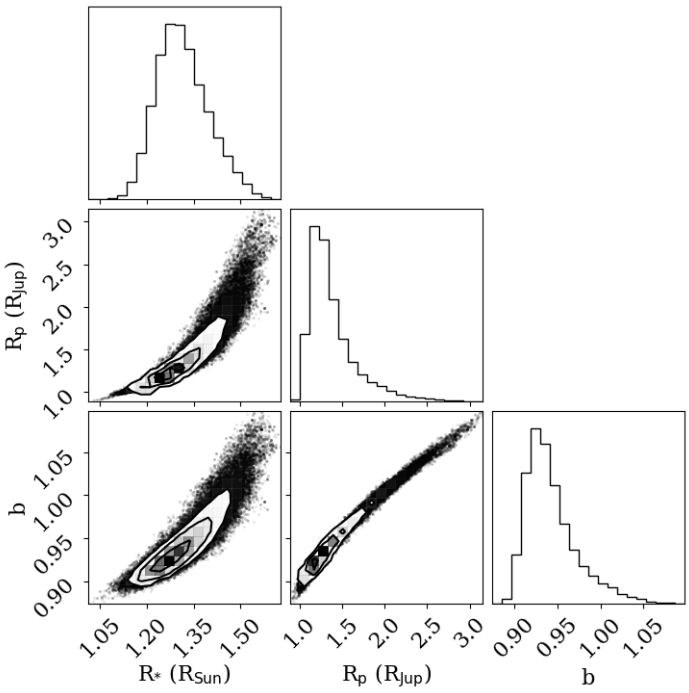


Figure 4.2: Probability distributions for the parameters $R_{\rm p}$, $R_*$ and $b$, created from the results of the second-mode MCMC run.

We calculated the 'grazing criterion', namely $(R_{\rm p}/R_* + b)$, which if $> 1$ implies a grazing transit (Smalley et al. 2011). We obtain $1.02^{+0.04}_{-0.02}$, which means that we cannot securely distinguish between grazing and near-grazing solutions.

We used the InfraRed Flux Method (IRFM, Blackwell & Shallis 1977) to obtain values for $T_{\rm eff}$ and the angular diameter $\theta$ of WASP-174 , which are quoted in Table 4.3. We then used $\theta$ and the *Gaia* DR2 parallax (Gaia Collaboration et al. 2016b; Gaia Collaboration et al. 2018) parallax, which is also quoted in Table 4.3, to estimate the stellar radius. We took reddening into account by measuring the equivalent width of the interstellar Na D lines using the stacked HARPS spectrum from Section 4.3, finding a width of $80\,{\rm m}\mathring{A}$ which equates to an extinction value of $E(B-V) = 0.02$ (Munari & Zwitter 1997). We have also taken into account the systematic offset in the *Gaia* parallax value (of 0.082 mas), as measured by Stassun & Torres (2018). We obtain a stellar radius of $1.35 \pm 0.10\,{\rm R}_\odot$ which is consistent with our fitted radius of 1.31 $\pm$

$0.08\,R_{\odot}$.

### 4.4.2 The planet's mass

The CORALIE and HARPS RVs are shown in Fig. 4.3. Due to the relatively large error bars in the out-of-transit RV measurements we do not regard the fitted semi-amplitude (of $0.08 \pm 0.03\,km\,s^{-1}$) to be a measure of the planet's mass. However, we were able to put a 95 % confidence upper limit on the mass of $1.3\,M_{Jup}$, and the predicted curve for this value is also shown in Fig. 4.3.

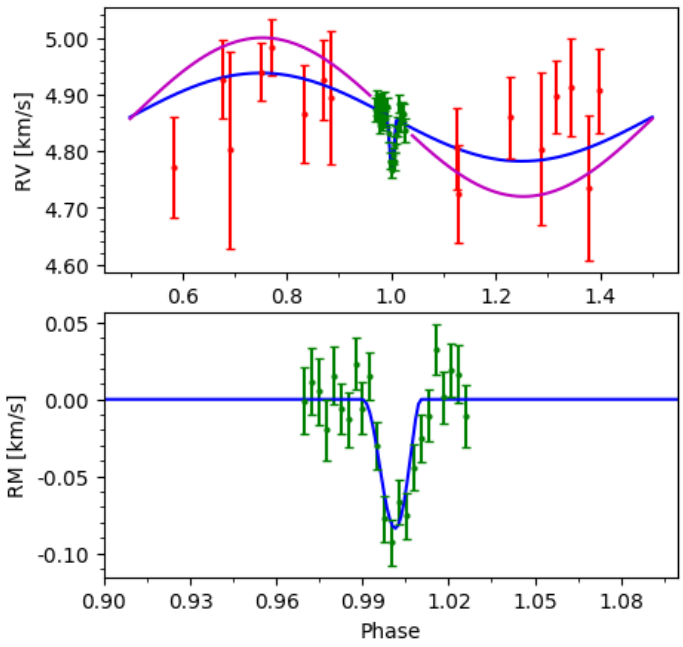


Figure 4.3: Top: The 16 CORALIE RVs (red points) obtained for WASP-174b . The magenta line shows the expected RV amplitude for a planet of $1.3\,M_{Jup}$, our derived upper limit (95 % confidence). The blue line shows the best-fit model including the RM fit. Bottom: the 23 through-transit HARPS RVs (green points). The blue line shows the best-fit model with the Keplerian RV curve subtracted, leaving only the fit to the RM effect.

### 4.4.3 The Doppler track

We display the tomographic data as a function of the planet's orbital phase in Fig. 4.4. In creating this plot we first remove the invariant stellar line profile by subtracting the average of the out-of-transit CCFs. We also display the simultaneous photometric observation to the left of the tomogram, and the residuals from subtracting the planet model on the right.

We interpret the resulting tomogram as showing a faint, prograde-moving planet signal crossing only the red-shifted portion of the plot. This is in line with the transit being grazing, such that the planet crosses only a short chord on the face of the star (see Fig. 4.5).

The planet's Doppler shadow appears very faint at the beginning and end of the transit (see Fig. 4.4). This is likely due to there being little of the planet on the face of the star near 1$^{st}$ and 4$^{th}$ contacts, owing to the near-grazing nature of the orbit.

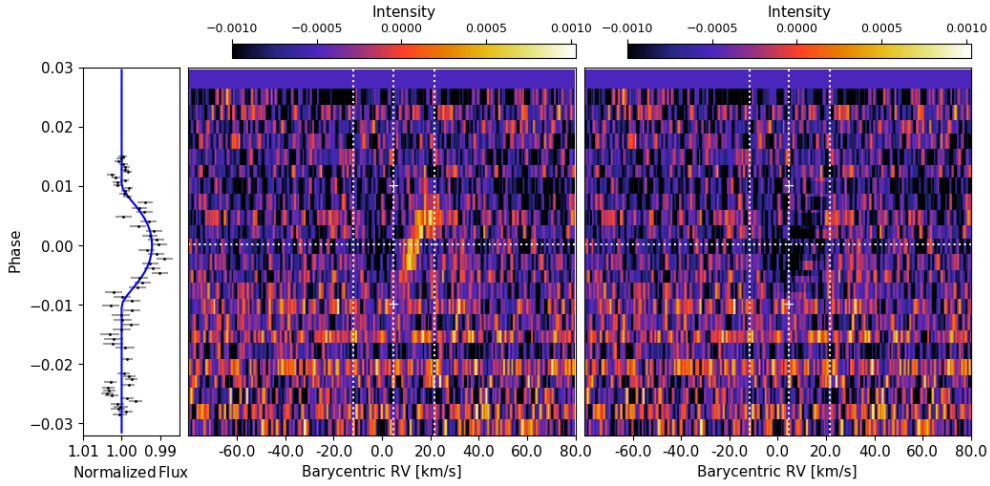


Figure 4.4: Middle: The line profiles through transit, with the mean of the out-of-transit CCFs subtracted. This shows a prograde-moving planet signal in the red-shifted section of the tomogram. Right: the line profile residuals after subtracting the planet model. In each, the white dotted vertical lines mark the positions of $\gamma$ and $\gamma \pm v \sin i_\star$. The phase of mid-transit is marked by the white horizontal dotted line. The white + symbols indicate $T_1$ and $T_4$, calculated using the adopted ephemeris. Left: The TRAPPIST-South lightcurve taken simultaneously with the tomographic observation.

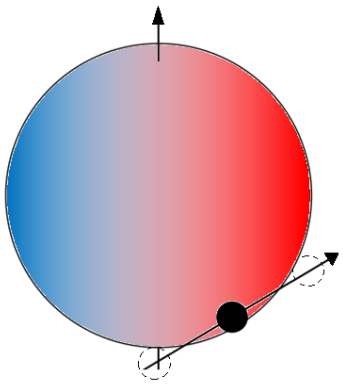

Figure 4.5: The transit chord calculated from the fitted values of $R_{\rm p}$, $R_*$, $b$ and $\lambda$ (see Table 4.3.) The dashed circles show the positions of the planet at 1$^{\rm st}$ and 4$^{\rm th}$ contacts.

## 4.5 Stellar age determination

We estimated the age of WASP-174 using the open source software BAGEMASS[1]. BAGEMASS uses the Bayesian method of Maxted, Serenelli & Southworth (2015) to fit the age, mass and initial metallicity of a star using the GARSTEC stellar evolution code (Weiss & Schlattl 2008). We applied constraints on the stellar temperature and metallicity ($T_{\rm eff} = 6400 \pm 100$ K and [Fe/H] $= 0.09 \pm 0.09$ as obtained in the spectral analysis) as well as the stellar density ($\rho_*/\rho_\odot = 0.6 \pm 0.2$ from the transit analysis). We adopt the solution obtained for solar values of He abundance and mixing length (the distance over which convection occurs), since enhancing the He abundance made no significant change to the fit while reducing the solar mixing length worsened the fit. We display the resulting isochrones and evolutionary tracks for this fit in Fig. 4.6 and the fitted values are given in Table 4.3.

We find WASP-174 to be consistent with a main-sequence star or one beginning to evolve off the main sequence. The Li abundance obtained in Section 4.3 is also consistent with the star being non-evolved, but for mid-F stars the Li abundance is not a good age indicator. For the measured value of $\log A(Li) = 2.48 \pm 0.10$, WASP-174

[1]Available at: http://sourceforge.net/projects/bagemass

could be up to a few Gyr old (Sestito & Randich 2005). If we define the main-sequence lifetime of a star to be the time taken for all hydrogen in the core to be exhausted, we can use the best-fit evolutionary track from BAGEMASS to estimate the age at which WASP-174 will leave the main sequence: $4.3 \pm 0.6$ Gyr.

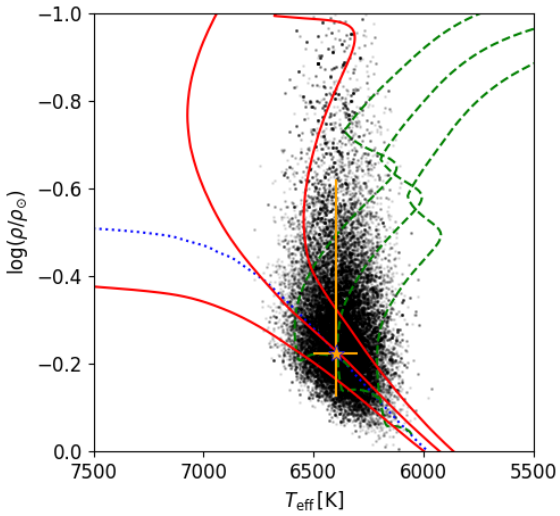


Figure 4.6: The best fitting evolutionary tracks and isochrones of WASP-174 obtained using BAGEMASS. Black points: individual steps in the MCMC. Dotted blue line: Zero-Age Main Sequence (ZAMS) at best-fit [Fe/H]. Green dashed lines: evolutionary track for the best-fit [Fe/H] and mass, plus $1\sigma$ bounds. Red lines: isochrone for the best-fit [Fe/H] and age, plus $1\sigma$ bounds. Orange star: measured values of $T_{\rm eff}$ and $\rho_*$ for WASP-174 obtained in the spectral and photometric analyses respectively.

## 4.6 Discussion and conclusions

WASP-174b is revealed by Doppler tomography to be a planet making a grazing transit of its host star in a misaligned orbit with an alignment angle of $\lambda = 31^\circ \pm 1^\circ$.

WASP-174 is an F6 star with an effective temperature of $T_{\rm eff} = 6400 \pm 100$ K and a measured $v \sin i_\star$ of $16.5 \pm 0.5$ km s$^{-1}$. This rotation rate, together with a fitted radius of $1.31 \pm 0.08$ R$_\odot$, implies a stellar rotation period of $P_{\rm rot} < 4.4$ d. Since the planet's

Table 4.3: All system parameters obtained for WASP-174b in this work.

| | | |
|---|---|---|
| 1SWASP J130310.57–412305.3 | | |
| 2MASS J13031055–4123053 | | |
| TIC ID:102192004 | | |
| RA = $13^{h}03^{m}10.57^{s}$, Dec = $-41°23'05.3''$ (J2000) | | |
| $V$ = 11.9 (NOMAD) | | |
| IRFM $T_{\rm eff}$ = 6380 ± 140 K | | |
| IRFM $\theta$ = 0.031 ± 0.002 mas | | |
| *Gaia* DR2 Proper Motions: | | |
| (RA) 0.043 ± 0.071 (Dec) –5.784 ± 0.112 mas/yr | | |
| *Gaia* DR2 Parallax: 2.41 ± 0.06 mas | | |
| Rotational Modulations: < 0.8 mmag (95%) | | |
| *Stellar parameters from spectral analysis:* | | |
| Parameter (Unit) | Value | |
| Spectral type | F6V | |
| $T_{\rm eff}$ (K) | $6400 \pm 100$ | |
| $\log g_*$ | $4.15 \pm 0.15$ | |
| [Fe/H] | $0.09 \pm 0.09$ | |
| $\log A(Li)$ | $2.48 \pm 0.10$ | |
| $v \sin i_*$ (km s$^{-1}$) | 16.5 ± 0.5 | |
| $v_{\rm mac}$ (km s$^{-1}$) | 6.3 km s$^{-1}$ | |
| *Parameters from photometric and RV analysis:* | | |
| Parameter (Unit) | DT Value (adopted): | RM Value: |
| $P$ (d) | 4.233700 ± 0.000003 | 4.233700 ± 0.000003 |
| $T_{\rm c}$ ($\rm BJD_{TDB}$) | 2457465.9336 ± 0.0004 | 2457465.9335 ± 0.0004 |
| $T_{14}$ (d) | 0.085 ± 0.002 | 0.085 ± 0.002 |
| $R_{\rm P}^2/R_*^2$ | 0.0086 ± 0.0003 | 0.0088 ± 0.0006 |
| $b$ | 0.94 ± 0.03 | 0.95 ± 0.04 |
| $i$ (°) | 84.2 ± 0.5 | 84.0 ± 0.7 |
| $a$ (AU) | 0.0559 ± 0.0009 | 0.0555 ± 0.0009 |
| $M_*$ ($M_\odot$) | 1.30 ± 0.06 | 1.31 ± 0.07 |
| $R_*$ ($R_\odot$) | 1.31 ± 0.08 | 1.3 ± 0.1 |
| $\log g_*$ (cgs) | 4.32 ± 0.04 | 4.31 ± 0.06 |
| $\rho_*$ ($\rho_\odot$) | 0.6 ± 0.2 | 0.6 ± 0.1 |
| $T_{\rm eff}$ (K) | 6400 ± 100 | 6400 ± 100 |
| [Fe/H] | 0.09 ± 0.09 | 0.09 ± 0.09 |
| $M_{\rm P}$ ($M_{\rm Jup}$) | < 1.3 (95%) | < 1.3 (95%) |
| $K$ (km s$^{-1}$) | < 0.14 (95%) | < 0.14 (95%) |
| $R_{\rm P}$ ($R_{\rm Jup}$) | 1.3 ± 0.5 | 1.4 ± 0.5 |
| $T_{\rm eql}$ (K) | 1490 ± 50 | 1500 ± 60 |
| *Parameters from RM and DT analyses:* | | |
| $\gamma$ (km s$^{-1}$) | 4.864 ± 0.005 | 4.860 ± 0.004 |
| $\lambda$ (°) | 31 ± 1 | 34 ± 5 |
| *Parameters from* BAGEMASS*:* | | |
| Parameter (Unit) | Value | |
| Age (Gyr) | $1.65 \pm 0.85$ | |
| $M_*$ ($M_\odot$) | $1.28 \pm 0.07$ | |
| $[\rm Fe/H]_{\rm init}$ | $0.12 \pm 0.08$ | |

orbital period is 4.23 d, this means that the stellar rotation period could be, but is not certain to be, shorter than the planet's orbit. Most hot-Jupiter systems have stellar rotation periods that are longer than the planet's orbit, but having $P_{\rm orb} > P_{\rm rot}$ has been found for other hot, more rapidly rotating host stars, including KELT-17b (Zhou et al. 2016b), WASP-167b/KELT-13b (Temple et al. 2017) and XO-6b (Crouzet et al. 2017). In systems with $P_{\rm orb} < P_{\rm rot}$ and with prograde orbits the tidal interaction is thought to produce decay of the planet's orbit, but this will be reversed in systems such as WASP-174, with a prograde orbit and with $P_{\rm orb} > P_{\rm rot}$ (see the discussions in Crouzet et al. (2017), and Section 3.7.1 or Temple et al. (2017)). The difference in dynamical evolution of hot-star hot Jupiters makes them interesting targets and is one reason for finding more examples of such systems.

Another dynamical difference is that hot-Jupiter orbits are much more likely to be misaligned around hotter stars, which might be related to reduced tidal damping in hotter stars with smaller or absent convective envelopes (Winn et al. 2010). With a misaligned orbit WASP-174b is in line with this trend. Of the 12 other systems confirmed with tomographic methods before the discovery of WASP-174b, 8 are at least moderately misaligned. These are WASP-33b (Collier Cameron et al. 2010b), HAT-P-57b (Hartman et al. 2015), KELT-17b (Zhou et al. 2016b), KELT-9b (Gaudi et al. 2017), KELT-19Ab (Siverd et al. 2018), XO-6b (Crouzet et al. 2017), WASP-167b/KELT-13b (Temple et al. 2017) and MASCARA-1b (Talens et al. 2017b).

High stellar irradiation produces hotter planetary atmospheres, and is thought to result in the inflated radii seen in many hot Jupiters (e.g., Hartman et al. 2016; Zhou et al. 2017; Siverd et al. 2018). With an equilibrium temperature of $1490 \pm 50\,{\rm K}$, we would thus expect WASP-174b to be moderately inflated.

The actual planetary radius is hard to measure owing to the grazing or near-grazing transit, which means that 2$^{\rm nd}$ and 3$^{\rm rd}$ contacts are not visible in the transit profile and the fitted radius is degenerate with the impact parameter (Fig. 4.2). Thus we can do no better than loosely constraining the radius to $R_P = 1.3 \pm 0.5\ {\rm R_{Jup}}$, which is consistent with that of an inflated hot Jupiter.

The mass of WASP-174b is also uncertain, since the hot host star limits the

accuracy and precision of radial-velocity measurements. We report only an upper limit of $1.3\,M_{Jup}$, so again WASP-174b is most likely a fairly typical inflated hot Jupiter.

At the time of discovery, WASP-174 was the faintest hot-Jupiter system for which the shadow of the planet had been detected by tomographic methods, with $V = 11.9$. It was followed by Kepler-448 at $V = 11.4$ (Bourrier et al. 2015a) and HAT-P-56 at $V = 10.9$ (Huang et al. 2015; Zhou et al. 2016a), which was initially confirmed with radial velocity measurements. Now, HATS-70b ($V = 12.574$, Zhou et al. 2019a) and WASP-190b ($V = 11.7$, Temple et al. 2019a) add to this group.

HAT-P-56b is also comparable to WASP-174 in that it has a near-grazing transit with an impact parameter of $b = 0.873^{+0.004}_{-0.006}$ (Huang et al. 2015), which compares with $b = 0.94 \pm 0.03$ for WASP-174b . As with our work the tomographic planet trace for HAT-P-56b is faint and possibly shows evidence for getting fainter when the planet is only partially occulting the star (i.e., at the beginning and end of the transit, (Zhou et al. 2016a)).

# 5 WASP-190b

**The material in this Chapter was published, largely in its current form, as part of Temple et al. (2019a). Acknowledgements are given where significant contributions were made by the co-authors thereof.**

## 5.1 Abstract

We report the discovery of WASP-190b, an exoplanet on a 5.37-day orbit around a mildly-evolved F6 IV-V star with $V = 11.7$, $T_{\rm eff} = 6400 \pm 100\,{\rm K}$, $M_* = 1.35 \pm 0.05\,M_\odot$ and $R_* = 1.6 \pm 0.1\,R_\odot$, which can be found in *TESS* Sector 2 as TIC ID:116156517 (Ricker et al. 2015; Stassun et al. 2018). We use both tomographic and RM analyses to determine the geometry of the system, and confirm the existence of the planet via the detection of its Doppler shadow and by measuring its mass using orbital RV measurements. The planet has a radius of $R_{\rm P} = 1.15 \pm 0.09\,R_{\rm Jup}$ and a mass of $M_{\rm P} = 1.0 \pm 0.1\,M_{\rm Jup}$, making it a mildly inflated hot Jupiter. It is the first hot Jupiter confirmed via Doppler tomography with an orbital period $> 5$ days. The orbit is also marginally misaligned with respect to the stellar rotation, with $\lambda = 21 \pm 6^\circ$ measured using Doppler tomography.

## 5.2 Data and observations

*With thanks to the WASP team for the acquisition and reduction of photometric and spectroscopic data.*

We observed WASP-190 using the WASP-South telescope (Hellier et al. 2011) at the South African Astronomical Observatory (SAAO) from 2006 to 2011. After the detection of a planet-like transit dip in the WASP lightcurve we confirmed the transit

with a follow-up lightcurve obtained using the TRAPPIST-South telescope (Jehin et al. 2011), and proceeded to obtain reconnaissance spectroscopy with the Euler/CORALIE spectrograph (Queloz et al. 2001b). These were sufficient to rule out a stellar-mass binary, but with relatively large errors were consistent with no motion at the level of $250\,\mathrm{m\,s^{-1}}$ and were inconclusive about whether the transiting body was a planet.

We thus attempted tomography of a transit, obtaining a series of 28 spectra through transit on the night of 2017 October 13 using the ESO 3.6-m/HARPS spectrograph (Pepe et al. 2002), accompanied by simultaneous photometry using the SPECULOOS-Europa telescope (Burdanov et al. 2018; Gillon 2018; Delrez et al. 2018). After tomographic detection of a planet-like signal, we obtained 5 further orbital RVs with HARPS to constrain the planetary mass. Details of the observations are provided in Table 5.1.

The HARPS spectra were cross-correlated over a window of $\pm\,350\,\mathrm{km\,s^{-1}}$, using a mask matching a G2 spectral type, and the standard HARPS Data Reduction Software as described by Baranne et al. (1996), Pepe et al. (2002) (see Sections 2.3.2, 2.3.3). We then analysed the CCFs themselves, and computed RV measurements from the CCFs which we list in Table 5.2 along with bisector spans (BS).

We used the WASP photometric data to look for any evidence of rotational modulation of the host star, using the methods of Maxted et al. (2011). We find no such variability at periods longer than a day, with a 95%-confidence upper limit on the amplitude of 1 mmag.

## 5.3 Stellar parameters from spectral analysis

*With thanks to B. Smalley (Keele Astrophysics Group) for carrying out the spectral analysis.*

In order to determine stellar parameters of WASP-190 we co-added the HARPS spectra obtained on the night of 2017 Oct 13 and performed a spectral analysis. We

Table 5.1: Observations of WASP-190b.

| Telescope or Instrument | Date | Notes |
|---|---|---|
| WASP-South | 2006–2011 | 30137 pts. |
| TRAPPIST-South | 2014 Nov 26 | $I+z$, 7s exp. |
| SPECULOOS-Europa | 2017 Oct 13 | $I+z$, 10s exp. |
| CORALIE | 2014 Aug–Oct | 5 RVs |
| HARPS | 2017 Oct 13 | 28 spectra taken including a transit |
| HARPS | 2018 Oct | 5 RVs |

Table 5.2: RV measurements of WASP-190, taken using the CORALIE and HARPS spectrographs for this work.

| $BJD_{TDB}$ –2,450,000 | RV (km $s^{-1}$) | $\sigma_{RV}$ (km $s^{-1}$) | BS (km $s^{-1}$) | $\sigma_{BS}$ (km $s^{-1}$) | $BJD_{TDB}$ –2,450,000 | RV (km $s^{-1}$) | $\sigma_{RV}$ (km $s^{-1}$) | BS (km $s^{-1}$) | $\sigma_{BS}$ (km $s^{-1}$) |
|---|---|---|---|---|---|---|---|---|---|
| CORALIE (out of transit): | | | | | 8040.669130 | 0.79 | 0.02 | 0.04 | 0.04 |
| 6871.794771 | 0.89 | 0.05 | –0.07 | 0.10 | 8040.680113 | 0.80 | 0.02 | 0.10 | 0.04 |
| 6895.811527 | 0.94 | 0.05 | –0.16 | 0.10 | 8040.690784 | 0.80 | 0.02 | 0.03 | 0.04 |
| 6922.731329 | 0.90 | 0.03 | –0.05 | 0.06 | 8040.701350 | 0.78 | 0.02 | –0.07 | 0.04 |
| 6952.511870 | 0.95 | 0.04 | 0.15 | 0.08 | 8040.712334 | 0.76 | 0.02 | –0.03 | 0.04 |
| 7000.625106 | 0.87 | 0.04 | –0.22 | 0.08 | 8040.723016 | 0.73 | 0.02 | –0.03 | 0.04 |
| 8392.595422 | 0.84 | 0.07 | –0.24 | 0.14 | 8040.733791 | 0.76 | 0.02 | –0.05 | 0.04 |
| HARPS (including a transit): | | | | | 8040.744670 | 0.73 | 0.03 | –0.05 | 0.06 |
| 8040.529251 | 0.84 | 0.02 | 0.04 | 0.04 | 8040.755341 | 0.76 | 0.03 | 0.05 | 0.06 |
| 8040.540026 | 0.82 | 0.02 | –0.04 | 0.04 | 8040.766220 | 0.77 | 0.03 | 0.09 | 0.06 |
| 8040.550489 | 0.84 | 0.02 | 0.05 | 0.04 | 8040.777100 | 0.81 | 0.03 | –0.10 | 0.06 |
| 8040.561472 | 0.86 | 0.02 | –0.02 | 0.04 | 8040.787770 | 0.83 | 0.03 | –0.02 | 0.06 |
| 8040.572351 | 0.85 | 0.02 | –0.05 | 0.04 | 8040.798545 | 0.82 | 0.03 | 0.10 | 0.06 |
| 8040.582918 | 0.85 | 0.02 | –0.02 | 0.04 | 8040.809112 | 0.85 | 0.03 | –0.06 | 0.06 |
| 8040.593797 | 0.87 | 0.02 | –0.00 | 0.04 | 8040.820107 | 0.82 | 0.03 | 0.06 | 0.06 |
| 8040.604572 | 0.92 | 0.02 | 0.02 | 0.04 | HARPS (out of transit): | | | | |
| 8040.615243 | 0.89 | 0.02 | –0.07 | 0.04 | 8393.843700 | 0.92 | 0.01 | –0.20 | 0.02 |
| 8040.626122 | 0.90 | 0.02 | –0.13 | 0.04 | 8396.706300 | 0.73 | 0.01 | 0.10 | 0.02 |
| 8040.636897 | 0.87 | 0.02 | –0.06 | 0.04 | 8397.590800 | 0.86 | 0.04 | –0.15 | 0.08 |
| 8040.647776 | 0.84 | 0.02 | –0.01 | 0.04 | 8398.611000 | 0.92 | 0.02 | –0.24 | 0.04 |
| 8040.658459 | 0.80 | 0.02 | –0.02 | 0.04 | 8399.542350 | 0.85 | 0.04 | –0.13 | 0.08 |

adopted a microturbulent velocity of $v_{\rm mic} = 1.6\,{\rm km\,s^{-1}}$ from the calibration of Bruntt et al. (2010) and a macroturbulent velocity of $v_{\rm mac} = 6.5\,{\rm km\,s^{-1}}$ from the calibration of Doyle et al. (2014). We used the H$\alpha$ line to determine an effective temperature $T_{\rm eff} = 6400 \pm 100\,{\rm K}$, while using the Na D feature to measure $\log g_\star = 3.9 \pm 0.1$. We also determined the projected stellar rotational velocity $v \sin i_\star = 13.8 \pm 0.7\,{\rm km\,s^{-1}}$, and the surface metallicity $[{\rm Fe/H}] = -0.02 \pm 0.05$. These results are also listed in Table 5.3. Using the MKCLASS program (Gray & Corbally 2014) we then obtained a spectral type of F6 IV–V.

## 5.4 Combined MCMC analysis

We conduct an analysis very similar to that conducted by Temple et al. (2018) for WASP-174b (see Chapter 4), which involves the use of MCMC methods to analyse the combined photometric and spectroscopic datasets. As one approach we use the in-transit spectroscopy data in the form of RV measurements, following the method of Hirano et al. (2011), and as a second approach we use the same data in the form of CCFs, following methods similar to that used by Brown et al. (2017); Temple et al. (2017). We call the former the Rossiter–McLaughlin (RM) analysis and the latter the tomographic analysis.

The code we use is described by Collier Cameron et al. (2007) and Pollacco et al. (2008), which in the latest version includes the tomographic analysis as described by Collier Cameron et al. (2010a). In both analyses, fitting the photometric lightcurves allows direct measurement of the planet-to-star area ratio $(R_{\rm p}/R_\star)^2$, the impact parameter $b$ and the key transit timing information $T_{\rm c}$, $P$, $T_{14}$ and by extension $T_{12}$. We use the value of $T_{\rm eff}$ obtained in the spectral analysis (see discussion in Section 5.7) as the starting value for the MCMC chains, and for each new value of $T_{\rm eff}$ we interpolate four-parameter law limb-darkening coefficients from the tables of Claret (2000); Claret (2004). Stellar mass is calculated at each step using the Enoch–Torres relation (Enoch et al. 2010; Torres, Andersen & Giménez 2010). The photometric data are displayed

in Fig. 5.1 along with the best-fit model and residuals of the fit.

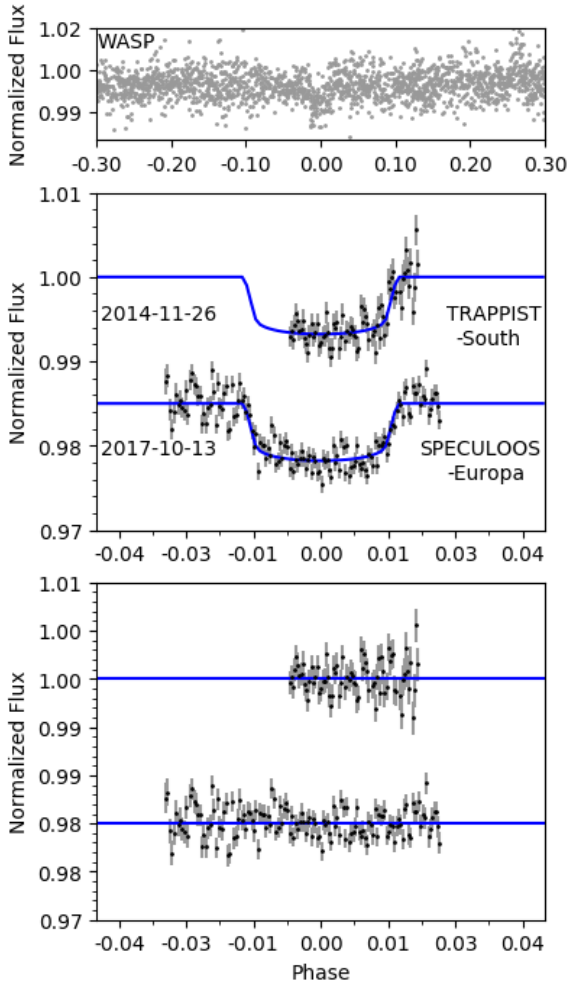


Figure 5.1: Top: the discovery lightcurve for WASP-190b (WASP-South). Middle: the two follow-up lightcurves with the best-fitting model shown in blue. Bottom: the residuals of the fits to the follow-up lightcurves.

The RV analysis then enables measurement of the barycentric system velocity $\gamma$ and the stellar reflex velocity semi-amplitude $K$. We expect that most hot Jupiters will settle into a circular orbit on a shorter timescale than their lifetimes (Pont et al. 2011), but with an orbital period of $\sim 5$ days WASP-190b is entering the regime where

eccentricity may remain. However, we do not have sufficient orbital RVs to constrain the eccentricity and so assume a circular orbit. We do not include the CORALIE measurements in the model adopted here, although including them changes the planetary mass by much less than the error bar.

Both the RM analysis and the tomographic analysis can allow the measurement of $v \sin i_\star$ and $\lambda$, while providing an additional constraint on the values of $\gamma$ and $b$. However, it can often be the case that for RM analysis a prior on $v \sin i_\star$ is required in order to obtain a well-constrained fit, and so we adopt the spectral $v \sin i_\star$ as a prior for both analyses. In the tomographic analysis we also fit the local line width $v_{\rm FWHM}$, resulting from stellar turbulence and instrumental broadening, which influences the width of the planetary perturbation of the line profiles, and whose shape is assumed to be Gaussian.

We show all RV measurements used in this work, along with the best fitting RV and RM models in Fig. 5.3. We also display the tomographic data (the time series of CCFs with the average of the out-of-transit CCFs subtracted from all CCFs) in Fig. 5.4, along with the best-fit planet model and residuals. The best fit parameters are listed in Table 5.3. We adopt the solution to the tomographic analysis (see Section 5.6) and, to avoid duplicating parameters derived from the same data (which are consistent in any case), the only parameters for which we list values from both analyses are $\gamma$, $v \sin i_\star$ and $\lambda$.

## 5.5 Results for the star

*With thanks to B. Smalley (Keele Astrophysics Group) for carrying out the IRFM analysis.*

We find WASP-190 to have a large radius of $R_* = 1.6 \pm 0.1\, R_\odot$ and a density of $\rho_* = 0.34 \pm 0.05\, \rho_\odot$. This implies that the star is beginning to evolve away from the main sequence, which would be consistent with the spectral type of F6 IV–V.

Table 5.3: All system parameters obtained in the combined analyses for WASP-190b.

| | |
|---|---|
| 1SWASP J003050.23–403424.3 | |
| 2MASS 00305023–4034243 | |
| TIC ID:116156517 | |
| Gaia DR2 4994237247949280000 | |
| RA = $00^{h}30^{m}50.233^{s}$, Dec = $-40°34'24.36''$ (J2000) | |
| $V = 11.7 \pm 0.1$ (TYCHO2) | |
| *Gaia* DR2 Proper Motions: | |
| (RA) $38.23 \pm 0.03$ (Dec) $-9.14 \pm 0.04$ mas/yr | |
| *Gaia* DR2 Parallax: $1.82 \pm 0.03$ mas | |
| Rotational Modulations: $< 1$ mmag (95%) | |
| *Stellar parameters from spectral analysis:* | |
| Parameter (Unit) | Value |
| Spectral type | F6 IV–V |
| $T_{\rm eff}$ (K) | $6400 \pm 100$ |
| $\log g_*$ | $3.9 \pm 0.1$ |
| [Fe/H] | $-0.02 \pm 0.05$ |
| $v \sin i_*$ (km s$^{-1}$) | 13.8 ± 0.7 |
| $v_{\rm mic}$ (km s$^{-1}$) | 1.6 (assumed) |
| $v_{\rm mac}$ (km s$^{-1}$) | 6.5 (assumed) |
| *Parameters from photometric and RV analysis:* | |
| Parameter (Unit) | DT Value (adopted): |
| $P$ (d) | 5.367753 ± 0.000004 |
| $T_{\rm c}$ (BJD$_{\rm TDB}$) | 2457799.1256 ± 0.0007 |
| $T_{14}$ (d) | 0.186 ± 0.002 |
| $T_{12} = T_{34}$ (d) | 0.017 ± 0.002 |
| $R_{\rm P}^2/R_*^2$ | 0.0062 ± 0.0002 |
| $b$ | 0.45 ± 0.09 |
| $i$ (°) | 87.1 ± 0.7 |
| $a$ (AU) | 0.0663 ± 0.0008 |
| $M_*$ ($M_\odot$) | 1.35 ± 0.05 |
| $R_*$ ($R_\odot$) | 1.6 ± 0.1 |
| $\log g_*$ (cgs) | 4.17 ± 0.04 |
| $\rho_*$ ($\rho_\odot$) | 0.34 ± 0.05 |
| $T_{\rm eff}$ (K) | 6400 ± 100 |
| [Fe/H] | –0.02 ± 0.05 |
| $K$ (km s$^{-1}$) | 0.099 ± 0.009 |
| $M_{\rm P}$ ($M_{\rm Jup}$) | 1.0 ± 0.1 |
| $R_{\rm P}$ ($R_{\rm Jup}$) | 1.15 ± 0.09 |
| $\log g_{\rm P}$ (cgs) | 3.2 ± 0.1 |
| $T_{\rm eql}$ (K) | 1500 ± 50 |

*Parameters from RM and DT analyses:*

| Parameter (Unit) | DT Value (adopted): | RM Value: |
|---|---|---|
| $\gamma$ (km s$^{-1}$) | 0.82 ± 0.01 | 0.823 ± 0.009 |
| $\lambda$ (°) | 21 ± 6 | 23 ± 12 |
| $v_{\rm FWHM}$ (km s$^{-1}$) | 10 ± 1 | – |
| $v \sin i_\star$ (km s$^{-1}$) | 13.3 ± 0.6 | 14.1 ± 0.7 |

The effective temperature ($T_{\rm eff}$) was also obtained using the Infrared Flux Method (IRFM, Blackwell & Shallis 1977). The stellar spectral energy distribution (SED) was obtained using literature broad-band photometry from 2MASS (Skrutskie et al. 2006), APASS9 $B$, $V$, $g'$, $r'$ and $i'$ (Henden et al. 2015), USNO-B1 $R$ (Monet et al. 2003) and WISE (Cutri & et al. 2012). The photometry was converted to fluxes and the best-fitting Kurucz (1993) model flux distribution found and integrated to determine a bolometric flux of $5.27 \pm 0.26 \times 10^{-10}$ erg s$^{-1}$ cm$^{-2}$. No visible interstellar lines were seen around the Na D line, so $E(B-V)$ was assumed to be zero. The IRFM was then used, with the 2MASS fluxes, to obtain a value of $T_{\rm eff} = 6560 \pm 140$ K as well as an angular diameter of $\theta = 0.029 \pm 0.001$ mas. The *Gaia* DR2 (Gaia Collaboration et al. 2016b; Gaia Collaboration et al. 2018) lists the parallax of WASP-190 as $1.82 \pm 0.03$ mas. Using these values and accounting for the correction to *Gaia* DR2 parallax values suggested by Stassun & Torres (2018), we obtain a stellar radius of $1.65 \pm 0.08\,R_{\odot}$, which is consistent with our result from the MCMC analysis.

We investigate the age of WASP-190 using the open source software BAGEMASS[1] (Maxted, Serenelli & Southworth 2015). BAGEMASS allows the user to fit $T_{\rm eff}$ and $M_*$ using stellar evolutionary models calculated for different He abundances and mixing lengths (GARSTEC; Weiss & Schlattl 2008). As inputs we use the values of $T_{\rm eff}$ and [Fe/H] derived from the spectral analysis in Section 5.3, and also use the value of $\rho_*$ obtained in the combined analysis (Section 5.4) as a constraint.

Assuming solar values for the He abundance and mixing length gave the best-fit solution. We display the corresponding isochrones and evolutionary tracks in Fig. 5.2. We find the current age of WASP-190 to be $2.8 \pm 0.4$ Gyr, implying that the star is beginning to evolve off the main sequence. This is consistent with our finding that the star has a radius larger than expected for a main sequence star. For comparison, the time taken to exhaust all hydrogen in the core is $3.8 \pm 0.5$ Gyr.

[1] Available at: http://sourceforge.net/projects/bagemass

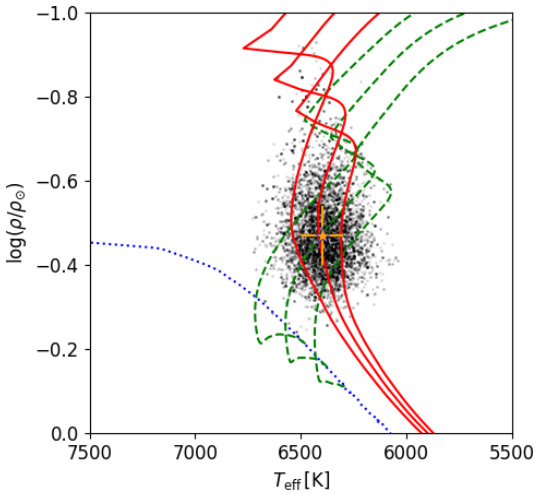


Figure 5.2: The best fitting evolutionary tracks and isochrones of WASP-190 obtained using BAGEMASS. Black points: individual realisations of the MCMC. Dotted blue line: Zero-Age Main Sequence (ZAMS) at best-fit [Fe/H]. Green dashed lines: evolutionary track for the best-fit [Fe/H] and mass, plus $1\sigma$ bounds. Red lines: isochrone for the best-fit [Fe/H] and age, plus $1\sigma$ bounds. Orange star: measured values of $T_{\rm eff}$ and $\rho_*$ for WASP-190 obtained in the spectral and photometric analyses respectively.

Table 5.4: Parameters for WASP-190 from BAGEMASS:

| Parameter (Unit) | Value |
|---|---|
| Age (Gyr) | $2.8 \pm 0.4$ |
| $M_*$ ($M_\odot$) | $1.30 \pm 0.05$ |
| $[\mathrm{Fe/H}]_{\rm init}$ | $0.03 \pm 0.04$ |

## 5.6 Results for the planet

We find a best fit $K$ of $0.099 \pm 0.009\,\mathrm{km\,s^{-1}}$, giving a planet mass of $M_{\rm p} = 1.0 \pm 0.1\,M_{\rm Jup}$. The fitted planetary radius is $1.15 \pm 0.09\,\mathrm{R_{Jup}}$.

The in-transit RVs, showing the RM effect, are displayed in the lower panel of Fig. 5.3. The equivalent tomogram of the same data is shown in Fig. 5.4. Both are consistent with a planet in a prograde orbit. The projected spin-orbit angle, $\lambda$, is

measured as $23 \pm 12°$ in the RM analysis and as $21 \pm 6°$ in the tomographic analysis. The planet trace is faint and hard to see, which we attribute to the star being relatively faint for tomographic analysis, at $V = 11.7$, and the transit dip being relatively shallow for a hot Jupiter, at 0.6%. The latter results from the star being relatively large at $1.6\,R_{\odot}$ when compared to the planet, which has only a mildly inflated radius of $1.15\,R_{Jup}$.

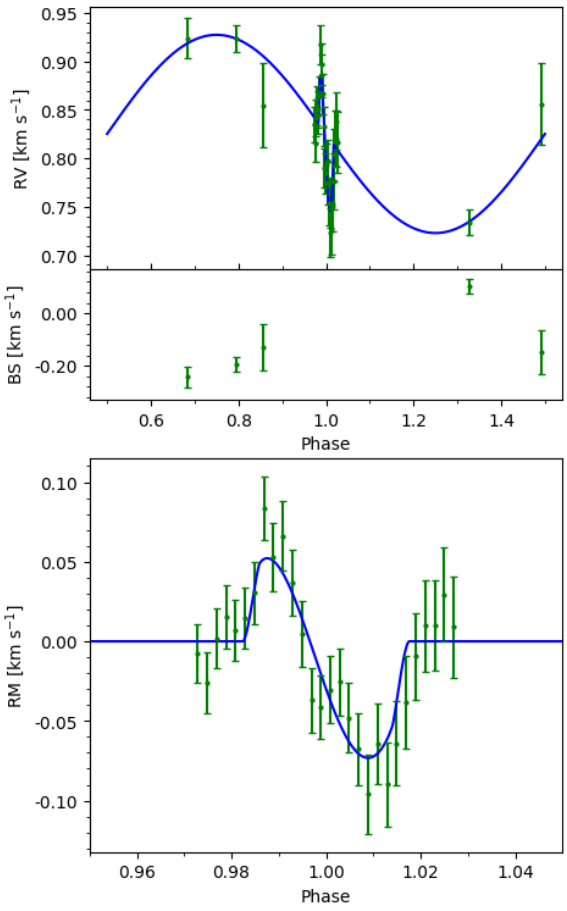


Figure 5.3: Top: The HARPS RV measurements used in the analysis of WASP-190b. The blue line shows the best-fit Keplerian RV curve and the fit to the RM effect. Centre: the bisectors for the out-of-transit RVs plotted against phase, which show no correlation with the RV measurements. Bottom: The region around transit on a larger scale.

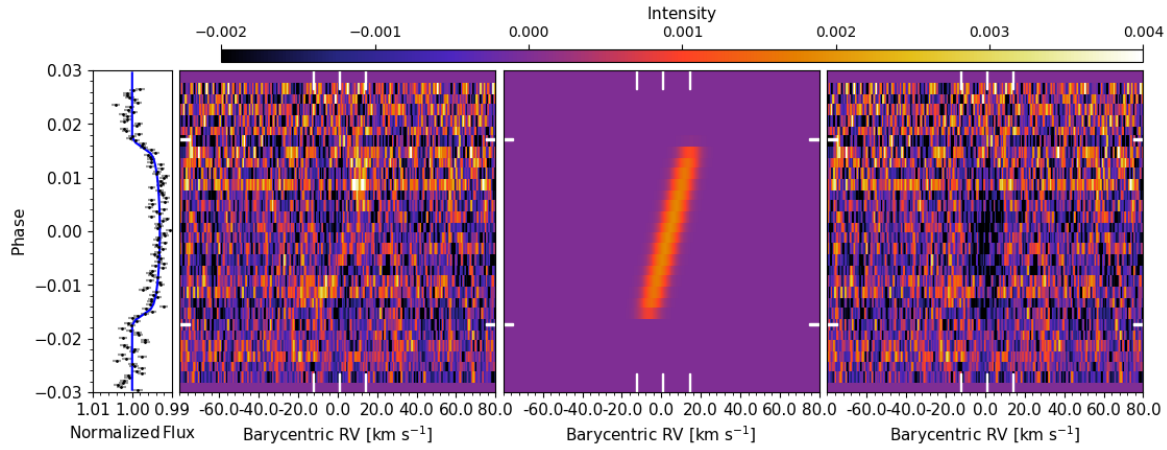


Figure 5.4: Centre-left: The Doppler tomogram comprised of the time series of residual HARPS CCFs calculated by subtracting the average of the out-of-transit CCFs from all CCFs. Left: the SPECULOOS-Europa lightcurve taken simultaneously with the HARPS observation. Centre-right: The best-fit planet model. Right: the residuals remaining after subtracting the best-fit planet model from the centre-left tomogram. In the three tomographic panels, the start and end times of the transit are marked with horizontal white dashes, while the vertical dashes mark respectively the positions of $\gamma$-$v \sin i_\star$ , $\gamma$ and $\gamma$+$v \sin i_\star$ . We interpret the tomogram as showing a very faint, prograde planet signal which in places is completely masked by background noise.

## 5.7 Discussion and Conclusions

We have shown that WASP-190b is a typical hot Jupiter with a mass of $1.0 \pm 0.1\, M_{\rm Jup}$ and a mildly inflated radius of $1.15 \pm 0.09\, R_{\rm Jup}$. It is in a 5.4-day orbit that is marginally misaligned with respect to the stellar rotation, with $\lambda = 21 \pm 6\,^\circ$.

The measured values of $v \sin i_\star$ and $\lambda$ are consistent between the spectral analysis, the tomographic analysis and the RM analysis. The tomographic analysis produced similar fits, giving a $v \sin i_\star$ value consistent with the spectroscopic value, regardless of whether we adopted the spectroscopic $v \sin i_\star$ as a prior. In contrast, the RM analysis was less constrained without a prior, and the fit tended to favour values that were too large. This often occurs for systems with a low impact parameter $b$, since it is difficult

to differentiate the effects of $v \sin i_\star$ and $\lambda$ on the shape of the RM curve when it is symmetrical (e.g., Albrecht et al. 2011). Since, in WASP-190, the impact parameter has a mid-level value of $b = 0.45$, this tendency should be reduced, but it may be that the low signal-to-noise of the data is leading the fit to be less constrained than usual. Overall, we found that the parameters were better constrained in the tomographic analysis than in the RM analysis, and so we adopt that fit.

While there is a well-established trend between the irradiation of a hot Jupiter and the inflation of its radius (e.g., Enoch, Collier Cameron & Horne 2012), hot Jupiters also display a wide range of radii (e.g., Burrows et al. 2007). Sestovic, Demory & Queloz (2018) investigates the relationship between planet radius, mass and irradiation, finding that a more massive planet is usually less inflated than a low-mass planet of the same temperature, due to the planet's gravity counteracting the inflation. In Fig. 5.5 we show planetary radius as a function of equilibrium temperature, and use planetary mass as a third dimension, for all planets with $0.6\,M_{\rm Jup} < M_{\rm p} < 4.0\,M_{\rm Jup}$ as listed in the TEPCat database (accessed 02/2019; Southworth 2011). The figure indicates that planets of a given mass and equilibrium temperature can have a wide range of radii, and shows that planets of $\sim 1\,M_{\rm Jup}$ like WASP-190b are not necessarily inflated, implying that the invocation of some third parameter is required. Possible causes of the disparity include different evolutionary histories, leading to different amounts of irradiation over time (e.g., Hartman et al. 2016), the possibility of internal heating mechanisms (e.g., Kurokawa & Inutsuka 2015; Ginzburg & Sari 2015; Thorngren & Fortney 2018; Ryu, Zingale & Perna 2018) and differences in the mass and metallicity of the planets' cores (e.g., Enoch, Collier Cameron & Horne 2012).

With $\lambda = 21 \pm 6^\circ$, WASP-190b is marginally misaligned. This is consistent with the known trend in hot-star systems, whereby planets around stars beyond the Kraft break have a wider range of obliquities, with most being in misaligned orbits (e.g., Winn et al. 2010; Dai & Winn 2017). The true orbit may be more strongly misaligned, however, since the value of $|\lambda|$ for non-polar misaligned orbits represents a lower limit for the true obliquity $|\psi|$. To measure $\psi$ it would be necessary to independently measure the stellar equatorial rotational velocity $v$ or stellar inclination $i_\star$ (for example, by

looking for differential rotation effects as described by Cegla et al. 2016a).

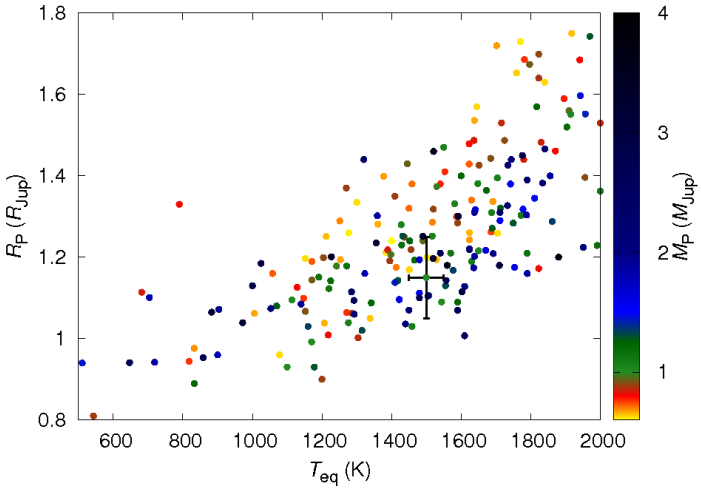


Figure 5.5: $R_p$ vs. $T_{eql}$, colour coded by mass, of all known planets with $0.6\,M_{Jup} < M_p < 4.0\,M_{Jup}$. WASP-190b is displayed including the error bars on the measured radius and temperature.

# 6 WASP-180Ab

**The material in this Chapter was published, largely in its current form, as part of Temple et al. (2019b). Acknowledgements are given where significant contributions were made by the co-authors thereof.**

## 6.1 Abstract

We report the discovery and characterisation of WASP-180Ab, a hot Jupiter confirmed by the detection of its Doppler shadow and by measuring its mass using radial velocities. We find the $0.9 \pm 0.1\,M_{\rm Jup}$, $1.24 \pm 0.04\,R_{\rm Jup}$ planet to be in a misaligned, retrograde orbit around an F7 star with $T_{\rm eff} = 6500\,{\rm K}$ and a moderate rotation speed of $v \sin i_\star = 19.9\,{\rm km\,s^{-1}}$. The host star is the primary of a $V = 10.7$ binary, where a secondary separated by $\sim$5″ ($\sim$1200 AU) contributes $\sim$30% of the light. WASP-180Ab thus adds to a small group of known hot Jupiters in near-equal mass stellar binaries. A 4.6-day modulation seen in the WASP data is likely to be the rotational modulation of the companion star, WASP-180B.

## 6.2 Data and Observations

*With thanks to the WASP team for the acquisition and reduction of photometric and spectroscopic data.*

WASP-180 is a known binary, listed as WDS 08136-0159 in the Washington Double Star Catalogue (Mason et al. 2001), with the two stars having *Gaia* magnitudes of 10.9 and 11.8. *Gaia* DR2 confirms the two stars to have the same parallax and proper motions, and we calculate the angular separation to be 4.854″ (Gaia Collaboration et al. 2016b; Gaia Collaboration et al. 2018). This separation is sufficient to avoid

contamination in high-resolution spectroscopic observations of the system.

We observed WASP-180A from November 2009 to March 2012 using the SuperWASP-North telescope (Pollacco et al. 2006) located at the Roque de los Muchachos Observatory in La Palma, as well as the WASP-South telescope (Hellier et al. 2011) located at the South African Astronomical Observatory (SAAO). The data contains light from both WASP-180A and WASP-180B.

Upon detecting a 3.4-d transit-like signal in the WASP data we obtained focused photometry with TRAPPIST-South (Jehin et al. 2011), resolving the two stars. These data were sufficient to show that the transit is of the brighter of the two stars, WASP-180A, but were otherwise of low quality and so we exclude the lightcurve from further analysis.

We proceeded to obtain RV measurements with the Euler/CORALIE (Queloz et al. 2001b) spectrograph. WASP-180A is a fast rotating F star with broad lines giving large RV errors, so the CORALIE RVs ruled out a stellar-mass transit mimic, but were not sufficient to give a measurement of the planet's mass. Thus we attempted Doppler tomography of a transit on the night of 2018 January 5 using the ESO 3.6-m/HARPS spectrograph (Pepe et al. 2002). Due to an auto-guiding issue three of the spectra obtained were of low signal-to-noise and were therefore discarded. Simultaneously during this transit we observed the lightcurve using TRAPPIST-South, using an aperture including both stars.

After tomographic confirmation of the planet we observed further follow-up lightcurves also using apertures including both stars. These were taken with TRAPPIST-North (Barkaoui et al. 2017; Barkaoui et al. 2019) at the Oukaïmden Observatory in Morocco and the SPECULOOS-Callisto telescope (Burdanov et al. 2018) at ESO Paranal Observatory. We also obtained 6 more RVs with HARPS to constrain the planet's mass. Details of the observations used in this work are provided in Table 6.1.

The RV measurements corresponding to each of the spectra obtained are listed in Table 6.2 with the corresponding bisector span (BS) measurements. These were measured from cross-correlation functions (CCFs) computed by cross-correlating the spectra using a mask matching a G2 spectral type, over a wide correlation window

Table 6.1: Details of the photometric and spectroscopic observations of WASP-180Ab carried out for this work.

| Telescope/Instrument | Date | Notes |
|---|---|---|
| WASP-North | 2009–2011 | 8329 points |
| WASP-South | 2011–2012 | 4359 points |
| TRAPPIST-South | 2018 Jan 5 | z'. 10s exp. |
| TRAPPIST-North | 2018 Jan 12 | z'. 11s exp. |
| SPECULOOS-Callisto | 2018 Jan 22 | z'. 8s exp. |
| ESO 3.6-m/HARPS | 2018 Jan 5 | 21 spectra through transit |
| Euler/CORALIE | 2015–2018 | 9 RVs |
| ESO 3.6-m/HARPS | 2018 Mar | 6 RVs |

covering –320 $\mathrm{km\,s^{-1}}$ to 380 $\mathrm{km\,s^{-1}}$.

## 6.3 Spectral analysis

*With thanks to B. Smalley (Keele Astrophysics Group) for carrying out the spectral analysis.*

We analysed a median-stacked HARPS spectrum created from the 18 HARPS spectra taken on the night of 2018 Jan 5, to obtain stellar parameters. We follow the methods of Doyle et al. (2013) to measure $T_{\rm eff} = 6500 \pm 150$ K and $\log g_\star = 4.5 \pm 0.2$ dex. We measure $v \sin i_\star = 18.3 \pm 1.1\,\mathrm{km\,s^{-1}}$ by assuming a microturbulence value of $v_{\rm mic} = 1.5\,\mathrm{km\,s^{-1}}$ from the calibration of Bruntt et al. (2010) and a macroturbulence value of $5.8\,\mathrm{km\,s^{-1}}$ extrapolated from the calibrations of Doyle et al. (2014), which is valid for stars up to 6400 K. We also measure the metallicity as [Fe/H] = 0.09±0.19, and finally, use the MKCLASS program (Gray & Corbally 2014) to obtain a spectral type of F7 V.

Table 6.2: RV measurements for WASP-180A taken using the CORALIE and HARPS spectrographs for this work. The values in italics are of low signal-to-noise due to an auto-guiding issue during observation.

| $BJD_{TDB}$ –2,450,000 | RV (km $s^{-1}$) | $\sigma_{RV}$ (km $s^{-1}$) | BS (km $s^{-1}$) | $\sigma_{BS}$ (km $s^{-1}$) |
|---|---|---|---|---|
| CORALIE: | | | | |
| 7092.644031 | 28.96 | 0.05 | –0.18 | 0.10 |
| 7697.849714 | 28.96 | 0.06 | 0.01 | 0.12 |
| 7751.760876 | 29.02 | 0.06 | –0.29 | 0.12 |
| 8077.824503 | 28.76 | 0.04 | –0.12 | 0.08 |
| 8079.836204 | 28.90 | 0.05 | –0.21 | 0.10 |
| 8094.796351 | 28.65 | 0.04 | –0.00 | 0.08 |
| 8140.848419 | 28.90 | 0.06 | –0.15 | 0.12 |
| 8212.592949 | 29.06 | 0.06 | –0.11 | 0.12 |
| 8222.600891 | 28.95 | 0.07 | –0.16 | 0.14 |
| HARPS: | | | | |
| 8198.604103 | 29.02 | 0.02 | –0.25 | 0.04 |
| 8199.643111 | 28.85 | 0.02 | –0.04 | 0.04 |
| 8201.610172 | 29.01 | 0.02 | –0.07 | 0.04 |
| 8202.589668 | 29.01 | 0.02 | –0.06 | 0.04 |
| 8203.572959 | 28.87 | 0.02 | –0.19 | 0.04 |
| 8204.571804 | 28.91 | 0.02 | –0.01 | 0.04 |
| HARPS (2018 Jan 05): | | | | |
| 8124.596974 | 28.99 | 0.02 | –0.23 | 0.04 |
| 8124.607854 | 29.05 | 0.02 | –0.21 | 0.04 |
| 8124.618421 | 28.98 | 0.02 | –0.17 | 0.04 |
| 8124.629200 | 28.96 | 0.02 | –0.15 | 0.04 |
| 8124.640806 | 28.90 | 0.02 | –0.11 | 0.04 |
| 8124.650841 | 28.76 | 0.02 | 0.03 | 0.04 |
| 8124.661525 | 28.76 | 0.02 | 0.22 | 0.04 |
| 8124.672312 | 28.81 | 0.02 | 0.17 | 0.04 |
| 8124.683285 | 28.91 | 0.02 | –0.12 | 0.04 |
| 8124.693748 | 29.02 | 0.02 | –0.31 | 0.04 |
| 8124.704420 | 29.10 | 0.02 | –0.48 | 0.04 |
| 8124.715299 | 29.20 | 0.03 | –0.75 | 0.06 |
| 8124.725971 | 29.16 | 0.03 | –0.63 | 0.06 |
| *8124.736434* | *29.02* | *0.04* | *0.10* | *0.08* |
| *8124.746794* | *29.16* | *0.04* | *–0.03* | *0.08* |
| *8124.758090* | *28.35* | *0.05* | *–1.30* | *0.10* |
| 8124.770313 | 28.91 | 0.02 | –0.18 | 0.04 |
| 8124.780059 | 28.95 | 0.02 | –0.22 | 0.04 |
| 8124.790510 | 28.91 | 0.02 | –0.19 | 0.04 |
| 8124.801182 | 28.88 | 0.02 | –0.22 | 0.04 |
| 8124.812062 | 28.91 | 0.03 | –0.18 | 0.06 |

## 6.4 The distant co-moving companion

The average parallax of WASP-180 measured by *Gaia* DR2 is 3.885 mas and the angular separation is 4.854″, which indicates a projected binary separation of ∼1200 AU. This would imply an orbit of ∼30 000 yrs, which is compatible with the fact that no significant change in separation or position angle is seen in measurements taken over a period of 120 years, as listed in the WDS.

### 6.4.1 Correcting for dilution

*With thanks to D. Evans (Keele Astrophysics Group) for determining dilution factors for the passbands used.*

Our photometry of WASP-180 was all extracted from an aperture including both A and B components. Thus we need to correct the lightcurves for dilution. We deduced correction factors in the different bands of SDSS z and Johnson V, the latter of which was used as an approximation for the WASP data. These are estimated from deducing the effective temperatures of the two stars from available photometry, as follows.

We fitted $T_{\rm eff}$, $\log g_\star$, and [Fe/H] by comparing resolved catalogue photometry to the synthetic photometry of Casagrande & VandenBerg (2014), Casagrande & VandenBerg (2018) which uses the MARCS stellar models of Gustafsson et al. (2008). The stars were assumed to have identical [Fe/H]. Interstellar reddening was found to be poorly constrained by the photometry, and was instead fixed at E(B–V) = 0.01, derived from the 3D dust map of Green et al. (2014, Green et al. (2015), adopting the closest reliable reddening measurements in the map, at approximately 400 pc. The choice of distance does not significantly affect the results, with the full line-of-sight reddening out to 8 kpc being E(B–V) = 0.02 ± 0.02. Resolved photometry was found in PANSTARRS-1 (*grizy*, Chambers et al. 2016), CMC15 (*r'*, Niels Bohr Institute, Institute of Astronomy & Real Instituto y Observatorio de La Armada 2014), DENIS (*IJK*,Epchtein et al. 1997), and 2MASS (*JHK*, Cutri et al. 2003). The PANSTARRS-1

Table 6.3: Third light dilution factors and stellar flux ratios obtained for WASP-180.

| Passband | Third Light | Flux Ratio |
|---|---|---|
| SDSS z | $0.325 \pm 0.007$ | $0.48 \pm 0.01$ |
| Johnson V | $0.260 \pm 0.006$ | $0.351 \pm 0.008$ |

catalogue does not include uncertainties for the measurements, and so a conservative uncertainty of 0.1 mag was assigned to all measurements in that catalogue.

Stellar parameters were derived by least-squares minimisation to find the minimum $\chi^2$, and uncertainties were determined by perturbing each parameter separately until a $\delta\chi^2$ of 1 was reached. We found $\log g_\star$ to be poorly constrained by the photometry, with the entire range of the synthetic photometry grids ($3.0 \leq \log g_\star \leq 5.0$) failing to give $\delta\chi^2 > 1$. Temperatures of $6540^{+80}_{-30}$ K and $5430^{+30}_{-25}$ K were obtained for the A and B components respectively, as well as a joint [Fe/H] value of $0.0^{+0.1}_{-0.5}$. The fitting was also repeated four further times, excluding each of the four photometric catalogues (PANSTARRS-1, CMC15, DENIS, 2MASS) in turn. The mean and standard deviation of the parameters from these four additional fits are $T_A = 6521 \pm 56$ K, $T_B = 5425 \pm 17$ K, and [Fe/H] = –0.01 ± 0.01: in good agreement with the full fit, indicating that none of the four photometric surveys is significantly biased. The values of $T_A$ we obtain are consistent with the value of $T_{\rm eff}$ from the spectral analysis (Sec. 6.3).

Using the stellar parameters from the full fit, and a fixed $\log g_\star$ of 4.5 (consistent with spectral analysis), flux ratios were estimated from the synthetic photometry for the z' and V bands. The fraction of light contributed by the secondary star was calculated, and thus the light curves corrected for the dilution of the planetary transit. The third light values and stellar flux ratios we obtained are given in Table 6.3.

### 6.4.2 IRFM analysis

*With thanks to B. Smalley (Keele Astrophysics Group) for carrying out the IRFM analysis.*

We use the InfraRed Flux Method (IRFM; Blackwell & Shallis 1977) to derive stellar angular diameters and IR temperatures for WASP-180A and WASP-180B. The IRFM makes use of the insensitivity of stellar surface flux to $T_{\rm eff}$ at IR wavelengths to determine $T_{\rm eff}$ from the ratio of total integrated flux to monochromatic flux, and thus measure the angular diameter of a star. We combine the angular diameters with the *Gaia* DR2 parallaxes for the two stars, applying the correction to *Gaia* DR2 parallaxes suggested by Stassun & Torres (2018), to estimate their radii. We calculate $R_{\star,\rm A} = 1.17 \pm 0.08 R_\odot$ and $R_{\star,\rm B} = 1.07 \pm 0.06 R_\odot$.

### 6.4.3 Rotational modulation search

*With thanks to P. Maxted (Keele Astrophysics Group) for carrying out the rotational modulation search.*

We perform a search of the WASP photometry following the method of Maxted et al. (2011), looking for rotational modulation or pulsation signals with frequencies of 0–1 cycles day$^{-1}$. The data were split into three parts according to the observing season and camera used. We find a signal with an average amplitude of $\sim 0.004$ mag and an average period of $4.57 \pm 0.05$ days. The strongest peak in the first set of data lies at half the modulation period $P_{\rm mod}$. The last set of data contained the clearest signal, and so was given double weight when computing the average. We display the periodograms for each set of data in Fig. 6.1, and give the individual best-fit amplitudes and periods in Table 6.4.

Using the measured $v \sin i_\star$ from spectral analysis ($18.3 \pm 1.1\,{\rm km\,s^{-1}}$) and the adopted stellar radius from the combined analysis ($1.19 \pm 0.06\,{\rm R_\odot}$), we obtain an upper limit on the rotation period of WASP-180A, finding $P_{\rm rot} < 3.3$ days. This compares with the modulation period of $\sim 4.6$ days, implying that the signal does not originate from rotational modulation in WASP-180A.

The co-moving companion star WASP-180B contributes $\sim 30\%$ of the total flux, and so the true amplitude of the signal if originating from the secondary would be $\sim 1\%$,

Table 6.4: The results of the rotational modulation search of the WASP photometry of WASP-180. The strongest peak in the periodogram for the first set of data lies at $P_{\rm mod}/2$ (see Fig. 6.1). The additional peaks around 1–2 days are ascribed to a combination of harmonics of the rotation period and 1-day aliases.

| Dates (HJD–2450000) | No. pts | Period (days) | Amplitude (mag) | False Alarm Probability |
|---|---|---|---|---|
| 5155–5272 | 3660 | 2.28 | 0.004 | 0.064 |
| 5520–5623 | 3744 | 4.68 | 0.003 | 0.099 |
| 5899–6018 | 3171 | 4.53 | 0.004 | $<0.001$ |

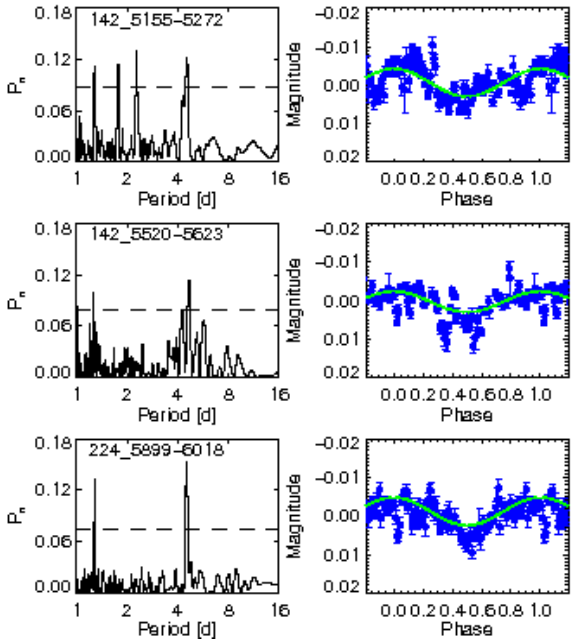


Figure 6.1: Results of the rotational modulation search of the WASP photometry of WASP-180. The three rows show the periodogram (left) and phase-folded light curve (right) for each chunk of data, displayed in the same order as they are listed in Table 6.4. The horizontal dashed line in each of the periodograms corresponds to a confidence level of 99%.

which is consistent with spot modulation on a fast-rotating later-type star. *Gaia* DR2 does not find any other close neighbours which may contribute to the total flux. Thus we believe the signal to belong to the visual companion star, which has a temperature

of $5430^{+30}_{-25}$ K. A rotation period of 4.6 days is fairly rapid for a star of $T_{\rm eff} = 5430^{+30}_{-25}$ K, which may imply a young age for the system, consistent with our BAGEMASS analysis in Section 6.6.

## 6.5 Combined MCMC analysis

We use an MCMC approach to fit the combined photometric and radial velocity data, as well as investigate the RM effect. We follow methods very similar to Temple et al. (2018) and Temple et al. (2019a), whereby we conduct both an RM analysis and a tomographic analysis and adopt the better-constrained solution. The RM analysis involves detecting the line-profile distortions as an apparent overall shift in radial velocity measurements (e.g, Triaud 2017), whereas the tomographic analysis requires one to directly map the motion of the distortion caused by the occulting body across the line profiles as a function of phase (e.g, Brown et al. 2017; Temple et al. 2017).

The code we use is described by Collier Cameron et al. (2007, Pollacco et al. (2008, Collier Cameron et al. (2010a). The combined photometric and RV fitting determines $P$, $T_{\rm c}$, $(R_{\rm p}/R_\star)^2$, $T_{14}$, $b$, $K_1$ and $\gamma$. We use the value of $T_{\rm eff}$ obtained in the dilution correction as input, and interpolate four-parameter limb darkening coefficients from the Claret (2000, Claret (2004) tables in each step using the current value of $T_{\rm eff}$. We use the stellar radius obtained in Sec. 6.4.2 ($1.17 \pm 0.08 R_\odot$) as a prior to constrain stellar parameters. In the fit we present we have assumed that the orbit is circular, as one would expect a hot Jupiter to circularise on a timescale shorter than its lifetime (Pont et al. 2011). However, a further fit was carried out to test this assumption, leading to an upper limit of $e < 0.27$ (95% confidence). We display the photometry and best-fit transit model in Fig. 6.2.

The RM fit and Doppler tomography give values for $v \sin i_\star$, $\lambda$ and the system $\gamma$-velocity. We use the calibrations of Hirano et al. (2011) to fit the RM effect. For Doppler tomography, we assume a Gaussian profile for the perturbation to the stellar-line profiles and fit the intrinsic Full-Width at Half-Maximum (FWHM) of the per-

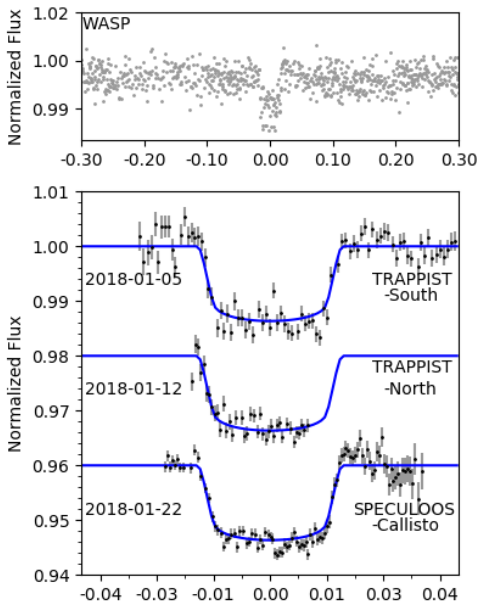


Figure 6.2: The WASP discovery photometry (top) and follow-up transit lightcurves (bottom) with the best-fitting model shown in blue. (see Section 6.5). The data for the three follow-up lightcurves, prior to the dilution correction, are available online as supporting material.

turbation, $v_{\rm FWHM}$. Both methods also provide an additional constraint on the impact parameter $b$, although the tomographic method fits this quantity more directly. We estimate the start value for $\gamma$ by fitting a Gaussian profile to the CCFs. We also apply the spectral $v \sin i_\star$ as a prior in both fitting modes.

We find that the tomographic method was better able to constrain $v \sin i_\star$ and $\lambda$. In the RM fit, the value of $v \sin i_\star$ was less constrained, even when using the spectral $v \sin i_\star$ as a prior. Thus we adopt the solution to the fit including Doppler tomography. We give the solutions for both methods in Table 6.5. The RV measurements used in this analysis and the best-fit RV and RM models are displayed in Fig. 6.3.

Figure 6.4 shows the tomographic dataset used in this analysis. We have subtracted an average of the out-of-transit CCFs in the dataset from each CCF in order to display the residual bump due to the planet transit. The planet signal is strong and

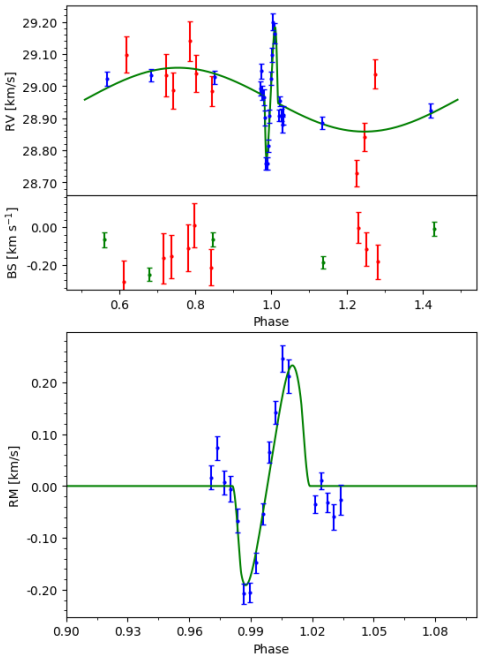


Figure 6.3: Top: All RV measurements of WASP-180A used in this work together with the best-fit model shown in green. The red points are CORALIE measurements and the blue points are HARPS measurements. Middle: the bisector (BS) measurements corresponding to the RVs in the top panel. Bottom: The RV measurements taken during transit and best-fit RM model.

clear, moving in a retrograde direction. Due to excluding three of the CCFs (having low signal-to-noise) we are missing the transit egress. We also show the simultaneous photometric observation in Fig. 6.4 and a residuals plot produced by subtracting the planet model from the tomographic data.

Table 6.5: All system parameters obtained for WASP-180 in this work. The quantities marked with * were used as priors in the combined MCMC analysis described in Section 6.5.

| | | | |
|---|---|---|---|
| *Stellar system* | | | |
| WASP-180A aliases: | 1SWASP J081334.15–015857.9 | 2MASS 08133416–0158579 | TIC ID:178367144 |
| WASP-180A Coordinates: | RA = $08^h13^m34.15^s$ Dec = $-01°58'57.9''$ (J2000) | | |
| Magnitude measurements: | | | |
| | WASP-180A | | WASP-180B |
| $B$ (ucac4rpm) | 11.221 ± 0.3 | | 12.732 ± 0.3 |
| $V$ (ucac4rpm) | 10.682 ± 0.3 | | 12.041 ± 0.3 |
| $g'$ (Pan-STARRS) | 10.96 ± 0.3 | | 12.336 ± 0.3 |
| $r'$ (Pan-STARRS) | 10.791 ± 0.3 | | 11.887 ± 0.3 |
| $i'$ (Pan-STARRS) | 10.786 ± 0.3 | | 11.713 ± 0.3 |
| $z'$ (Pan-STARRS) | 10.836 ± 0.3 | | 11.637 ± 0.3 |
| $G$ (Gaia DR2) | 10.9134 ± 0.0007 | | 11.7712 ± 0.0008 |
| $J$ (2MASS) | 10.11 ± 0.05 | | 10.68 ± 0.03 |
| *SED analysis* | | | |
| $T_{\rm eff}$ | $6540^{+80}_{-30}$ K* | | $5430^{+30}_{-25}$ K |
| [Fe/H] | $0.0^{+0.1}_{-0.5}$ | | $0.0^{+0.1}_{-0.5}$ |
| *IRFM, distance and proper motions* | | | |
| $T_{\rm eff}$ | 6530 ± 190 K | | 5450 ± 130 K |
| $\theta$ | 0.040 ± 0.002 mas | | 0.038 ± 0.004 mas |
| *Gaia* DR2 Proper Motions: | | | |
| RA | $-14.05 \pm 0.09$ mas yr$^{-1}$ | | $-12.7 \pm 0.2$ mas yr$^{-1}$ |
| DEC | $-3.17 \pm 0.06$ mas yr$^{-1}$ | | $-2.7 \pm 0.1$ mas yr$^{-1}$ |
| *Gaia* DR2 Parallax | 3.909 ± 0.052 mas | | 3.862 ± 0.073 mas |
| $R_\star$ | $1.17 \pm 0.08 R_\odot$* | | $1.07 \pm 0.06 R_\odot$ |
| *Stellar parameters of WASP-180A from spectral analysis:* | | | |
| Parameter (Unit) | Value | Parameter (Unit) | Value |
| $T_{\rm eff}$ (K) | 6500 ± 150 | $v \sin i_\star$ (km s$^{-1}$) | 18.3 ± 1.1* |
| $\log g_\star$ | 4.5 ± 0.2 | [Fe/H] | 0.09 ± 0.19 |
| $v_{\rm mac}$ | 5.8 | Spectral type | F7 V |
| $v_{\rm mic}$ | 1.5 | | - |

*Parameters from combined analyses:*

| Parameter (Unit) | DT Value (adopted): | RM Value: | Parameter (Unit) | DT Value (adopted): | RM Value: |
|---|---|---|---|---|---|
| $P$ (d) | 3.409264 ± 0.000001 | 3.409265 ± 0.000001 | $T_{\rm eff}$ (K) | 6600 ± 200 | 6600 ± 100 |
| $T_{\rm c}$ ($\rm BJD_{TDB}$) | 2457763.3150 ± 0.0001 | 2457763.3148 ± 0.0003 | [Fe/H] | 0.1 ± 0.2 | 0.1 ± 0.2 |
| $T_{14}$ (d) | 0.1299 ± 0.0004 | 0.1285 ± 0.0009 | $M_{\rm P}$ ($M_{\rm Jup}$) | 0.9 ± 0.1 | 0.9 ± 0.2 |
| $T_{12} = T_{34}$ (d) | 0.0141 ± 0.0002 | 0.0145 ± 0.0008 | $R_{\rm P}$ ($R_{\rm Jup}$) | 1.24 ± 0.04 | 1.28 ± 0.09 |
| $R_{\rm P}^2/R_*^2$ | 0.0123 ± 0.0002 | 0.0125 ± 0.0002 | $\log g_{\rm P}$ (cgs) | 3.12 ± 0.05 | 3.10 ± 0.06 |
| $b$ | 0.29 ± 0.02 | 0.34 ± 0.06 | $\rho_{\rm P}$ ($\rho_{\rm J}$) | 0.46 ± 0.05 | 0.43 ± 0.07 |
| $i$ (°) | 88.1 ± 0.1 | 87.8 ± 0.4 | $K_1$ (km s$^{-1}$) | 0.10 ± 0.01 | 0.10 ± 0.01 |
| $a$ (AU) | 0.048 ± 0.001 | 0.049 ± 0.004 | $T_{\rm eql}$ (K) | 1540 ± 40 | 1560 ± 40 |
| $M_*$ ($M_\odot$) | 1.3 ± 0.1 | 1.3 ± 0.3 | $v \sin i_\star$ (km s$^{-1}$) | 19.9 ± 0.6 | 20.8 ± 1.5 |
| $R_*$ ($R_\odot$) | 1.19 ± 0.06 | 1.17 ± 0.08 | $\lambda$ (°) | –157 ± 2 | –162 ± 5 |
| $\log g_\star$ (cgs) | 4.42 ± 0.01 | 4.42 ± 0.04 | $\gamma$ (km s$^{-1}$) | 28.9 ± 0.1 | 29.0 ± 0.1 |
| $\rho_*$ ($\rho_\odot$) | 0.83 ± 0.01 | 0.82 ± 0.06 | $v_{\rm FWHM}$ (km s$^{-1}$) | 7.9 ± 0.2 | – |

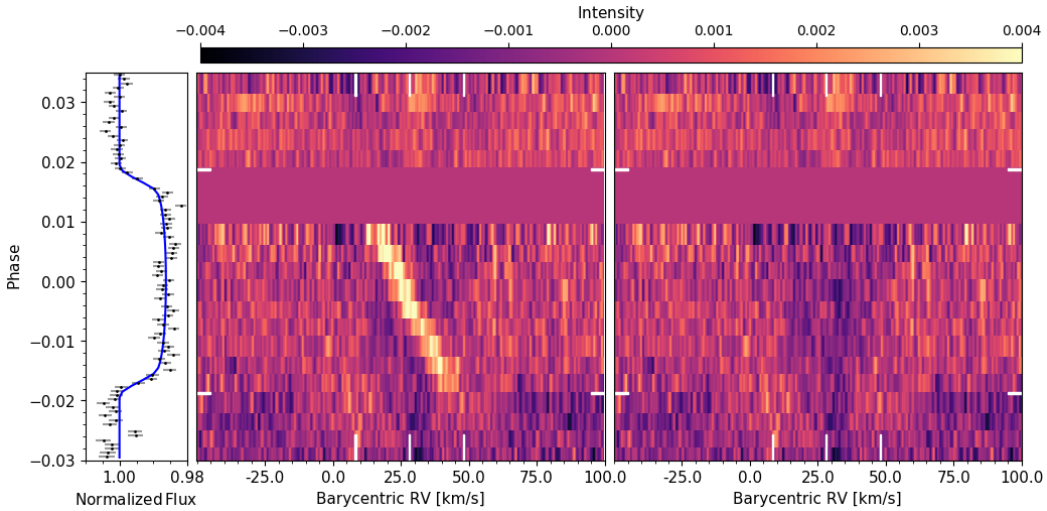


Figure 6.4: The Doppler tomogram for WASP-180Ab, showing the strong retrograde planet trace (middle) and simultaneous photometric observation alongside (left). The right-hand panel shows the residuals remaining after subtracting the fit to the perturbation due to the planet (see Section 6.5). The white vertical dashes in the centre and right-hand panels mark the positions of $\gamma$ and $\gamma \pm v \sin i_\star$ while the white horizontal dashes indicate the times of 1$^{\rm st}$ and 4th contacts of the planet.

## 6.6 System age determination

We used the open source software BAGEMASS[1] to determine the age of the system following a Bayesian approach as described by Maxted, Serenelli & Southworth (2015). BAGEMASS takes constraints on the stellar temperature, density and metallicity to fit the age, mass and initial metallicity of a star using the GARSTEC stellar evolution code (Weiss & Schlattl 2008). We set $T_{\rm eff} = 6500 \pm 150$ K and $[{\rm Fe/H}] = 0.09 \pm 0.19$ (from spectral analysis) and $\rho_*/\rho_\odot = 0.83 \pm 0.01$ (from photometry), and use different combinations of mixing lengths and He abundances. We find that the best-fitting parameter set was obtained when using a solar He abundance and mixing length, and thus adopt that solution. We give this solution in Table 6.6 while displaying the evolutionary

[1]Available at: http://sourceforge.net/projects/bagemass

tracks, isochrones and the distribution of explored values for this fit in Fig. 6.5.

We find WASP-180A to be consistent with being on the main sequence, with an age of $1.2 \pm 1.0$ Gyr. From the best-fit evolutionary tracks we determine that the expected main sequence lifetime of the star, taken to be the point at which WASP-180A has depleted all hydrogen in the core, is $4.17^{+0.09}_{-0.71}$ Gyr.

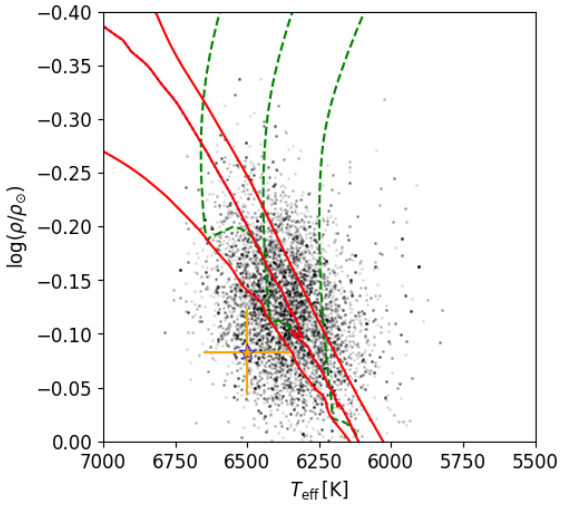


Figure 6.5: The best fitting evolutionary tracks and isochrones of WASP-180A obtained using BAGEMASS. Black points: individual steps in the MCMC. Green dashed lines: evolutionary track for the best-fit [Fe/H] and mass, plus $1\sigma$ bounds. The Red lines: isochrone for the best-fit [Fe/H] and age, plus $1\sigma$ bounds. The lower bound isochrone is also the Zero-Age Main Sequence (ZAMS) at best-fit [Fe/H]. Orange star: measured values of $T_{\rm eff}$ and $\rho_*$ for WASP-180A obtained in the spectral and photometric analyses respectively.

We also extract stellar isochrones from Marigo et al. (2017) for stellar ages in the range $10^8$–$5\times10^9$ yr, using the metallicity from spectral analysis ([Fe/H] $\sim 0.09$) to estimate appropriate mass fractions, obtaining $Z = 0.024$ and $Y = 0.27$. These are displayed on a colour–magnitude diagram in Fig. 6.6 along with the positions of WASP-180A and WASP-180B. The position of WASP-180A implies a system age of 1 Gyr while the position of WASP-180B implies an age close to 3 Gyr, although both are unconstrained by this method. These ages would imply approximate stellar masses of

Table 6.6: Results for the masses of WASP-180A and WASP-180B, and the age of the system.

| *Parameters from* BAGEMASS*:* | |
|---|---|
| Parameter (Unit) | Value |
| Age | 1.22 ± 0.99 |
| $M_{\star,A}$ ($M_\odot$) | 1.18 ± 0.08 |
| $[\mathrm{Fe/H}]_{\mathrm{init}}$ | –0.06 ± 0.16 |
| *Parameters from stellar isochrones:* | |
| $M_{\star,A}$ ($M_\odot$) | 1.3 |
| $M_{\star,B}$ ($M_\odot$) | 1.0 |

1.3 $M_\star$ and 1.0 $M_\star$ respectively, leading to a mass ratio of $M_{\star,B}/M_{\star,A} \approx 0.77$.

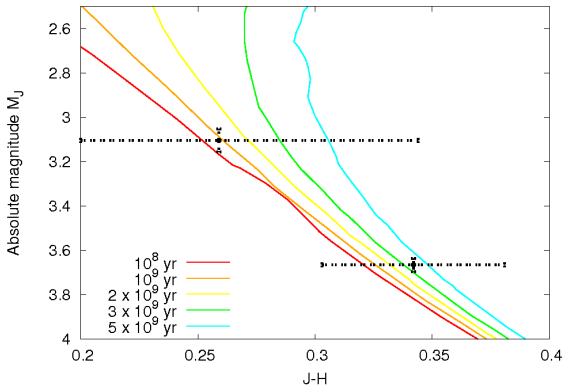


Figure 6.6: A colour-magnitude diagram showing the positions of WASP-180A and its comoving companion star with respect to isochrones from Marigo et al. (2017) for the ages 0.1, 1, 2, 3 and 5 Gyr (Z = 0.024 ∼ [Fe/H] = 0.09, Y=0.27).

## 6.7 Conclusions and discussion

WASP-180Ab is a $0.9 \pm 0.1\,M_{\mathrm{Jup}}$, $1.24 \pm 0.04\,M_{\mathrm{Jup}}$ hot Jupiter orbiting an F7 V star with $T_{\mathrm{eff}} = 6500\,\mathrm{K}$ and $v \sin i_\star = 19.9\,\mathrm{km\,s^{-1}}$. The planet's large radius is in line with

the expectation for a Jovian-mass planet in a close orbit around a fairly hot star to be inflated due to the high level of irradiation (e.g, Enoch, Collier Cameron & Horne 2012; Sestovic, Demory & Queloz 2018).

The orbit is misaligned and retrograde, with a projected obliquity of $\lambda = -157 \pm 2\,^{\circ}$. This is also in line with known trends amongst hot Jupiters orbiting hot stars, since the majority of such planets are found to be in misaligned orbits (e.g, Winn et al. 2010; Albrecht et al. 2012; Dai & Winn 2017; Triaud 2017).

WASP-180 is a known binary system. We can ask whether the secondary, WASP-180B, is responsible for the retrograde, misaligned orbit seen in WASP-180Ab. It has long been theorized that a distant stellar companion can induce Lidov-Kozai oscillations in a Jupiter's orbit, leading to high-eccentricity migration of the planet which produces a misaligned, short-period orbit. This would then be followed by realignment of the host star with the planet's orbit via tidal dissipation, an effect that would be less efficient for stellar hosts lacking convective envelopes, and thus this theory is consistent with the observed tendency of systems with stars hotter than $\sim 6250\,\mathrm{K}$ being more likely to have planetary orbits which are misaligned with respect to the stellar rotation axis (Winn et al. 2010; Albrecht et al. 2012).

While the Lidov-Kozai effect has long been thought able to produce oblique orbits, the pathways leading from high-eccentricity migration to the observed distribution of system obliquities are still a topic of avid research (e.g, Anderson, Storch & Lai 2016; Storch, Lai & Anderson 2017). Anderson, Storch & Lai (2016) places an upper limit on the final period of a hot Jupiter which has migrated due to Lidov-Kozai oscillations of $P_{\mathrm{orb}} < 4\,\mathrm{days}$, while Petrovich (2015) finds that the stellar separations of binaries with hot Jupiters are preferentially in the range 400–1500 AU, and so with $P_{\mathrm{orb}} = 3.4\,\mathrm{days}$ and an estimated stellar separation of 1200 AU it is feasible for WASP-180Ab to have formed in this way. Anderson, Storch & Lai (2016) also finds that the expected timescale required for the migration of a hot Jupiter of $1\,\mathrm{M_{Jup}}$ via Lidov-Kozai oscillations is in the range $\sim$0.5–5 Gyr, with lower mass planets taking longer to migrate. The system age of $1.2 \pm 1.0\,\mathrm{Gyr}$ is consistent with being within this range. It is possible that some eccentricity could remain, however, and our measured upper

limit of $e < 0.27$ at 95% confidence implies a possibly eccentric, but likely near circular orbit.

WASP-180Ab has $T_{\rm eff} = 6500\,{\rm K}$ and $v \sin i_\star = 19.9 \pm 0.6\,{\rm km\,s^{-1}}$. Other examples of HJs in multiple-star systems with early type hosts are MASCARA-4b ($T_{\rm eff} = 7800\,{\rm K}$ and $v \sin i_\star = 46.5$; Dorval et al. 2019) and KELT-19Ab ($T_{\rm eff} = 7500\,{\rm K}$ and $v \sin i_\star = 84 \pm 2\,{\rm km\,s^{-1}}$; Siverd et al. 2018). Both MASCARA-4b and KELT-19Ab have retrograde orbits, with measured obliquities of $\lambda = 247.5°$ and $\lambda = -179°$ respectively. KELT-19Ab is also similar to WASP-180Ab in that the primary and secondary stars in the system are of similar brightness. Evans et al. (2018) show that there is a dearth of planets in wide binary systems with stars of similar mass, though this is likely in part due to selection bias: in systems with stars of similar mass and thus brightness, as in the case of WASP-180, the light from the planet hosting star is significantly diluted in the light of the other star, reducing the apparent transit depth and making detection via the transit method more difficult. Other examples include K2-29b (Santerne et al. 2016) and HAT-P-20b (Bakos et al. 2011).

Also, Ngo et al. (2015, Piskorz et al. (2015, Ngo et al. (2016) studied known exoplanet systems with FGK host stars, searching for previously unseen stellar companions and attempting to find a correlation between the presence of a distant stellar companion and the measured obliquity and eccentricity of a hot Jupiter's orbit. They find no evidence of such a trend and conclude that, although a significant fraction of hot Jupiters reside in wide binary systems, fewer than 20% of hot Jupiters could have ended up in their current orbits as a result of Lidov-Kozai oscillations. Although both KELT-19Ab and WASP-180Ab are in misaligned, retrograde orbits, this is not necessarily related to the fact that they are in binary systems, since the tendency for hot Jupiters orbiting hot stars to be misaligned is well established (Winn et al. 2010; Albrecht et al. 2012).

# 7 Tomographic non-detections of exoplanet candidates

Of the 10 candidates for which tomographic datasets were successfully obtained (listed in Sec. 2.2), 4 did not show evidence of a planetary origin for the transit signal. This Chapter summarises the follow-up campaigns for the 4 tomographic non-detections.

### 7.0.1 Candidate SW0551

SW0551 has a host star with an IRFM temperature of $7090 \pm 150$ K, implying a spectral type of A9–A8. The WASP data contained a transit-like signal with a period of 1.55 d and a depth of 0.7%. The candidate was initially followed up with 4 RV measurements and a (partial) transit lightcurve taken on the night of 2013-10-27 with a blue-blocking filter. The RVs showed no motion $> 500\,\mathrm{m\,s^{-1}}$ and the cross-correlation functions indicated a projected rotational velocity of $v \sin i_\star \sim 70\,\mathrm{km\,s^{-1}}$. The transit observation was timed as predicted with the ephemeris obtained by analysing the WASP data and the transit depth was measured at $\sim 0.5\,\%$. SW0551 was thus selected for tomographic follow up.

Candidate SW0551 was observed with HARPS on the night of 2016-01-02, leading to the collection of 24 CCFs including a transit. The tomogram, constructed by subtracting the mean of the out-of-transit CCFs from all CCFs and plotting the result as a function of phase, is displayed in Figure 7.1. No evidence of a planet trace is seen. A series of short MCMC runs were carried out in an attempt to search for very faint signals, wherein a solution could be considered valid if it were reproducible in independent runs and if the fitted values of $(R_\mathrm{p}/R_\star)$ and $b$ were consistent with those obtained from photometry alone, to within $1\sigma$. No such solution was found, making this target a likely BEB. This conclusion was later supported by a second photometric transit observation on the night of 2016-10-11 in the $z'$ band, which had a measured depth of $\sim 1\,\%$. The colour-dependence of the transit depth indicates a stellar origin

for the signal.

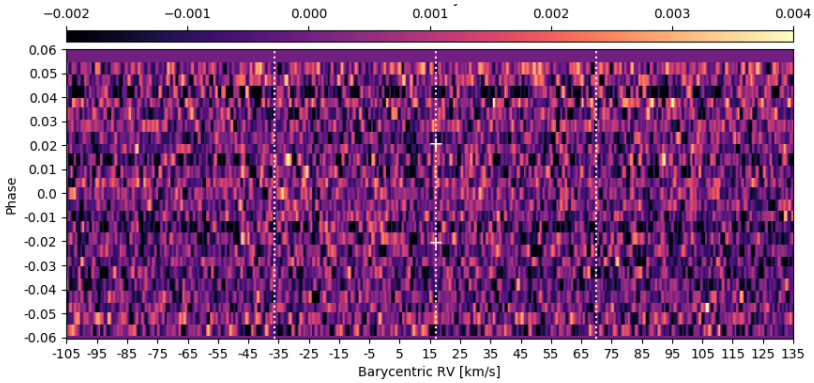


Figure 7.1: The tomogram taken on the night of 2016-01-02 of SW0551. The expected transit start and end phases are marked with white crosses. The white vertical dotted lines show the positions of the $\gamma$-velocity of the system and $\gamma \pm v_\star \sin i$.

### 7.0.2 Candidate SW0647

SW0647 has a host star with an IRFM temperature of $6390 \pm 140$ K, implying a spectral type of F4–F5. A transit signal was detected in the WASP data, having a period of 1.12 d and a depth of 0.3%. A follow-up partial) transit lightcurve was obtained on the night of 2014-02-22 using a blue-blocking filter, which showed a consistent transit depth of $\sim 0.4$ %. A tomographic observation was taken on the night of 15/01/2016 comprising 17 CCFs. The (mean-subtracted) tomogram is displayed in Figure 7.2 and shows no evidence of a planet. The target is likely a BEB. Again, another lightcurve was taken using a $z'$ filter on the night of 2016-11-10. The measured depth was $\sim 0.5$ %.

### 7.0.3 Candidate SW0623

SW0623 has a host star with an IRFM temperature of $5940 \pm 140$ K implying a spectral type of G0–F8. The WASP data revealed a transit signal with an ultra-short period of 0.84 d and a depth of 1.3%. The transit was confirmed via with an observation on the

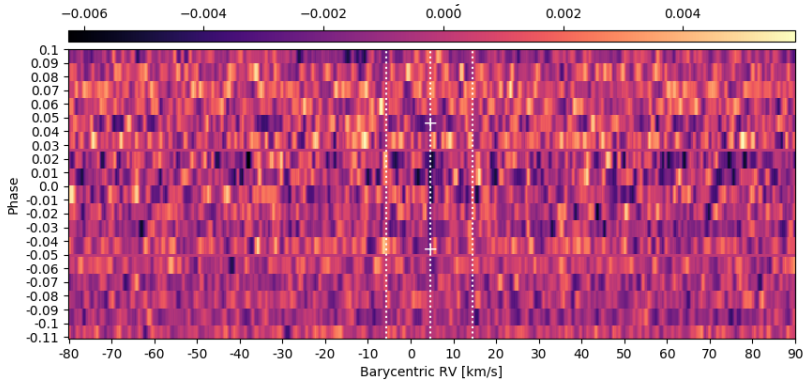


Figure 7.2: The tomogram taken on the night of 2016-01-15 of SW0647. The expected transit start and end phases are marked with white crosses. The white vertical dotted lines show the positions of the $\gamma$-velocity of the system and $\gamma \pm v_\star \sin i$.

night of 2014-11-04 using a $z'$ filter. This was followed up with 6 RV measurements and the collection of a tomographic dataset on the night of 30/10/2017, comprising 15 CCFs. The RVs were consistent with no orbital motion $> 40\,\mathrm{m\,s^{-1}}$ and the tomogram (Fig. 7.3) showed no evidence of a planet, making this target a likely BEB.

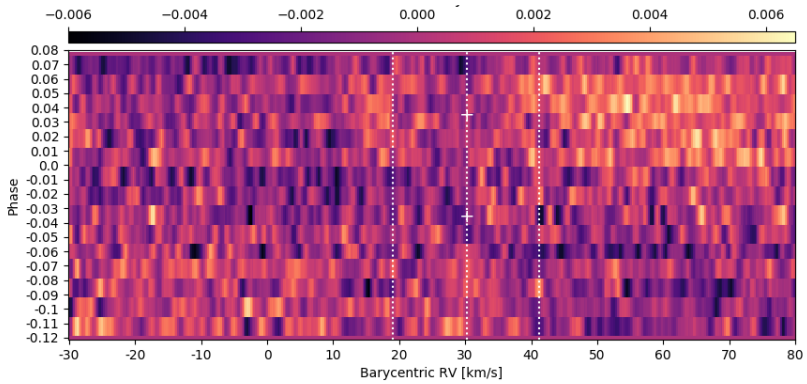


Figure 7.3: The tomogram taken on the night of 2017-10-30 of SW0623. The expected transit start and end phases are marked with white crosses. The white vertical dotted lines show the positions of the $\gamma$-velocity of the system and $\gamma \pm v_\star \sin i$.

### 7.0.4 Candidate SW0025

SW0025 has a host star with an IRFM temperature of $6240 \pm 270$ K implying a spectral type of F6–F7. The analysis of WASP data measured a transit-like signal with a period of 2.3 d and a depth of 1.0%. 4 CORALIE spectra were taken, showing no motion $> 2\,\mathrm{km\,s^{-1}}$. The candidate was subsequently observed with HARPS on the night of 28/10/2017 leading to the collection of 20 CCFs. The minimum-subtracted tomogram is displayed in Figure 7.3. No evidence of a planet trace is seen. This target was later entered in the KELT False Positives catalogue as a nearby BEB, placing the eclipse on a companion star at $6''$ separation (Collins et al. 2018). Interestingly, the tomogram contains evidence of stellar pulsations.

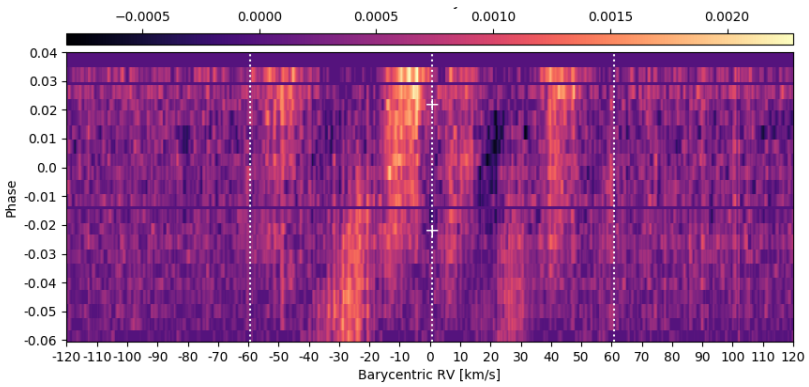


Figure 7.4: The tomogram taken on the night of 2017-10-28 data of SW0025. The expected transit start and end phases are marked with white crosses. The white vertical dotted lines show the positions of the $\gamma$-velocity of the system and $\gamma \pm v_\star \sin i$.

# 8 Discussion

In this work, the discovery of four new planets is reported: WASP-167b/KELT-13b, WASP-174b, WASP-190b and WASP-180b. These discoveries add to a small but growing sample of known planets with A–mid-F spectral type host stars: 17 out of the 21 planets that were discovered using Doppler tomography as a confirmation method were found in the last three years. This Chapter will put these planets into context, via comparison with the whole exoplanet population.

## 8.1 The known exoplanet population

Figure 8.1 displays the current known exoplanet population as a function of mass vs. period, colour-coded by discovery method. The figure clearly demonstrates the bias of the transit method towards shorter orbital periods, since the number of long period planets ($P > 10$ days) discovered by the transit method is significantly fewer than those found with the RV method.

There are three distinct groups within the mass-period diagram: low-mass rocky planets (bottom); short-period gas giants (top left) and giant planets with longer periods (top right). The planets presented in this work, and most of the planets confirmed via Doppler tomography, lie comfortably within the short-period gas-giant group. Although easy to detect, population studies involving Kepler data have revealed that hot Jupiters comprise only a small portion of the gas giant population, being $\sim$10 times less abundant than long-period giants when looking at FGK main-sequence stars (Laughlin 2018). As noted in Section 1.5, studies have also shown that the number of such planets with earlier host star spectral types are even rarer (e.g., Borgniet et al. 2017). A recent study of Kepler candidates with A-type stars by Sabotta et al. (2019) find that just 0.75 % of them host hot Jupiters.

In addition, low-mass rocky planets are much more prevalent than giant planets. The occurrence rate of planets with $\sim$1–4$R_{\mathrm{Earth}}$, periods less than 1 year and orbiting

FGK stars is ∼50%, while ∼10% of FGK stars host giant planets with periods less than a few years (Winn & Fabrycky 2015). Fig. 8.1 does not adequately demonstrate the lack of hot Jupiters with respect to rocky planets, since a large number of Kepler candidates, which have radii consistent with the low-mass group of planets but which do not have accurately measured masses, are not included.

As mentioned in Section 1.1, the population of short-period gas giants defied expectations when they were first discovered, since it was theorised that giants could only form at greater distances from their stars (due to the stratification of material in the protoplanetary disc). Now it is considered likely that they did indeed form at larger distances, but then migrated through some dynamical process, resulting in much shorter orbits (see Section 1.6.3).

Of note is the lack of planets with masses in the range 0.1–0.3 $M_{Jup}$, which has been noted in the past (e.g., Matsakos & Königl 2016) and is consistent with the core accretion model of planet formation, which allows planets to grow rapidly through this range via runaway gas accretion. There is also a lack of giant planets in the period range 10–100 days, a property of the mass-period diagram which is not so well understood. While it is possible that such planets would not be abundantly discovered via the transit method (due to the decreased transit probability), the same bias does not apply to the radial velocity method and thus it is clear that there are a dearth of such planets (Winn & Fabrycky 2015). This implies that the migration mechanisms behind the formation of hot Jupiters must favour periods shorter than 10 days.

Also consistent with the core accretion model of planet formation, is the apparent lack of low-mass planets at periods longer than ∼100 days. One can suppose that, should such planets exist, the longer period and smaller planetary radius would make them difficult to detect via the transit method, since they would be less likely to transit and would produce a smaller transit depth than a larger planet with the same host star size. Meanwhile, the longer period and smaller mass would result in a smaller RV semi-amplitude (recall eq. 1.10 in Section 1.4.1), thus biasing the RV method against finding such objects. Despite this, the RV method and the transit method have indeed been used in the discovery of a small number of low-mass planets with periods longer

than 100 days, and one might expect that, should there be an abundance of such objects, the Kepler space telescope would have revealed more owing to the high precision of Kepler data, the large number of stars surveyed and the length of the campaign. The longest period low-mass planets in Fig. 8.1 were found using the microlensing technique: OGLE-2005-BLG-390L b ($P = 3285^{+3285}_{-1095}$ days, $M_p = 0.017^{+0.017}_{-0.008}\,M_{Jup}$, Beaulieu et al. 2006) and MOA-2009-BLG-266L b ($P = 2774^{+2810.5}_{-547.5}$ days, $M_p = 0.033 \pm 0.005\,M_{Jup}$, Muraki et al. 2011).

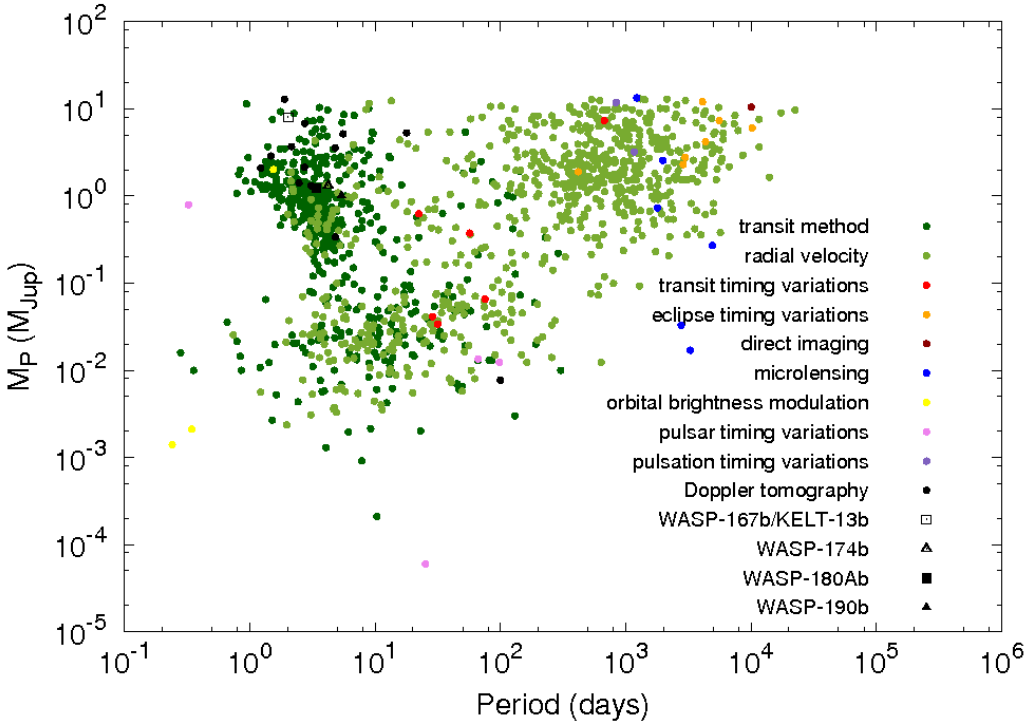


Figure 8.1: A mass-period diagram showing the known exoplanet population with masses below the deuterium-burning limit (13 $M_{Jup}$), as listed in the NASA exoplanet archive[1]. The colour of the points indicates the discovery method, with black marking those discovered via the transit method and confirmed using Doppler tomography. The positions of WASP-167b/KELT-13b, WASP-174b, WASP-190b and WASP-180b are indicated. With the exception of WASP-167b/KELT-13b and WASP-174b, which have only an upper limit for the mass and are thus displayed with an outline, only planets whose masses have been measured are included.

## 8.2 Mass-radius diagram

In the discussion section on WASP-190b, a plot of $M_{\rm p}$ as a function of $T_{\rm eql}$ was presented, which used $M_{\rm p}$ as an auxiliary axis (Fig. 5.5). The plot showed the positions of all gas giant planets in the mass range $0.6\,M_{\rm Jup} < M_{\rm p} < 4.0\,M_{\rm Jup}$ as listed in the TEPCat database (Southworth 2011). This was to demonstrate that gas giants can have a wide range of radii for a given mass and equilibrium temperature. Fig. 8.2 now shows $R_{\rm p}$ vs. $M_{\rm p}$ with $T_{\rm eql}$ as the auxiliary axis, for all known planets with mass measurements listed in the NASA exoplanet archive[1] (Akeson et al. 2013), along with WASP-167b/KELT-13b, WASP-174b, WASP-190b and WASP-180b.

Fig. 8.2 shows a number of interesting properties relating to the dependence of $R_{\rm p}$ on $M_{\rm p}$ and $T_{\rm eql}$. First, when considering the low-mass regime ($<0.6\,{\rm M_{Jup}}$) it is clear that $R_{\rm p}$ is strongly correlated with $M_{\rm p}$. There is not much dispersion compared to higher mass planets, nor a clear dependence on temperature. This is due to the fact that low-mass planets do not have extended gaseous envelopes, which can become inflated due to the injection of heat into the interior via stellar irradiation.

Second, moving towards higher masses leads to a weaker dependence of radius on mass, reflective of a move towards more gaseous bodies. A number of studies have tried to determine the breakpoint between 'small' planets, whose radii depend strongly on mass, and 'large' planets, whose radii are less strongly correlated with mass. A recent example is the work of Bashi et al. (2017), who used a sample of 274 planets with well-measured masses and radii (with uncertainties) spanning a broad range of masses. They suggest that the boundary between the small and large planets lies at $M_{\rm p} = 124 \pm 7\,{\rm M_{Earth}}$, $R_{\rm p} = 12.1 \pm 0.5\,{\rm R_{Earth}}$. For small planets they find $R \propto M^{0.55\pm0.02}$ and for large planets they find $R \propto M^{0.01\pm0.02}$. The much weaker dependence of radius on mass for large planets is attributed to the high abundance of H and He, leading to a stronger dependence on composition and the equations of state for light elements (e.g., Fortney, Marley & Barnes 2007), combined with greater

[1] Available at: https://exoplanetarchive.ipac.caltech.edu/

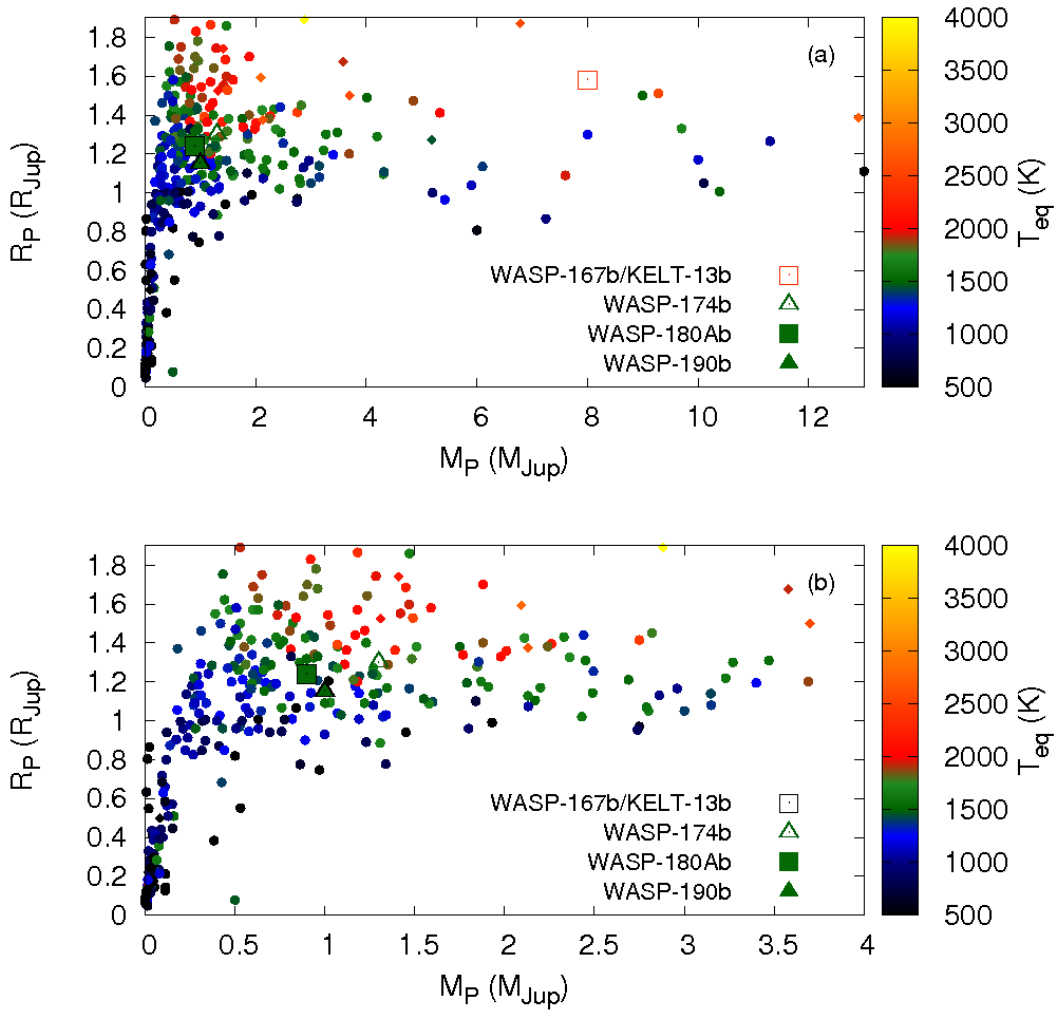


Figure 8.2: (a) A mass-radius diagram showing the known exoplanet population with masses below the deuterium-burning limit ($13\,M_{Jup}$), as listed in the NASA exoplanet archive[1]. (b) As for (a), but only showing masses up to $4\,M_{Jup}$. The colour of the points indicates the planetary equilibrium temperature. The positions of WASP-167b/KELT-13b, WASP-174b, WASP-190b and WASP-180b are indicated. With the exception of WASP-167b/KELT-13b and WASP-174b, which have only an upper limit for the mass and are thus displayed with an outline, only planets whose masses have been measured are included.

compression by a stronger gravitational field (e.g., Guillot 2005).

Third, higher mass planets also display a greater dispersion of radii than low

mass planets. Fig. 8.2 shows that the radii of planets $>0.6\,M_{Jup}$depend on temperature to some degree. Beyond $\sim$2 $M_{Jup}$ the planets are less significantly inflated than those in the range 0.6–2 $M_{Jup}$, which is likely due to more massive planets being more difficult to inflate due to having a stronger gravitational field, but they still display some dispersion. As discussed in Section 5.7, the large amount of dispersion in radii for a given mass and temperature is evidence of some additional underlying process, which inflates some planets beyond that expected due to stellar irradiation.

Of the planets presented in this work, WASP-167b/KELT-13b and WASP-180Ab are inflated. WASP-174b is possibly inflated with an uncertain radius, owing to the grazing nature of the transit. WASP-190b, meanwhile, is only moderately inflated. None of these planets are exceptionally inflated, however, and are in line with the observed distribution of exoplanet radii.

## 8.3 The distribution of obliquities

Of great interest to the exoplanet community is the distribution of projected spin-orbit misalignment angles ($\lambda$). Until recently, very few misalignment angles had been measured, but their relevance to planet formation and evolution models have lead astronomers to seek measurements for many known planets, and the measurement is now often made for new systems at discovery.

As has been discussed at length, the mechanisms behind the observed distribution of obliquities are not well understood (see Section 1.6.3, and the discussion sections in Chapters 3, 4, 5 and 6). Of particular interest is the apparent trend for planets with early type stars, such as those presented in this work, to be more often misaligned. Of the planets presented in this work, WASP-167b/KELT-13b and WASP-180Ab are in misaligned and retrograde orbits, WASP-174b is moderately misaligned and WASP-190b is marginally misaligned.

Fig. 8.3 shows $\lambda$ vs. $T_{\rm eff}$ for all planets with obliquity measurements listed in TEPCat (Southworth 2011). Fig. 8.4 then displays $\lambda$ as a function of semi-major axis

$a$, and Fig. 8.5 shows $\lambda$ as a function of $M_{\rm p}$.

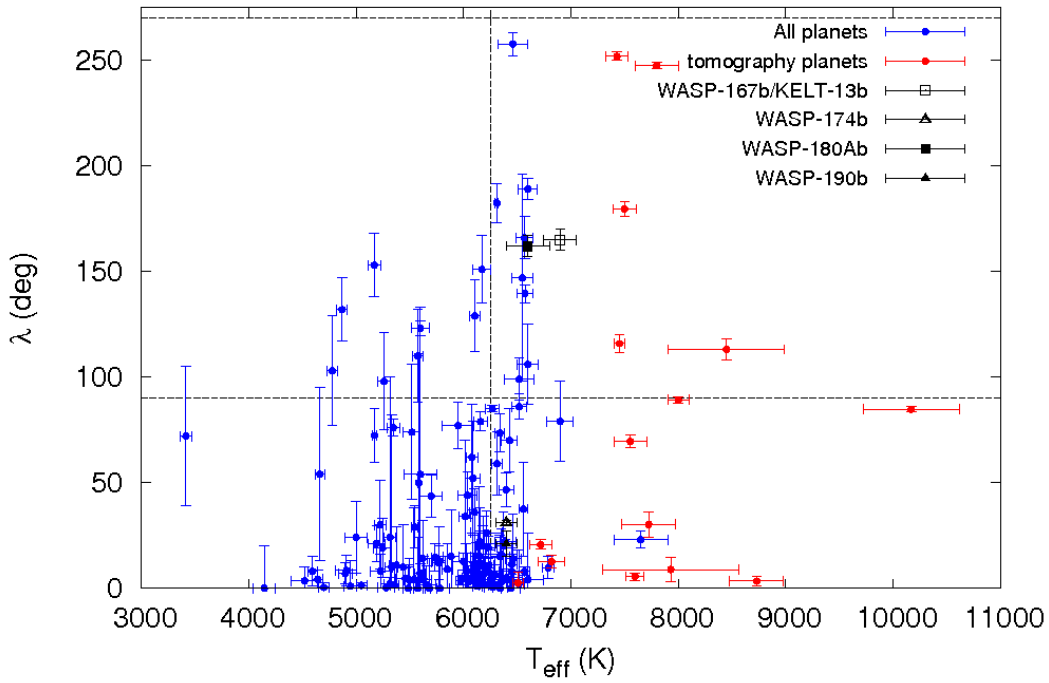


Figure 8.3: $\lambda$ vs. $T_{\rm eff}$ for all known planets with obliquity measurements listed in the TEPCat database. The positions of WASP-167b/KELT-13b, WASP-174b, WASP-190b and WASP-180Ab are marked. Red points indicate other systems which were confirmed via Doppler tomography. The vertical dashed line at $T_{\rm eff} = 6250\,{\rm K}$ marks the position of the Kraft break. The horizontal dashed lines mark $\lambda$ values of 90° and 270°, between which an orbit is considered to be retrograde.

Fig. 8.3 clearly demonstrates the tendency for systems beyond the Kraft break at $T_{\rm eff} = 6250\,{\rm K}$ to display a broad range of obliquities. Using the data extracted from TEPCat and adopting a tentative alignment threshold of $|\lambda| < 20°$, ∼65% of planets with stars of 6250 K or cooler are in aligned orbits. For stars hotter than 6250 K this drops to ∼40%, and for stars hotter than 6500 K the occurrence rate of aligned orbits is even lower at ∼16%. So far, there is no singularly accepted explanation for this trend, and studies attempting to consolidate theoretical migration mechanisms with the observed range in obliquities are ongoing (see Section 1.6.3).

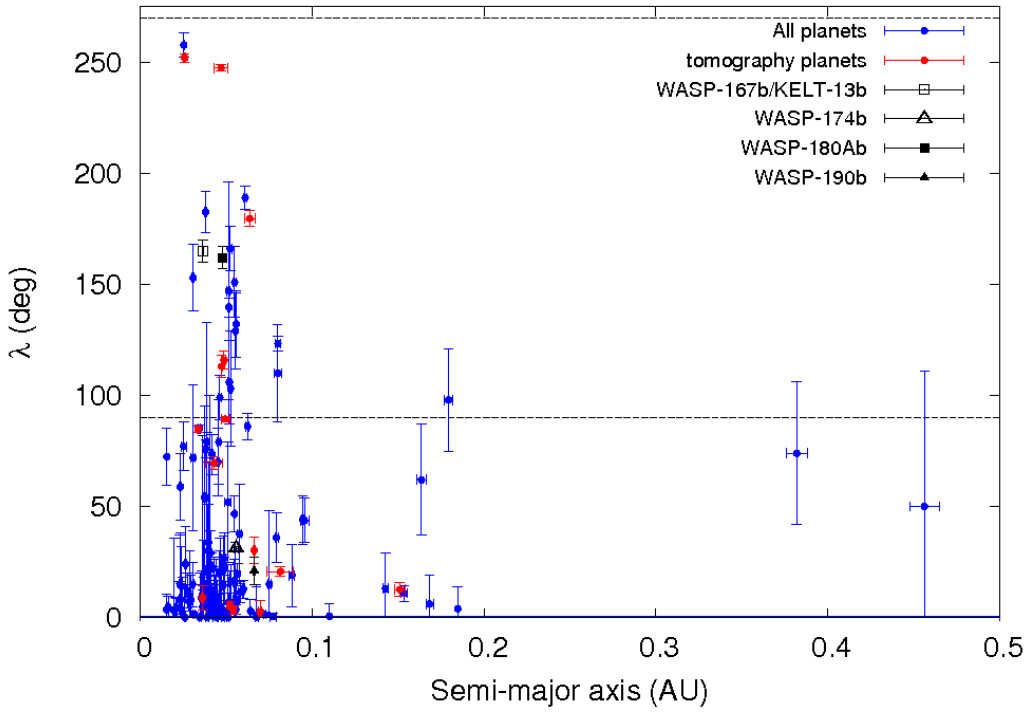


Figure 8.4: $\lambda$ vs. $a$ for all known planets with obliquity measurements listed in the TEPCat database. The positions of WASP-167b/KELT-13b, WASP-174b, WASP-190b and WASP-180Ab are marked. Red points indicate other systems which were confirmed via Doppler tomography. The horizontal dashed lines mark $\lambda$ values of 90° and 270°, between which and orbit is considered to be retrograde.

In support of theories surrounding the Lidov-Kozai effect being able to cause misalignment, WASP-180Ab has a retrograde orbit and a distant stellar companion, joining systems such as KELT-19Ab ($\lambda = -179°$) and MASCARA-4b ($|\lambda| = 247.5°$). However, with there being few known planets in binaries with obliquity measurements, and with the tendency for the planets of hotter stars to be more often misaligned, it is difficult to say whether the misalignment of the orbits of WASP-180Ab, KELT-19Ab and MASCARA-4b is related to the presence of stellar companions, or solely a consequence of them having early-type host stars.

In Section 6.7, the works of Knutson et al. (2014); Ngo et al. (2015); Piskorz et al. (2015) and Ngo et al. (2016) were discussed. Despite finding that $72\% \pm 16\%$

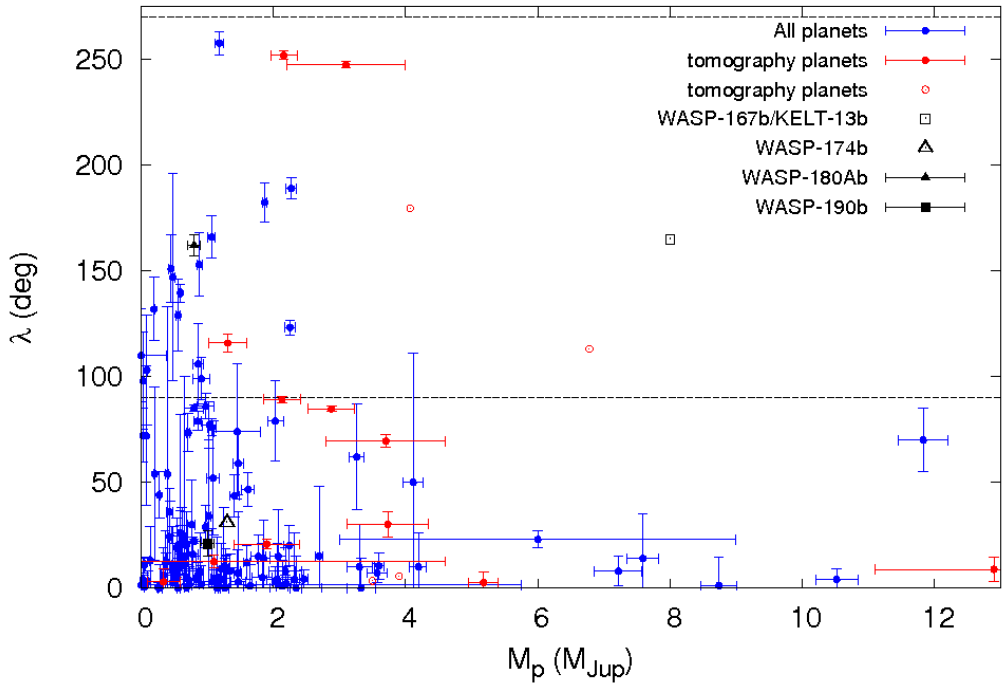


Figure 8.5: $\lambda$ vs. $M_{\rm p}$ for all known planets with obliquity and mass measurements listed in the TEPCat database. The positions of WASP-167b/KELT-13b, WASP-174b, WASP-190b and WASP-180Ab are marked. Red points indicate other systems which were confirmed via Doppler tomography. The tomography planets with only upper limits measured for the mass are shown as an outline. The horizontal dashed lines mark $\lambda$ values of 90° and 270°, between which and orbit is considered to be retrograde.

of hot Jupiters have planetary or stellar companions, with $47\% \pm 7\%$ having stellar companions at separations of 50–2000 AU, less than 20% of hot Jupiter orbits could have feasibly been produced by Lidov-Kozai oscillations. Additionally, a significant fraction of planets with early-type hosts have misaligned orbits but no known stellar companions. Torquing of a protoplanetary disc also requires a stellar companion or stellar fly-by, but other causes of high eccentricity migration include secular interactions and planet-planet scattering (Dawson & Johnson 2018). Planets with early-type stars that are aligned with respect to the stellar rotation may have migrated via tidal interactions with an aligned protoplanetary disc, or formed in situ (e.g., KELT-24b).

Fig. 8.4 and 8.5 demonstrate that there are a number of factors which may influence the alignment or misalignment of a planet's orbit. In Fig. 8.4, it appears that planets on shorter orbits are more often strongly misaligned or retrograde, though with limited measurements for planets beyond ∼0.1 AU it is difficult to make any conclusions about trends. In Fig. 8.5, it appears that planets with larger masses are less misaligned. This may be reflective of larger planets having stronger tidal interactions with their stars, leading to shorter realignment timescales. In any case, it seems that the reasons behind the misalignment of a planet's orbit are not clear-cut, and could depend on a number of system and planet properties.

## 8.4 Prospects for further characterisation

One of the biggest areas of exoplanetary research is that of atmospheric characterisation (see Section 1.6.1). Planets which have inflated gaseous envelopes and high day-side temperatures are favoured targets for such analyses. Although WASP-167b/KELT-13b is the hottest and most inflated planet presented in this work, it is not an ideal candidate for atmospheric characterisation due to the stellar pulsations of the planet host that were evidenced in the spectroscopic data (see Section 3.7.3). WASP-180Ab was also inflated, though not exceptionally so, and does not fall within the ultra-hot class of hot Jupiters ($R_{\rm p} = 1.24\,{\rm R_{Jup}}$, $T_{\rm eql} = 1540 \pm 40\,{\rm K}$). More ideal targets of such analysis include KELT-9b ($R_{\rm p} = 1.89\,{\rm R_{Jup}}$, $T_{\rm eql} = 4050\,{\rm K}$) and KELT-20b ($R_{\rm p} = 1.74\,{\rm R_{Jup}}$, $T_{\rm eql} = 2262 \pm 40\,{\rm K}$) , which also have the benefit of being bright systems with $V = 7.55$ and $V = 7.58$ respectively (Gaudi et al. 2017; Lund et al. 2017).

Further analysis of the pulsations seen in WASP-167/KELT-13 could be of use in determining whether or not the planet could be responsible for the observed pulsations. Similar suggestions have been made for other planets with pulsating host stars (see Section 3.7.3). From the analysis in Section 3.5 it is clear that HARPS is a suitable instrument for detecting the pulsations, but determining the type and mode of oscillation, as well as measuring the period and amplitude, would require a long baseline of

observations outside transit.

The strength of the planet signal in tomography for WASP-180Ab makes it a potential candidate for looking for differential rotation following the RM reloaded technique of Cegla et al. (2016a), through which the effects of differential rotation and the perturbation due to the planet can be disentangled. To bring out the effect of differential rotation on the spectroscopic transit more clearly, the higher spectral resolution and greater light collecting power of ESPRESSO on the VLT would be of use.

The RM reloaded technique of Cegla et al. (2016a) is also one way to measure the true obliquity of a planet's orbit. Understanding the range of true obliquities that planets can have would be important for models of planet formation and evolution. As an example, WASP-178b orbits a star with $T_{\rm eff} = 9350\,{\rm K}$, yet the projected stellar rotation rate is an order of magnitude lower than expected for a main sequence star of that type (Hellier et al. 2019a)). Thus the system must be inclined such that the star is seen almost pole-on, implying that the projected obliquity will also be very discrepant from the true obliquity, although $\lambda$ has not yet been measured for this system. Measuring the true obliquity of planets such as WASP-190b (with $\lambda = 21 \pm 6^{\circ}$) could be particularly useful, since it is near the boundary between aligned and misaligned planets.

WASP-174b is an interesting target, being faint and in a grazing orbit, but these properties also make it a difficult target for further characterisation. It would be of benefit to attempt to better constrain the planetary radius, which would require a very precise transit lightcurve. It would also be of use to determine the mass more accurately, which may be possible using more precise RV measurements taken out-of-transit using HARPS.

## 8.5 The future of exoplanet search

As we begin to fill the extremes of the exoplanet population, one may look ahead to the future of exoplanet study. The launch of TESS in 2018 is expected to supersede

the highly successful ground-based planet search projects, with early estimates of the occurrence rate of hot Jupiters measured from TESS data being consistent with that measured by Kepler, at $0.41 \pm 0.10\,\%$ (Zhou et al. 2019c). TESS will likely discover a large number of planetary candidates across a range of spectral types and planet size, and since it is optimised for a similar magnitude range to the ground-based missions, these candidates can then be followed up extensively, unlike many of those discovered by Kepler.

In the previous subsection, we discussed the possibility of utilising the higher spectral resolution and greater light collecting power of ESPRESSO on the VLT, in order to produce the SNR required to perform the more sophisticated analysis of Cegla et al. (2016a). These properties also make ESPRESSO the ideal choice for confirming some of the more challenging tomography candidates. Faint candidate systems would benefit from the greater light grasp, while those with cooler, more slowly rotating host stars require a higher spectral resolution in order to resolve the planet bump. It has been shown time and again that Doppler tomography provides a more accurate and precise method of constraining $v \sin i_\star$ and $\lambda$ than the more traditional RM technique. Therefore, being able to apply the tomographic method to confirming planets with later spectral types would lead to refinement of those parameters. Note, however, that the range of stellar spectral types for which tomography can be used as a confirmation method will also be limited by stellar macroturbulence. Another use of ESPRESSO could be in confirming planets on very short orbits, whose shorter transit duration would mean that the transit may not be very well sampled in time if using HARPS. The light grasp of the VLT would allow for shorter exposure times and thus better sampling of shorter transit events, again leading to a more precise determination of system properties.

December 2019 saw the launch of CHEOPS, a space-based photometric exoplanet follow-up mission whose goal is to constrain planetary radii and masses as precisely as possible, to reduce uncertainty in studies of planetary atmospheres (Rando et al. 2019; Futyan et al. 2020). And, looking further into the future, PLATO is expected to launch in 2026. It will search for planets around bright Sun-like stars with orbits up

to the habitable zone, and will also aim to provide highly accurate planetary masses and radii, as well as system ages (Ramos et al. 2019). Thus the prospects for future exoplanet search and characterisation are great.

# Publications

## Refereed

- Temple L. Y., Hellier C., Albrow M. D., Anderson D. R., Bayliss D., Beatty T. G., Bieryla A., Brown D. J. A., Cargile P. A., Collier Cameron A., Collins K. A., Colón K. D., Curtis I. A., D'Ago G., Delrez L., Eastman J., Gaudi B. S., Gillon M., Gregorio J., James D., Jehin E., Joner M. D., Kielkopf J. F., Kuhn R. B., Labadie-Bartz J., Latham D. W., Lendl M., Lund M. B., Malpas A. L., Maxted P. F. L., Myers G., Oberst T. E., Pepe F., Pepper J., Pollacco D., Queloz D., Rodriguez J. E., Ségransan D., Siverd R. J., Smalley B., Stassun K. G., Stevens D. J., Stockdale C., Tan T. G., Triaud A. H. M. J., Udry S., Villanueva S., West R. G., Zhou G., 2017, MNRAS, 471, 2743

- Temple L. Y., Hellier C., Almleaky Y., Anderson D. R., Bouchy F., Brown D. J. A., Burdanov A., Cameron C., Delrez L., Gillon M., Hall R., Jehin E., Lendl M., Maxted P. F. L., Nielsen L. D., Pepe F., Pollacco D., Queloz D., Ségransan D., Smalley B., Sohy S., Thompson S., Triaud A. H. M. J., Turner O. D., Udry S., West R. G., 2018, MNRAS, 480, 5307

- Temple L. Y., Hellier C., Almleaky Y., Anderson D. R., Bouchy F., Brown D. J. A., Burdanov A., Collier Cameron A., Delrez L., Gillon M., Jehin E., Lendl M., Maxted P. F. L., Murray C., Nielsen L. D., Pepe F., Pollacco D., Queloz D., Ségransan D., Smalley B., Thompson S., Triaud A. H. M. J., Turner O. D., Udry S., West R. G., 2019a, AJ, 157, 141

- Hellier C., Anderson D. R., Triaud A. H. M. J., Bouchy F., Burdanov A., Collier Cameron A., Delrez L., Ehrenreich D., Gillon M., Jehin E., Lendl M., Linder E., Nielsen L. D., Maxted P. F. L., Pepe F., Pollacco D., Queloz D., Ségransan D., Smalley B., Spake J. J., Temple L. Y., Udry S., West R. G., Wyttenbach A., 2019b, MNRAS, 488, 3067

- Temple L. Y., Hellier C., Anderson D. R., Barkaoui K., Bouchy F., Brown D. J. A., Burdanov A., Collier Cameron A., Delrez L., Ducrot E., Evans D., Gillon M., Jehin E., Lendl M., Maxted P. F. L., McCormac J., Murray C., Nielsen L. D., Pepe F., Pollacco D., Queloz D., Ségransan D., Smalley B., Thompson S., Triaud A. H. M. J., Turner O. D., Udry S., West R. G., Zouhair B., 2019b, MNRAS, 490(2), 2467

## Submitted

- Anderson D. R., Temple L. Y., Nielsen L. D., Burdanov A., Hellier C., Bouchy F., Brown D. J. A., Collier Cameron A., Gillon M., Jehin E., Maxted P. F. L., Pepe F., Pollacco D., Pozuelos F. J., Queloz D., Ségransan D., Smalley B., Triaud A. H. M. J., Turner O. D., Udry S., West R. G., 2018, ArXiv e-prints, 2018arXiv180904897A

# Bibliography

Adibekyan V., 2019, Geosciences, 9, 105

Aerts C., Christensen-Dalsgaard J., Kurtz D. W., 2010, Asteroseismology

Akeson R. L., Chen X., Ciardi D., Crane M., Good J., Harbut M., Jackson E., Kane S. R., Laity A. C., Leifer S., Lynn M., McElroy D. L., Papin M., Plavchan P., Ramírez S. V., Rey R., von Braun K., Wittman M., Abajian M., Ali B., Beichman C., Beekley A., Berriman G. B., Berukoff S., Bryden G., Chan B., Groom S., Lau C., Payne A. N., Regelson M., Saucedo M., Schmitz M., Stauffer J., Wyatt P., Zhang A., 2013, PASP, 125, 989

Akeson R. L., Christiansen J., Ciardi D. R., Ramirez S., Schlieder J., Van Eyken J. C., NASA Exoplanet Archive Team, 2017, American Astronomical Society Meeting Abstracts #229, American Astronomical Society Meeting Abstracts Vol. 229, p. 146.16

Albrecht S., Winn J. N., Johnson J. A., Butler R. P., Crane J. D., Shectman S. A., Thompson I. B., Narita N., Sato B., Hirano T., Enya K., Fischer D., 2011, ApJ, 738, 50

Albrecht S., Winn J. N., Johnson J. A., Howard A. W., Marcy G. W., Butler R. P., Arriagada P., Crane J. D., Shectman S. A., Thompson I. B., Hirano T., Bakos G., Hartman J. D., 2012, ApJ, 757, 18

Alonso R., Brown T. M., Charbonneau D., Dunham E. W., Belmonte J. A., Deeg H. J., Fernández J. M., Latham D. W., Mandushev G., O'Donovan F. T., Rabus M., Torres G., 2007, in Afonso C., Weldrake D., Henning T., eds, Transiting Extrapolar Planets Workshop, Astronomical Society of the Pacific Conference Series Vol. 366, p. 13

Anderson D. R., Collier Cameron A., Gillon M., Hellier C., Jehin E., Lendl M., Maxted P. F. L., Queloz D., Smalley B., Smith A. M. S., Triaud A. H. M. J., West R. G., Pepe F., Pollacco D., Ségransan D., Todd I., Udry S., 2012, MNRAS, 422, 1988

Anderson D. R., Temple L. Y., Nielsen L. D., Burdanov A., Hellier C., Bouchy F., Brown D. J. A., Collier Cameron A., Gillon M., Jehin E., Maxted P. F. L., Pepe F., Pollacco D., Pozuelos F. J., Queloz D., Ségransan D., Smalley B., Triaud A. H. M. J., Turner O. D., Udry S., West R. G., 2018, ArXiv e-prints

Anderson K. R., Storch N. I., Lai D., 2016, MNRAS, 456, 3671

Arcangeli J., Désert J.-M., Line M. R., Bean J. L., Parmentier V., Stevenson K. B., Kreidberg L., Fortney J. J., Mansfield M., Showman A. P., 2018, ApJL, 855, L30

Argelander F., Aufforderung an Freunde der Astronomie, zur Anstellung von eben so interessanten und nützlichen, als leicht auszuführenden Beobachtungen über mehrere wichtige Zweige der Himmelskunde, p. 122, 1844

Baglin A., Auvergne M., Barge P., Deleuil M., Catala C., Michel E., Weiss W., COROT Team, 2006, in Fridlund M., Baglin A., Lochard J., Conroy L., eds, The CoRoT Mission Pre-Launch Status - Stellar Seismology and Planet Finding, ESA Special Publication Vol. 1306, p. 33

Bagnuolo, Jr. W. G., Gies D. R., 1991, ApJ, 376, 266

Bakos G. Á., Hartman J., Torres G., Latham D. W., Kovács G., Noyes R. W., Fischer D. A., Johnson J. A., Marcy G. W., Howard A. W., Kipping D., Esquerdo G. A., Shporer A., Béky B., Buchhave L. A., Perumpilly G., Everett M., Sasselov D. D., Stefanik R. P., Lázár J., Papp I., Sári P., 2011, ApJ, 742, 116

Bakos G. Á., Csubry Z., Penev K., Bayliss D., Jordán A., Afonso C., Hartman J. D., Henning T., Kovács G., Noyes R. W., Béky B., Suc V., Csák B., Rabus M., Lázár J., Papp I., Sári P., Conroy P., Zhou G., Sackett P. D., Schmidt B., Mancini L., Sasselov D. D., Ueltzhoeffer K., 2013, PASP, 125, 154

Baranne A., Queloz D., Mayor M., Adrianzyk G., Knispel G., Kohler D., Lacroix D., Meunier J.-P., Rimbaud G., Vin A., 1996, A&AS, 119, 373

Barkaoui K., Gillon M., Benkhaldoun Z., Emmanuel J., Elhalkouj T., Daassou A., Burdanov A., Delrez L., 2017, Journal of Physics Conference Series, Journal of Physics Conference Series Vol. 869, p. 012073

Barkaoui K., Burdanov A., Hellier C., Gillon M., Smalley B., Maxted P. F. L., Lendl M., Triaud A. H. M. J., Anderson D. R., McCormac J., Jehin E., Almleaky Y., Armstrong D. J., Benkhaldoun Z., Bouchy F., Brown D. J. A., Cameron A. C., Daassou A., Delrez L., Ducrot E., Foxell E., Murray C., Nielsen L. D., Pepe F., Pollacco D., Pozuelos F. J., Queloz D., Segransan D., Udry S., Thompson S., West R. G., 2019, AJ, 157, 43

Baruteau C., Bai X., Mordasini C., Mollière P., 2016, SSRv, 205, 77

Baruteau C., Meru F., Paardekooper S.-J., 2011, MNRAS, 416, 1971

Bashi D., Helled R., Zucker S., Mordasini C., 2017, A&A, 604, A83

Batygin K., Bodenheimer P. H., Laughlin G. P., 2016, ApJ, 829, 114

Beatty T. G., Madhusudhan N., Tsiaras A., Zhao M., Gilliland R. L., Knutson H. A., Shporer A., Wright J. T., 2017, AJ, 154, 158

Beaulieu J.-P., Bennett D. P., Fouqué P., Williams A., Dominik M., Jørgensen U. G., Kubas D., Cassan A., Coutures C., Greenhill J., Hill K., Menzies J., Sackett P. D., Albrow M., Brillant S., Caldwell J. A. R., Calitz J. J., Cook K. H., Corrales E., Desort M., Dieters S., Dominis D., Donatowicz J., Hoffman M., Kane S., Marquette J.-B., Martin R., Meintjes P., Pollard K., Sahu K., Vinter C., Wambsganss J., Woller K., Horne K., Steele I., Bramich D. M., Burgdorf M., Snodgrass C., Bode M., Udalski A., Szymański M. K., Kubiak M., Więckowski T., Pietrzyński G., Soszyński I., Szewczyk O., Wyrzykowski Ł., Paczyński B., Abe F., Bond I. A., Britton T. R., Gilmore A. C., Hearnshaw J. B., Itow Y., Kamiya K., Kilmartin

P. M., Korpela A. V., Masuda K., Matsubara Y., Motomura M., Muraki Y., Nakamura S., Okada C., Ohnishi K., Rattenbury N. J., Sako T., Sato S., Sasaki M., Sekiguchi T., Sullivan D. J., Tristram P. J., Yock P. C. M., Yoshioka T., 2006, Nature, 439, 437

Bell T. J., Zhang M., Cubillos P. E., Dang L., Fossati L., Todorov K. O., Cowan N. B., Deming D., Zellem R. T., Stevenson K. B., Crossfield I. J. M., Dobbs-Dixon I., Fortney J. J., Knutson H. A., Line M. R., 2019, arXiv e-prints

Benedict G. F., McArthur B., Chappell D. W., Nelan E., Jefferys W. H., van Altena W., Lee J., Cornell D., Shelus P. J., Hemenway P. D., Franz O. G., Wasserman L. H., Duncombe R. L., Story D., Whipple A. L., Fredrick L. W., 1999, AJ, 118, 1086

Bennett D. P., Rhie S. H., 2002, ApJ, 574, 985

Bennett D. P., Anderson J., Bond I. A., Udalski A., Gould A., 2006, ApJL, 647, L171

Bertin E., Arnouts S., 1996, A&AS, 117, 393

Bieryla A., Hartman J. D., Bakos G. Á., Bhatti W., Kovács G., Boisse I., Latham D. W., Buchhave L. A., Csubry Z., Penev K., de Val-Borro M., Béky B., Falco E., Torres G., Noyes R. W., Berlind P., Calkins M. C., Esquerdo G. A., Lázár J., Papp I., Sári P., 2014, AJ, 147, 84

Bieryla A., Collins K., Beatty T. G., Eastman J., Siverd R. J., Pepper J., Gaudi B. S., Stassun K. G., Cañas C., Latham D. W., Buchhave L. A., Sanchis-Ojeda R., Winn J. N., Jensen E. L. N., Kielkopf J. F., McLeod K. K., Gregorio J., Colón K. D., Street R., Ross R., Penny M., Mellon S. N., Oberst T. E., Fulton B. J., Wang J., Berlind P., Calkins M. L., Esquerdo G. A., DePoy D. L., Gould A., Marshall J., Pogge R., Trueblood M., Trueblood P., 2015, AJ, 150, 12

Bitsch B., Izidoro A., Johansen A., Raymond S. N., Morbidelli A., Lambrechts M., Jacobson S. A., 2019, A&A, 623, A88

Black D. C., 1997, ApJL, 490, L171

Blackwell D. E., Shallis M. J., 1977, MNRAS, 180, 177

Bodenheimer P., D'Angelo G., Lissauer J. J., Fortney J. J., Saumon D., 2013, ApJ, 770, 120

Bodenheimer P., Hubickyj O., Lissauer J. J., 2000, Icarus, 143, 2

Boley A. C., Granados Contreras A. P., Gladman B., 2016, ApJL, 817, L17

Bond I. A., Udalski A., Jaroszyński M., Rattenbury N. J., Paczyński B., Soszyński I., Wyrzykowski L., Szymański M. K., Kubiak M., Szewczyk O., Żebruń K., Pietrzyński G., Abe F., Bennett D. P., Eguchi S., Furuta Y., Hearnshaw J. B., Kamiya K., Kilmartin P. M., Kurata Y., Masuda K., Matsubara Y., Muraki Y., Noda S., Okajima K., Sako T., Sekiguchi T., Sullivan D. J., Sumi T., Tristram P. J., Yanagisawa T., Yock P. C. M., OGLE Collaboration, 2004, ApJL, 606, L155

Bonfils X., Delfosse X., Udry S., Forveille T., Mayor M., Perrier C., Bouchy F., Gillon M., Lovis C., Pepe F., Queloz D., Santos N. C., Ségransan D., Bertaux J.-L., 2013, A&A, 549, A109

Borgniet S., Lagrange A.-M., Meunier N., Galland F., 2017, A&A, 599, A57

Boss A. P., Butler R. P., Hubbard W. B., Ianna P. A., Kürster M., Lissauer J. J., Mayor M., Meech K. J., Mignard F., Penny A. J., Quirrenbach A., Tarter J. C., Vidal-Madjar A., 2007, Transactions of the International Astronomical Union, Series A, 26, 183

Boué G., Montalto M., Boisse I., Oshagh M., Santos N. C., 2013, A&A, 550, A53

Bourrier V., Lecavelier des Etangs A., Hébrard G., Santerne A., Deleuil M., Almenara J. M., Barros S. C. C., Boisse I., Bonomo A. S., Bruno G., Courcol B., Diaz R. F., Montagnier G., Moutou C., 2015a, A&A, 579, A55

Bourrier V., Lecavelier des Etangs A., Hébrard G., Santerne A., Deleuil M., Almenara J. M., Barros S. C. C., Boisse I., Bonomo A. S., Bruno G., Courcol B., Diaz R. F., Montagnier G., Moutou C., 2015b, A&A, 579, A55

Brown D. J. A., Triaud A. H. M. J., Doyle A. P., Gillon M., Lendl M., Anderson D. R., Collier Cameron A., Hébrard G., Hellier C., Lovis C., Maxted P. F. L., Pepe F., Pollacco D., Queloz D., Smalley B., 2017, MNRAS, 464, 810

Bruntt H., Bedding T. R., Quirion P.-O., Lo Curto G., Carrier F., Smalley B., Dall T. H., Arentoft T., Bazot M., Butler R. P., 2010, MNRAS, 405, 1907

Burdanov A., Delrez L., Gillon M., Jehin E., SPECULOOS Exoplanet Search and Its Prototype on TRAPPIST, p. 1, Springer International Publishing, Cham, 2018

Burrows A., Hubeny I., Budaj J., Hubbard W. B., 2007, ApJ, 661, 502

Butler R. P., Marcy G. W., Fischer D. A., Brown T. M., Contos A. R., Korzennik S. G., Nisenson P., Noyes R. W., 1999, ApJ, 526, 916

Caballero J. A., 2018, Geosciences, 8, 362

Campbell B., Walker G. A. H., Yang S., 1988, ApJ, 331, 902

Casagrande L., VandenBerg D. A., 2014, MNRAS, 444, 392

Casagrande L., VandenBerg D. A., 2018, MNRAS, 475, 5023

Cauley P. W., Shkolnik E. L., Ilyin I., Strassmeier K. G., Redfield S., Jensen A., 2019, AJ, 157, 69

Cegla H. M., Lovis C., Bourrier V., Beeck B., Watson C. A., Pepe F., 2016a, A&A, 588, A127

Cegla H. M., Oshagh M., Watson C. A., Figueira P., Santos N. C., Shelyag S., 2016b, ApJ, 819, 67

Chabrier G., 2003, PASP, 115, 763

Chabrier G., Baraffe I., Allard F., Hauschildt P., 2000, ApJL, 542, L119

Chabrier G., Johansen A., Janson M., Rafikov R., 2014, Protostars and Planets VI, , 619

Chadney J. M., Galand M., Unruh Y. C., Koskinen T. T., Sanz-Forcada J., 2015, Icarus, 250, 357

Chambers K. C., Magnier E. A., Metcalfe N., Flewelling H. A., Huber M. E., Waters C. Z., Denneau L., Draper P. W., Farrow D., Finkbeiner D. P., Holmberg C., Koppenhoefer J., Price P. A., Rest A., Saglia R. P., Schlafly E. F., Smartt S. J., Sweeney W., Wainscoat R. J., Burgett W. S., Chastel S., Grav T., Heasley J. N., Hodapp K. W., Jedicke R., Kaiser N., Kudritzki R.-P., Luppino G. A., Lupton R. H., Monet D. G., Morgan J. S., Onaka P. M., Shiao B., Stubbs C. W., Tonry J. L., White R., Bañados E., Bell E. F., Bender R., Bernard E. J., Boegner M., Boffi F., Botticella M. T., Calamida A., Casertano S., Chen W.-P., Chen X., Cole S., Deacon N., Frenk C., Fitzsimmons A., Gezari S., Gibbs V., Goessl C., Goggia T., Gourgue R., Goldman B., Grant P., Grebel E. K., Hambly N. C., Hasinger G., Heavens A. F., Heckman T. M., Henderson R., Henning T., Holman M., Hopp U., Ip W.-H., Isani S., Jackson M., Keyes C. D., Koekemoer A. M., Kotak R., Le D., Liska D., Long K. S., Lucey J. R., Liu M., Martin N. F., Masci G., McLean B., Mindel E., Misra P., Morganson E., Murphy D. N. A., Obaika A., Narayan G., Nieto-Santisteban M. A., Norberg P., Peacock J. A., Pier E. A., Postman M., Primak N., Rae C., Rai A., Riess A., Riffeser A., Rix H. W., Röser S., Russel R., Rutz L., Schilbach E., Schultz A. S. B., Scolnic D., Strolger L., Szalay A., Seitz S., Small E., Smith K. W., Soderblom D. R., Taylor P., Thomson R., Taylor A. N., Thakar A. R., Thiel J., Thilker D., Unger D., Urata Y., Valenti J., Wagner J., Walder T., Walter F., Watters S. P., Werner S., Wood-Vasey W. M., Wyse R., 2016, arXiv e-prints

Charbonneau D., Brown T. M., Latham D. W., Mayor M., 2000, ApJL, 529, L45

Chauvin G., Lagrange A.-M., Dumas C., Zuckerman B., Mouillet D., Song I., Beuzit J.-L., Lowrance P., 2004, A&A, 425, L29

Chauvin G., Lagrange A.-M., Dumas C., Zuckerman B., Mouillet D., Song I., Beuzit J.-L., Lowrance P., 2005, A&A, 438, L25

Choi J., McCarthy C., Marcy G. W., Howard A. W., Fischer D. A., Johnson J. A., Isaacson H., Wright J. T., 2013, ApJ, 764, 131

Choi J., Dotter A., Conroy C., Cantiello M., Paxton B., Johnson B. D., 2016, ApJ, 823, 102

Claret A., 2000, A&A, 363, 1081

Claret A., 2004, A&A, 428, 1001

Cochran W. D., Hatzes A. P., Endl M., Paulson D. B., Walker G. A. H., Campbell B., Yang S., 2002, AAS/Division for Planetary Sciences Meeting Abstracts #34, Bulletin of the American Astronomical Society Vol. 34, p. 916

Cody A. M., Sasselov D. D., 2002, ApJ, 569, 451

Collier Cameron A., Pollacco D., Street R. A., Lister T. A., West R. G., Wilson D. M., Pont F., Christian D. J., Clarkson W. I., Enoch B., Evans A., Fitzsimmons A., Haswell C. A., Hellier C., Hodgkin S. T., Horne K., Irwin J., Kane S. R., Keenan F. P., Norton A. J., Parley N. R., Osborne J., Ryans R., Skillen I., Wheatley P. J., 2006, MNRAS, 373, 799

Collier Cameron A., Wilson D. M., West R. G., Hebb L., Wang X.-B., Aigrain S., Bouchy F., Christian D. J., Clarkson W. I., Enoch B., Esposito M., Guenther E., Haswell C. A., Hébrard G., Hellier C., Horne K., Irwin J., Kane S. R., Loeillet B., Lister T. A., Maxted P., Mayor M., Moutou C., Parley N., Pollacco D., Pont F., Queloz D., Ryans R., Skillen I., Street R. A., Udry S., Wheatley P. J., 2007, MNRAS, 380, 1230

Collier Cameron A., Bruce V. A., Miller G. R. M., Triaud A. H. M. J., Queloz D., 2010a, MNRAS, 403, 151

Collier Cameron A., Guenther E., Smalley B., McDonald I., Hebb L., Andersen J., Augusteijn T., Barros S. C. C., Brown D. J. A., Cochran W. D., Endl M., Fossey S. J., Hartmann M., Maxted P. F. L., Pollacco D., Skillen I., Telting J., Waldmann I. P., West R. G., 2010b, MNRAS, 407, 507

Collins K. A., Collins K. I., Pepper J., Labadie-Bartz J., Stassun K. G., Gaudi B. S., Bayliss D., Bento J., COLÓN K. D., Feliz D., James D., Johnson M. C., Kuhn R. B., Lund M. B., Penny M. T., Rodriguez J. E., Siverd R. J., Stevens D. J., Yao X., Zhou G., Akshay M., Aldi G. F., Ashcraft C., Awiphan S., Baştürk Ö., Baker D., Beatty T. G., Benni P., Berlind P., Berriman G. B., Berta-Thompson Z., Bieryla A., Bozza V., Calchi Novati S., Calkins M. L., Cann J. M., Ciardi D. R., Clark I. R., Cochran W. D., Cohen D. H., Conti D., Crepp J. R., Curtis I. A., D'Ago G., Diazeguigure K. A., Dressing C. D., Dubois F., Ellingson E., Ellis T. G., Esquerdo G. A., Evans P., Friedli A., Fukui A., Fulton B. J., Gonzales E. J., Good J. C., Gregorio J., Gumusayak T., Hancock D. A., Harada C. K., Hart R., Hintz E. G., Jang-Condell H., Jeffery E. J., Jensen E. L. N., Jofré E., Joner M. D., Kar A., Kasper D. H., Keten B., Kielkopf J. F., Komonjinda S., Kotnik C., Latham D. W., Leuquire J., Lewis T. R., Logie L., Lowther S. J., Macqueen P. J., Martin T. J., Mawet D., Mcleod K. K., Murawski G., Narita N., Nordhausen J., Oberst T. E., Odden C., Panka P. A., Petrucci R., Plavchan P., Quinn S. N., Rau S., Reed P. A., Relles H., Renaud J. P., Scarpetta G., Sorber R. L., Spencer A. D., Spencer M., Stephens D. C., Stockdale C., Tan T.-G., Trueblood M., Trueblood P., Vanaverbeke S., Villanueva, Jr. S., Warner E. M., West M. L., Yalçınkaya S., Yeigh R., Zambelli R., 2018, AJ, 156, 234

Crida A., Batygin K., 2014, in Ballet J., Martins F., Bournaud F., Monier R., Reylé C., eds, SF2A-2014: Proceedings of the Annual meeting of the French Society of Astronomy and Astrophysics, p. 217

Crouzet N., McCullough P. R., Long D., Montanes Rodriguez P., Lecavelier des Etangs A., Ribas I., Bourrier V., Hébrard G., Vilardell F., Deleuil M., Herrero E., Garcia-Melendo E., Akhenak L., Foote J., Gary B., Benni P., Guillot T., Conjat M., Mékarnia D., Garlitz J., Burke C. J., Courcol B., Demangeon O., 2017, AJ, 153, 94

Cutri R. M., et al., 2012, VizieR Online Data Catalog, 2311

Cutri R. M., Skrutskie M. F., van Dyk S., Beichman C. A., Carpenter J. M., Chester T., Cambresy L., Evans T., Fowler J., Gizis J., Howard E., Huchra J., Jarrett T., Kopan E. L., Kirkpatrick J. D., Light R. M., Marsh K. A., McCallon H., Schneider S., Stiening R., Sykes M., Weinberg M., Wheaton W. A., Wheelock S., Zacarias N., 2003, VizieR Online Data Catalog, 2246

Dai F., Winn J. N., 2017, AJ, 153, 205

Dawson R. I., Johnson J. A., 2018, ARA&A, 56, 175

de Wit J., Lewis N. K., Knutson H. A., Fuller J., Antoci V., Fulton B. J., Laughlin G., Deming D., Shporer A., Batygin K., Cowan N. B., Agol E., Burrows A. S., Fortney J. J., Langton J., Showman A. P., 2017, ArXiv e-prints

Delrez L., Gillon M., Queloz D., Demory B.-O., Almleaky Y., de Wit J., Jehin E., Triaud A. H. M. J., Barkaoui K., Burdanov A., Burgasser A. J., Ducrot E., McCormac J., Murray C., Silva Fernandes C., Sohy S., Thompson S. J., Van Grootel V., Alonso R., Benkhaldoun Z., Rebolo R., 2018, Society of Photo-Optical Instrumentation Engineers (SPIE) Conference Series, Society of Photo-Optical Instrumentation Engineers (SPIE) Conference Series Vol. 10700, p. 107001I

Demory B.-O., Seager S., 2011, ApJS, 197, 12

Dong S., Katz B., Socrates A., 2014, ApJL, 781, L5

Dorval P., Talens G. J. J., Otten G. P. P. L., Brahm R., Jordán A., Vanzi L., Zapata A., Henry T., Paredes L., Jao W. C., James H., Hinojosa R., Bakos G. A., Csubry

Z., Bhatti W., Suc V., Osip D., Mamajek E. E., Mellon S. N., Wyttenbach A., Stuik R., Kenworthy M., Bailey J., Ireland M., Crawford S., Lomberg B., Kuhn R., Snellen I., 2019, arXiv e-prints

Doyle A. P., Smalley B., Maxted P. F. L., Anderson D. R., Cameron A. C., Gillon M., Hellier C., Pollacco D., Queloz D., Triaud A. H. M. J., West R. G., 2013, MNRAS, 428, 3164

Doyle A. P., Davies G. R., Smalley B., Chaplin W. J., Elsworth Y., 2014, MNRAS, 444, 3592

Eastman J., Gaudi B. S., Agol E., 2013, PASP, 125, 83

Eastman J., Siverd R., Gaudi B. S., 2010, PASP, 122, 935

Enoch B., Collier Cameron A., Horne K., 2012, A&A, 540, A99

Enoch B., Collier Cameron A., Parley N. R., Hebb L., 2010, A&A, 516, A33

Epchtein N., de Batz B., Capoani L., Chevallier L., Copet E., Fouqué P., Lacombe P., Le Bertre T., Pau S., Rouan D., Ruphy S., Simon G., Tiphène D., Burton W. B., Bertin E., Deul E., Habing H., Borsenberger J., Dennefeld M., Guglielmo F., Loup C., Mamon G., Ng Y., Omont A., Provost L., Renault J.-C., Tanguy F., Kimeswenger S., Kienel C., Garzon F., Persi P., Ferrari-Toniolo M., Robin A., Paturel G., Vauglin I., Forveille T., Delfosse X., Hron J., Schultheis M., Appenzeller I., Wagner S., Balazs L., Holl A., Lépine J., Boscolo P., Picazzio E., Duc P.-A., Mennessier M.-O., 1997, The Messenger, 87, 27

Evans T. M., Sing D. K., Kataria T., Goyal J., Nikolov N., Wakeford H. R., Deming D., Marley M. S., Amundsen D. S., Ballester G. E., Barstow J. K., Ben-Jaffel L., Bourrier V., Buchhave L. A., Cohen O., Ehrenreich D., García Muñoz A., Henry G. W., Knutson H., Lavvas P., Lecavelier Des Etangs A., Lewis N. K., López-Morales M., Mandell A. M., Sanz-Forcada J., Tremblin P., Lupu R., 2017, Nature, 548, 58

Evans D. F., Southworth J., Smalley B., Jørgensen U. G., Dominik M., Andersen M. I., Bozza V., Bramich D. M., Burgdorf M. J., Ciceri S., D'Ago G., Figuera Jaimes R., Gu S.-H., Hinse T. C., Henning T., Hundertmark M., Kains N., Kerins E., Korhonen H., Kokotanekova R., Kuffmeier M., Longa-Peña P., Mancini L., MacKenzie J., Popovas A., Rabus M., Rahvar S., Sajadian S., Snodgrass C., Skottfelt J., Surdej J., Tronsgaard R., Unda-Sanzana E., von Essen C., Wang Y.-B., Wertz O., 2018, A&A, 610, A20

Fabrycky D., Tremaine S., 2007, ApJ, 669, 1298

Fűresz G., 2008, PhD thesis, Univ. Svezged, Hungary

Fielding D. B., McKee C. F., Socrates A., Cunningham A. J., Klein R. I., 2015, MNRAS, 450, 3306

Fortney J. J., Lodders K., Marley M. S., Freedman R. S., 2008a, ApJ, 678, 1419

Fortney J. J., Marley M. S., Saumon D., Lodders K., 2008b, ApJ, 683, 1104

Fortney J. J., Marley M. S., Barnes J. W., 2007, ApJ, 659, 1661

Fossati L., Haswell C. A., Froning C. S., Hebb L., Holmes S., Kolb U., Helling C., Carter A., Wheatley P., Collier Cameron A., Loeillet B., Pollacco D., Street R., Stempels H. C., Simpson E., Udry S., Joshi Y. C., West R. G., Skillen I., Wilson D., 2010, ApJL, 714, L222

Futyan D., Fortier A., Beck M., Ehrenreich D., Bekkelien A., Benz W., Billot N., Bourrier V., Broeg C., Collier Cameron A., Deline A., Kuntzer T., Lendl M., Queloz D., Rohlfs R., Simon A. E., Wildi F., 2020, arXiv e-prints, , arXiv:2001.05587

Gaia Collaboration, Brown A. G. A., Vallenari A., Prusti T., de Bruijne J. H. J., Mignard F., Drimmel R., Babusiaux C., Bailer-Jones C. A. L., Bastian U., et al., 2016a, A&A, 595, A2

Gaia Collaboration, Prusti T., de Bruijne J. H. J., Brown A. G. A., Vallenari A., Babusiaux C., Bailer-Jones C. A. L., Bastian U., Biermann M., Evans D. W., et al., 2016b, A&A, 595, A1

Gaia Collaboration, Brown A. G. A., Vallenari A., Prusti T., de Bruijne J. H. J., Babusiaux C., Bailer-Jones C. A. L., Biermann M., Evans D. W., Eyer L., et al., 2018, A&A, 616, A1

Gandolfi D., Hébrard G., Alonso R., Deleuil M., Guenther E. W., Fridlund M., Endl M., Eigmüller P., Csizmadia S., Havel M., Aigrain S., Auvergne M., Baglin A., Barge P., Bonomo A. S., Bordé P., Bouchy F., Bruntt H., Cabrera J., Carpano S., Carone L., Cochran W. D., Deeg H. J., Dvorak R., Eislöffel J., Erikson A., Ferraz-Mello S., Gazzano J.-C., Gibson N. B., Gillon M., Gondoin P., Guillot T., Hartmann M., Hatzes A., Jorda L., Kabath P., Léger A., Llebaria A., Lammer H., MacQueen P. J., Mayor M., Mazeh T., Moutou C., Ollivier M., Pätzold M., Pepe F., Queloz D., Rauer H., Rouan D., Samuel B., Schneider J., Stecklum B., Tingley B., Udry S., Wuchterl G., 2010, A&A, 524, A55

Gandolfi D., Barragán O., Livingston J. H., Fridlund M., Justesen A. B., Redfield S., Fossati L., Mathur S., Grziwa S., Cabrera J., García R. A., Persson C. M., Van Eylen V., Hatzes A. P., Hidalgo D., Albrecht S., Bugnet L., Cochran W. D., Csizmadia S., Deeg H., Eigmüller P., Endl M., Erikson A., Esposito M., Guenther E., Korth J., Luque R., Montañes Rodríguez P., Nespral D., Nowak G., Pätzold M., Prieto-Arranz J., 2018, A&A, 619, L10

Gaudi B. S., Stassun K. G., Collins K. A., Beatty T. G., Zhou G., Latham D. W., Bieryla A., Eastman J. D., Siverd R. J., Crepp J. R., Gonzales E. J., Stevens D. J., Buchhave L. A., Pepper J., Johnson M. C., Colon K. D., Jensen E. L. N., Rodriguez J. E., Bozza V., Novati S. C., D'Ago G., Dumont M. T., Ellis T., Gaillard C., Jang-Condell H., Kasper D. H., Fukui A., Gregorio J., Ito A., Kielkopf J. F., Manner M., Matt K., Narita N., Oberst T. E., Reed P. A., Scarpetta G., Stephens D. C., Yeigh R. R., Zambelli R., Fulton B. J., Howard A. W., James

D. J., Penny M., Bayliss D., Curtis I. A., Depoy D. L., Esquerdo G. A., Gould A., Joner M. D., Kuhn R. B., Labadie-Bartz J., Lund M. B., Marshall J. L., McLeod K. K., Pogge R. W., Relles H., Stockdale C., Tan T. G., Trueblood M., Trueblood P., 2017, Nature, 546, 514

Gibson N. P., Nikolov N., Sing D. K., Barstow J. K., Evans T. M., Kataria T., Wilson P. A., 2017, MNRAS, 467, 4591

Gillon M., 2018, Nature Astronomy, 2, 344

Gillon M., Lanotte A. A., Barman T., Miller N., Demory B.-O., Deleuil M., Montalbán J., Bouchy F., Collier Cameron A., Deeg H. J., Fortney J. J., Fridlund M., Harrington J., Magain P., Moutou C., Queloz D., Rauer H., Rouan D., Schneider J., 2010, A&A, 511, A3

Gillon M., Jehin E., Magain P., Chantry V., Hutsemékers D., Manfroid J., Queloz D., Udry S., 2011, European Physical Journal Web of Conferences, European Physical Journal Web of Conferences Vol. 11, p. 06002

Gillon M., Triaud A. H. M. J., Fortney J. J., Demory B.-O., Jehin E., Lendl M., Magain P., Kabath P., Queloz D., Alonso R., Anderson D. R., Collier Cameron A., Fumel A., Hebb L., Hellier C., Lanotte A., Maxted P. F. L., Mowlavi N., Smalley B., 2012, A&A, 542, A4

Gillon M., Anderson D. R., Collier-Cameron A., Doyle A. P., Fumel A., Hellier C., Jehin E., Lendl M., Maxted P. F. L., Montalbán J., Pepe F., Pollacco D., Queloz D., Ségransan D., Smith A. M. S., Smalley B., Southworth J., Triaud A. H. M. J., Udry S., West R. G., 2013, A&A, 552, A82

Giménez A., 2006, ApJ, 650, 408

Ginzburg S., Sari R., 2015, ApJ, 803, 111

Goda S., Matsuo T., 2019, arXiv e-prints

Goldreich P., Lynden-Bell D., 1965, MNRAS, 130, 97

Goodricke J., 1783, Philosophical Transactions of the Royal Society of London Series I, 73, 474

Gray R. O., Corbally C. J., 2014, AJ, 147, 80

Gray D. F., Hatzes A. P., 1997, ApJ, 490, 412

Gray D. F., 1992, The observation and analysis of stellar photospheres.

Gray D. F., 1997, Nature, 385, 795

Green G. M., Schlafly E. F., Finkbeiner D. P., Jurić M., Rix H.-W., Burgett W., Chambers K. C., Draper P. W., Flewelling H., Kudritzki R. P., Magnier E., Martin N., Metcalfe N., Tonry J., Wainscoat R., Waters C., 2014, ApJ, 783, 114

Green G. M., Schlafly E. F., Finkbeiner D. P., Rix H.-W., Martin N., Burgett W., Draper P. W., Flewelling H., Hodapp K., Kaiser N., Kudritzki R. P., Magnier E., Metcalfe N., Price P., Tonry J., Wainscoat R., 2015, ApJ, 810, 25

Guillot T., 2005, Annual Review of Earth and Planetary Sciences, 33, 493

Gustafsson B., Edvardsson B., Eriksson K., Jørgensen U. G., Nordlund Å., Plez B., 2008, A&A, 486, 951

Hartman J. D., Bakos G., Stanek K. Z., Noyes R. W., 2004, AJ, 128, 1761

Hartman J. D., Bakos G. Á., Buchhave L. A., Torres G., Latham D. W., Kovács G., Bhatti W., Csubry Z., de Val-Borro M., Penev K., Huang C. X., Béky B., Bieryla A., Quinn S. N., Howard A. W., Marcy G. W., Johnson J. A., Isaacson H., Fischer D. A., Noyes R. W., Falco E., Esquerdo G. A., Knox R. P., Hinz P., Lázár J., Papp I., Sári P., 2015, AJ, 150, 197

Hartman J. D., Bakos G. Á., Bhatti W., Penev K., Bieryla A., Latham D. W., Kovács G., Torres G., Csubry Z., de Val-Borro M., Buchhave L., Kovács T., Quinn S.,

Howard A. W., Isaacson H., Fulton B. J., Everett M. E., Esquerdo G., Béky B., Szklenar T., Falco E., Santerne A., Boisse I., Hébrard G., Burrows A., Lázár J., Papp I., Sári P., 2016, AJ, 152, 182

Hasegawa Y., Yu T. Y. M., Hansen B. M. S., 2019, arXiv e-prints

Haswell C. A., 2010, Transiting Exoplanets

Haswell C. A., Fossati L., Ayres T., France K., Froning C. S., Holmes S., Kolb U. C., Busuttil R., Street R. A., Hebb L., Collier Cameron A., Enoch B., Burwitz V., Rodriguez J., West R. G., Pollacco D., Wheatley P. J., Carter A., 2012, ApJ, 760, 79

Hatzes A. P., Cochran W. D., Johns-Krull C. M., 1997, ApJ, 478, 374

Haworth T. J., Facchini S., Clarke C. J., 2015, MNRAS, 446, 1098

Hay K. L., Collier-Cameron A., Doyle A. P., Hébrard G., Skillen I., Anderson D. R., Barros S. C. C., Brown D. J. A., Bouchy F., Busuttil R., Delorme P., Delrez L., Demangeon O., Díaz R. F., Gillon M., Gómez Maqueo Chew Y., Gonzàlez E., Hellier C., Holmes S., Jarvis J. F., Jehin E., Joshi Y. C., Kolb U., Lendl M., Maxted P. F. L., McCormac J., Miller G. R. M., Mortier A., Pallé E., Pollacco D., Prieto-Arranz J., Queloz D., Ségransan D., Simpson E. K., Smalley B., Southworth J., Triaud A. H. M. J., Turner O. D., Udry S., Vanhuysse M., West R. G., Wilson P. A., 2016, MNRAS, 463, 3276

Hebb L., Collier-Cameron A., Loeillet B., Pollacco D., Hébrard G., Street R. A., Bouchy F., Stempels H. C., Moutou C., Simpson E., Udry S., Joshi Y. C., West R. G., Skillen I., Wilson D. M., McDonald I., Gibson N. P., Aigrain S., Anderson D. R., Benn C. R., Christian D. J., Enoch B., Haswell C. A., Hellier C., Horne K., Irwin J., Lister T. A., Maxted P., Mayor M., Norton A. J., Parley N., Pont F., Queloz D., Smalley B., Wheatley P. J., 2009, ApJ, 693, 1920

Helled R., Bodenheimer P., Podolak M., Boley A., Meru F., Nayakshin S., Fortney J. J., Mayer L., Alibert Y., Boss A. P., 2014, Protostars and Planets VI, , 643

Heller R., 2019, A&A, 628, A42

Hellier C., Anderson D. R., Collier Cameron A., Gillon M., Lendl M., Lister T. A., Maxted P. F. L., Pollacco D., Queloz D., Smalley B., Triaud A. H. M. J., West R. G., 2011, European Physical Journal Web of Conferences, European Physical Journal Web of Conferences Vol. 11, p. 01004

Hellier C., Anderson D. R., Cameron A. C., Delrez L., Gillon M., Jehin E., Lendl M., Maxted P. F. L., Pepe F., Pollacco D., Queloz D., Ségransan D., Smalley B., Smith A. M. S., Southworth J., Triaud A. H. M. J., Udry S., West R. G., 2014, MNRAS, 440, 1982

Hellier C., Anderson D. R., Barkaoui K., Benkhaldoun Z., Bouchy F., Burdanov A., Collier Cameron A., Delrez L., Gillon M., Jehin E., Nielsen L. D., Maxted P. F. L., Pepe F., Pollacco D., Pozuelos F. J., Queloz D., Segransan D., Smalley B., Triaud A. H. M. J., Turner O. D., Udry S., West R. G., 2019a, arXiv e-prints

Hellier C., Anderson D. R., Bouchy F., Burdanov A., Cameron A. C., Delrez L., Gillon M., Jehin E., Lendl M., Nielsen L. D., Maxted P. F. L., Pepe F., Pollacco D., Queloz D., Ségransan D., Smalley B., Triaud A. H. M. J., Udry S., West R. G., 2019b, MNRAS, 482, 1379

Henden A. A., Levine S., Terrell D., Welch D. L., 2015, American Astronomical Society Meeting Abstracts #225, American Astronomical Society Meeting Abstracts Vol. 225, p. 336.16

Heng K., Showman A. P., 2015, Annual Review of Earth and Planetary Sciences, 43, 509

Henry G. W., Marcy G. W., Butler R. P., Vogt S. S., 2000, ApJL, 529, L41

Herrero E., Morales J. C., Ribas I., Naves R., 2011, A&A, 526, L10

Hilditch R. W., 2001, An Introduction to Close Binary Stars

Hirano T., Suto Y., Winn J. N., Taruya A., Narita N., Albrecht S., Sato B., 2011, ApJ, 742, 69

Hjorth M., Albrecht S., Talens G. J. J., Justesen A. B., Otten G. P. P. L., Antoci V., Dorval P., Foxell E., Fredslund Andersen M., Grundahl F., Murgas F., Palle E., Stuik R., Snellen I. A. G., Van Eylen V., 2019, arXiv e-prints

Hoeijmakers H. J., Ehrenreich D., Heng K., Kitzmann D., Grimm S. L., Allart R., Deitrick R., Wyttenbach A., Oreshenko M., Pino L., Rimmer P. B., Molinari E., Di Fabrizio L., 2018, Nature, 560, 453

Hoeijmakers H. J., Ehrenreich D., Kitzmann D., Allart R., Grimm S. L., Seidel J. V., Wyttenbach A., Pino L., Nielsen L. D., Fisher C., Rimmer P. B., Bourrier V., Cegla H. M., Lavie B., Lovis C., Patzer A. B. C., Stock J. W., Pepe F. A., Heng K., 2019, A&A, 627, A165

Høg E., Fabricius C., Makarov V. V., Urban S., Corbin T., Wycoff G., Bastian U., Schwekendiek P., Wicenec A., 2000, A&A, 355, L27

Horne K., 1985, MNRAS, 213, 129

Huang C. X., Hartman J. D., Bakos G. Á., Penev K., Bhatti W., Bieryla A., de Val-Borro M., Latham D. W., Buchhave L. A., Csubry Z., Kovács G., Béky B., Falco E., Berlind P., Calkins M. L., Esquerdo G. A., Lázár J., Papp I., Sári P., 2015, AJ, 150, 85

Huang C. X., Burt J., Vanderburg A., Günther M. N., Shporer A., Dittmann J. A., Winn J. N., Wittenmyer R., Sha L., Kane S. R., Ricker G. R., Vand erspek R. K., Latham D. W., Seager S., Jenkins J. M., Caldwell D. A., Collins K. A., Guerrero N., Smith J. C., Quinn S. N., Udry S., Pepe F., Bouchy F., Ségransan D.,

Lovis C., Ehrenreich D., Marmier M., Mayor M., Wohler B., Haworth K., Morgan E. H., Fausnaugh M., Ciardi D. R., Christiansen J., Charbonneau D., Dragomir D., Deming D., Glidden A., Levine A. M., McCullough P. R., Yu L., Narita N., Nguyen T., Morton T., Pepper J., Pál A., Rodriguez J. E., Stassun K. G., Torres G., Sozzetti A. r., Doty J. P., Christensen-Dalsgaard J., Laughlin G., Clampin M., Bean J. L., Buchhave L. A., Bakos G. Á., Sato B., Ida S., Kaltenegger L., Palle E., Sasselov D., Butler R. P., Lissauer J., Ge J., Rinehart S. A., 2018, ApJL, 868(2), L39

Jacob W. S., 1855, MNRAS, 15, 228

Janson M., Bonavita M., Klahr H., Lafrenière D., Jayawardhana R., Zinnecker H., 2011, ApJ, 736, 89

Janson M., Bonavita M., Klahr H., Lafrenière D., 2012, ApJ, 745, 4

Jehin E., Gillon M., Queloz D., Magain P., Manfroid J., Chantry V., Lendl M., Hutsemékers D., Udry S., 2011, The Messenger, 145, 2

Johnson M. C., Cochran W. D., Collier Cameron A., Bayliss D., 2015, ApJL, 810, L23

Johnson M. C., Rodriguez J. E., Zhou G., Gonzales E. J., Cargile P. A., Crepp J. R., Penev K., Stassun K. G., Gaudi B. S., Colón K. D., Stevens D. J., Strassmeier K. G., Ilyin I., Collins K. A., Kielkopf J. F., Oberst T. E., Maritch L., Reed P. A., Gregorio J., Bozza V., Calchi Novati S., D'Ago G., Scarpetta G., Zambelli R., Latham D. W., Bieryla A., Cochran W. D., Endl M., Tayar J., Serenelli A., Silva Aguirre V., Clarke S. P., Martinez M., Spencer M., Trump J., Joner M. D., Bugg A. G., Hintz E. G., Stephens D. C., Arredondo A., Benzaid A., Yazdi S., McLeod K. K., Jensen E. L. N., Hancock D. A., Sorber R. L., Kasper D. H., Jang-Condell H., Beatty T. G., Carroll T., Eastman J., James D., Kuhn R. B., Labadie-Bartz J., Lund M. B., Mallonn M., Pepper J., Siverd R. J., Yao X., Cohen D. H., Curtis I. A., DePoy D. L., Fulton B. J., Penny M. T., Relles H., Stockdale C., Tan T.-G., Villanueva, Jr. S., 2018, AJ, 155, 100

Jung Y. K., Hwang K.-H., Ryu Y.-H., Gould A., Han C., Yee J. C., Albrow M. D., Chung S.-J., Shin I.-G., Shvartzvald Y., Zang W., Cha S.-M., Kim D.-J., Kim H.-W., Kim S.-L., Lee C.-U., Lee D.-J., Lee Y., Park B.-G., Pogge R. W., 2018, AJ, 156, 208

Kempton E. M.-R., Lupu R., Owusu-Asare A., Slough P., Cale B., 2017, PASP, 129(4), 044402

Kley W., 2019, From Protoplanetary Disks to Planet Formation, Saas-Fee Advanced Course, Volume 45. ISBN 978-3-662-58686-0. Springer-Verlag GmbH Germany, part of Springer Nature, 2019, p. 151, 45, 151

Knutson H. A., Fulton B. J., Montet B. T., Kao M., Ngo H., Howard A. W., Crepp J. R., Hinkley S., Bakos G. Á., Batygin K., Johnson J. A., Morton T. D., Muirhead P. S., 2014, ApJ, 785, 126

Kopal Z., 1950a, Harvard College Observatory Circular, 454, 1

Kopal Z., 1950b, Harvard Observatory Monographs, 8

Kopal Z., 1979, Ap&SS, 66, 91

Kovács G., Kovács T., Hartman J. D., Bakos G. Á., Bieryla A., Latham D., Noyes R. W., Regály Z., Esquerdo G. A., 2013, A&A, 553, A44

Kovács G., Zucker S., Mazeh T., 2002, A&A, 391, 369

Kraft R. P., 1967, ApJ, 150, 551

Kreidberg L., 2015, PASP, 127, 1161

Kreidberg L., Line M. R., Bean J. L., Stevenson K. B., Désert J.-M., Madhusudhan N., Fortney J. J., Barstow J. K., Henry G. W., Williamson M. H., Showman A. P., 2015, ApJ, 814, 66

Kreidberg L., Line M. R., Parmentier V., Stevenson K. B., Louden T., Bonnefoy M., Faherty J. K., Henry G. W., Williamson M. H., Stassun K., Beatty T. G., Bean J. L., Fortney J. J., Showman A. P., Désert J.-M., Arcangeli J., 2018a, AJ, 156, 17

Kreidberg L., Line M. R., Thorngren D., Morley C. V., Stevenson K. B., 2018b, ApJL, 858, L6

Kuhn R. B., Rodriguez J. E., Collins K. A., Lund M. B., Siverd R. J., Colón K. D., Pepper J., Stassun K. G., Cargile P. A., James D. J., Penev K., Zhou G., Bayliss D., Tan T. G., Curtis I. A., Udry S., Segransan D., Mawet D., Dhital S., Soutter J., Hart R., Carter B., Gaudi B. S., Myers G., Beatty T. G., Eastman J. D., Reichart D. E., Haislip J. B., Kielkopf J., Bieryla A., Latham D. W., Jensen E. L. N., Oberst T. E., Stevens D. J., 2016, MNRAS, 459, 4281

Kurokawa H., Inutsuka S.-i., 2015, ApJ, 815, 78

Kurucz R., 1993, ATLAS9 Stellar Atmosphere Programs and 2 km/s grid. Kurucz CD-ROM No. 13. Cambridge, Mass.: Smithsonian Astrophysical Observatory, 1993., 13

Laughlin G., Mass-Radius Relations of Giant Planets: The Radius Anomaly and Interior Models, 1, 2018

Levrard B., Winisdoerffer C., Chabrier G., 2009, ApJL, 692, L9

Li G., Winn J. N., 2016, ApJ, 818, 5

Lin D. N. C., Bodenheimer P., Richardson D. C., 1996, Nature, 380, 606

Linsky J. L., Yang H., France K., Froning C. S., Green J. C., Stocke J. T., Osterman S. N., 2010, ApJ, 717, 1291

Locci D., Cecchi-Pestellini C., Micela G., 2019, A&A, 624, A101

Lucas P. W., Roche P. F., 2000, MNRAS, 314, 858

Lund M. B., Rodriguez J. E., Zhou G., Gaudi B. S., Stassun K. G., Johnson M. C., Bieryla A., Oelkers R. J., Stevens D. J., Collins K. A., Penev K., Quinn S. N., Latham D. W., Villanueva, Jr. S., Eastman J. D., Kielkopf J. F., Oberst T. E., Jensen E. L. N., Cohen D. H., Joner M. D., Stephens D. C., Relles H., Corfini G., Gregorio J., Zambelli R., Esquerdo G. A., Calkins M. L., Berlind P., Ciardi D. R., Dressing C., Patel R., Gagnon P., Gonzales E., Beatty T. G., Siverd R. J., Labadie-Bartz J., Kuhn R. B., Colón K. D., James D., Pepper J., Fulton B. J., McLeod K. K., Stockdale C., Calchi Novati S., DePoy D. L., Gould A., Marshall J. L., Trueblood M., Trueblood P., Johnson J. A., Wright J., McCrady N., Wittenmyer R. A., Johnson S. A., Sergi A., Wilson M., Sliski D. H., 2017, AJ, 154, 194

Machida M. N., Inutsuka S.-i., Matsumoto T., 2011, ApJ, 729, 42

Madhusudhan N., Amin M. A., Kennedy G. M., 2014, ApJL, 794, L12

Malhotra R., Black D., Eck A., Jackson A., 1992, Nature, 356, 583

Marigo P., Girardi L., Bressan A., Rosenfield P., Aringer B., Chen Y., Dussin M., Nanni A., Pastorelli G., Rodrigues T. S., Trabucchi M., Bladh S., Dalcanton J., Groenewegen M. A. T., Montalbán J., Wood P. R., 2017, ApJ, 835, 77

Marley M. S., Fortney J., Seager S., Barman T., 2007, Protostars and Planets V, , 733

Marois C., Macintosh B., Barman T., Zuckerman B., Song I., Patience J., Lafrenière D., Doyon R., 2008, Science, 322, 1348

Marsh T. R., Horne K., 1988, MNRAS, 235, 269

Mason B. D., Wycoff G. L., Hartkopf W. I., Douglass G. G., Worley C. E., 2001, AJ, 122, 3466

Matsakos T., Königl A., 2016, ApJL, 820, L8

Matsumura S., Peale S. J., Rasio F. A., 2010, ApJ, 725, 1995

Maxted P. F. L., Anderson D. R., Collier Cameron A., Hellier C., Queloz D., Smalley B., Street R. A., Triaud A. H. M. J., West R. G., Gillon M., Lister T. A., Pepe F., Pollacco D., Ségransan D., Smith A. M. S., Udry S., 2011, PASP, 123, 547

Maxted P. F. L., Bloemen S., Heber U., Geier S., Wheatley P. J., Marsh T. R., Breedt E., Sebastian D., Faillace G., Owen C., Pulley D., Smith D., Kolb U., Haswell C. A., Southworth J., Anderson D. R., Smalley B., Collier Cameron A., Hebb L., Simpson E. K., West R. G., Bochinski J., Busuttil R., Hadigal S., 2014, MNRAS, 437, 1681

Maxted P. F. L., Anderson D. R., Collier Cameron A., Delrez L., Gillon M., Hellier C., Jehin E., Lendl M., Neveu-VanMalle M., Pepe F., Pollacco D., Queloz D., Ségransan D., Smalley B., Smith A. M. S., Southworth J., Triaud A. H. M. J., Udry S., Wagg T., West R. G., 2016, A&A, 591, A55

Maxted P. F. L., Serenelli A. M., Southworth J., 2015, A&A, 575, A36

Mayor M., Queloz D., 1995, Nature, 378, 355

Mazeh T., Perets H. B., McQuillan A., Goldstein E. S., 2015, ApJ, 801, 3

McCullough P. R., Stys J. E., Valenti J. A., Fleming S. W., Janes K. A., Heasley J. N., 2005, PASP, 117, 783

McLaughlin D. B., 1924, ApJ, 60

McQuillan A., Mazeh T., Aigrain S., 2013, ApJL, 775, L11

Miller N., Fortney J. J., 2011, ApJL, 736, L29

Monet D. G., Levine S. E., Canzian B., Ables H. D., Bird A. R., Dahn C. C., Guetter H. H., Harris H. C., Henden A. A., Leggett S. K., Levison H. F., Luginbuhl C. B., Martini J., Monet A. K. B., Munn J. A., Pier J. R., Rhodes A. R., Riepe B., Sell

S., Stone R. C., Vrba F. J., Walker R. L., Westerhout G., Brucato R. J., Reid I. N., Schoening W., Hartley M., Read M. A., Tritton S. B., 2003, AJ, 125, 984

Mordasini C., Alibert Y., Benz W., Klahr H., Henning T., 2012, A&A, 541, A97

Moulton F. R., 1899, AJ, 20, 33

Močnik T., Hellier C., Anderson D. R., Clark B. J. M., Southworth J., 2017, MNRAS, 469, 1622

Mróz P., Udalski A., Skowron J., Poleski R., Kozłowski S., Szymański M. K., Soszyński I., Wyrzykowski Ł., Pietrukowicz P., Ulaczyk K., Skowron D., Pawlak M., 2017, Nature, 548, 183

Munari U., Zwitter T., 1997, A&A, 318, 269

Muraki Y., Han C., Bennett D. P., Suzuki D., Monard L. A. G., Street R., Jorgensen U. G., Kundurthy P., Skowron J., Becker A. C., Albrow M. D., Fouqué P., Heyrovský D., Barry R. K., Beaulieu J.-P., Wellnitz D. D., Bond I. A., Sumi T., Dong S., Gaudi B. S., Bramich D. M., Dominik M., Abe F., Botzler C. S., Freeman M., Fukui A., Furusawa K., Hayashi F., Hearnshaw J. B., Hosaka S., Itow Y., Kamiya K., Korpela A. V., Kilmartin P. M., Lin W., Ling C. H., Makita S., Masuda K., Matsubara Y., Miyake N., Nishimoto K., Ohnishi K., Perrott Y. C., Rattenbury N. J., Saito T., Skuljan L., Sullivan D. J., Sweatman W. L., Tristram P. J., Wada K., Yock P. C. M., MOA Collaboration, Christie G. W., DePoy D. L., Gorbikov E., Gould A., Kaspi S., Lee C.-U., Mallia F., Maoz D., McCormick J., Moorhouse D., Natusch T., Park B.-G., Pogge R. W., Polishook D., Shporer A., Thornley G., Yee J. C., $\mu$FUN Collaboration, Allan A., Browne P., Horne K., Kains N., Snodgrass C., Steele I., Tsapras Y., RoboNet Collaboration, Batista V., Bennett C. S., Brillant S., Caldwell J. A. R., Cassan A., Cole A., Corrales R., Coutures C., Dieters S., Dominis Prester D., Donatowicz J., Greenhill J., Kubas D., Marquette J.-B., Martin R., Menzies J., Sahu K. C., Waldman I., Williams A., Zub M., PLANET Collaboration, Bourhrous H., Matsuoka Y., Nagayama T.,

Oi N., Randriamanakoto Z., IRSF Observers, Bozza V., Burgdorf M. J., Calchi Novati S., Dreizler S., Finet F., Glitrup M., Harpsøe K., Hinse T. C., Hundertmark M., Liebig C., Maier G., Mancini L., Mathiasen M., Rahvar S., Ricci D., Scarpetta G., Skottfelt J., Surdej J., Southworth J., Wambsganss J., Zimmer F., MiNDSTEp Consortium, Udalski A., Poleski R., Wyrzykowski Ł., Ulaczyk K., Szymański M. K., Kubiak M., Pietrzyński G., Soszyński I., OGLE Collaboration, 2011, ApJ, 741, 22

Murray C. D., Correia A. C. M., Keplerian Orbits and Dynamics of Exoplanets, p. 15, 2010

Naef D., Mayor M., Beuzit J. L., Perrier C., Queloz D., Sivan J. P., Udry S., 2004, A&A, 414, 351

Nagasawa M., Ida S., Bessho T., 2008, ApJ, 678, 498

Narang M., Manoj P., Furlan E., Mordasini C., Henning T., Mathew B., Banyal R. K., Sivarani T., 2018, AJ, 156, 221

Ngo H., Knutson H. A., Hinkley S., Crepp J. R., Bechter E. B., Batygin K., Howard A. W., Johnson J. A., Morton T. D., Muirhead P. S., 2015, ApJ, 800, 138

Ngo H., Knutson H. A., Hinkley S., Bryan M., Crepp J. R., Batygin K., Crossfield I., Hansen B., Howard A. W., Johnson J. A., Mawet D., Morton T. D., Muirhead P. S., Wang J., 2016, ApJ, 827, 8

Nichols J. D., Wynn G. A., Goad M., Alexander R. D., Casewell S. L., Cowley S. W. H., Burleigh M. R., Clarke J. T., Bisikalo D., 2015, ApJ, 803, 9

Niels Bohr Institute, Institute of Astronomy C., Real Instituto y Observatorio de La Armada, 2014, VizieR Online Data Catalog, 1327

Owen J. E., Lai D., 2018, MNRAS, 479, 5012

Parmentier V., Line M. R., Bean J. L., Mansfield M., Kreidberg L., Lupu R., Visscher C., Désert J.-M., Fortney J. J., Deleuil M., Arcangeli J., Showman A. P., Marley M. S., 2018, A&A, 617, A110

Parmentier V., Showman A. P., Lian Y., 2013, A&A, 558, A91

Pepe F., Mayor M., Rupprecht G., Avila G., Ballester P., Beckers J.-L., Benz W., Bertaux J.-L., Bouchy F., Buzzoni B., Cavadore C., Deiries S., Dekker H., Delabre B., D'Odorico S., Eckert W., Fischer J., Fleury M., George M., Gilliotte A., Gojak D., Guzman J.-C., Koch F., Kohler D., Kotzlowski H., Lacroix D., Le Merrer J., Lizon J.-L., Lo Curto G., Longinotti A., Megevand D., Pasquini L., Petitpas P., Pichard M., Queloz D., Reyes J., Richaud P., Sivan J.-P., Sosnowska D., Soto R., Udry S., Ureta E., van Kesteren A., Weber L., Weilenmann U., Wicenec A., Wieland G., Christensen-Dalsgaard J., Dravins D., Hatzes A., Kürster M., Paresce F., Penny A., 2002, The Messenger, 110, 9

Pepper J., Pogge R. W., DePoy D. L., Marshall J. L., Stanek K. Z., Stutz A. M., Poindexter S., Siverd R., O'Brien T. P., Trueblood M., Trueblood P., 2007, PASP, 119, 923

Pepper J., Kuhn R. B., Siverd R., James D., Stassun K., 2012, PASP, 124, 230

Pepper J., Rodriguez J. E., Collins K. A., Johnson J. A., Fulton B. J., Howard A. W., Beatty T. G., Stassun K. G., Isaacson H., Colón K. D., Lund M. B., Kuhn R. B., Siverd R. J., Gaudi B. S., Tan T. G., Curtis I., Stockdale C., Mawet D., Bottom M., James D., Zhou G., Bayliss D., Cargile P., Bieryla A., Penev K., Latham D. W., Labadie-Bartz J., Kielkopf J., Eastman J. D., Oberst T. E., Jensen E. L. N., Nelson P., Sliski D. H., Wittenmyer R. A., McCrady N., Wright J. T., Relles H. M., Stevens D. J., Joner M. D., Hintz E., 2017, AJ, 153, 215

Petrovich C., 2015, ApJ, 799, 27

Pfahl E., Arras P., Paxton B., 2008, ApJ, 679, 783

Piskorz D., Knutson H. A., Ngo H., Muirhead P. S., Batygin K., Crepp J. R., Hinkley S., Morton T. D., 2015, ApJ, 814, 148

Pollacco D. L., Skillen I., Collier Cameron A., Christian D. J., Hellier C., Irwin J., Lister T. A., Street R. A., West R. G., Anderson D. R., Clarkson W. I., Deeg H., Enoch B., Evans A., Fitzsimmons A., Haswell C. A., Hodgkin S., Horne K., Kane S. R., Keenan F. P., Maxted P. F. L., Norton A. J., Osborne J., Parley N. R., Ryans R. S. I., Smalley B., Wheatley P. J., Wilson D. M., 2006, PASP, 118, 1407

Pollacco D., Skillen I., Collier Cameron A., Loeillet B., Stempels H. C., Bouchy F., Gibson N. P., Hebb L., Hébrard G., Joshi Y. C., McDonald I., Smalley B., Smith A. M. S., Street R. A., Udry S., West R. G., Wilson D. M., Wheatley P. J., Aigrain S., Alsubai K., Benn C. R., Bruce V. A., Christian D. J., Clarkson W. I., Enoch B., Evans A., Fitzsimmons A., Haswell C. A., Hellier C., Hickey S., Hodgkin S. T., Horne K., Hrudková M., Irwin J., Kane S. R., Keenan F. P., Lister T. A., Maxted P., Mayor M., Moutou C., Norton A. J., Osborne J. P., Parley N., Pont F., Queloz D., Ryans R., Simpson E., 2008, MNRAS, 385, 1576

Pont F., Husnoo N., Mazeh T., Fabrycky D., 2011, MNRAS, 414, 1278

Prager R., 1931, Astronomische Nachrichten, 243, 359

Queloz D., Eggenberger A., Mayor M., Perrier C., Beuzit J. L., Naef D., Sivan J. P., Udry S., 2000, A&A, 359, L13

Queloz D., Henry G. W., Sivan J. P., Baliunas S. L., Beuzit J. L., Donahue R. A., Mayor M., Naef D., Perrier C., Udry S., 2001a, A&A, 379, 279

Queloz D., Mayor M., Udry S., Burnet M., Carrier F., Eggenberger A., Naef D., Santos N., Pepe F., Rupprecht G., Avila G., Baeza F., Benz W., Bertaux J.-L., Bouchy F., Cavadore C., Delabre B., Eckert W., Fischer J., Fleury M., Gilliotte A., Goyak D., Guzman J. C., Kohler D., Lacroix D., Lizon J.-L., Megevand D., Sivan J.-P., Sosnowska D., Weilenmann U., 2001b, The Messenger, 105, 1

Ramos G., Valverde Guijarro A. L., Rodrigo M. T., Sierra M. A., Gómez L. J., Borreguero E., Álvarez L., Manjón A., Balado A., Barrado D., Mas J. M., 2019, Proc. SPIE, Society of Photo-Optical Instrumentation Engineers (SPIE) Conference Series Vol. 11115, p. 1111508

Rando N., Asquier J., Corral Van Damme C., Isaak K., Ratti F., Safa F., Gehler M., Southworth R., Broeg C., Beck T., Benz W., Borges A., Cortes D., Palacios R., 2019, Proc. SPIE, Society of Photo-Optical Instrumentation Engineers (SPIE) Conference Series Vol. 11116, p. 1111605

Rasio F. A., Ford E. B., 1996, Science, 274, 954

Raynard L., Goad M. R., Gillen E., Nielsen L. D., Watson C. A., Thompson A. P. G., McCormac J., Bayliss D., Soto M., Csizmadia S., Chaushev A., Burleigh M. R., Alexander R., Armstrong D. J., Bouchy F., Briegal J. T., Cabrera J., Casewell S. L., Chazelas B., Cooke B. F., Eigmüller P., Erikson A., Gänsicke B. T., Grange A., Günther M. N., Hodgkin S. T., Hooton M. J., Jenkins J. S., Lambert G., Louden T., Metrailler L., Moyano M., Pollacco D., Poppenhaeger K., Queloz D., Raddi R., Rauer H., Read A. M., Smalley B., Smith A. M. S., Turner O., Udry S., Walker S. R., West R. G., Wheatley P. J., 2018, MNRAS, 481, 4960

Ribas I., Tuomi M., Reiners A., Butler R. P., Morales J. C., Perger M., Dreizler S., Rodríguez-López C., González Hernández J. I., Rosich A., Feng F., Trifonov T., Vogt S. S., Caballero J. A., Hatzes A., Herrero E., Jeffers S. V., Lafarga M., Murgas F., Nelson R. P., Rodríguez E., Strachan J. B. P., Tal-Or L., Teske J., Toledo-Padrón B., Zechmeister M., Quirrenbach A., Amado P. J., Azzaro M., Béjar V. J. S., Barnes J. R., Berdiñas Z. M., Burt J., Coleman G., Cortés-Contreras M., Crane J., Engle S. G., Guinan E. F., Haswell C. A., Henning T., Holden B., Jenkins J., Jones H. R. A., Kaminski A., Kiraga M., Kürster M., Lee M. H., López-González M. J., Montes D., Morin J., Ofir A., Pallé E., Rebolo R., Reffert S., Schweitzer A., Seifert W., Shectman S. A., Staab D., Street R. A., Suárez

Mascareño A., Tsapras Y., Wang S. X., Anglada-Escudé G., 2018, Nature, 563, 365

Ricker G. R., Winn J. N., Vanderspek R., Latham D. W., Bakos G. Á., Bean J. L., Berta-Thompson Z. K., Brown T. M., Buchhave L., Butler N. R., Butler R. P., Chaplin W. J., Charbonneau D., Christensen-Dalsgaard J., Clampin M., Deming D., Doty J., De Lee N., Dressing C., Dunham E. W., Endl M., Fressin F., Ge J., Henning T., Holman M. J., Howard A. W., Ida S., Jenkins J. M., Jernigan G., Johnson J. A., Kaltenegger L., Kawai N., Kjeldsen H., Laughlin G., Levine A. M., Lin D., Lissauer J. J., MacQueen P., Marcy G., McCullough P. R., Morton T. D., Narita N., Paegert M., Palle E., Pepe F., Pepper J., Quirrenbach A., Rinehart S. A., Sasselov D., Sato B., Seager S., Sozzetti A., Stassun K. G., Sullivan P., Szentgyorgyi A., Torres G., Udry S., Villasenor J., 2015, Journal of Astronomical Telescopes, Instruments, and Systems, 1(1), 014003

Rodriguez J. E., Colón K. D., Stassun K. G., Wright D., Cargile P. A., Bayliss D., Pepper J., Collins K. A., Kuhn R. B., Lund M. B., Siverd R. J., Zhou G., Gaudi B. S., Tinney C. G., Penev K., Tan T. G., Stockdale C., Curtis I. A., James D., Udry S., Segransan D., Bieryla A., Latham D. W., Beatty T. G., Eastman J. D., Myers G., Bartz J., Bento J., Jensen E. L. N., Oberst T. E., Stevens D. J., 2016, AJ, 151, 138

Rodriguez J. E., Zhou G., Cargile P. A., Stevens D. J., Osborn H. P., Shappee B. J., Reed P. A., Lund M. B., Relles H. M., Latham D. W., Eastman J., Stassun K. G., Bieryla A., Esquerdo G. A., Berlind P., Calkins M. L., Vanderburg A., Gaidos E., Ansdell M., Siverd R. J., Beatty T. G., Kochanek C. S., Pepper J., Gaudi B. S., West R. G., Pollacco D., James D., Kuhn R. B., Stanek K. Z., Holoien T. W.-S., Prieto J. L., Johnson S. A., Sergi A., McCrady N., Johnson J. A., Wright J. T., Wittenmyer R. A., Horner J., 2017a, ApJ, 836, 209

Rodriguez J. E., Zhou G., Vanderburg A., Eastman J. D., Kreidberg L., Cargile P. A.,

Bieryla A., Latham D. W., Irwin J., Calkins M. L., Esquerdo G. A., Mink J., 2017b, ArXiv e-prints

Rodriguez J. E., Eastman J. D., Zhou G., Quinn S. N., Beatty T. G., Penev K., Johnson M. C., Cargile P. A., Latham D. W., Bieryla A., Collins K. A., Dressing C. D., Ciardi D. R., Relles H. M., Murawski G., Nishiumi T., Yonehara A., Lund M. B., Stevens D. J., Stassun K. G., Gaudi B. S., Colón K. D., Pepper J., Narita N., Awiphan S., Chuanraksasat P., Benni P., Ishimaru R., Yoshida F., Zambelli R., Garrison L. H., Wilson M. L., Cornachione M. A., Wang S. X., Labadie-Bartz J., Rodríguez R., Siverd R. J., Yao X., Bayliss D., Berlind P., Calkins M. L., Christiansen J. L., Cohen D. H., Conti D. M., Curtis I. A., Depoy D. L., Esquerdo G. A., Evans P., Feliz D., Fulton B. J., Gregorio J., Holoien T. W. S., James D. J., Jayasinghe T., Jang-Condell H., Jensen E. L. N., Johnson J. A., Joner M. D., Kielkopf J. F., Kuhn R. B., Manner M., Marshall J. L., McLeod K. K., McCrady N., Oberst T. E., Oelkers R. J., Penny M. T., Reed P. A., Sliski D. H., Shappee B. J., Stephens D. C., Stockdale C., Tan T.-G., Trueblood M., Trueblood P., Villanueva, Jr. S., Wittenmyer R. A., Wright J. T., 2019, arXiv e-prints

Rossiter R. A., 1924, ApJ, 60

Rowe J. F., Coughlin J. L., Antoci V., Barclay T., Batalha N. M., Borucki W. J., Burke C. J., Bryson S. T., Caldwell D. A., Campbell J. R., Catanzarite J. H., Christiansen J. L., Cochran W., Gilliland R. L., Girouard F. R., Haas M. R., Hełminiak K. G., Henze C. E., Hoffman K. L., Howell S. B., Huber D., Hunter R. C., Jang-Condell H., Jenkins J. M., Klaus T. C., Latham D. W., Li J., Lissauer J. J., McCauliff S. D., Morris R. L., Mullally F., Ofir A., Quarles B., Quintana E., Sabale A., Seader S., Shporer A., Smith J. C., Steffen J. H., Still M., Tenenbaum P., Thompson S. E., Twicken J. D., Van Laerhoven C., Wolfgang A., Zamudio K. A., 2015, ApJS, 217, 16

Ruciński S. M., 1973, AcA, 23, 79

Russell H. N., Merrill J. E., 1952, The determination of the elements of eclipsing binaries

Russell I. H. N., Shapley H., 1912, ApJ, 36, 239

Russell H. N., 1912a, ApJ, 35, 315

Russell H. N., 1912b, ApJ, 36, 54

Rutten R. G. M., Dhillon V. S., 1994, A&A, 288, 773

Rybicki G. B., Lightman A. P., 1979, Radiative processes in astrophysics

Ryu T., Zingale M., Perna R., 2018, MNRAS, 481, 5517

Sabotta S., Kabath P., Korth J., Guenther E. W., Dupkala D., Grziwa S., Klocova T., Skarka M., 2019, MNRAS

Safronov V. S., 1960, Annales d'Astrophysique, 23, 979

Sahlmann J., Ségransan D., Queloz D., Udry S., Santos N. C., Marmier M., Mayor M., Naef D., Pepe F., Zucker S., 2011, A&A, 525, A95

Sahlmann J., Lazorenko P. F., Ségransan D., Martín E. L., Queloz D., Mayor M., Udry S., 2013, A&A, 556, A133

Samus' N. N., Kazarovets E. V., Durlevich O. V., Kireeva N. N., Pastukhova E. N., 2017, Astronomy Reports, 61, 80

Santerne A., Díaz R. F., Almenara J.-M., Lethuillier A., Deleuil M., Moutou C., 2013, in Cambresy L., Martins F., Nuss E., Palacios A., eds, SF2A-2013: Proceedings of the Annual meeting of the French Society of Astronomy and Astrophysics, p. 555

Santerne A., Hébrard G., Lillo-Box J., Armstrong D. J., Barros S. C. C., Demangeon O., Barrado D., Debackere A., Deleuil M., Delgado Mena E., Montalto M., Pollacco

D., Osborn H. P., Sousa S. G., Abe L., Adibekyan V., Almenara J.-M., André P., Arlic G., Barthe G., Bendjoya P., Behrend R., Boisse I., Bouchy F., Boussier H., Bretton M., Brown D. J. A., Carry B., Cailleau A., Conseil E., Coulon G., Courcol B., Dauchet B., Dalouzy J.-C., Deldem M., Desormières O., Dubreuil P., Fehrenbach J.-M., Ferratfiat S., Girelli R., Gregorio J., Jaecques S., Kugel F., Kirk J., Labrevoir O., Lachurié J.-C., Lam K. W. F., Le Guen P., Martinez P., Maurin L. P. A., McCormac J., Pioppa J.-B., Quadri U., Rajpurohit A., Rey J., Rivet J.-P., Roy R., Santos N. C., Signoret F., Strabla L., Suarez O., Toublanc D., Tsantaki M., Vienney J.-M., Wilson P. A., Bachschmidt M., Colas F., Gerteis O., Louis P., Mario J.-C., Marlot C., Montier J., Perroud V., Pic V., Romeuf D., Ubaud S., Verilhac D., 2016, ApJ, 824, 55

Santos N. C., Adibekyan V., Figueira P., Andreasen D. T., Barros S. C. C., Delgado-Mena E., Demangeon O., Faria J. P., Oshagh M., Sousa S. G., Viana P. T. P., Ferreira A. C. S., 2017, A&A, 603, A30

Schlafly E. F., Finkbeiner D. P., 2011, ApJ, 737, 103

Schlaufman K. C., 2018, ApJ, 853, 37

Schlesinger F., 1910, Publications of the Allegheny Observatory of the University of Pittsburgh, 1, 123

Schneider J., Definition of Exoplanets and Brown Dwarfs, p. 611, Springer International Publishing, Cham, 2018

See T. J. J., 1895, AJ, 15, 180

Sestito P., Randich S., 2005, A&A, 442, 615

Sestovic M., Demory B.-O., Queloz D., 2018, A&A, 616, A76

Shporer A., Jenkins J. M., Rowe J. F., Sanderfer D. T., Seader S. E., Smith J. C., Still M. D., Thompson S. E., Twicken J. D., Welsh W. F., 2011, AJ, 142, 195

Shporer A., O'Rourke J. G., Knutson H. A., Szabó G. M., Zhao M., Burrows A., Fortney J., Agol E., Cowan N. B., Desert J.-M., Howard A. W., Isaacson H., Lewis N. K., Showman A. P., Todorov K. O., 2014, ApJ, 788, 92

Siverd R. J., Beatty T. G., Pepper J., Eastman J. D., Collins K., Bieryla A., Latham D. W., Buchhave L. A., Jensen E. L. N., Crepp J. R., Street R., Stassun K. G., Gaudi B. S., Berlind P., Calkins M. L., DePoy D. L., Esquerdo G. A., Fulton B. J., Fűrész G., Geary J. C., Gould A., Hebb L., Kielkopf J. F., Marshall J. L., Pogge R., Stanek K. Z., Stefanik R. P., Szentgyorgyi A. H., Trueblood M., Trueblood P., Stutz A. M., van Saders J. L., 2012, ApJ, 761, 123

Siverd R. J., Collins K. A., Zhou G., Quinn S. N., Gaudi B. S., Stassun K. G., Johnson M. C., Bieryla A., Latham D. W., Ciardi D. R., Rodriguez J. E., Penev K., Pinsonneault M., Pepper J., Eastman J. D., Relles H., Kielkopf J. F., Gregorio J., Oberst T. E., Aldi G. F., Esquerdo G. A., Calkins M. L., Berlind P., Dressing C. D., Patel R., Stevens D. J., Beatty T. G., Lund M. B., Labadie-Bartz J., Kuhn R. B., Colón K. D., James D., Yao X., Johnson J. A., Wright J. T., McCrady N., Wittenmyer R. A., Johnson S. A., Sliski D. H., Jensen E. L. N., Cohen D. H., McLeod K. K., Penny M. T., Joner M. D., Stephens D. C., Villanueva, Jr. S., Zambelli R., Stockdale C., Evans P., Tan T.-G., Curtis I. A., Reed P. A., Trueblood M., Trueblood P., 2018, AJ, 155, 35

Skrutskie M. F., Cutri R. M., Stiening R., Weinberg M. D., Schneider S., Carpenter J. M., Beichman C., Capps R., Chester T., Elias J., Huchra J., Liebert J., Lonsdale C., Monet D. G., Price S., Seitzer P., Jarrett T., Kirkpatrick J. D., Gizis J. E., Howard E., Evans T., Fowler J., Fullmer L., Hurt R., Light R., Kopan E. L., Marsh K. A., McCallon H. L., Tam R., Van Dyk S., Wheelock S., 2006, AJ, 131, 1163

Smalley B., Anderson D. R., Collier Cameron A., Hellier C., Lendl M., Maxted P. F. L., Queloz D., Triaud A. H. M. J., West R. G., Bentley S. J., Enoch B., Gillon M.,

Lister T. A., Pepe F., Pollacco D., Segransan D., Smith A. M. S., Southworth J., Udry S., Wheatley P. J., Wood P. L., Bento J., 2011, A&A, 526, A130

Southworth J., 2011, MNRAS, 417, 2166

Spiegel D. S., Burrows A., Milsom J. A., 2011, ApJ, 727, 57

Spiegel D. S., Silverio K., Burrows A., 2009, ApJ, 699, 1487

Stassun K. G., Torres G., 2018, ApJ, 862, 61

Stassun K. G., Oelkers R. J., Pepper J., Paegert M., De Lee N., Torres G., Latham D. W., Charpinet S., Dressing C. D., Huber D., Kane S. R., Lépine S., Mann A., Muirhead P. S., Rojas-Ayala B., Silvotti R., Fleming S. W., Levine A., Plavchan P., 2018, AJ, 156, 102

Stetson P. B., 1987, PASP, 99, 191

Stevenson K. B., Bean J. L., Madhusudhan N., Harrington J., 2014, ApJ, 791, 36

Storch N. I., Lai D., Anderson K. R., 2017, MNRAS, 465, 3927

Struve O., 1952, The Observatory, 72, 199

Sumi T., Kamiya K., Bennett D. P., Bond I. A., Abe F., Botzler C. S., Fukui A., Furusawa K., Hearnshaw J. B., Itow Y., Kilmartin P. M., Korpela A., Lin W., Ling C. H., Masuda K., Matsubara Y., Miyake N., Motomura M., Muraki Y., Nagaya M., Nakamura S., Ohnishi K., Okumura T., Perrott Y. C., Rattenbury N., Saito T., Sako T., Sullivan D. J., Sweatman W. L., Tristram P. J., Udalski A., Szymański M. K., Kubiak M., Pietrzyński G., Poleski R., Soszyński I., Wyrzykowski Ł., Ulaczyk K., Microlensing Observations in Astrophysics (MOA) Collaboration, 2011, Nature, 473, 349

Talens G. J. J., Albrecht S., Spronck J. F. P., Lesage A.-L., Otten G. P. P. L., Stuik R., Van Eylen V., Van Winckel H., Pollacco D., McCormac J., Grundahl F., Fredslund Andersen M., Antoci V., Snellen I. A. G., 2017a, A&A, 606, A73

Talens G. J. J., Albrecht S., Spronck J. F. P., Lesage A.-L., Otten G. P. P. L., Stuik R., Van Eylen V., Van Winckel H., Pollacco D., McCormac J., Grundahl F., Fredslund Andersen M., Antoci V., Snellen I. A. G., 2017b, A&A, 606, A73

Talens G. J. J., Spronck J. F. P., Lesage A.-L., Otten G. P. P. L., Stuik R., Pollacco D., Snellen I. A. G., 2017c, A&A, 601, A11

Talens G. J. J., Justesen A. B., Albrecht S., McCormac J., Van Eylen V., Otten G. P. P. L., Murgas F., Palle E., Pollacco D., Stuik R., Spronck J. F. P., Lesage A.-L., Grundahl F., Fredslund Andersen M., Antoci V., Snellen I. A. G., 2018, A&A, 612, A57

Tamuz O., Mazeh T., Zucker S., 2005, MNRAS, 356, 1466

Teitler S., Königl A., 2014, ApJ, 786, 139

Temple L. Y., Hellier C., Albrow M. D., Anderson D. R., Bayliss D., Beatty T. G., Bieryla A., Brown D. J. A., Cargile P. A., Collier Cameron A., Collins K. A., Colón K. D., Curtis I. A., D'Ago G., Delrez L., Eastman J., Gaudi B. S., Gillon M., Gregorio J., James D., Jehin E., Joner M. D., Kielkopf J. F., Kuhn R. B., Labadie-Bartz J., Latham D. W., Lendl M., Lund M. B., Malpas A. L., Maxted P. F. L., Myers G., Oberst T. E., Pepe F., Pepper J., Pollacco D., Queloz D., Rodriguez J. E., Ségransan D., Siverd R. J., Smalley B., Stassun K. G., Stevens D. J., Stockdale C., Tan T. G., Triaud A. H. M. J., Udry S., Villanueva S., West R. G., Zhou G., 2017, MNRAS, 471, 2743

Temple L. Y., Hellier C., Almleaky Y., Anderson D. R., Bouchy F., Brown D. J. A., Burdanov A., Cameron C., Delrez L., Gillon M., Hall R., Jehin E., Lendl M., Maxted P. F. L., Nielsen L. D., Pepe F., Pollacco D., Queloz D., Ségransan D., Smalley B., Sohy S., Thompson S., Triaud A. H. M. J., Turner O. D., Udry S., West R. G., 2018, MNRAS, 480, 5307

Temple L. Y., Hellier C., Almleaky Y., Anderson D. R., Bouchy F., Brown D. J. A., Burdanov A., Collier Cameron A., Delrez L., Gillon M., Jehin E., Lendl M.,

Maxted P. F. L., Murray C., Nielsen L. D., Pepe F., Pollacco D., Queloz D., Ségransan D., Smalley B., Thompson S., Triaud A. H. M. J., Turner O. D., Udry S., West R. G., 2019a, AJ, 157, 141

Temple L. Y., Hellier C., Anderson D. R., Barkaoui K., Bouchy F., Brown D. J. A., Burdanov A., Collier Cameron A., Delrez L., Ducrot E., Evans D., Gillon M., Jehin E., Lendl M., Maxted P. F. L., McCormac J., Murray C., Nielsen L. D., Pepe F., Pollacco D., Queloz D., Ségransan D., Smalley B., Thompson S., Triaud A. H. M. J., Turner O. D., Udry S., West R. G., Zouhair B., 2019b, MNRAS, 490(2), 2467

Thorngren D. P., Fortney J. J., 2018, AJ, 155, 214

Todorov K., Luhman K. L., McLeod K. K., 2010, ApJL, 714, L84

Torres G., Andersen J., Giménez A., 2010, A&A Rv, 18, 67

Triaud A. H. M. J., The Rossiter–McLaughlin Effect in Exoplanet Research, p. 1, Springer International Publishing, Cham, 2017

Udalski A., Szymański M. K., Szymański G., 2015, AcA, 65, 1

Valsecchi F., Rasio F. A., 2014, ApJ, 786, 102

van de Kamp P., 1982, Vistas in Astronomy, 26, 141

Vanderspek R., Huang C. X., Vanderburg A., Ricker G. R., Latham D. W., Seager S., Winn J. N., Jenkins J. M., Burt J., Dittmann J., Newton E., Quinn S. N., Shporer A., Charbonneau D., Irwin J., Ment K., Winters J. G., Collins K. A., Evans P., Gan T., Hart R., Jensen E. L. N., Kielkopf J., Mao S., Waalkes W., Bouchy F., Marmier M., Nielsen L. D., Ottoni G., Pepe F., Ségransan D., Udry S., Henry T., Paredes L. A., James H.-S., Hinojosa R. H., Silverstein M. L., Palle E., Berta-Thompson Z., Crossfield I., Davies M. D., Dragomir D., Fausnaugh M., Glidden A., Pepper J., Morgan E. H., Rose M., Twicken J. D., Villaseñor J. N. S.,

Yu L., Bakos G., Bean J., Buchhave L. A., Christensen-Dalsgaard J., Christiansen J. L., Ciardi D. R., Clampin M., De Lee N., Deming D., Doty J., Jernigan J. G., Kaltenegger L., Lissauer J. J., McCullough P. R., Narita N., Paegert M., Pal A., Rinehart S., Sasselov D., Sato B., Sozzetti A., Stassun K. G., Torres G., 2019, ApJL, 871, L24

Vincent A., Piskunov N. E., Tuominen I., 1993, A&A, 278, 523

Vogel H. C., 1890, Astronomische Nachrichten, 123, 289

Vogt S. S., Penrod G. D., 1983, PASP, 95, 565

von Essen C., Czesla S., Wolter U., Breger M., Herrero E., Mallonn M., Ribas I., Strassmeier K. G., Morales J. C., 2014, A&A, 561, A48

Vorobyov E. I., 2013, A&A, 552, A129

Walker G. A. H., Bohlender D. A., Walker A. R., Irwin A. W., Yang S. L. S., Larson A., 1992, ApJL, 396, L91

Weiss A., Schlattl H., 2008, Ap&SS, 316, 99

Wheatley P. J., West R. G., Goad M. R., Jenkins J. S., Pollacco D. L., Queloz D., Rauer H., Udry S., Watson C. A., Chazelas B., Eigmüller P., Lambert G., Genolet L., McCormac J., Walker S., Armstrong D. J., Bayliss D., Bento J., Bouchy F., Burleigh M. R., Cabrera J., Casewell S. L., Chaushev A., Chote P., Csizmadia S., Erikson A., Faedi F., Foxell E., Gänsicke B. T., Gillen E., Grange A., Günther M. N., Hodgkin S. T., Jackman J., Jordán A., Louden T., Metrailler L., Moyano M., Nielsen L. D., Osborn H. P., Poppenhaeger K., Raddi R., Raynard L., Smith A. M. S., Soto M., Titz-Weider R., 2018, MNRAS, 475, 4476

Whitworth A., 2018, arXiv e-prints

Winn J. N., Fabrycky D. C., 2015, ARA&A, 53, 409

Winn J. N., 2010, ArXiv e-prints

Winn J. N., Fabrycky D., Albrecht S., Johnson J. A., 2010, ApJL, 718, L145

Wolszczan A., 1994, Science, 264, 538

Wood D. B., 1973, Publications of the Astronomical Society of the Pacific, 85, 253

Wright J. T., Gaudi B. S., Exoplanet Detection Methods, 489, 2013

Wu Y., Murray N., 2003, ApJ, 589, 605

Wyttenbach A., Ehrenreich D., Lovis C., Udry S., Pepe F., 2015, A&A, 577, A62

Yadav R. K., Thorngren D. P., 2017, ApJL, 849, L12

Yan F., Henning T., 2018, Nature Astronomy

Zhou G., Latham D. W., Bieryla A., Beatty T. G., Buchhave L. A., Esquerdo G. A., Berlind P., Calkins M. L., 2016a, MNRAS, 460, 3376

Zhou G., Rodriguez J. E., Collins K. A., Beatty T., Oberst T., Heintz T. M., Stassun K. G., Latham D. W., Kuhn R. B., Bieryla A., Lund M. B., Labadie-Bartz J., Siverd R. J., Stevens D. J., Gaudi B. S., Pepper J., Buchhave L. A., Eastman J., Colón K., Cargile P., James D., Gregorio J., Reed P. A., Jensen E. L. N., Cohen D. H., McLeod K. K., Tan T. G., Zambelli R., Bayliss D., Bento J., Esquerdo G. A., Berlind P., Calkins M. L., Blancato K., Manner M., Samulski C., Stockdale C., Nelson P., Stephens D., Curtis I., Kielkopf J., Fulton B. J., DePoy D. L., Marshall J. L., Pogge R., Gould A., Trueblood M., Trueblood P., 2016b, AJ, 152, 136

Zhou G., Bakos G. Á., Hartman J. D., Latham D. W., Torres G., Bhatti W., Penev K., Buchhave L., Kovács G., Bieryla A., Quinn S., Isaacson H., Fulton B. J., Falco E., Csubry Z., Everett M., Szklenar T., Esquerdo G., Berlind P., Calkins M. L., Béky B., Knox R. P., Hinz P., Horch E. P., Hirsch L., Howell S. B., Noyes R. W., Marcy G., de Val-Borro M., Lázár J., Papp I., Sári P., 2017, AJ, 153, 211

Zhou G., Bakos G. Á., Bayliss D., Bento J., Bhatti W., Brahm R., Csubry Z., Espinoza N., Hartman J. D., Henning T., Jordán A., Mancini L., Penev K., Rabus M., Sarkis P., Suc V., de Val-Borro M., Rodriguez J. E., Osip D., Kedziora-Chudczer L., Bailey J., Tinney C. G., Durkan S., Lázár J., Papp I., Sári P., 2019a, AJ, 157, 31

Zhou G., Huang C. X., Bakos G. Á., Hartman J. D., Latham D. W., Quinn S. N., Collins K. A., Winn J. N., Wong I., Kovács G., Csubry Z., Bhatti W., Penev K., Bieryla A., Esquerdo G. A., Berlind P., Calkins M. L., de Val-Borro M., Noyes R. W., Lázár J., Papp I., Sári P., Kovács T., Buchhave L. A., Szklenár T., Beky B., Johnson M. C., Cochran W. D., Kniazev A. Y., Stassun K. G., Fulton B. J., Shporer A., Espinoza N., Bayliss D., Everett M., Howell S. B., Hellier C., Anderson D. R., Collier Cameron A., West R. G., Brown D. J. A., Schanche N., Barkaoui K., Pozuelos F., Gillon M., Jehin E., Benkhaldoun Z., Daassou A., Ricker G., Vanderspek R., Seager S., Jenkins J. M., Lissauer J. J., Armstrong J. D., Collins K. I., Gan T., Hart R., Horne K., Kielkopf J. F., Nielsen L. D., Nishiumi T., Narita N., Palle E., Relles H. M., Sefako R., Tan T. G., Davies M., Goeke R. F., Guerrero N., Haworth K., Villanueva S., 2019b, arXiv e-prints

Zhou G., Huang C. X., Bakos G. Á., Hartman J. D., Latham D. W., Quinn S. N., Collins K. A., Winn J. N., Wong I., Kovács G., Csubry Z., Bhatti W., Penev K., Bieryla A., Esquerdo G. A., Berlind P., Calkins M. L., de Val-Borro M., Noyes R. W., Lázár J., Papp I., Sári P., Kovács T., Buchhave L. A., Szklenar T., Béky B., Johnson M. C., Cochran W. D., Kniazev A. Y., Stassun K. G., Fulton B. J., Shporer A., Espinoza N., Bayliss D., Everett M., Howell S. B., Hellier C., Anderson D. R., Collier Cameron A., West R. G., Brown D. J. A., Schanche N., Barkaoui K., Pozuelos F., Gillon M., Jehin E., Benkhaldoun Z., Daassou A., Ricker G., Vand erspek R., Seager S., Jenkins J. M., Lissauer J. J., Armstrong J. D., Collins K. I., Gan T., Hart R., Horne K., Kielkopf J. F., Nielsen L. D., Nishiumi T., Narita N., Palle E., Relles H. M., Sefako R., Tan T. G., Davies M., Goeke R. F., Guerrero N., Haworth K., Villanueva S., 2019c, AJ, 158(4), 141